The Dynamics of Buoyant Releases in Confined Spaces

Steven John Barnett

Submitted to the University of Cambridge
for the degree of
Doctor of Philosophy

Emmanuel College
October 1991

The Dynamics of Buoyant Releases in Confined Spaces
by
Steven John Barnett

SUMMARY

The flows that may result from the release of a buoyant fluid from a small source in a confined space are varied and complex, depending on the source characteristics, the confining geometry and container ventilation. Previous work has generally been based on the 'filling-box' model (Baines & Turner 1969). This model, however, may only be applied when the source has little or no initial momentum, is in a container with a height/width aspect ratio less than unity and does not interact with the side boundaries. In this thesis some situations in which the 'filling-box' model may not be applied are investigated.

In chapter 1 the 'filling-box' model and the work based on it are reviewed and its limitations discussed. Sources are usually modelled as a turbulent jet, plume or buoyant jet; thus in chapter 2 the established properties of jets and plumes are summarised using established theoretical arguments and experimental results. In order to improve some of the theoretical predictions, the effects of previously neglected second order terms and intermittency factor variation are investigated.

In most practical situations the source is a buoyant jet. In chapter 3 the flow of an initially horizontal buoyant jet is examined, concentrating on obtaining simple analytical results from the conservation equations and investigating the effect of the nature of the entrainment assumption.

The effect of source momentum is examined in chapter 4, in which the flow of a vertical jet with high initial momentum flux in a long, ventilated tunnel is studied. The bulk flow variables are deduced and compared with experimental measurements. A method for calculating the total number of vents required to vent the source fluid is given - this result is particularly important in applications to hazardous releases.

In chapter 5 the effect of the aspect ratio, a, on the 'filling-box' model is investigated. It is found that when the aspect ratio is very large ($a \gtrsim 6$) the flow is quite different to that observed in the 'filling-box' case. Theoretical models are derived both when $a \gtrsim 6$ and when $a \lesssim 6$, and the results are compared with experimental measurements. In chapter 6 the study of chapter 5 is extended, investigating the effect of placing the tank at an angle to the vertical. The flow in the large aspect ratio case is significantly different to that of chapter 5 and is modelled theoretically, comparing the predictions with experimental measurements.

Finally, in chapter 7 the general results are reviewed. The current knowledge of flows resulting from buoyant releases in a confined space is then summarised in a simple tabular form, which also indicates areas for future research.

Preface

The research described in this thesis was carried out from October 1988 to September 1991 in the Department of Applied Mathematics and Theoretical Physics, University of Cambridge. Except where stated it represents my own work and includes nothing that is the outcome of work done in collaboration. No part of this thesis has been submitted for a degree, diploma or any other qualification at any other university.

I would like to thank my supervisor, Dr P.F. Linden, for his encouragement and advice, and for his careful reading of the drafts of this thesis. I would also like to thank Dr R.P. Cleaver for many helpful suggestions and for providing an industrial viewpoint.

I am also grateful to the members of my research group for not only making DAMTP a stimulating environment, but for providing many good laughs too. Thanks are also due to my friends at Emmanuel whom have made Cambridge such an enjoyable place and to Emmanuel College itself for the use of their pianos.

Finally, I would like to thank my family for their love and support throughout my student years; special thanks go to Lucy for her love, patience and encouragement.

Financial support has been provided by the Science and Engineering Research Council and British Gas PLC., and I am also grateful for some generous conference funding from the Department and Emmanuel College.

Steven J Barnett

to my family

Contents

Chapter One

General Introduction

There are a large and diverse number of flows that may result from the release of a buoyant fluid in a confined space, including the flow of the buoyant jet itself, the effects of the confining geometry and the interaction between the source and its environment.

The majority of previous research has been based on the 'filling-box' model. This model is described and its limitations are discussed, followed by a brief review of the further work based on it. The basic experimental procedures that have been used in this thesis are then described. The chapter ends with a plan of the thesis.

---

1. Motivation

The dynamics of a release of buoyant fluid in a confined space have applications in many areas, including industry, the environment and geophysical flows. For example, a leakage of natural gas or smoke from a fire in a building, dumping of chemical waste or convection in the surface layer of the ocean could all be considered as confined buoyant releases. Gas leakages are often confined by the boundaries of the building; buoyant releases in the environment or convective elements in geophysical flows can be effectively confined by density interfaces, a free surface or the presence of other sources.

The dynamics of a continuous buoyant release in a volume of limited extent are inherently different to that of a release in an infinite space. In a confined region the flow of the source increasingly contaminates the environment which is therefore being modified as the flow continues. Conversely, this modification of the environment continuously affects the behaviour of the source.

It is desirable to be able to predict the flow produced by a buoyant release in a given physical situation. For example, in the case of natural gas leaking in a room or building, it would be advantageous to be able to predict the maximum gas concentrations reached after a given length of time and the motion of the escaping gas. To predict the flow, the factors that affect it must be understood. In general, such flows are controlled by:

i) the source characteristics (i.e. the source volume, momentum and buoyancy fluxes);

ii) the source orientation with respect to the container;

iii) the geometry of the container;

iv) interaction between the source and the container boundaries;

v) ventilation of the container.

Since each of these factors will play a part in determining the resultant flow, by studying their effects a greater understanding of the overall problem will be gained. In the above case of the gas leak, such knowledge could be used to prevent hazardous concentrations from being reached, for example by including suitable ventilation or design features in the building.

2. Previous work - the 'filling-box' model

The majority of previous research on the release of a buoyant fluid in a confined space has been based on the 'filling-box' model, the name given by Turner (1973) to the theory of Baines & Turner (1969) describing the flow produced by convection from a source in a confined region.

This model will now be described and its limitations discussed. Some of the work that has been developed from it will then be reviewed briefly.

2.1 The 'filling-box' model

Consider the convection flow from a point source at the base of a container which is chosen, for simplicity, to be a rectangular tank (see figure 1). It is assumed that the convecting fluid is lighter than that of its environment and forms a plume which flows up towards the top of the tank. When the plume fluid first reaches the top of the tank it spreads out in a thin horizontal layer with a density discontinuity or front below it. The dynamics of the horizontal spreading-out flow are ignored and it is assumed that the stable stratification surpresses any mixing with the environment. The plume fluid entering this thin layer now entrains fluid that is lighter than the original environmental fluid and so the plume fluid now reaching the

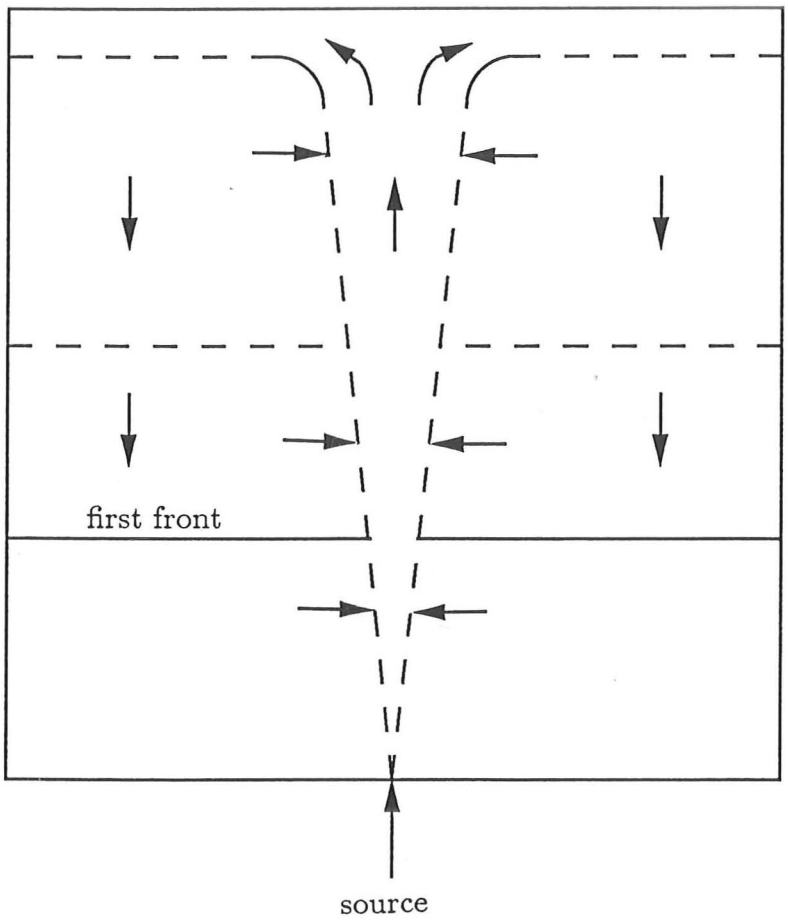

FIGURE 1. A schematic diagram of the 'filling-box' model of Baines & Turner (1969). The diagram shows the motions of the plume, the environment and the entrainment flow, with the position of the first front marked at two times.

top of the container is lighter than the preceding layer. Hence when this plume fluid spreads horizontally, the first density front formed is pushed down with the lighter layer above it. This process continues, leading to increasing stratification of the environmental fluid.

Baines & Turner (1969) conducted several experiments to illustrate the stability of the environmental stratification by injecting dye into the plume. They observed that the dyed layers remained horizontal and well defined, as they are pushed down the tank.

The fully time-dependent problem has proved to be impossible to solve analytically, although Worster & Huppert (1983) have obtained approximate analytical solutions which agreed well with their numerical results. Baines & Turner (1969) were able to derive an expression for the position of the first front as this effectively depends only on the motion of the plume in the uncontaminated environmental fluid ahead of it (see Morton, Taylor & Turner 1956). By assuming that the density profiles increase linearly in time with a fixed distribution, they were able to derive a solution for the asymptotic state achieved at large times in which the plume properties are asymptotically constant in time. The analytical results agreed well with their experiments.

2.2 Limitations of the model

In the description of the model above it is clear that it relies on several assumptions which restrict its application.

Firstly, the source is required to be one of buoyancy only. Inputs with a non-zero initial volume flux are usually relatively unimportant as the volume increases they imply for closed containers can be accommodated by including vents or a free surface (particularly in experiments), depending on the problem being considered. In general the volume flux of the source will be much smaller than the volume of the container and so the velocities induced (and hence the effects on the flow) by having, say, a vent on a remote boundary would be negligible. There may be situations in which this is not the case, for example the removal of natural gas from a pipe section by purging it with nitrogen, but in these situations the high volume flux of the source is an essential part of the flow and cannot be neglected.

What may be more important is the effect of a source with a significant non-zero initial momentum flux. In this case, when the buoyant jet impinges on the tank boundary, its additional momentum means that the effect of the impingement 'splash' will be important, causing mixing of the environment. Thus in the 'filling-box' model, if the source had a

significant non-zero initial momentum flux, then the assumption that the plume fluid spreads out horizontally, with little mixing of the environment, may not be valid. For sources with small initial momentum, this effect may not be important as the buoyancy of the fluid will increasingly dominate the momentum forces with increasing distance from the source and the behaviour will be plume-like when it reaches the top of the tank. However if the source has high momentum (for example, if the source was a high velocity gas leak), then any impingement of the source on a boundary could cause mixing of the environment which may totally alter the nature of the flow.

Even if the source is a pure plume, its momentum flux will increase with increasing distance from the source. Thus over-turning of the environment could still occur if the momentum flux at the top of the container was significantly larger than the stabilising buoyancy force of the stratified environment. Baines & Turner (1969) showed that this momentum/buoyancy ratio, reflective of the tendency towards over-turning, is proportional to the square of the aspect (height/width) ratio, a, of the tank. Baines & Turner (1969) conducted some experiments to investigate the effect of varying the aspect ratio, finding indications of over-turning when $a > 1$. Consequently they restricted their analysis to containers in which the height is less than or equal to the width.

There are further idealisations made in the model which might not be realised in physical situations. In particular, it was assumed that there was no interaction between the plume and the boundaries of the container (except at the top). In practice it is unlikely that the source would be in the centre of the container and vertically directed. The effects of source position and orientation are unlikely to have major effects for a purely buoyant release. However if the source has high momentum, any interaction with the boundary could significantly affect the flow.

2.3 Previous research based on the 'filling-box' model

Although the theory has some limitations, as described above, it has been readily applied and developed to model many other physical situations.

Germeles (1975) used the theory to model a phenomenon known as tank 'roll-over' which can occur when additional liquified natural gas (LNG) is injected into a tank containing LNG at a slightly different density (see figure 2). This injection can result in stratification of the liquid gas (in the 'filling-box' manner). The compositional and temperature gradients may

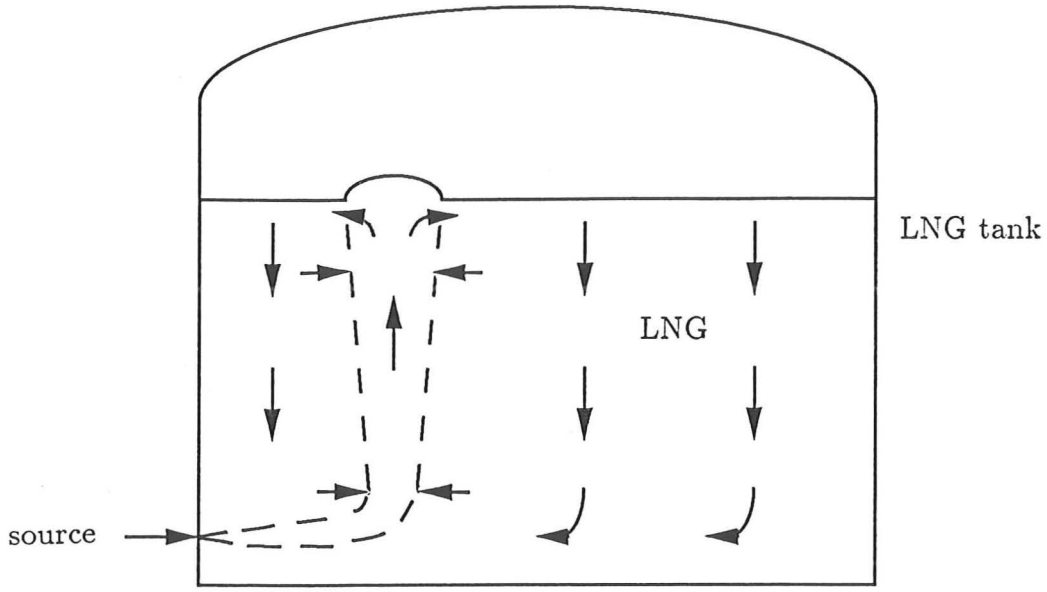

FIGURE 2. The LNG tank injection problem considered by Germeles (1975).

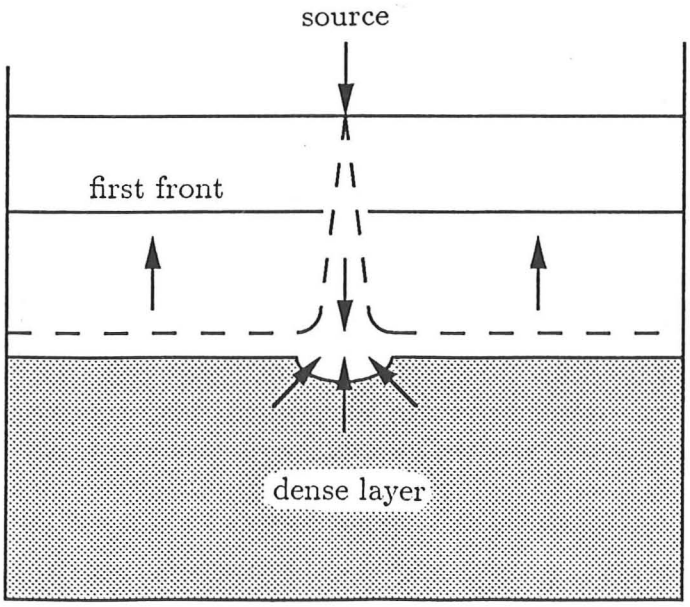

FIGURE 3. The two-layer problem considered by Kumagai (1984) showing the entrainment into the plume as it impinges on the interface and the position of the first front.

cause overturning ('roll-over'), resulting in a large-scale boil-off of methane vapour, which can lead to dangerously high pressures within the tank. Germeles modelled the flow using the 'filling-box' equations, modified to include mass inputs by allowing the free surface to rise. He used a numerical method to describe the unsteady development of the density distribution before the asymptotic state derived by Baines & Turner (1969) is reached and conducted experiments to check the numerical results. He also relaxed the vertical source condition, modifying the conservation equations of Morton, Taylor & Turner (1956) appropriately for inclined sources, although his equations break down in the case of an initially horizontal release. The good agreement between the numerical solution and the experimental results have helped to establish the validity of the 'filling-box' model when applied to tanks with buoyant injections from a nozzle.

The assumption of fixed rigid boundaries makes the 'filling-box' model a little unrealistic when applied to geophysical flows. Baines (1975) relaxed the condition of insulating boundaries on the upper surface to allow entrainment into the impinging plume. Kumagai (1984) considered the flow of a plume entering a two-layered region consisting of a layer of fresh water on top of a layer of salt solution (see figure 3). The plume enters at the level of the free surface and at first cannot penetrate the interface. The evolution of the fresh water layer is governed by the filling-box process, but as in the case considered by Baines (1975), there is also entrainment through the end of the plume which impinges on the density interface. Kumagai (1984) found that the entrainment rate in the upper layer (as it changes in thickness) and the buoyancy flux across the interface can be expressed as functions of the Froude number, Fr. Manins (1979) also relaxed the condition of non-conductivity of the boundaries with a diffusive boundary at the source level and diffusion of density in the environment of the plume. The radiation of buoyancy allows enclosures with intense local heating from below, for example the Earth's mantle, to be modelled. The essential aspect of the 'filling-box' process is the vertical confinement which causes the plume fluid to descend and be re-entrained; this may not be appropriate in some geophysical cases.

Killworth & Turner (1982) pointed out that buoyancy sources in nature are rarely uniform in time. They investigated the dependence of the 'filling-box' asymptotic state on the time-dependent behaviour of the source buoyancy flux, concentrating mainly on cyclic sources. Using laboratory experiments, numerical solutions and analytical theory, they showed that the asymptotic state is qualitatively similar to that which would be produced by a source of steady buoyancy flux with the same value as the maximum of the variable buoyancy flux.

In the asymptotic solution of Baines & Turner (1969), the buoyancy flux of the plume varies linearly with position. Worster & Huppert (1983) made the hypothesis that for earlier times the buoyancy flux varies linearly between the top of the tank and the position of the first front. With this approximation, they found a time-dependent analytical solution to the 'filling-box' equations which was correct at $t = 0$, tended to the asymptotic solution of Baines & Turner (1969) as $t \to \infty$ and agreed well with their numerical results.

There may be other circumstances in which the asymptotic solution of Baines & Turner (1969) may not be applicable. For example, if the density is a function of two components (for example, heat and salinity), double-diffusive phenomena may occur in the environment before the first front has advanced very far. This has been studied by McDougall (1983) who described the formation of double-diffusive interfaces, which separate the environment into discrete well-mixed layers.

Linden, Marshall & Cleaver (1991) have examined the effect of jet orientation and position on a small-scale model of a natural gas release in a closed cubical container, concentrating particularly on the flow produced when the source is some distance from the bottom of the tank. They found that, in general, for non-vertical sources, gas mixing was confined to the region above the lowest point of penetration of the jet, with weak stable stratification above it and a sharp interface between the gas and fresh layers.

Linden, Marshall & Cleaver (1991) have also conducted some experiments to investigate the effect of initial source momentum on horizontal, dense sources. A small ventilation point was provided in both the top and the bottom of a cubical test chamber to allow for the volume inputs. Three regimes were observed (see figure 4) depending on the ratio δ between the 'jet-length' L_j, the length scale of a buoyant jet (see for example Turner 1973 or chapters 2, 3 and 4) and the distance between the nozzle and the boundary nearest to it. For values of $\delta \lesssim 1$ the (negatively) buoyant fluid below the source was well-mixed with fresh water above, separated by a stable interface. For values of $1 \lesssim \delta \lesssim 6$ the jet was still nearly horizontal on impingement and mixed some of the fluid above the source, above which was layer of fresh water. The level of the interface depends on the value of δ. For values of $\delta \gtrsim 6$ the whole tank was mixed.

Linden, Lane-Serff & Smeed (1990) have discussed the fluid mechanics of 'natural ventilation', this being ventilation driven by buoyancy differences between the interior and exterior fluids of a chamber. They studied the effects of internal sources of buoyancy (which might result from radiators, people or machinery) finding that these allowed steady states to be

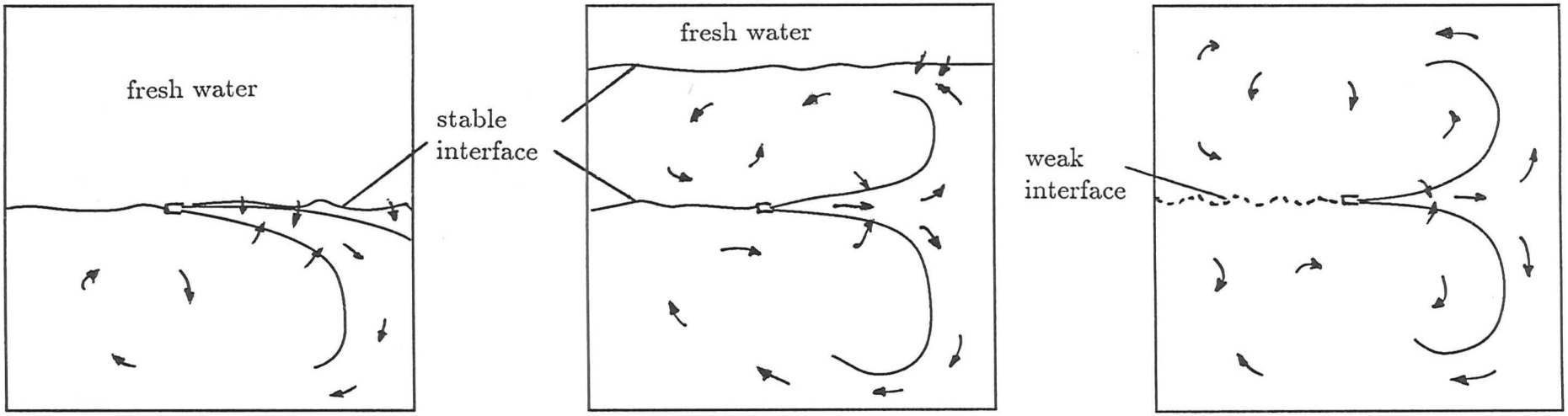

FIGURE 4. The experimental flows observed by Linden, Marshall & Cleaver (1991), showing the flow from a centrally placed horizontal nozzle with various source conditions. (*a*) $\delta \lesssim 1$; (*b*) $1 \lesssim \delta \lesssim 6$; (*c*) $6 \lesssim \delta$.

established, which they described using extended filling-box models with the addition of a continuous exchange of fluid with the environment.

Baines, Turner & Campbell (1990) studied the effect of opposing buoyancy and momentum fluxes on the 'filling-box' model. They injected dense fluid upwards from the bottom of a tank, which was initially filled with uniform fluid. The turbulent 'fountain' which formed rose to a maximum height and then fell back, spreading out along the base of the tank, to be re-entrained into the fountain. A stable stratification then built up in the 'filling-box' manner. The volume flux of the inputs was significant and was compensated for by having a free upper surface which rose in time. They found that the top of the fountain rose linearly with time at approximately half the rate of rise of the free surface. Eventually the front rose above the top of the fountain, and the density profile of the mixed fluid above the fountain then remained unchanged in time.

In summary, it is clear that the 'filling-box' model has been the subject of considerable application and development. The initial work of Baines & Turner (1969) and the results of Germeles (1975) showed that the model provides accurate predictions of the density distributions resulting from a source of buoyancy (and volume in the latter case) in a confined region. Analytical solutions exist in the asymptotic analysis for large times (Baines & Turner 1969) and approximate solutions have been derived by Worster & Huppert (1983) for earlier times. The model has been developed for application to geophysical flows by Baines (1975), Manins (1979), Killworth & Turner (1982), McDougall (1983) and Kumagai (1984). The effect of source momentum has been considered by Linden, Marshall & Cleaver (1991), the effect of container ventilation has been considered by Linden, Lane-Serff & Smeed (1990) and the effect of reversing buoyancy by Baines, Turner & Campbell (1990) for a more realistic application to industrial and domestic situations.

However, there are several areas which have been relatively neglected. Firstly the effects of a source with a high volume flux have not been examined (in the case of Baines, Turner & Campbell 1990, the volume flux was significant, but still sufficiently small for its effect on the flow to be ignored, except for the rise of the free upper surface) and also, with the exception of Linden, Marshall & Cleaver (1991), the effects of high source momentum flux have not been studied. In practical circumstances, particularly in applications to gas leakages and other industrial flows, the volume and momentum fluxes of the source may be large and may substantially affect the resultant flow. Currently there is insufficient knowledge on the flows resulting from such sources for reliable predictions to be made and so more research is

required.

Furthermore, all of the above experimental studies have been carried out with approximately cubical or flatter containers. This is to comply with the restriction that Baines & Turner (1969) made on their 'filling-box' model, limiting its application to tanks of aspect ratio less than unity. With the exception of Huppert *et al.* (1986), who measured density difference profiles in a 'filling-box' experiment in which $a = 3.5$, the effects of using a tank with aspect ratio greater than unity have received little attention.

3. Laboratory models and experimental techniques

It is always important to compare the results of theoretical or numerical work with appropriate physical measurements. In the following chapters this has been done by performing laboratory experiments, using many different techniques. The experimental procedure will be described in detail within each particular chapter - however there are some experimental techniques which have been used generally and are described here, together with some comments on the use of small-scale models.

3.1 Laboratory models

It was stated above that two of the factors controlling the flow of a buoyant release within a confined region are the geometry of the space and any interaction between the source and the container boundaries. It is not practical to examine every possible type of container experimentally. However, by choosing a geometry with one or more specific features, it is possible to investigate the effects of these features on the flow produced in order to build up an overall understanding of the dependence of the resultant flow on the container geometry.

In this thesis, particular geometries have been studied using models made from clear perspex. The ambient uniform fluid is modelled using fresh water and the buoyant fluid source using a dyed salt solution, which is heavier than water. In all of the flows studied the density differences are small and, using the Boussinesq approximation, the acceleration of a buoyant parcel (the 'reduced gravity') is given by $g' = g\Delta\rho/\rho$, where ρ is the environment density, $\Delta\rho$ is the density difference between the source and the environment and g is the acceleration due to gravity. Thus, for applications in which the source is lighter than the ambient fluid, the apparatus is simply turned upside-down (still using the relatively dense salt solution to model the source, which will flow downwards instead of up) and inverted

mentally on viewing (so that it now appears that the source fluid is less dense, flowing upwards) whilst ensuring that the absolute value of the reduced gravity in the experiment matches that of the real situation (when scaled appropriately). Much of this research may be applied to leakages of natural (or perhaps a dense) gas or the movement of smoke within a building or other confined space. It may be asked if it is appropriate to apply the predictions of a small-scale fluid model to the full-scale gaseous situation.

The use of small-scale liquid models for modelling larger-scale gas models has been justified by Lane-Serff (1989) who explained that problems will only occur if there are large temperature changes or very high velocities in the real situation. Then the flow may not be regarded as incompressible, which is presumed in the use of a water model. Problems may also arise when large density differences occur in the real situation; the use of a salt solution/water model assumes that the density differences are small. In the majority of the physical applications considered here, the velocities are not sufficient to cause compression and there are no large temperature differences: the buoyancy forces are generally a result of density differences between the source fluid and the environment due to differences in composition rather than temperature. In most cases the effects of viscosity and diffusion are also small (compared with the mixing produced by the bulk motion of the flow), so that the Reynolds and Péclet numbers are large - the flow is then independent of these numbers. Hence to model these flows in the laboratory it is necessary to ensure that the Reynolds and Péclet numbers in the experiment are also high - which should be achievable in a model using water as the environmental fluid. Linden, Marshall & Cleaver (1991) compared some small-scale water/salt solution experiments with their full-scale air/natural gas counterparts, and found good agreement in the measured concentrations.

Of course, it may not be practicable to produce a perfectly scaled model. For example, in chapter 4 the flow produced by a high momentum gas leak in a long tunnel is modelled. Suppose that the tunnel is 12 m long with square cross-section of side 60 cm, and a 1/6th scale model of it is required. This would imply a model 2 m long with square cross-section of side 10 cm. Typically, the source may be formed by gas escaping from a small crack in a pipe caused by corrosion - a hole with diameter, say, 1.2 mm. This means that the experimental nozzle should have a diameter of 0.2 mm. However, because of engineering limitations, the smallest nozzle that can be made has a diameter of 0.5 mm. Using a nozzle of this size, it is not possible to have both the exit velocity and the flow rate at the experimentally required levels.

Scale	Model/Real scale ratio
Time	$(l_M g'_R / l_R g'_M)^{\frac{1}{2}}$
Velocity	$(l_M g'_M / l_R g'_R)^{\frac{1}{2}}$
Volume flux	$(l_M^5 g'_M / l_R^5 g'_R)^{\frac{1}{2}}$
Momentum flux	$(l_M^3 g'_M / l_R^3 g'_R)$
Buoyancy flux	$(l_M^5 {g'_M}^3 / l_R^5 {g'_R}^3)^{\frac{1}{2}}$

TABLE 1. Model/Real scale ratios.

In a problem of this sort, flow-rates, density differences or some other adjustable experimental value would be altered making sure, however, that the most important flow parameters are still accurately scaled so that the model and experiment are still dynamically the same. Such adjustments may mean that the experimental results cannot be applied immediately to the real situation without first comparing the appropriate scales.

Denoting the length scale by l and the reduced gravity by g', with subscripts M for the model and R for the real situation, then the model/real ratio of the scales for time, velocity, volume flux, momentum flux and buoyancy flux are given in table 1 above (see also Lane-Serff 1989).

These ratios must be taken into account when applying experimental results to the real situation. If, say, the time scale ratios are the same in both the experiment and the model, then the model/real time scale ratio given in table 1 will have a value of unity; if this ratio has a value less than one then the experiment proceeds at a faster rate than the full-scale situation and vice-versa. In all experiments, the major consideration is of the parameters that are important to maintain dynamic similarity and the parameters that may be changed.

3.2 Experimental techniques

The experimental techniques used depends on the experiment being performed. However, the shadowgraph visualisation technique is common to all of the experiments described in this thesis and is explained below. This is followed by a description of the methods of measuring density that have been used.

3.2.1 Shadowgraph visualisation

The use of perspex models makes illumination and visualisation of experiments relatively easy, the simplest method of visualisation being the shadowgraph.

Light is shone through the apparatus onto a translucent screen fixed to the side of the apparatus opposite the light (see figure 5). The shadowgraph method relies on variations in the refractive index in different parts of the fluid caused by density differences or fluctuations. In a region of uniform density stratification (i.e. the density gradient is constant) the gradient of refractive index is constant, and the image will be similar to that obtained from a region of uniform density. However, if there are large variations in the density gradient (i.e. large values of the second derivative of the density) then there will be large variations in the gradient of the refractive index of the fluid which are marked by light and dark areas on the image. These move with the flow and provide a good method of visualising the motion of the fluid. Clearly it is the changes in the density gradient through the apparatus perpendicular to the screen that are observed, making this method particularly suitable for visualising two-dimensional flows. In three dimensional flows, the shadowgraph technique may still be used to visualise the flow in a particular plane, illuminating with a single sheet of light. It is also clear that it is important to have as near parallel a beam as possible through the apparatus to minimise the parallax in the projected image on the screen. This is usually achieved by placing the light source far from the apparatus or by using a suitable lens.

3.2.2 Density measurement

The need for accurate density measurements is important in all of the experiments performed in this thesis. There are several methods of measuring density, for example, the refractometer, electronic density meter, conductivity probes and digital video analysis. All but the third of these methods have been used, usually in conjunction with one another.

Refractometer

The refractometer is the easiest method of measuring the density of salt solution and is used when rapid measurements or quick estimates of density are required. Like the shadowgraph above it uses the property of salt solution that the refractive index varies with density (i.e. salt concentration). The refractive index is measured as light passes through a drop of solution and is then compared with a data table to calculate the density. This method is normally used when preparing large tanks of salt solution. Measuring density using a refractometer requires a sample size of less than 1 ml and is accurate to within $0.5 \times 10^{-3}\,\mathrm{g\,cm^{-3}}$.

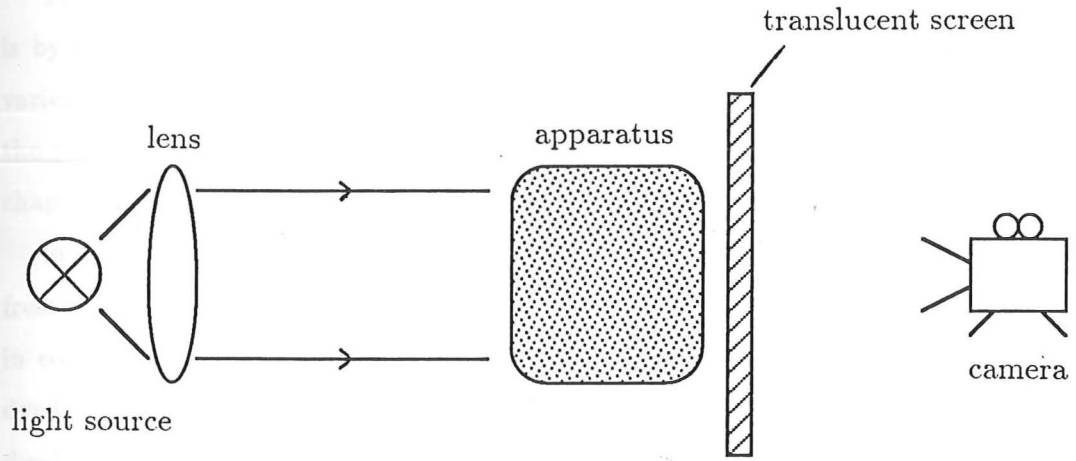

FIGURE 5. The shadow-graph visualisation technique. A parallel light source is shone through the apparatus onto a translucent screen. The image caused by refraction effects is recorded onto video tape or simply observed by eye.

Density meter

The density of liquids can be found electronically using an Anton Paar density meter which measures the resonant frequency of a small tube filled with the sample. This method is up to 3000 times more accurate than the refractometer but takes a few minutes for each measurement to be made. This method is normally used to measure the density of samples taken from an experiment and for use in calibrating the digital measurements below.

Digital video analysis

The most recently developed method for measuring densities and concentration variations is by digital analysis of a video tape of the experiment. The application of this technique varies depending on the experiment and so only a brief general description is given here - the particular approach for each experiment will be described in more detail in the relevant chapter.

In order to use this method the source fluid is dyed (whereas the environment fluid, usually fresh water, is clear), with the observed variations in dye intensity corresponding to variations in concentration. The experimental apparatus must be clear, so that when illuminated the dyed fluid is clearly visible (for example on a shadowgraph screen). The flow of the buoyant, dyed fluid may then be captured easily on video tape whilst the experiment is running.

The video picture is divided digitally into a grid of pixels and the intensity of each pixel is calculated and given an integer value between 0 (black) and 255 (white). Variations in the background illumination can be removed by dividing the intensities of the picture by those of the background (from an initial frame) at each point. It will be shown that the dye concentration varies linearly with measured intensity for small dye concentrations. So by making one density measurement at a specific point in the flow from a fluid sample (using the Paar density meter) and comparing it to the intensity value there, it is easy to calculate the density/intensity relationship.

In practice more than one density measurement is made for greater reliability. An intensity/concentration calibration experiment is carried out before each group of experiments to calculate the concentration at which non-linearity in the intensity/concentration relationship becomes significant for that particular experimental apparatus. The measured intensity will also vary with the thickness of the dyed region. It is important to point out that the refractometer and density meter measure the density of a sample of fluid drawn from a specific point of the flow; the digital technique measures the mean density (i.e. an integrated measurement) on a line through the flow between the light source and the camera, although

point measurements may be made by illuminating the experiment with a single sheet of light passing through it.

4. A plan of this thesis

It is clear from section 2.3 that the 'filling-box' model has been developed and applied to a large variety of cases. However, there are still problems to solve and questions to answer. In this thesis some flows resulting from a release of buoyancy in a confined space, in which the 'filling-box' model may not be applied, are investigated.

Throughout this thesis and in all of the previous work, the release of fluid has been modelled as a buoyant jet. In chapter 2, the existing basic theoretical and experimental knowledge of jets and plumes is reviewed. Dimensional arguments are used to calculate the well known axial velocity and density variations. Two methods, due to Tollmien (1926) and Goertler (1942), of modelling turbulence to derive the transverse distribution of the axial velocity component are given. In order to improve the agreement between these two theories and experimental results, the effect of including the previously neglected smaller terms and variation of the intermittency factor is then investigated.

In chapter 3 the effect of assumptions about the behaviour of the entrainment constant on a theoretical model of a buoyant jet is examined. In most models of buoyant jet behaviour, the entrainment constant has been assumed to be constant (see for example Lane-Serff 1989). However, the entrainment constant is known to be different for jets and plumes (see Fischer *et al.* 1979) and will therefore vary along the course of a buoyant jet, which undergoes a transition between these states. Assumptions on the nature of the entrainment constant in a theoretical model will therefore affect the physical accuracy of its predictions. Two contrasting assumptions are made about the behaviour of the entrainment constant in a model of the flow of an initially horizontally directed buoyant jet and the theoretical predictions are compared with experiments. Accurate knowledge of the trajectory of a buoyant jet is important when considering confined buoyant releases, as it will provide information on the likelihood of the jet impinging on the container boundaries.

In chapter 4 the effects of high source momentum and ventilation are investigated by examining the flow of a vertical, high momentum buoyant jet in a long horizontal tunnel. The high momentum of the source dramatically alters the flow from that assumed in the 'filling-box' case and so this model cannot be applied. A new model is developed in which

the bulk flow variables and concentration time-dependence are deduced and compared with experimental measurements. The effects of tunnel ventilation on the flow are studied.

In section 2.2 it was explained that 'filling-box' theory cannot be accurately applied to containers with aspect ratio greater than unity. In chapter 5 the flow resulting from a vertical plume flowing into a tall chamber (large aspect ratio) is studied. The nature of the flow is found to depend on the actual value of the aspect ratio. The applicability of the 'filling-box' equations to containers of moderate aspect ratio is investigated before presenting a model for the flow in a container of large aspect ratio. Theoretical and numerical results are compared with experiments in each case.

In chapter 6 the work of chapter 5 is continued, studying the flow from sources of buoyancy in tall angled chambers. The resultant flow is quite different to that of the vertical case. A simple model of the flow is presented and the theoretical predictions are compared with experimental measurements.

Finally the general results are reviewed in chapter 7, outlining their implications for gas leakages and applications to other practical situations. Chapter 7 concludes with a table which summarises the current understanding of confined buoyant jet flows.

Each chapter begins with a brief synopsis of its contents followed by an introduction to the subject under discussion. The chapters end with a summary of the notation used, provided for reference purposes rather than precise definitions. Sections, equations, tables and figures are numbered within each chapter and any reference to part of another chapter will be stated explicitly. The references follow chapter 7.

The emphasis throughout is on the use of simple models in the hope that, where possible, results may be obtained analytically or failing that by simple numerical analysis. In general this means that mean values are calculated; turbulence is included by modelling its effect rather than by examining the turbulent fluctuations themselves. The flow produced by a buoyant release in a confined space is often extremely complex and more detailed or sophisticated models would require the use of computational fluid dynamics (CFD) for their solution. However, CFD solutions are usually calculated for a given situation and so do not necessarily provide physical explanations for the predicted flows. Simple models, based on physical observation and interpretation, can often provide a greater understanding of the dynamical processes involved, allowing a more ready application of the results to other similar situations.

Notation

Below is a list of the symbols used in this chapter, provided for reference purposes.

a	Height/width aspect ratio of the tank
Fr	Froude number, $Fr = U^2/g'l$
g	Acceleration due to gravity
g'	Reduced gravity
I	Intensity measured by digital video analysis
l	Length scale
L_j	Length scale of a buoyant jet or 'jet-length'
$Pé$	Péclet number, $Pé = Ul/\kappa$
Re	Reynolds number, $Re = Ul/\nu$
t	Time
U	Velocity scale
δ	Ratio of L_j to the shortest distance between the jet nozzle and the nearest boundary
κ	Thermal conductivity
ν	Kinematic viscosity
ρ	Density

Chapter Two

Jets and Plumes

Throughout this thesis, the source of a buoyant release will be modelled using the theory of turbulent jets, plumes and buoyant jets. These source types are defined followed by a brief review of their properties, described using established experimental and theoretical results.

The equations of incompressible fluid motion are then stated and are applied to the flow of a turbulent jet in order to predict some of the flow characteristics observed experimentally. Many previous solutions have modelled the turbulent velocity products using either an eddy viscosity or a mixing length model and have neglected the smaller terms in the momentum equations. It has been established that neither of these models gives good agreement with the experimental results over the whole cross-section of the jet flow. In order to improve the agreement between the theoretical predictions and experimental measurements, the effect of the smaller, second order terms and the effect of variation of the turbulent intermittency factor are examined. This results in a significant improvement of the theoretical predictions, particularly near to the edge of the jet.

---

1. Introduction

In most applications of practical interest, a release of buoyant fluid is likely to originate from a source of small extent and may be modelled theoretically, using the theory of turbulent jets and plumes. For example, gas leaking into a building will probably be escaping from a small hole or crack in a pipe formed by corrosion; waste discharged into the environment may often originate from the open end of a submerged pipe or a series of jets, called a multiport diffuser. In the latter case jetting the waste into the environment is often a very effective

means of reducing its concentration, as jets and plumes entrain large volumes of ambient fluid, rapidly diluting the waste product. In all of the flows resulting from buoyant releases in confined spaces considered later in this thesis, the source will be modelled as a buoyant jet or plume and so it is important to review the basic properties of jets and plumes.

A *jet* is the discharge of fluid from an orifice into a large body of the same fluid, for example the flow from the nozzle of a garden hose when held under water. The flow is driven by the momentum of the source, and the source and ambient fluid have the same density.

A *plume* is the flow resulting from a potential energy source that provides the fluid at the source with buoyancy relative to its surroundings, for example hot air rising from a radiator. In a plume the fluid at the source has no initial momentum and is driven by buoyancy forces.

In practice, many sources are neither jets nor plumes having both initial momentum and a different density to the environment. These sources are called *buoyant jets* or *forced plumes.* The initial flow is often driven by the momentum of the fluid at the source and behaves like a jet, but the density difference means that the fluid is acted on by buoyancy forces and will ultimately behave as a plume (as will be shown later).

Near to the source, the flow is usually controlled by the starting conditions, namely the initial fluxes of mass, momentum and buoyancy. These are defined below.†

i) The *mass flux*, ρQ_0, is the rate of mass flow through a jet cross-section and is given by

$$\rho Q_0 = \frac{1}{\pi} \int_S \rho u_0 \, dS, \tag{1.1}$$

where ρ is the density of the fluid, u_0 is the time-averaged (mean) velocity at the source and dS denotes integration across a cross-section (S) of the jet. Q_0 is the *specific* mass flux or *volume flux* of the jet.

ii) The *momentum flux*, ρM_0, of the jet is the rate at which streamwise momentum passes through a jet cross-section and is given by

$$\rho M_0 = \frac{1}{\pi} \int_S \rho u_0^2 \, dS. \tag{1.2}$$

M_0 is called the *specific* momentum flux.

† Some authors do not include the $1/\pi$ factors, which are included here for later convenience when using circular nozzles.

iii) The *buoyancy flux*, ρB_0, is the rate of flow of density difference through a jet cross-section and is given by

$$\rho B_0 = \frac{1}{\pi} \int_S g \Delta\rho u_0 \, dS, \tag{1.3}$$

where $\Delta\rho$ is the density difference between the surrounding fluid and the jet fluid. B_0 is the *specific* buoyancy flux.

Local fluxes of mass, momentum and buoyancy are defined in the same way without the zero subscript which is used to denote evaluation at the source. The above notation is used throughout this thesis.

Jets and plumes may be laminar or turbulent but it is not yet possible to predict (theoretically) the Reynolds number,

$$Re = \frac{2u_m b}{\nu}, \tag{1.4}$$

where b is the transverse length scale, u_m is the axial velocity scale and ν is the kinematic viscosity, at which a laminar jet will become turbulent. In most cases, if the Reynolds number exceeds 2000 the jet flow will be turbulent, although Fischer *et al.* (1979) state that there is evidence that the turbulence may not be fully developed until a Reynolds number of about 4000 is reached. In all of the flow sources considered in this thesis, the lower limit, $Re > 2000$, will be attained and so the sources will be considered to be turbulent.

In the following sections the basic properties of turbulent jets, plumes and buoyant jets, obtained from both theoretical and experimental results, will be reviewed. The equations of fluid motion will then be introduced. When applied to jet flow, it is possible to compare the orders of magnitude of each term in the equations of motion. By selecting the largest terms, and modelling turbulence using mixing length and eddy viscosity hypotheses, Tollmien (1926) and Goertler (1942) were able to find predictions for the mean velocity, although neither solution agreed well with the experimental results across the whole of the flow.

Finally, in order to try to improve the agreement between the theoretical predictions and the experimental measurements, the effects of including the (previously neglected) smaller terms and variation of the intermittency factor in the analysis will be examined. This will give an indication of the relative importance of the neglected terms. No similar studies (of the effects of the smaller terms and intermittency factor) are known to the author. The chapter ends with a discussion of the results.

2. A review of the elementary properties of jets and plumes

The basic properties of jets, plumes and buoyant jets will now be reviewed, drawing on established theoretical and experimental results.

2.1 The pure jet

A pure jet has been defined above to be a source of mass and momentum but not buoyancy; in practice, a jet is usually the discharge from a nozzle in a body of the same fluid. Turbulent jets have been studied extensively both theoretically and experimentally so that there is now a good understanding of their behaviour. Some of the experimental studies are listed in table 1 (for reviews see Rajaratnam 1976, Fischer *et al.* 1979 and List 1982).

2.1.1 Experimental observations

Figure 1 shows the flow of a turbulent jet schematically, divided into two distinct regions or zones.

In the first region, known as the 'flow development region' or the 'zone of flow establishment', the shear between the source fluid and the environmental fluid causes turbulence which penetrates progressively towards the axis of the jet destroying the potential core of undiminished mean velocity. Ambient fluid is entrained into the jet which consequently increases in width. This first region is about six nozzle diameters in length, after which the turbulence has penetrated to the jet axis and the potential core has disappeared. This is the 'fully developed flow region' or 'zone of established flow'.

In the fully developed region, the jet continues to expand by entraining ambient fluid. Experimental measurements have shown that mean velocities and (tracer) concentrations in this region are 'self-similar', expressible in terms of velocity and concentration scales, respectively, (u_m and C_m, the values of the axial (x) velocity and concentration (or tracer) on the axis) and a length scale, or measure of the width. Figure 2 shows measurements of the transverse (y) variation of the axial velocity, u, for a planar turbulent free jet (data due to Zijnen 1958) in which the solid line is a Gaussian fit. The velocity distributions from different cross-sections fall on a common curve which is approximately Gaussian in shape (as a consequence, the axial velocity distributions of jets and plumes are often assumed to be Gaussian for analytical simplicity). However, the scales of velocity and length must be known before this property of similarity may be used.

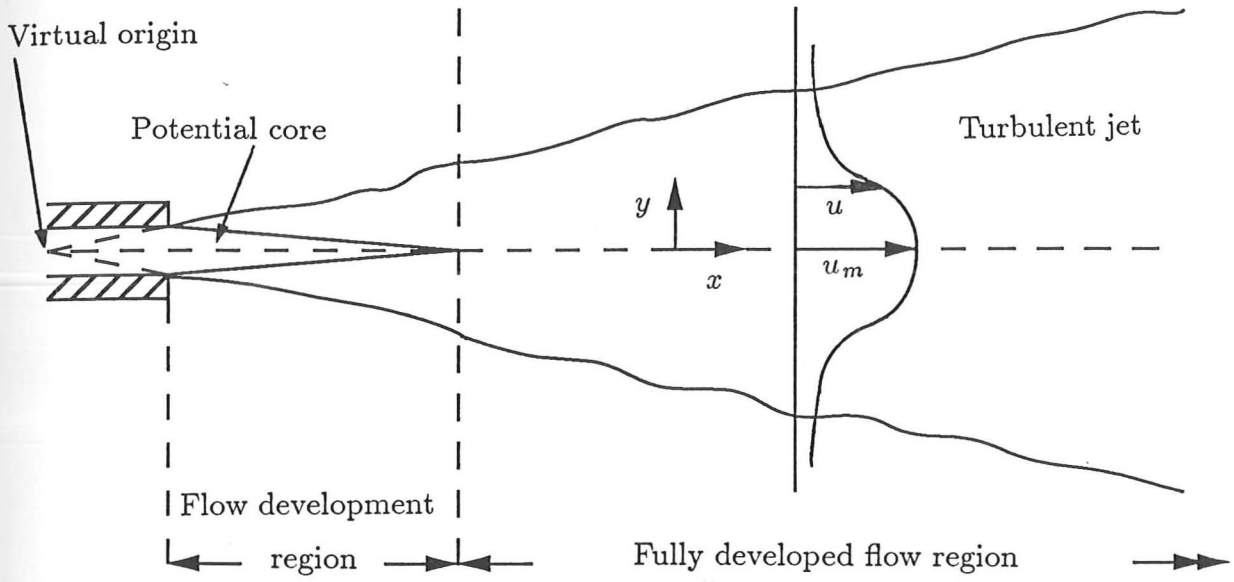

FIGURE 1. A schematic diagram showing the different regions of the flow of a pure jet.

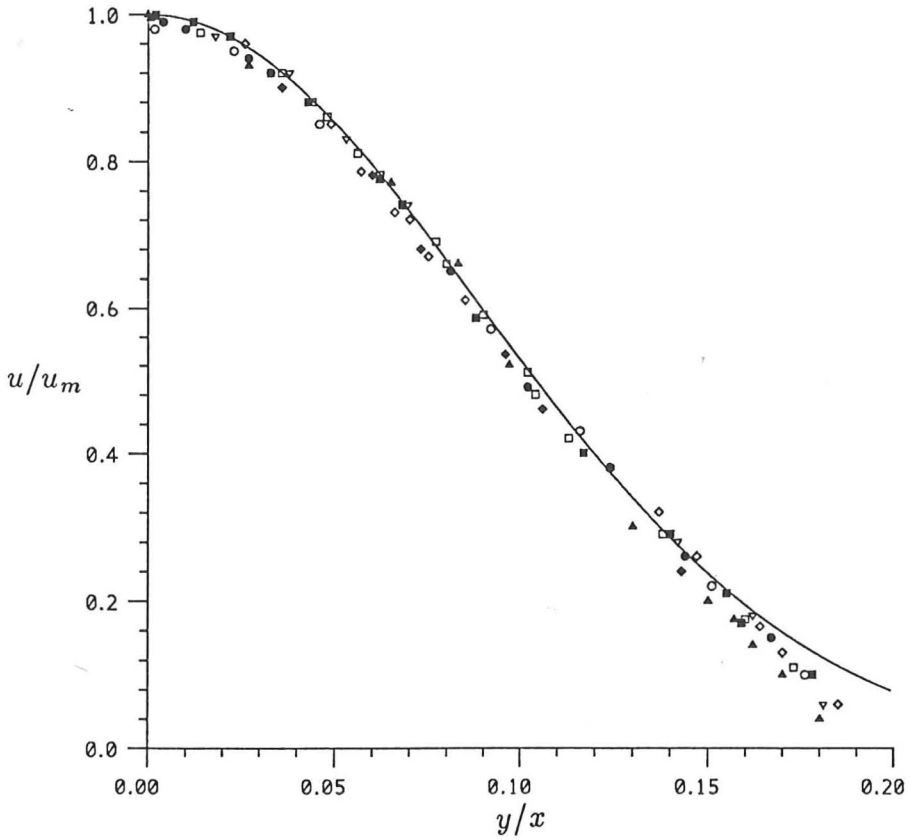

FIGURE 2. The axial velocity profile of a plane turbulent jet showing self-similarity (data from Zijnen 1958).

Experimentalist	Nozzle radius b_0 (mm)	Range x/b_0	$Re \times 10^4$	Mean flow quantities measured	Turbulent quantities measured
Forthmann (1936) †	15.0	50	7.0	u	
Miller & Comings (1957)	6.35	80	2.0	u, p	$\overline{u'^2}$
Van der Hegge Zijnen (1958)	2.5, 5.0	80	1.33	u, v	$\overline{u'^2}$, $\overline{v'^2}$, $\overline{u'v'}$
Ricou & Spalding (1961)	0.8 – 15.9	418	0.1-8.0	u, p, Q, Q_x	
Bradbury (1965)	4.765	140	3.0	u, v, p	$\overline{u'^2}$, $\overline{v'^2}$, $\overline{w'^2}$, $\overline{u'v'}$, l
Heskestad (1965)	6.35	320	0.47-3.7	u	$\overline{u'^2}$, $\overline{v'^2}$, $\overline{w'^2}$, $\overline{u'v'}$ $\overline{u'_i u'_j u'_k}$
Sami *et al.* (1967)	30.0	40	22.0	u, v, p	$\overline{u'^2}$, $\overline{u'v'}$, $\overline{p'}$
Wygnanski & Fiedler (1969)	13.0	400	10.0	u	$\overline{u'^2}$, $\overline{v'^2}$, $\overline{w'^2}$, $\overline{u'v'}$ $\overline{u'_i u'_j u'_k}$
Mih & Hoopes (1972)	0.865	280-600	1.77-3.14	u	$\overline{u'^2}$, $\overline{v'^2}$, $\overline{u'v'}$, l
Gutmark & Wygnanski (1976)	6.5	240	3.0	u, v	$\overline{u'^2}$, $\overline{v'^2}$, $\overline{w'^2}$, $\overline{u'v'}$ $\overline{u'_i u'_j u'_k}$

u, v are the mean axial and transverse/radial velocities; Q is the volume flux; u', v', w' are the velocity fluctuations; p is the static pressure; p' is the pressure fluctuation; l is the mixing length.

†Details of this paper have been taken from Rajaratnam (1976).

TABLE 1. Experimental investigations of laminar and turbulent free jets

2.1.2 The velocity and length scales

The scales of velocity and length can be calculated by integrating the equations of motion over a cross-section of the jet and assuming similarity of the flow. This integral technique,

suggested by Morton, Taylor & Turner (1956), has been widely used and developed (see, for example, Kotsovinos 1977). However, it is possible to predict the scales of velocity and length using simple dimensional analysis.

If x is the axial distance from the nozzle, then dimensional analysis assumes that, for Re sufficiently large so that the effects of molecular viscosity are negligible, the scales of velocity, length, concentration, volume flux and momentum flux must be dependent on x, M_0 and Q_0. Thus

$$u_m = f_1(M_0, Q_0, x), \quad b = f_2(M_0, Q_0, x), \quad C_m = f_3(M_0, Q_0, x),$$
$$Q = f_4(M_0, Q_0, x), \quad M = f_5(M_0, Q_0, x), \tag{2.1}$$

where f_i, $i = 1, ..., 5$, are functions to be deduced.

Considering circular jets first, then following Fischer *et al.* (1979) a characteristic length scale for the axial motion may be obtained from M_0 and Q_0, namely

$$L_{ax} = \frac{Q_0}{M_0^{\frac{1}{2}}}, \tag{2.2}$$

and $L_{ax} = b_0$, where b_0 is the nozzle radius, if the nozzle velocity has a uniform profile (see equations (1.1) and (1.2)). Fischer *et al.* (1979) also argue that, for sufficiently large values of x/L_{ax}, the effect of the initial volume flux on the jet behaviour is negligible compared with that of the initial momentum flux. Hence, at large distances downstream, all of the above properties must be defined in terms of x and M_0. The only way to obtain the dimensions of velocity from these is by using $\sqrt{M_0}/x$. Hence

$$u_m = c_1 \frac{\sqrt{M_0}}{x}, \tag{2.3}$$

for some constant c_1. Clearly the only way to obtain dimensions of length is using x and so

$$b = c_2 x, \tag{2.4}$$

for some constant c_2. This method also implies the well-known result that the momentum flux is constant in jets (although this was disputed by Kotsovinos 1991). The dependences of the other quantities on x and M_0 can be deduced similarly and are summarised in table 2, together with the analogous results for planar jets. The constants c_i, c_i', may be estimated from experimental measurements, which have also confirmed the dimensional results (see

Parameter	Circular jets	Planar jets
Characteristic axial length scale L_{ax}	$Q_0/\sqrt{M_0}$	Q_0^2/M_0
Velocity scale u_m	$c_1\sqrt{M_0}/x$	$c_1'\sqrt{M_0/x}$
Radial/transverse length scale b	$c_2 x$	$c_2' x$
Tracer/velocity length scale ratio b_t/b_u	1.19 ± 0.06	1.35 ± 0.05
Concentration scale C_m	$c_3/\sqrt{M_0}x$	$c_3'/\sqrt{M_0 x}$
Volume flux scale Q	$c_4\sqrt{M_0}x$	$c_4'\sqrt{M_0 x}$
Momentum flux scale M	Constant, M_0	Constant, M_0

TABLE 2. Summary of the properties of turbulent jets.

Fischer *et al.* 1979). One curious observation is that the transverse length scales of velocity and tracer concentration (b_u and b_t) are measured to be different, Fischer *et al.* (1979) quoting $b_t/b_u = 1.19$ for circular jets and $b_t/b_u = 1.35$ for planar jets. This has lead to unresolved speculation as to why there should be a difference in the length scales, b_t and b_u.

2.2 The pure plume

A pure plume has been defined to be a source of potential energy, giving the fluid at the source buoyancy relative to its surroundings. Whilst a large number of experimental investigations of pure turbulent jets have been performed, there are very few studies of pure plumes (see table 3 and List 1982). However, the pure plume is easier to analyse theoretically than the jet as there is no initial volume or momentum flux.

2.2.1 Experimental observations

Morton, Taylor & Turner (1956) quoted the paper by Schmidt (1941) as the first consideration of plumes rising from heated bodies. Rouse, Yih & Humphries (1952) gave the results of measurements made in plumes above a single gas burner, although they did not consider turbulent fluxes. Rouse *et al.* found that, like the pure jet, the mean velocity and temperature distributions of pure plumes could be fitted quite well to Gaussian profiles. Also, Rouse *et al.* found that using a line source the velocity varied over a slightly larger scale

Experimentalist	Flow type	Quantities measured
Schmidt (1942) †	P	w
Rouse, Yih & Humphries (1952)	P	w, C
Lee & Emmons (1961)	P	C, b, Q, Q_x, B
George *et al.* (1977)	P	w, C, $\overline{w'^2}$, $\overline{c'^2}$, $\overline{w'c'}$
Kotsovinos & List (1977)	BJ	w, C, b_w, b_T, M, Q, Ri
Kotsovinos (1977)	BJ	$\overline{w'^2}$, $\overline{c'^2}$
Ramaprian & Chandrasekhara (1983) ‡	BJ,P	w, C, b_w, b_T, $\overline{w'^2}$, $\overline{c'^2}$
Kotsovinos (1985)	P	C, b_T, $\overline{c'^2}$
Papanicolaou & List (1988)	BJ	w, v, b_w, b_t, $\overline{w'^2}$, $\overline{v'^2}$, $\overline{c'^2}$, $\overline{w'c'}$, Q, M

w, v are the mean axial and transverse/radial velocities; C is the concentration; w', v', c' are the turbulent fluctuations; Q, M, B are the fluxes of volume, momentum and buoyancy; b_w, b_T are the length scales of velocity and concentration; Ri is the Richardson number.

P denotes study of plumes and BJ denotes study of buoyant jets.

†Details of this paper have been taken from Morton, Taylor & Turner (1956); ‡details taken from Papanicolaou & List (1988).

TABLE 3. Experimental investigations of turbulent free plumes and buoyant jets.

than the buoyancy, but with a circular source the opposite was true. In both planar and circular jets, the tracer concentration also varies over a slightly larger scale than the velocity and so there must be some doubt about the validity of the results of Rouse *et al.*. Lee & Emmons (1961) only measured the temperature profiles above a line source and so their results cannot be used to clarify the situation. Kotsovinos & List (1977) have conducted quite a thorough investigation. From the results of their study, they calculated the temperature to velocity length scale ratio $\lambda = b_T/b_w$, finding that $\lambda \simeq 1.35$ for planar jets and plumes and $\lambda \simeq 1.16$ for circular jets and plumes. George *et al.* (1977) have attempted to measure the turbulent properties in axisymmetric plumes. They found that the mean velocity varied over a larger length scale than the concentration, which contradicts the results of Kotsovinos & List (1977).

2.2.2 Dimensional analysis

The pure plume has no initial volume or momentum flux and so the flow variables must depend only on the source buoyancy flux, B_0, and the distance from the source z (z is used as pure plumes must flow vertically, with velocity w), assuming that the Reynolds number is sufficiently large for the flow to be considered fully turbulent (i.e. viscous effects are negligible). This has the immediate consequence that there is no characteristic axial length scale for the pure plume.

Considering circular plumes first, the only way to construct dimensions of velocity from B_0 and z is by using $(B_0/z)^{\frac{1}{3}}$ and so

$$w_m = d_1 \left(\frac{B_0}{z}\right)^{\frac{1}{3}}, \tag{2.5}$$

where w_m is the velocity scale (the value on the axis), for some constant d_1. Clearly there is only one way to construct dimensions of length, i.e. using z, and so

$$b = d_2 z, \tag{2.6}$$

for some constant d_2. In the case of the pure jet, dimensional analysis implies that the momentum flux is constant; in pure plumes the above analysis implies that the buoyancy flux is constant. This standard result, proved by Morton, Taylor & Turner (1956), will be derived more rigorously using an integral approach in chapter 3.

The dependencies of the other flow quantities on B_0 and z can be derived similarly and are summarised in table 4 together with the analogous results for planar plumes. As in the case of the pure jet, the constants d_i, d_i' may be deduced from experimental measurements. The dimensional dependencies have been shown to be in good agreement with the available data (see, for example, Rouse *et al.* 1952 and Fischer *et al.* 1979). However, there are still only a few detailed experimental studies and some debate about the values of the constants still exists (see List 1982). The concentration/velocity length scale ratios given in table 4 have been taken from Fischer *et al.* (1979) and are the average values of the available experimental measurements.

2.3 Buoyant jets

A buoyant jet is defined to be a jet in which the source fluid has a different density to the environmental fluid. Initially a buoyant jet has jet-like characteristics, depending on its initial

Parameter	Circular plume	Planar plume
Velocity scale w_m	$d_1 B_0^{\frac{1}{3}} z^{-\frac{1}{3}}$	$d_1' B_0^{\frac{1}{3}}$
Radial/transverse length scale b	$d_2 z$	$d_2' z$
Concentration/velocity length scale ratio b_T/b_w	1.20 ± 0.07	1.35 ± 0.05
Concentration scale C_m	$d_3 B_0^{-\frac{1}{3}} z^{-\frac{5}{3}}$	$d_3' B_0^{-\frac{1}{3}} z^{-1}$
Volume flux scale Q	$d_4 B_0^{\frac{1}{3}} z^{\frac{5}{3}}$	$d_4' B_0^{\frac{1}{3}} z$
Momentum flux scale M	$d_5 B_0^{\frac{2}{3}} z^{\frac{4}{3}}$	$d_5' B_0^{\frac{2}{3}} z$
Buoyancy flux scale B	Constant, B_0	Constant, B_0

TABLE 4. Summary of the properties of turbulent plumes.

volume and momentum fluxes, but because of the density difference, it also has plume-like characteristics depending on its initial buoyancy flux.

2.3.1 Experimental observations

Some of the experimental work on buoyant jets is listed in table 3. Kotsovinos & List (1977) conducted a detailed experimental investigation of planar buoyant jets and were the first to measure turbulent fluctuations (see also Kotsovinos 1977). Their experiments confirmed that the flow variables initially behaved as would be expected for a pure jet (see table 2), and that after passing through a transition stage, the flow behaved like a pure plume (see table 4). They also found that 10% of the transport in jets and as much as 40% of the transport in plumes is due to turbulence. Ramaprian & Chandrasekhara (1983 - details of this report have been obtained from Papanicolaou & List 1988) have repeated Kotsovinos' experiments with more accurate equipment, finding lower turbulent flux contributions.

The most detailed study has been by Papanicolaou & List (1988) who measured the mean velocity, concentration, volume flux and momentum flux distributions, the turbulent velocity (both axial and radial) and concentration distributions, and the distributions of skewness and flatness factors, in axisymmetric buoyant jets. Papanicolaou & List (1988) attempted to produce conclusive results using laser-Doppler anemometry to measure velocity and a laser-induced-fluoresence concentration measurement technique. They found that

buoyancy-produced turbulence was responsible for 15-20% of the tracer transport whereas the jet turbulence was responsible for 7-12%. These figures seem reasonable as in plumes there is both the production of turbulence by the shear stress, as in jets, but also a direct transfer of potential energy to turbulent kinetic energy by the buoyant work done. Papanicolaou & List (1988) also resolved the disagreements regarding the difference in the scales of the transverse variation of mean concentration and mean velocity. Their measurements, taken in the fully developed flow region, showed that the concentration varies over a larger scale than the velocity in both jets and plumes, with $\lambda \simeq 1.19$ being a good average value over the path of a circular turbulent buoyant jet. The converse result of George *et al.* (1977) is probably attributable to the fact that their measurements were taken very close to the source.

2.3.2 Dimensional analysis

It is possible to construct two independent scales of length from the initial source conditions, namely (for a circular buoyant jet)

$$L_{ax} = \frac{Q_0}{M_0^{\frac{1}{2}}} \quad \text{and} \quad L_j = \frac{M_0^{\frac{3}{4}}}{B_0^{\frac{1}{2}}}, \tag{2.7}$$

the first of which is simply the axial length scale for a pure jet, introduced in section 2.1. The second is called the 'jet-length' (see, for example, Turner 1973) which gives an indication of the length scale over which momentum forces will dominate buoyancy. Consider a vertical buoyant jet with no initial volume flux. In this case, the flow variables must all be functions of z/L_j. Near to the nozzle (small z), z/L_j is small - however small values of this parameter (and consequently identical flows) may also be obtained by having small B_0 or large M_0, for which jet-like flow would be observed. Hence jet-like flow is expected for small values of z. Conversely, large values of z/L_j may be obtained by having large z, large B_0 or small M_0; i.e. at large distances from the nozzle the flow is plume-like. Thus the length scale L_j is the parameter controlling the transition in a buoyant jet from a jet-like to a plume-like state. The above argument has shown that when $z \ll L_j$ the flow is jet-like and when $z \gg L_j$ the flow is plume-like. This jet-plume transition and the control of L_j on it will be pursued further in chapter 3, and the work of Linden, Marshall & Cleaver (1991, see chapter 1) has shown the importance of L_j in controlling the mixing produced by a source in a confined (cubical) space.

Similar dimensional arguments can be applied to planar buoyant jets, for which the axial and 'jet-length' scales are

$$L_{ax} = \frac{Q_0^2}{M_0} \quad \text{and} \quad L_j = \frac{M_0}{B_0^{\frac{2}{3}}}. \tag{2.8}$$

3. The equations of fluid flow

Having summarised the basic features of jets, plumes and buoyant jets obtained from experimental results and simple dimensional analysis, it is desirable to be able to predict some of the experimental results analytically, using the equations of fluid motion. The following analysis is restricted to a consideration of pure jets, so that there are no density differences, although similar analysis may also be applied to plume flow (Yih 1981). The most interesting feature of buoyant jet flow is the jet-plume transition and this will be examined theoretically using an integral approach in chapter 3.

3.1 The momentum equations

The Navier-Stokes equations for a viscous incompressible fluid may be written in the form, using rectangular coordinates x_i, (see, for example, Townsend 1956)

$$\frac{\partial(u_i + u_i')}{\partial t} + (u_j + u_j')\frac{\partial(u_i + u_i')}{\partial x_j} = -\frac{\partial(p + p')}{\partial x_i} + \nu\frac{\partial^2(u_i + u_i')}{\partial x_j^2}, \tag{3.1}$$

where u_i is the ith component of the time-averaged (mean) velocity and u_i' is the fluctuating part; p and p' are the mean and fluctuating pressures, and ν is the kinematic viscosity. The condition of incompressibility is written

$$\frac{\partial(u_i + u_i')}{\partial x_i} = 0. \tag{3.2}$$

Taking the time-average of these equations gives the equations of mean motion

$$u_j\frac{\partial u_i}{\partial x_j} + \overline{u_j'\frac{\partial u_i'}{\partial x_j}} = -\frac{\partial p}{\partial x_i} + \nu\frac{\partial^2 u_i}{\partial x_j^2} \quad \text{and} \quad \frac{\partial u_i}{\partial x_i} = 0. \tag{3.3a, b}$$

Subtracting equation (3.3b) from (3.2) yields $\partial u_i'/\partial x_i = 0$ and so equations (3.3a) may be written in the usual form of the momentum equation

$$u_j\frac{\partial u_i}{\partial x_j} + \frac{\partial\overline{u_i'u_j'}}{\partial x_j} = -\frac{\partial p}{\partial x_i} + \nu\frac{\partial^2 u_i}{\partial x_j^2}. \tag{3.4}$$

This is the form of the momentum equation that will be used in the following analysis and later in this thesis.

4. Application of the momentum equations to planar jets

The momentum equations (3.4) will now be applied to the flow of a planar jet in order to predict the flow characteristics. The analogous results for circular jets will be summarised briefly in section 5. Planar jets are perhaps less commonly occurring in practical circumstances than circular jets, although the jet from a multiport diffuser may be regarded as being planar when the ports are sufficiently close together. However, the analysis is slightly simpler in the two-dimensional case and so this will be considered first.

Assuming the flow to be two dimensional ($w = 0$) in the $x - y$ plane, denoting the axial (x) velocity by u and the transverse (y) velocity by v, then the time-averaged momentum equations become

$$u\frac{\partial u}{\partial x} + v\frac{\partial u}{\partial y} = -\frac{1}{\rho}\frac{\partial p}{\partial x} - \left(\frac{\partial \overline{u'^2}}{\partial x} + \frac{\partial \overline{u'v'}}{\partial y}\right) + \nu\left(\frac{\partial^2 u}{\partial x^2} + \frac{\partial^2 u}{\partial y^2}\right), \tag{4.1}$$

$$u\frac{\partial v}{\partial x} + v\frac{\partial v}{\partial y} = -\frac{1}{\rho}\frac{\partial p}{\partial y} - \left(\frac{\partial \overline{u'v'}}{\partial x} + \frac{\partial \overline{v'^2}}{\partial y}\right) + \nu\left(\frac{\partial^2 v}{\partial x^2} + \frac{\partial^2 v}{\partial y^2}\right), \tag{4.2}$$

and the continuity equation is now

$$\frac{\partial u}{\partial x} + \frac{\partial v}{\partial y} = 0. \tag{4.3}$$

4.1 Order of magnitude analysis

Experimental observations (see table 1) have shown that the transverse velocity and axial gradients are an order of magnitude smaller than the axial velocity and transverse gradients, respectively, and that mean squares of products of turbulent velocity fluctuations are also at least an order of magnitude less than the square of the axial velocity scale. Thus if $O(v) = \ell O(u_m)$, $O(\partial/\partial x) = \ell O(\partial/\partial y)$ and $O(u', v') = \varepsilon O(u_m)$, where ℓ is a dimensionless quantity with magnitude an order of magnitude less than unity and $O(\varepsilon^2) = O(\ell)$, the orders of magnitude of each term in (4.1) and (4.2) above may be compared.

Writing the equations of motion, (4.1) and (4.2), again with the order of magnitude of each term written below

$$u\frac{\partial u}{\partial x} + v\frac{\partial u}{\partial y} = -\frac{1}{\rho}\frac{\partial p}{\partial x} - \left(\frac{\partial \overline{u'^2}}{\partial x} + \frac{\partial \overline{u'v'}}{\partial y}\right) + \nu\left(\frac{\partial^2 u}{\partial x^2} + \frac{\partial^2 u}{\partial y^2}\right),$$

$$1 \qquad 1 \qquad 1 \qquad \varepsilon^2 \qquad \varepsilon^2/\ell \qquad 1/Re \quad 1/\ell^2 Re \tag{4.1a}$$

$$u\frac{\partial v}{\partial x} + v\frac{\partial v}{\partial y} = -\frac{1}{\rho}\frac{\partial p}{\partial y} - \left(\frac{\partial \overline{u'v'}}{\partial x} + \frac{\partial \overline{v'^2}}{\partial y}\right) + \nu\left(\frac{\partial^2 v}{\partial x^2} + \frac{\partial^2 v}{\partial y^2}\right),$$

$$\ell \qquad \ell \qquad 1 \qquad \varepsilon^2 \qquad \varepsilon^2/\ell \qquad \ell/Re \quad 1/\ell Re \tag{4.2a}$$

it is clear that the terms range in order of magnitude from $1/\ell$ to ℓ/Re.

4.2 First order equations of motion

Having estimated the order of magnitude of each term of the equations describing planar jet flow, analytical solutions to the equations will be obtained by neglecting all but the highest order of magnitude terms in each equation.

If the Reynolds number is high and the jet is fully turbulent, the viscous terms may be neglected. Examination of (4.1a) and (4.2a) shows that in (4.1) the first three and fifth terms are of order unity whereas the fourth term is of order ℓ, (recall that ℓ is small and $O(\varepsilon^2) = O(\ell)$), and in (4.2) the third and fifth terms are of order unity or greater. Thus to order of magnitude unity the equations (4.1) and (4.2) may be approximated by

$$u\frac{\partial u}{\partial x} + v\frac{\partial u}{\partial y} = -\frac{1}{\rho}\frac{\partial p}{\partial x} - \frac{\partial \overline{u'v'}}{\partial y}, \tag{4.3}$$

$$0 = -\frac{1}{\rho}\frac{\partial p}{\partial y} - \frac{\partial \overline{v'^2}}{\partial y}, \tag{4.4}$$

with the continuity equation remaining unchanged (each term is of order unity)

$$\frac{\partial u}{\partial x} + \frac{\partial v}{\partial y} = 0. \tag{4.5}$$

The second of these, equation (4.4), may now be integrated with respect to y giving

$$p = p_\infty - \rho\overline{v'^2}, \tag{4.6}$$

in which p_∞ is the pressure outside the jet where the turbulent fluctuations are zero. Substituting (4.6) into (4.3) gives

$$u\frac{\partial u}{\partial x} + v\frac{\partial u}{\partial y} = -\frac{1}{\rho}\frac{dp_\infty}{dx} - \frac{\partial \overline{u'v'}}{\partial y} + \frac{\partial}{\partial x}\overline{v'^2}. \tag{4.7}$$

Again restricting the analysis to terms of order unity, the last term, which is of order of magnitude ℓ, is neglected. Also, in a large number of practical problems, the axial pressure gradient outside of the jet is small, and so the dp_∞/dx term is ignored. With these further simplifications the equations reduce to

$$u\frac{\partial u}{\partial x} + v\frac{\partial u}{\partial y} = \frac{1}{\rho}\frac{\partial \tau}{\partial y} \quad \text{and} \quad \frac{\partial u}{\partial x} + \frac{\partial v}{\partial y} = 0, \tag{4.8a,b}$$

where $\tau = -\rho\overline{u'v'}$ is the turbulent shear stress. These are the approximate equations of motion for a two-dimensional jet.

The integral momentum equation and entrainment hypothesis

Before showing how equations (4.8) may be solved, two important results may be obtained simply by integrating these equations with respect to y, namely the integral momentum equation and the conservation of volume equation.

Integrating (4.8a) with respect to y from $y = -\infty$ to $y = \infty$ gives

$$\int_{-\infty}^{\infty} u\frac{\partial u}{\partial x}\,dy + \int_{-\infty}^{\infty} v\frac{\partial u}{\partial y}\,dy = \int_{-\infty}^{\infty} \frac{1}{\rho}\frac{\partial \tau}{\partial y}\,dy. \tag{4.9}$$

Each term may be rewritten as follows

$$\int_{-\infty}^{\infty} u\frac{\partial u}{\partial x}\,dy = \frac{1}{2}\frac{d}{dx}\int_{-\infty}^{\infty} u^2\,dy,$$

$$\int_{-\infty}^{\infty} v\frac{\partial u}{\partial y}\,dy = \left(uv|_{-\infty}^{\infty} - \int_{-\infty}^{\infty} u\frac{\partial v}{\partial y}dy\right) = \left(\int_{-\infty}^{\infty} u\frac{\partial u}{\partial x}\,dy\right) = \frac{1}{2}\frac{d}{dx}\int_{-\infty}^{\infty} u^2\,dy \quad \text{and}$$

$$\int_{-\infty}^{\infty} \frac{\partial \tau}{\partial y}\,dy = \tau|_{-\infty}^{\infty} = \tau(\infty) - \tau(-\infty) = 0.$$

Hence (4.9) reduces to

$$\frac{d}{dx}\int_{-\infty}^{\infty} u^2\,dy = 0. \tag{4.10}$$

This standard result (see, for example, Rajaratnam 1976) states that the specific momentum flux in the axial direction is a constant, M_0, which agrees with the prediction of the dimensional analysis of section 2.1.2.

A second important result may be obtained by integrating (4.8*b*) similarly, giving

$$\frac{d}{dx}\int_{-\infty}^{\infty} u\,dy = \int_{-\infty}^{\infty} u_x\,dy = -\int_{-\infty}^{\infty} v_y = -2v(\infty). \tag{4.11}$$

The velocity contribution, $-v(\infty)$, is the velocity of fluid being entrained into the jet from the environment. Morton, Taylor & Turner (1956) proposed, on dimensional grounds, that $v(\infty) = -\alpha_j u_m$ where α_j is an 'entrainment coefficient' for a pure jet; i.e. the velocity of the fluid being entrained is proportional to the local velocity scale of the jet. Thus

$$\frac{dQ}{dx} = \frac{d}{dx}\int_{-\infty}^{\infty} u\,dy = 2\alpha_j u_m. \tag{4.12}$$

The value and nature of the entrainment constant α_j has been the subject of considerable experimental investigation. However, its value is still not known precisely - there is a large degree of discrepancy in the measured values of α_j (Fischer *et al.* 1979 record measured values of α_j which vary by up to $\pm 22\%$ of the mean value), possibly because α_j may vary with the manner in which the experiments are performed (see Bradshaw 1977). What is established, though, is that the value of the entrainment constant is different for jets and plumes (see Fischer *et al.* 1979) - the effect of this variation on a model of a horizontally released buoyant jet is investigated in chapter 3.

4.3 Turbulent solutions to the first order equations

Equations (4.8) were solved by Tollmien (1926) and Goertler (1942) who used the self-similar nature of the flow with mixing length and eddy viscosity hypotheses, respectively, to express the turbulent product $\overline{u'v'}$ in terms of the mean flow variables.

4.3.1 Goertler Solution

Goertler (1942 - the details of this paper have been taken from Rajaratnam 1976) used an eddy viscosity, $\epsilon(x)$, to model the turbulent shear stress

$$\tau = \rho\epsilon(x)\frac{\partial u}{\partial y}. \tag{4.13}$$

The eddy viscosity is assumed to be constant over any jet cross-section in the fully developed flow region. On dimensional grounds Goertler assumed that $\epsilon \propto u_m b$ or $\epsilon = k u_m b$ for some constant k. The assumption that the jet has reached a state of self-similarity implies that all variables can be expressed in terms of a similarity variable, $\eta = y/\sigma x$ for some constant σ, with magnitude of order ℓ, to be determined by comparison between the theoretical results and experimental measurements. Thus using the dimensional result that $u_m \sim x^{-\frac{1}{2}}$, it is convenient to write

$$u(x,y) = u_m(x)F'(\eta), \quad \text{where} \quad \eta = \frac{y}{\sigma x}, \quad \text{and} \quad u_m(x) = \frac{n}{\sqrt{x}} = c_1'\sqrt{\frac{M_0}{x}}, \tag{4.14}$$

in which the constant, n, controlling the magnitude of the velocity, has been set to agree with the dimensional results of section 2.1.2 (see table 2), and the primes denote differentiation with respect to η. The continuity equation (4.8*b*) requires that

$$v(x,y) = \frac{n\sigma}{\sqrt{x}}(\eta F' - F/2). \tag{4.15}$$

Substituting (4.14) and (4.15) into the equation of motion (4.8*a*) and integrating with respect to η gives

$$\frac{1}{2}FF' + \frac{kc_2'}{\sigma^2}F'' = A, \tag{4.16}$$

where the dimensional result that $b = c_2'x$ has been used in the expression for $\epsilon(x)$ and A is a constant of integration. The boundary conditions at $y = 0$ or $\eta = 0$ are $u/u_m = F'(0) = 1$, $F''(0) = 0$ and $F(0) = 0$, which set $A = 0$. The free parameter σ may be chosen to be $\sigma = 2\sqrt{kc_2'}$, so that then (4.16) becomes

$$2FF' + F'' = 0, \tag{4.17}$$

which may be integrated to

$$F^2 + F' = \tilde{A}. \tag{4.18}$$

The above boundary conditions set the integration constant, $\tilde{A} = 1$. Equation (4.18) then becomes

$$F^2 + F' = 1, \tag{4.19}$$

which has solution

$$F = \tanh\eta \quad \text{and} \quad F' = 1 - \tanh^2\eta \qquad \text{i.e.} \tag{4.20}$$

$$u(x,y) = u_m\left(1-\tanh^2\eta\right) \quad \text{and} \quad v(x,y) = u_m\sigma\left(\eta - \eta\tanh^2\eta - \frac{1}{2}\tanh\eta\right). \qquad (4.21a,b)$$

The streamfunction of the flow is

$$\psi(x,y) = u_m x\sigma\ \tanh\eta = n\sigma\sqrt{x}\tanh\eta, \qquad (4.22)$$

and for large x, the streamlines take the form

$$y \sim \sqrt{x}. \qquad (4.23)$$

A good fit to the experimental results of Zijnen (1958) is found when $\sigma \simeq 0.118$. Equation (4.21a) is shown using this value of σ, together with the data of figure 2, in figure 3. The agreement is good in the central region of the jet but is less so near to the edge of the jet.

4.3.2 Tollmien Solution

Tollmien (1926 - details of the results of this paper were obtained from Rajaratnam 1976) used the Prandtl mixing length formula

$$\tau = -\rho l^2\left(\frac{\partial u}{\partial y}\right)^2, \qquad (4.24)$$

where l is the mixing length. On dimensional grounds Tollmien assumed that $l \propto b$ or $l = \beta b$ for some constant β. The previous dimensional results (see table 2) then imply that

$$l = \beta c_2' x. \qquad (4.25)$$

Using the same form for the velocity components as in the previous solution, equations (4.14) and (4.15), and substituting these into the equation of motion (4.8a), using (4.24) and (4.25), gives after some simplification

$$2F''F''' - FF'' - F'^2 = 0 \quad \text{or} \quad 2F''F''' - \frac{d}{d\eta}(FF') = 0, \qquad (4.26)$$

in which σ has been set by $\sigma^3 = 2(\beta c_2')^2$. Equation (4.26) may be integrated giving

$$F''^2 - FF' = A_1,$$

where A_1 is a constant of integration. The boundary conditions (the same as before) imply that $A_1 = 0$ and so

$$F''^2 - FF' = 0. \qquad (4.27)$$

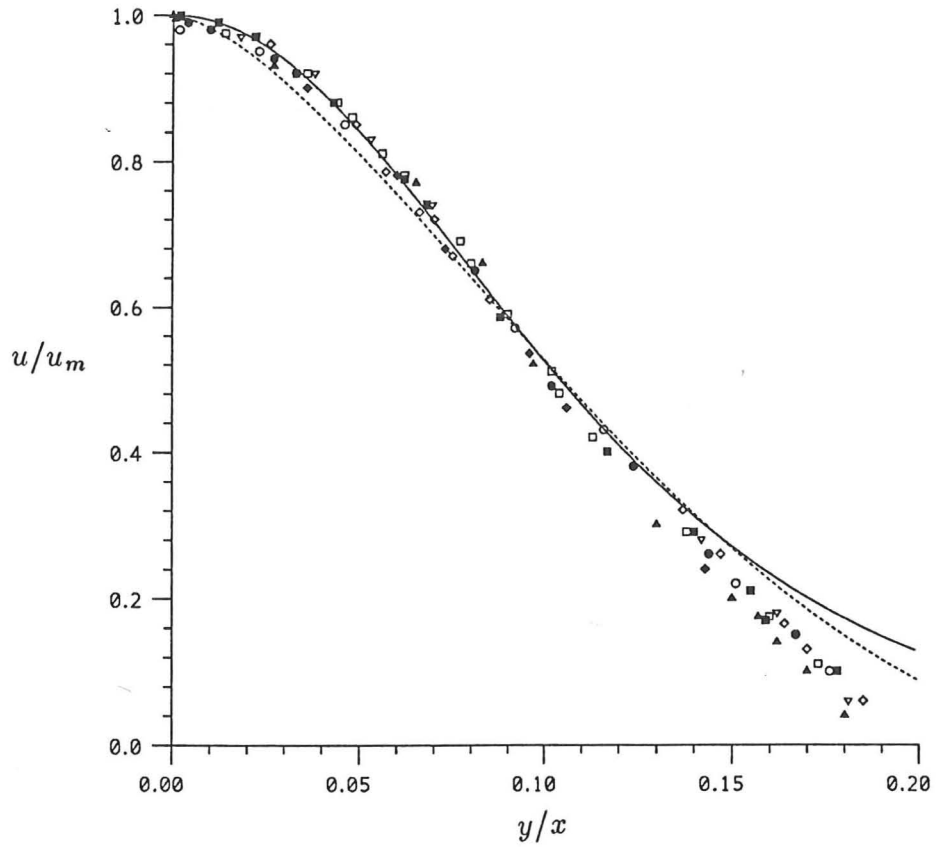

FIGURE 3. The solutions of the first order equations of motion for a planar turbulent jet compared with experimental data (Zijnen 1958).

—— Goertler (1942); - - - - Tollmien (1926).

This equation may be solved numerically - the solution for F' (i.e. u/u_m), with $\sigma = 0.108$, obtained using a NAG Fortran routine, is given in figure 3 (the dotted line). This figure also shows the Goertler solution (solid line), which in general shows better agreement with the data than the Tollmien solution, particularly near to the axis. The Tollmien solution achieves slightly lower values near to the edge of the jet and so agrees slightly better with the experimental data there than the Goertler solution, although neither solution is ideal. It should be pointed out that the experimental errors are largest at the edge of the jet as the velocities are small there and may be affected by any external effects (for example, the walls of the tank) or by the measuring equipment (for example, flows induced by hot-wire measuring devices). However, overall the Goertler solution is preferable having a simple analytical form.

The streamfunction for the Tollmien solution is given by

$$\psi(x, y) = n\sigma\sqrt{x}F(\eta), \tag{4.28}$$

and for large x, $F(\eta) \simeq \eta$, and the streamlines take the approximate form (as in the previous case: see equation 4.23)

$$y \sim \sqrt{x}. \tag{4.29}$$

4.4 The effect of including the second order terms

It has been shown that neither the Goertler nor the Tollmien solutions of the first order equations agreed well with the experimental data over the whole cross-section of the jet flow. However several terms were neglected and assumptions made which must inevitably affect the accuracy of these predictions. In order to improve the accuracy of the theoretical predictions, inclusion of the terms of second order (i.e. of order of magnitude ℓ) in equations (4.1) and (4.2) may be considered. It is unlikely that these terms will have a significant effect near to the axis of the jet as they are at least an order of magnitude smaller than the first order terms, however they may improve the solution near the edge of the jet where the transverse velocity component becomes comparable to the axial velocity and the ($\overline{v'^2} - \overline{u'^2}$) turbulent term may be non-negligible (Townsend 1956).

The pressure contributions may be eliminated by cross-differentiating and subtracting, $\frac{\partial}{\partial y}(4.1) - \frac{\partial}{\partial x}(4.2)$, giving

$$\frac{\partial}{\partial y}\left(u\frac{\partial u}{\partial x} + v\frac{\partial u}{\partial y}\right) - \frac{\partial}{\partial x}\left(u\frac{\partial v}{\partial x} + v\frac{\partial v}{\partial y}\right) = \left(\frac{\partial^2}{\partial x^2} - \frac{\partial^2}{\partial y^2}\right)\overline{u'v'} + \frac{\partial^2}{\partial x \partial y}(\overline{v'^2} - \overline{u'^2}), \tag{4.30}$$

in which the Reynolds number is assumed to be sufficiently high for the viscous terms to be neglected. This is the new, second order, equation of motion for a turbulent planar jet.

The turbulent products may be modelled with the use of the eddy viscosity model using the general expression

$$-\overline{u_i' u_j'} = \epsilon(x)\left(\frac{\partial u_i}{\partial x_j} + \frac{\partial u_j}{\partial x_i}\right) - \frac{1}{3}\overline{u_k' u_k'}\delta_{ij}, \tag{4.31}$$

where δ_{ij} is the Kronecker-delta tensor. Thus

$$\overline{u'v'} = -\epsilon(x)\left(\frac{\partial u}{\partial y} + \frac{\partial v}{\partial x}\right) \quad \text{and} \tag{4.32}$$

$$\overline{v'^2} - \overline{u'^2} = 2\epsilon(x)\left(\frac{\partial u}{\partial x} - \frac{\partial v}{\partial y}\right) = 4\epsilon(x)\frac{\partial u}{\partial x}. \tag{4.33}$$

Initially the equations will be considered without the inclusion of the latter term (in equation (4.30)) as a comparison between the form of ($\overline{v'^2} - \overline{u'^2}$) predicted by (4.33), using the solution given in equation (4.21a), with experimental data (Heskestad 1965) reveals a rather poor match (see figure 4). Thus substituting the previous forms of $u(x,y)$ and $v(x,y)$, given in equations (4.14) and (4.15) into (4.30), using (4.32) but neglecting the ($\overline{v'^2} - \overline{u'^2}$) term, gives

$$-\frac{n^2}{2\sigma x^3}(FF''' + 3F'F'') - \frac{\sigma n^2}{2x^3}\left(3\eta F'^2 + 3\eta^2 F'F'' + 3\eta FF'' + \eta^2 FF'''\right) = \frac{kn^2 c_2' F^{iv}}{\sigma^3 x^3}$$

$$-\frac{kn^2 c_2'}{\sigma x^3}(2F'' + 4\eta F''' + \eta^2 F^{iv}) - \frac{kn^2 c_2'\sigma}{x^3}\left(\frac{1}{2}F - 5\eta F' - \frac{71}{4}\eta^2 F'' - 9\eta^3 F''' - \eta^4 F^{iv}\right)$$

$$-\frac{kn^2 c_2'}{\sigma x^3}\left(\frac{15}{4}F'' + 5\eta F''' + \eta^2 F^{iv}\right), \tag{4.34}$$

where the first terms on each side correspond to the terms that would be obtained using the first order approximations. Note that the second term on the left and the second, fourth and fifth terms on the right are of order of magnitude ℓ^2 compared with the first terms on each side, whereas the third term on the right hand side is of order ℓ^4.

Simplifying and integrating with respect to η gives

$$-\frac{1}{2}(FF'' + F'^2) - \frac{\sigma^2}{2}\left(\eta^2 FF'' + \eta^2 F'^2 + \eta FF' - \frac{F^2}{2}\right) = \frac{kc_2'}{\sigma^2}F''' - kc_2'(\eta^2 F''' + 2\eta F'')$$

$$+kc_2'\sigma^2\left(\eta^4 F''' + 5\eta^3 F'' + \frac{11}{4}\eta^2 F' - \frac{1}{2}\eta F\right) - kc_2'\left(\eta^2 F''' + 3\eta F'' + \frac{3}{4}F'\right) + K, \tag{4.35}$$

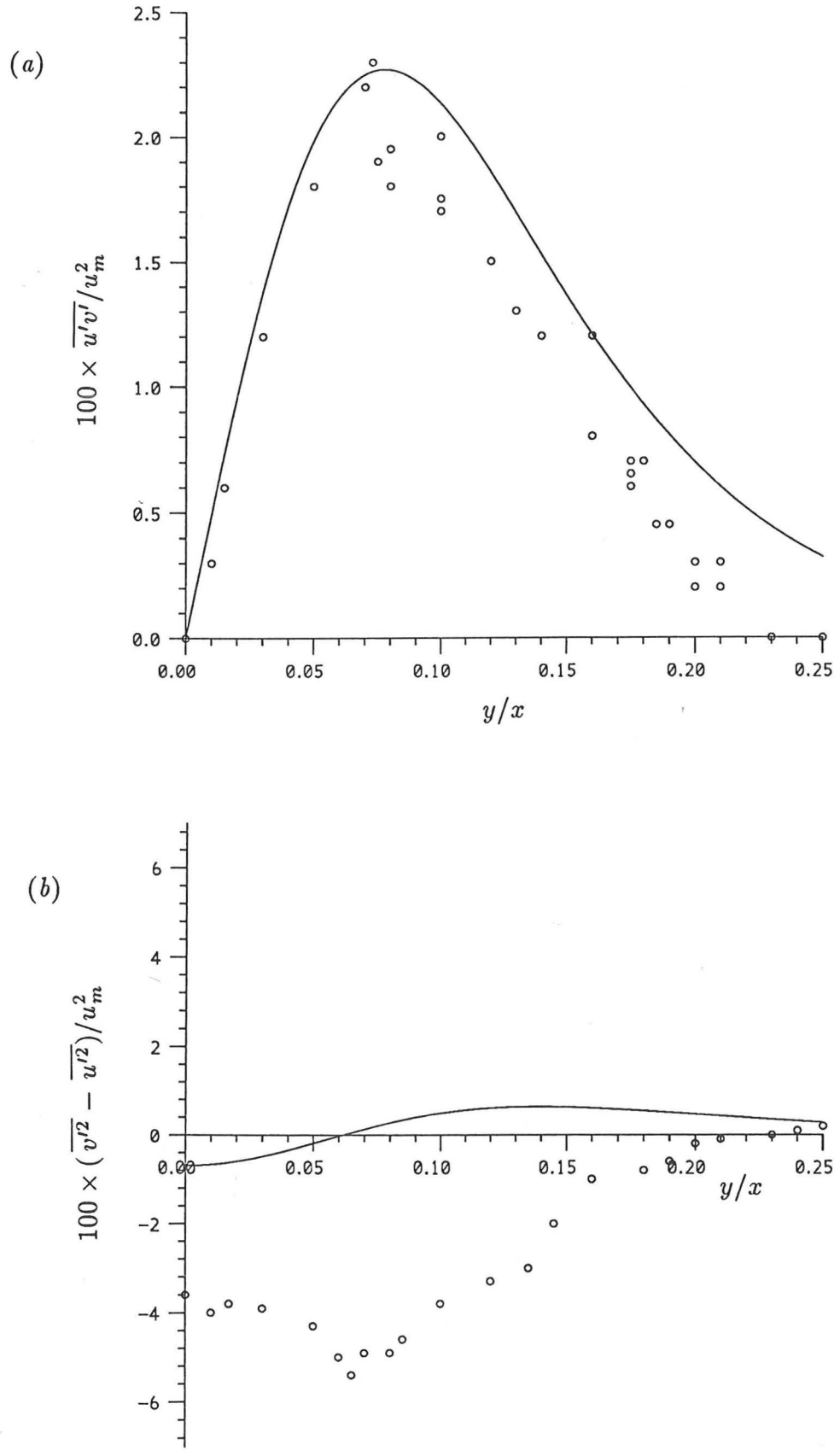

FIGURE 4. Experimental measurements (Heskestad 1965, see Rajaratnam 1976) of the turbulent velocity products compared with the predictions of the eddy viscosity model for a planar turbulent jet. (*a*) $\overline{u'v'}/u_m^2$; (*b*) $(\overline{v'^2} - \overline{u'^2})/u_m^2$.

where K is a constant of integration. Equation (4.35) may be integrated once more giving

$$-\frac{1}{2}FF' - \frac{\sigma^2}{2}\left(\eta^2 FF' - \eta\frac{F^2}{2}\right) = \frac{kc_2'}{\sigma^2}F'' - kc_2'(\eta^2 F'')$$

$$+kc_2'\sigma^2\left(\eta^4 F'' + \eta^3 F' - \frac{1}{4}\eta^2 F\right) - kc_2'\left(\eta^2 F'' + \eta F' - \frac{1}{4}F\right) + K\eta + L, \qquad (4.36)$$

where L is a constant of integration. The boundary condition at $\eta = 0$ implies that $L = 0$ and consideration of the largest terms in the limit $\eta \to \infty$ requires that $K = 0$ for a solution in which $u \to 0$ as $\eta \to \infty$. Application of the boundary conditions at $\eta = 0$ in equation (4.35) gives

$$-\frac{1}{2} = \frac{kc_2'}{\sigma^2}F'''(0) - \frac{3kc_2'}{4}. \qquad (4.37)$$

Assuming that for small η the required solution is to agree with the first order solution, (4.20), in which $F'''(0) = -2$, then (4.37) implies that

$$4kc_2' = \frac{\sigma^2}{1 + 3\sigma^2/8}. \qquad (4.38)$$

Thus equation (4.36) reduces to

$$F'' + 2\lambda FF' = \sigma^2\left(2\eta^2 F'' + \eta F' - \frac{1}{4}F - \lambda(2\eta^2 FF' - \eta F^2) - \sigma^2\left[\eta^4 F'' + \eta^3 F' - \frac{1}{4}\eta^2 F\right]\right), \qquad (4.39)$$

where $\lambda = (1 + 3\sigma^2/8)$. This final equation shows clearly that the modifications to the first order approximate equation, (4.17), are of order of magnitude ℓ^2.

The solution to equation (4.39), obtained using a NAG Fortran routine, was used to calculate the axial velocity distribution. The solution, with $\sigma = 0.118$, is shown in figure 5 (dotted line) in which the first order solution (solid line) is also included. It can be seen that the higher order terms make very little difference to the solution, even near to the edge of the jet. At the point $y/x = 0.2$, the modified solution is approximately 6% lower than the first order solution. Therefore it must be concluded that neglecting the second order terms in the first order approximate solution was not the cause of the poor agreement between the theoretical solution and the experimental data.

In the above analysis the $(\overline{v'^2} - \overline{u'^2})$ turbulent term was neglected. For completeness, the effect of including this term should be examined.

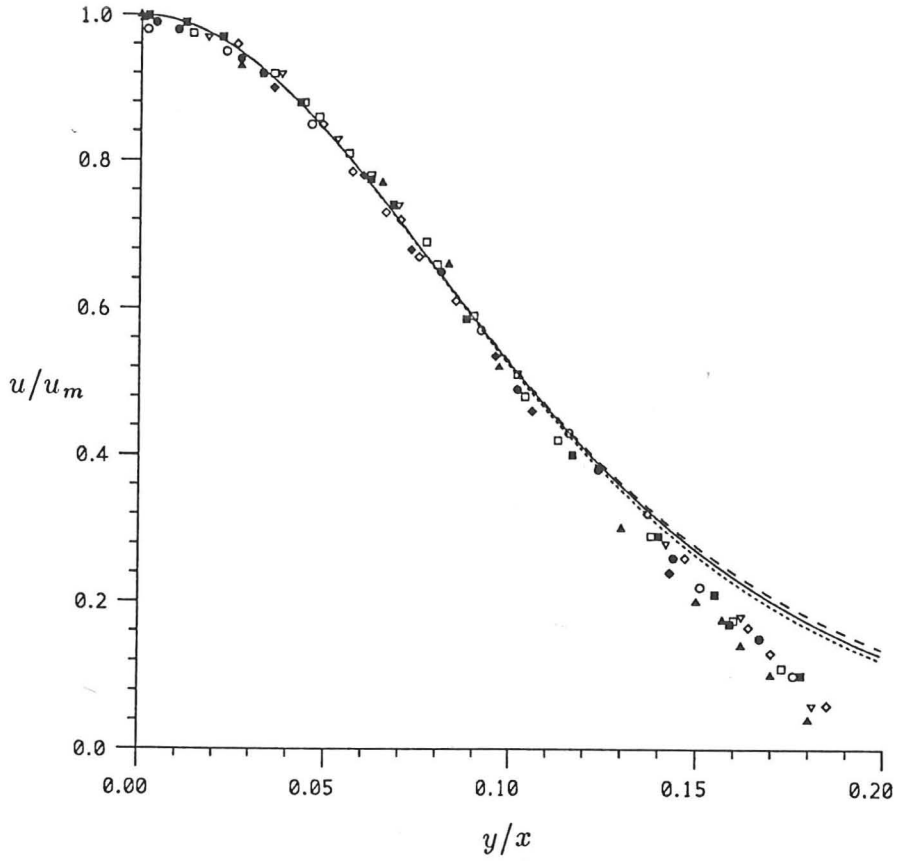

FIGURE 5. The solution to the second order equation of motion of a planar turbulent jet, using the eddy viscosity model with $\sigma = 0.118$, compared with experimental data (Zijnen 1958).

—— First order solution; - - - - second order, not including the $(\overline{v'^2} - \overline{u'^2})$ term;
— — — second order, including the $(\overline{v'^2} - \overline{u'^2})$ term.

Using the general expression (4.31), the turbulent quantity $(\overline{v'^2} - \overline{u'^2})$ was expressed in terms of the axial gradient of the mean axial velocity,

$$(\overline{v'^2} - \overline{u'^2}) = 4\epsilon(x)\frac{\partial u}{\partial x}.$$

Inclusion of this term brings in the following extra term to the right hand side of equation (4.34)

$$\frac{4kc_2'n^2}{\sigma x^3}\left(\eta^2 F^{iv} + \frac{9}{2}\eta F'' + 3F''\right), \tag{4.40}$$

which may be integrated twice, bringing extra terms

$$4kc_2'\left(\eta^2 F''' + \frac{5}{2}\eta F'' + \frac{1}{2}F'\right) \quad \text{and} \tag{4.41}$$

$$4kc_2'\left(\eta^2 F'' + \frac{1}{2}\eta F'\right), \tag{4.42}$$

to the right hand sides of equations (4.35) and (4.36) respectively. The $\eta = 0$ boundary condition, (4.38), is modified to

$$4kc_2' = \frac{\sigma^2}{1 - 5\sigma^2/8}. \tag{4.43}$$

The numerical solution of the new equation of motion, (4.36) with (4.42), is shown in figure 5 (dashed line), and it can be seen clearly that the inclusion of this term makes the agreement between the theoretical solution and experimental results slightly worse. At the point $y/x = 0.2$, this new theoretical solution is now about 7.5% higher than the first order solution. The discrepancy between the theoretical predictions and experimental results must therefore be due to some effect other than those of the second order terms. However, some of the disagreement may be due to the poor predictions of the eddy viscosity model when used to model the $(\overline{v'^2} - \overline{u'^2})$ term (see figure 4) - greater agreement may be obtained using some other turbulence model.

Use of the mixing length hypothesis (see section 4.3.2) in equation (4.30), but neglecting the $(\overline{v'^2} - \overline{u'^2})$ term, also gives no significant improvement on the first order (Tollmien) solution. In this case the equation of motion, (4.27) is modified to

$$F''^2 - FF' = \sigma^2\left(\eta^2 F''^2 + \eta^2 FF' - \frac{\eta}{2}F^2\right), \tag{4.44}$$

in which it may be clearly seen that the modifications are of order of magnitude ℓ^2. The numerical solution, obtained using a NAG Fortran routine (with $\sigma = 0.107$), was used to calculate the axial velocity and is shown in figure 6 - the dashed line is the modified solution and the solid line is the first order approximate solution. At the point $y/x = 0.2$, the value of the modified solution is approximately 4.4% lower than the first order solution. This result also confirms the conclusions made when using the eddy viscosity model, i.e. that neglecting the second order terms is not the cause of the poor agreement between the theoretical and the experimental velocity values near to the edge of the jet.

4.5 The effect of including variation of the intermittency factor

There is, however, one physical effect that has not yet been considered. Wygnanski & Fiedler (1969) pointed out that the turbulent intermittency factor, γ, the probability of finding fully developed turbulence at a given point, should be included in the definition of the eddy viscosity. Moreover they also found that γ was approximately constant in the region $0 \leqslant y/x \leqslant 0.1$ and decreases when $y/x > 0.1$. With this modification, equation (4.13) becomes

$$\tau = \rho\epsilon(x)\gamma\frac{\partial(u/\gamma)}{\partial y}. \tag{4.45}$$

The investigation of section 4.4 above shows that it is satisfactory to use the first order approximate equation of motion, (4.8). With the use of (4.45) this becomes

$$u\frac{\partial u}{\partial x} + v\frac{\partial u}{\partial y} = \epsilon(x)\left[\frac{\partial^2 u}{\partial y^2} - \frac{1}{\gamma}\frac{\partial\gamma}{\partial y}\frac{\partial u}{\partial y} + \frac{u}{\gamma^2}\left(\frac{\partial\gamma}{\partial y}\right)^2 - \frac{u}{\gamma}\frac{\partial^2\gamma}{\partial y^2}\right]. \tag{4.46}$$

In order to include the intermittency factor in the numerical analysis, an approximation for the behaviour of $\gamma(x, y)$ is required. Experimental measurements (Heskestad 1965, Rajaratnam 1976) have shown that, for sufficiently large distances from the nozzle, γ reaches a self-similar state and can be expressed as a function of η. Figure 7 shows these measurements fitted to a curve of the form

$$\gamma(\eta) = \frac{1}{2}(1 - \tanh\Delta) \quad \text{where} \quad \Delta = \kappa(\eta - \eta_t), \tag{4.47a,b}$$

in which κ and η_t are constants with values $\kappa \simeq (14.5\pm0.5)\sigma$ and $\eta_t = 0.1955/\sigma$. Substitution of (4.47) into (4.46) using (4.14) and (4.15) gives (after simplification)

$$-\frac{n^2}{x^2}(FF'' + F'^2) = \frac{n^2 k c_2'}{a^2 x^2}\left(F''' + \frac{\kappa\,\mathrm{sech}^2\Delta}{(1 - \tanh\Delta)}F'' + \kappa^2\,\mathrm{sech}^2\Delta\,F'\right). \tag{4.48}$$

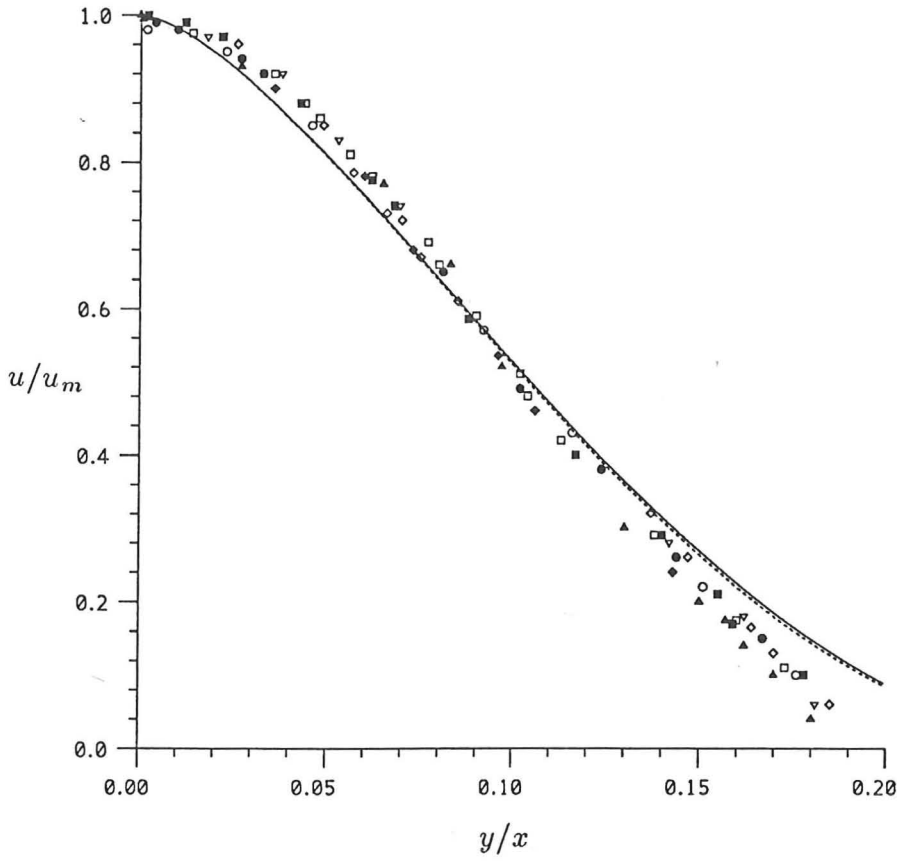

FIGURE 6. The solution to the second order equation of motion of a planar turbulent jet, using the mixing length hypothesis with $\sigma = 0.108$, compared with experimental data (Zijnen 1958).

—— First order solution; - - - - second order solution.

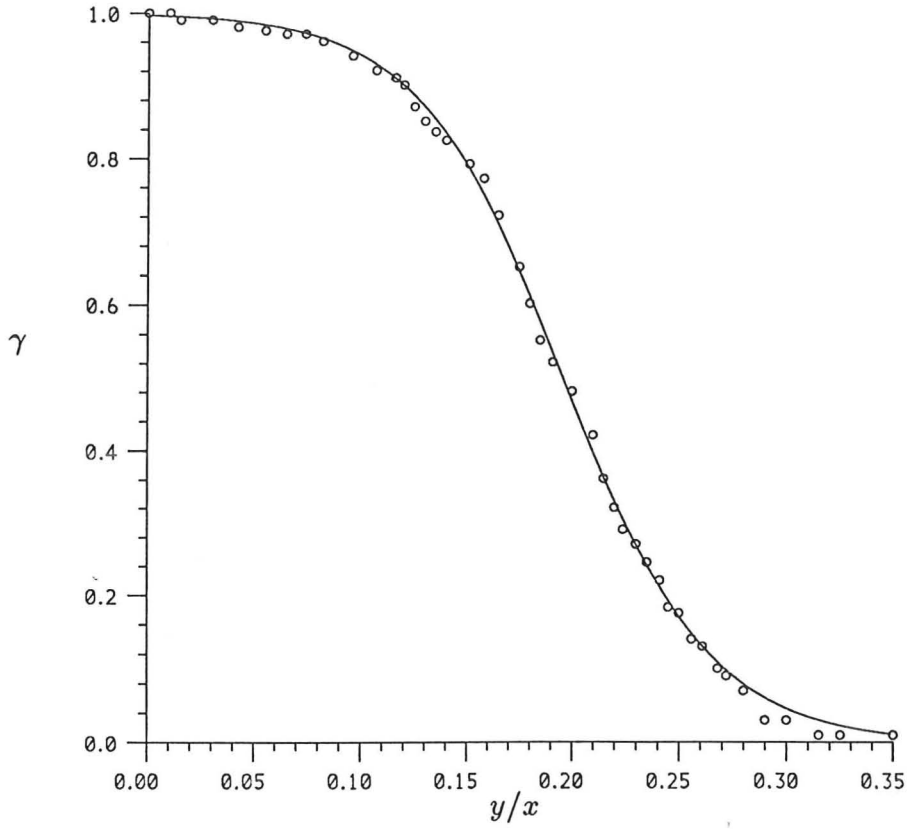

FIGURE 7. The behaviour of the intermittency factor, γ, (data due to Heskestad 1965, see Rajaratnam 1976) and the fitted curve, equation (4.46a).

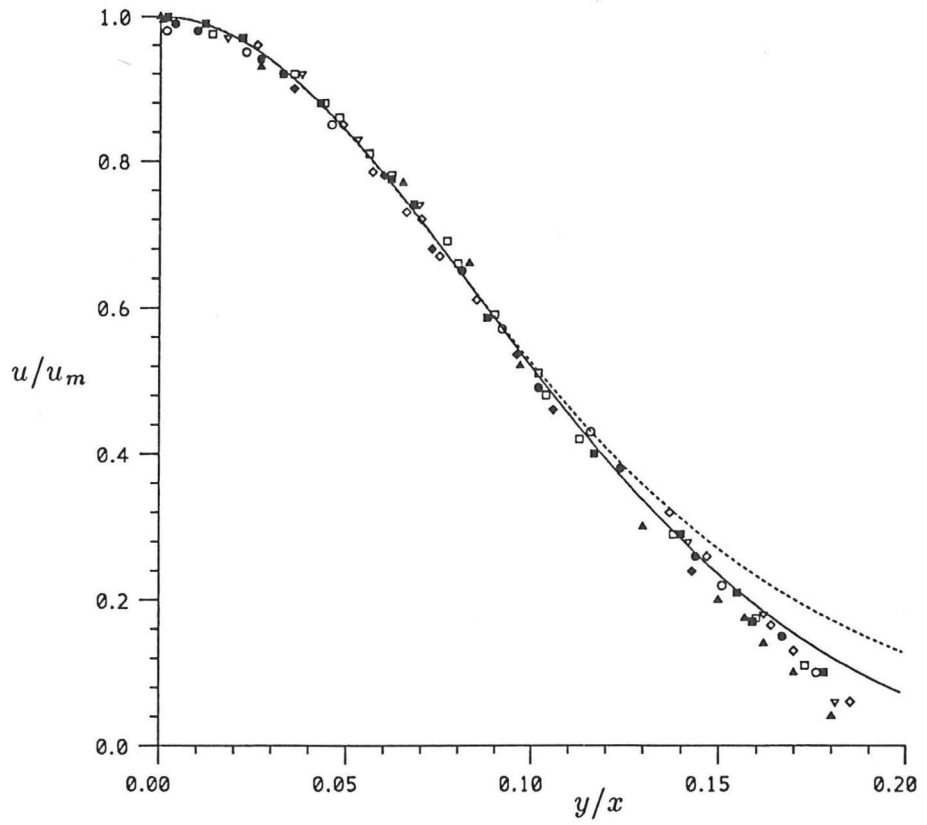

FIGURE 8. The solution to the first order equation of motion for a planar turbulent jet including variation of the intermittency factor, compared with experimental data (Zijnen 1958).

——— Solution with intermittency variation; - - - - first order solution with constant intermittency.

This equation may be integrated with respect to η giving

$$-\frac{1}{2}FF' = \frac{kc_2'}{\sigma^2}\left(F'' + \kappa(1 + \tanh\Delta)F'\right), \tag{4.49}$$

in which the integration constant has been set to zero by the boundary conditions.

Equation (4.49) was solved numerically using a NAG Fortran routine and the solution for the axial velocity is shown in figure 8 (with $\sigma = 0.1225$ - chosen so that the solution matches the first order solution near to the axis). The dotted line is the first order solution obtained in section 4.3.1 (with effectively constant intermittency factor and $\sigma = 0.118$). Clearly the agreement with the experimental data is greatly improved by the use of the variable intermittency factor (by up to 45%) - the theoretical solution shows excellent agreement for $y/x < 0.18$, whereas the first order solution can only be considered accurate for $y/x < 0.12$. The agreement is also better than that of the Gaussian fit shown in figure 2. Hence it must be concluded that neglecting the variation of the intermittency factor was probably the main cause of the poor agreement between the theoretical and experimental results near to the edge of the jet.

One of the useful features of the first order solution was that it had a convenient analytical form. In this case, the solution for the axial velocity may be approximated by

$$\frac{u}{u_m} = F'(\eta) \simeq \gamma(\eta)\,\mathrm{sech}^2\eta = \frac{1}{2}(1 - \tanh\Delta)\,\mathrm{sech}^2\eta, \tag{4.50}$$

which is accurate to within 3% in the range $0 \leqslant y/x \leqslant 0.18$.

5. Application of the momentum equations to circular jets

The analysis of the previous section may be applied to circular jets, obtaining analogous results. The general methods are very similar and so only brief details of the working are given here.

Assuming that the flow is perfectly axisymmetric with zero swirl, $u_\phi = 0$, axial (x) velocity, $u(x,r)$ and radial (r) velocity, $v(x,r)$, then the time-averaged momentum equations in cylindrical coordinates are

$$u\frac{\partial u}{\partial x} + v\frac{\partial u}{\partial r} = -\frac{1}{\rho}\frac{\partial p}{\partial x} - \left(\frac{\partial}{\partial r}\overline{u'v'} + \frac{\partial}{\partial x}\overline{u'^2} + \frac{\overline{u'v'}}{r}\right) + \nu\left(\frac{\partial^2}{\partial x^2} + \frac{1}{r}\frac{\partial}{\partial r}r\frac{\partial}{\partial r}\right)u, \tag{5.1}$$

$$u\frac{\partial v}{\partial x}+v\frac{\partial v}{\partial r}=-\frac{1}{\rho}\frac{\partial p}{\partial r}-\left(\frac{\partial}{\partial r}\overline{v'^2}+\frac{\partial}{\partial x}\overline{u'v'}+\frac{\overline{v'^2}}{r}\right)+\nu\left(\frac{\partial}{\partial x^2}+\frac{\partial}{\partial r}\frac{1}{r}\frac{\partial}{\partial r}r\right)v, \tag{5.2}$$

and the continuity equation is

$$\frac{\partial}{\partial x}ru+\frac{\partial}{\partial r}rv=0, \tag{5.3}$$

where, as before, the primes denote the turbulent fluctuating velocity components.

5.1 First order equations and solutions

As in the case of the planar jet, experimental observations show that the scales of the radial velocity and axial gradients are an order of magnitude less than those of the axial velocity and radial gradients respectively. Assuming that the Reynolds number is sufficiently high for viscous terms to be ignored, then neglecting all but the first order terms yields

$$\frac{1}{\rho}\frac{\partial p}{\partial r}=-\frac{\partial}{\partial r}\overline{v'^2}, \tag{5.4}$$

$$u\frac{\partial u}{\partial x}+v\frac{\partial u}{\partial r}=-\frac{1}{\rho}\frac{\partial p}{\partial x}-\left(\frac{\partial}{\partial r}\overline{u'v'}+\frac{\overline{u'v'}}{r}\right). \tag{5.5}$$

Integrating (5.4) with respect to r, substituting the result into (5.5) and simplifying (as in the two-dimensional case) gives

$$u\frac{\partial u}{\partial x}+v\frac{\partial u}{\partial r}=\frac{1}{\rho r}\frac{\partial r\tau}{\partial r}\quad\text{and}\quad\frac{\partial}{\partial x}ru+\frac{\partial}{\partial r}rv=0, \tag{5.6a,b}$$

where the axial pressure gradient outside of the jet has been assumed to be negligible, and τ is the turbulent shear stress $\tau=-\rho\overline{u'v'}$. These are the first order equations of motion for a circular jet.

Multiplying (5.6a) by r, integrating $\int_0^\infty\int_0^{2\pi} r\,d\phi dr$ and simplifying, yields the analogous result to equation (4.10), namely that the specific momentum flux is constant

$$\frac{d}{dx}\int_0^\infty 2ru^2dr=0. \tag{5.7}$$

Equation (5.6b) may be integrated similarly yielding the analogous result to equation (4.12), stating that the rate of change of volume flux is equal to the rate of entrainment

$$\frac{dQ}{dx}=\frac{d}{dx}\int_0^\infty 2ur\,dr=2b\alpha_j u_m, \tag{5.8}$$

where b is the length scale or 'radius' of the jet (note that α_j may have a different value in circular jets to that of the planar jet case).

Two solutions, analogous to the solutions of Goertler (1942) and Tollmien (1926) described in section 4.3, may also be found in the axisymmetric case. It is convenient to write

$$u(r,x) = u_m \frac{F'(\xi)}{\xi} \quad \text{where} \quad \xi = \frac{r}{\sigma x} \quad \text{and} \quad u_m = \frac{n}{x}, \quad n = c_1\sqrt{M_0} \tag{5.9}$$

so that

$$\psi(r,x) = nx\sigma^2 F(\xi) \quad \text{and} \quad v(r,x) = \frac{n\sigma}{x}\left(F'(\xi) - \frac{F}{\xi}\right). \tag{5.10}$$

Solution using the eddy viscosity model

Using the eddy viscosity model it is assumed that

$$\tau = \rho\epsilon(x)\frac{\partial u}{\partial r}, \tag{5.11}$$

where on dimensional grounds $\epsilon(x) = knc_2$, i.e. ϵ is a constant (where the dimensional result of equation (2.4) has been used). Substitution of (5.9), (5.10) and (5.11) into (5.6a) and integrating with respect to ξ gives an equation for $F(\xi)$,

$$FF' = F' - \xi F'', \tag{5.12}$$

in which σ has been set by $\sigma^2 = kc_2$ and the boundary conditions have set the integration constant to zero. The solution satisfying the boundary conditions, $F(0) = 0$, $F'(0) = 0$ and $[F'\xi](0) = 1$ is

$$F(\xi) = \frac{4\xi^2}{8+\xi^2}, \tag{5.13}$$

and therefore

$$u(r,x) = u_m \frac{1}{(1+\xi^2/8)^2} \quad \text{and} \quad v(r,x) = u_m\sigma\frac{\xi(1-\xi^2/8)}{2(1+\xi^2/8)^2}. \tag{5.14}$$

The streamlines are given by

$$r^2 = \left(\frac{8\psi x^2}{4nx - \psi/\sigma^2}\right), \tag{5.15}$$

and for large x the streamlines take the approximate form

$$r \sim \sqrt{x}. \tag{5.16}$$

Hence the particles asymptotically follow the same paths (within a plane through the jet) in the three dimensional case as in two dimensions (see equations (4.23) or (4.29)).

Solution using the mixing length model

A mixing length formula may also be used to model the turbulent stress, τ,

$$\tau = -\rho l^2 \left(\frac{\partial u}{\partial r}\right)^2, \tag{5.17}$$

where l is the mixing length with $l = \beta b = \beta c_2 x$ on dimensional grounds (using equation (2.4)).

Substituting this into the first order equation of motion, (5.6a), and integrating gives

$$\left(F'' - \frac{F'}{\xi}\right)^2 = FF', \tag{5.18}$$

in which σ has been set by $\sigma^3 = \beta^2 c_2^2$. An analytical solution does not exist, although a series solution may be derived (Abramovitch 1963).

The eddy viscosity solution (with $\sigma = 0.046$, solid line) and a numerical solution to equation (5.18) (obtained using a NAG Fortran routine with $\sigma = 0.069$, dotted line) were used to calculate the axial velocity distribution and are shown in figure 9 together with some experimental data (from Wygnanski & Fiedler 1969). As in the two-dimensional case, neither solution agrees well over the whole cross-section of the jet flow, although the mixing length solution is generally quite good. As was the case for planar jets, the eddy viscosity solution shows the best agreement near to the jet axis and the mixing length solution is better near to the edge of the jet. Further details of the above two solutions may be found in Rajaratnam (1976).

5.2 Second order equations

Although figure 9 shows that the mixing length solution shows a good general agreement over the jet cross-section, the effects of including the second order terms and the intermittency

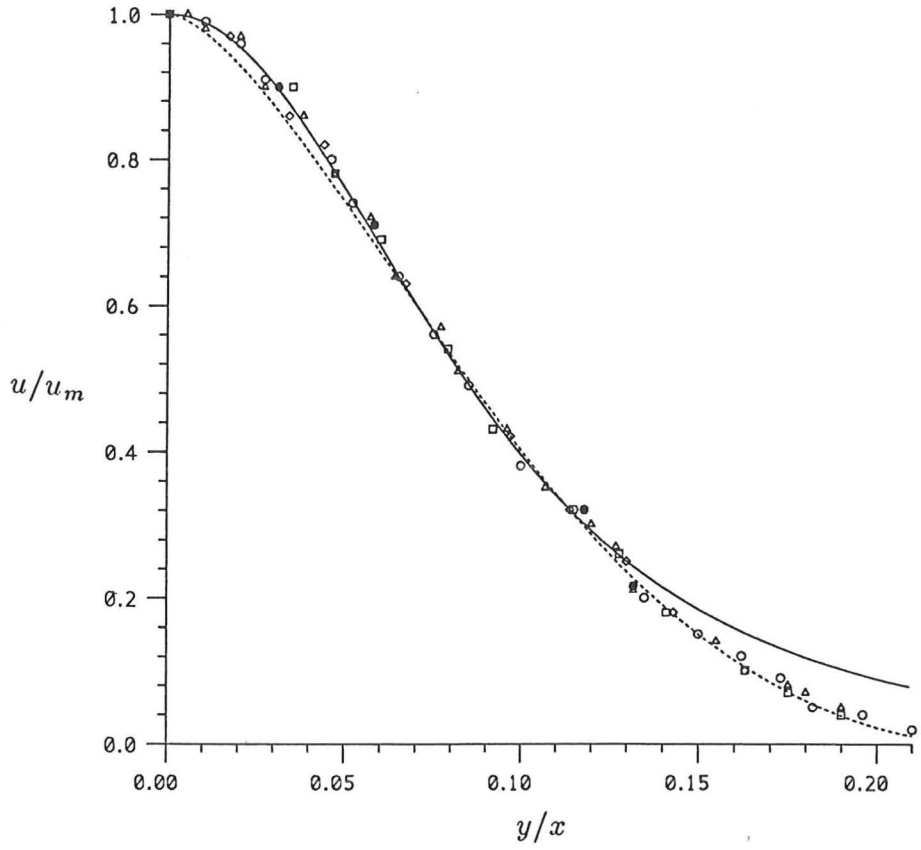

FIGURE 9. The solutions to the first order equation of motion for a circular turbulent jet compared with experimental data (from Wygnanski & Fielder 1969).

—— Eddy viscosity solution; - - - - mixing-length solution.

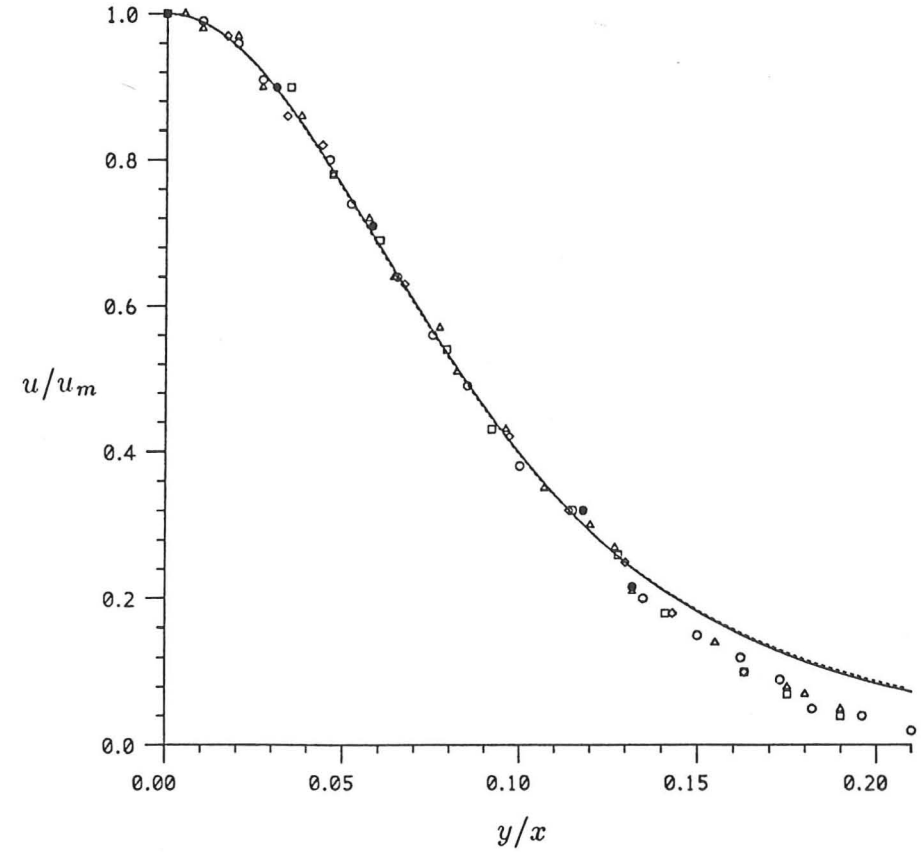

FIGURE 10. The solution to the second order equation of motion for a circular turbulent jet compared with experimental data (from Wygnanski & Fielder 1969).

—— Second order solution; - - - - first order solution.

factor on the solution when using the eddy viscosity model may still be examined. Eliminating the pressure from equations (5.1) and (5.2), neglecting the viscous terms, gives

$$\frac{\partial}{\partial r}\left(u\frac{\partial u}{\partial x}+v\frac{\partial u}{\partial r}\right)-\frac{\partial}{\partial x}\left(u\frac{\partial v}{\partial x}+v\frac{\partial v}{\partial r}\right)=\left(\frac{\partial^2}{\partial x^2}-\frac{\partial}{\partial r}\frac{1}{r}\frac{\partial}{\partial r}r\right)\overline{u'v'}-\frac{\partial^2}{\partial x\partial r}\overline{u'^2}+\frac{\partial}{\partial x}\frac{1}{r}\frac{\partial}{\partial r}(r\,\overline{v'^2}). \tag{5.19}$$

The turbulent products may be modelled using an eddy viscosity, with

$$\overline{u'v'}=-\frac{\tau}{\rho}=-\epsilon(x)\left(\frac{\partial u}{\partial r}+\frac{\partial v}{\partial x}\right). \tag{5.20}$$

The eddy viscosity model was not found to predict the terms in $\overline{u'^2}$ and $\overline{v'^2}$ in the two-dimensional case very well and so these terms are not included here.

Substituting (5.20) into (5.19) using equations (5.9) and (5.10) gives

$$\frac{n^2}{\sigma\xi^2x^4}\left(\frac{3}{\xi^2}(F'^2\xi+FF''\xi-FF'-\xi^2F'F'')-FF'''\right)-\frac{\sigma n^2}{x^4}(3F'F''+FF''')=$$

$$\frac{kn^2c_2}{\sigma^3x^4\xi^4}(F^{iv}\xi^3-2F'''\xi^2+3F''\xi-3F')-\frac{kn^2c_2}{\sigma x^4}(\xi F^{iv}+3F''')$$

$$-\frac{kn^2c_2}{\sigma x^4}(\xi F^{iv}+3F''')+\frac{kn^2c_2\sigma}{x^4}(12\xi F''+8\xi^2F'''+\xi^3F^{iv}), \tag{5.21}$$

where the first terms on each side correspond to those that would be obtained using the first order equations. Rearranging and integrating gives

$$-\frac{1}{\xi^3}(\xi FF''+\xi F'^2-FF')-\sigma^2(FF''+F'^2)=\frac{kc_2}{\sigma^2\xi^3}(\xi^2F'''-\xi F''+F')-kc_2(\xi F'''+2F'')$$

$$-kc_2(\xi F'''+2F'')+kc_2\sigma^2(\xi^3F'''+5\xi^2F''+2\xi F'-2F)+\tilde{K}, \tag{5.22}$$

where $\tilde{K}$ is a constant of integration. This equation may be rewritten as

$$-\frac{1}{\xi}\frac{d}{d\xi}\left(\frac{FF'}{\xi}\right)+\frac{\sigma^2}{\xi}\frac{d}{d\xi}\left(\frac{F^2}{2}-\xi FF'\right)=-\frac{kc_2}{\sigma^2\xi}\frac{d}{d\xi}\left(\frac{F'}{\xi}-F''\right)-\frac{kc_2}{\xi}\frac{d}{d\xi}(\xi^2F'')$$

$$-\frac{kc_2}{\xi}\frac{d}{d\xi}(\xi^2F'')+\frac{kc_2\sigma^2}{\xi}\frac{d}{d\xi}(\xi^4F''+\xi^3F'-\xi^2F)+\frac{1}{\xi}\frac{d}{d\xi}\left(\frac{\tilde{K}\xi^2}{2}\right). \tag{5.23}$$

Equation (5.23) may be rearranged and integrated again giving

$$FF' - \sigma^2\xi\left(\frac{F^2}{2} - \xi FF'\right) = \frac{kc_2\xi}{\sigma^2}\left(\frac{F'}{\xi} - F''\right) + 2kc_2(\xi^3 F'')$$

$$-kc_2\sigma^2\xi(\xi^4 F'' + \xi^3 F' - \xi^2 F) - \frac{\tilde{K}\xi^3}{2} + \tilde{L}\xi, \tag{5.24}$$

where $\tilde{L}$ is a constant of integration. The boundary condition at $\xi = 0$ insists that $\tilde{L} = 0$, and consideration of the limit $\xi \to \infty$ requires that $\tilde{K} = 0$ for a solution in which $u \to 0$ as $\xi \to \infty$. Application of the boundary condition at $\xi = 0$ in equation (5.22), assuming that for small ξ the solution is required to agree with the first order solution (5.13) in which $F''(0) = 1$, $[F/\xi^2](0) = 1/2$, $[F'''/\xi](0) = -3/2$ and $[F'/\xi^3 - F''/\xi^2](0) = 1/2$, insists that

$$kc_2 = \left(\frac{\sigma^2}{1 + 4\sigma^2}\right). \tag{5.25}$$

Thus (5.24) may be written

$$\xi F'' - F' + \tilde{\lambda}FF' = \sigma^2\xi\left(2\xi^2 F'' + \tilde{\lambda}\left[\frac{1}{2}F^2 - \xi FF'\right] - \sigma^2(\xi^4 F'' + \xi^3 F' - \xi^2 F)\right), \tag{5.26}$$

where $\tilde{\lambda} = (1 + 4\sigma^2)$.

The numerical solution to equation (5.26), obtained using a NAG Fortran routine with $\sigma = 0.046$, was used to calculate the axial velocity variation and is shown in figure 10 (solid line) together with the first order solution (dotted line). Clearly the inclusion of the second order terms has had little effect, as in the case of the two dimensional jet. At the point $y/x = 0.21$ the second order solution is approximately 4.5% lower than the first order solution. Hence it must be concluded that neglecting the second order terms was not the cause of the poor agreement between the first order eddy viscosity solution and the experimental data.

5.3 Including variation of the intermittency factor

In the earlier case of the planar jet, it was found that the intermittency factor, γ, varied over a cross-section of the jet and that inclusion of this variation in the first order analysis (using the eddy viscosity model) significantly improved the theoretical predictions. The intermittency factor also varies over a cross-section of a circular jet (Wygnanski & Fiedler 1969)

and inclusion of this variation may also improve the eddy-viscosity model of the circular jet above.

Measurements of the intermittency factor in a circular jet are shown in figure 11 (from Wygnanski & Fiedler 1969) fitted to a curve of the form used in the planar jet case (see equations (4.46)),

$$\gamma(\xi) = \frac{1}{2}(1 - \tanh\Delta) \quad \text{where} \quad \Delta = \kappa(\xi - \xi_t), \tag{5.27}$$

and in this case the best agreement is found when $\kappa \simeq (26.0 \pm 0.5)\sigma$ and $\xi_t = 0.162/\sigma$. Substitution of (5.27) into the first order equation of motion, (5.6*a*), with

$$\tau = \rho\epsilon(x)\gamma\frac{\partial(u/\gamma)}{\partial r}, \tag{5.28}$$

gives after some simplification

$$\frac{1}{\xi^2}(FF' - \xi F'^2 - \xi FF'') = \frac{kc_2}{\sigma^2}\left(\frac{F'}{\xi^2} - \frac{F''}{\xi} + F''' + \kappa(1 + \tanh\Delta)F'' + \kappa^2\,\mathrm{sech}^2\Delta F'\right). \tag{5.29}$$

This may be integrated with respect to ξ giving

$$F' - FF' - \xi F'' = \kappa\xi(1 + \tanh\Delta)F', \tag{5.30}$$

(compare this with equation (5.12)) in which the boundary conditions have set the integration constant to zero and σ has been set by $\sigma^2 = kc_2$ (as in the first order solution).

Equation (5.30) may be solved numerically and the solution, (obtained using a NAG Fortran routine with $\sigma = 0.0463$) used to calculate the axial velocity, is shown in figure 12. The value of σ (previously $\sigma = 0.0460$) was adjusted slightly to maintain a good agreement between the solution and the first order solution (the dotted line in figure 12) near to the jet axis. Clearly, the agreement between the theoretical prediction and the experimental measurements has been greatly improved by the inclusion of a variable intermittency factor in the eddy viscosity model. At the point $y/x = 0.21$, the theoretical prediction has been improved by approximately 76% compared with the first order solution. As in the two dimensional case, the solution for the axial velocity may be approximated by

$$u/u_m = \frac{F'}{\xi} \simeq \frac{\gamma(\xi)}{(1 + \xi^2/8)^2} = \frac{1}{2}\frac{(1 - \tanh\Delta)}{(1 + \xi^2/8)^2}, \tag{5.31}$$

which is accurate to within 12% in the range $0 \leqslant y/x \leqslant 0.21$.

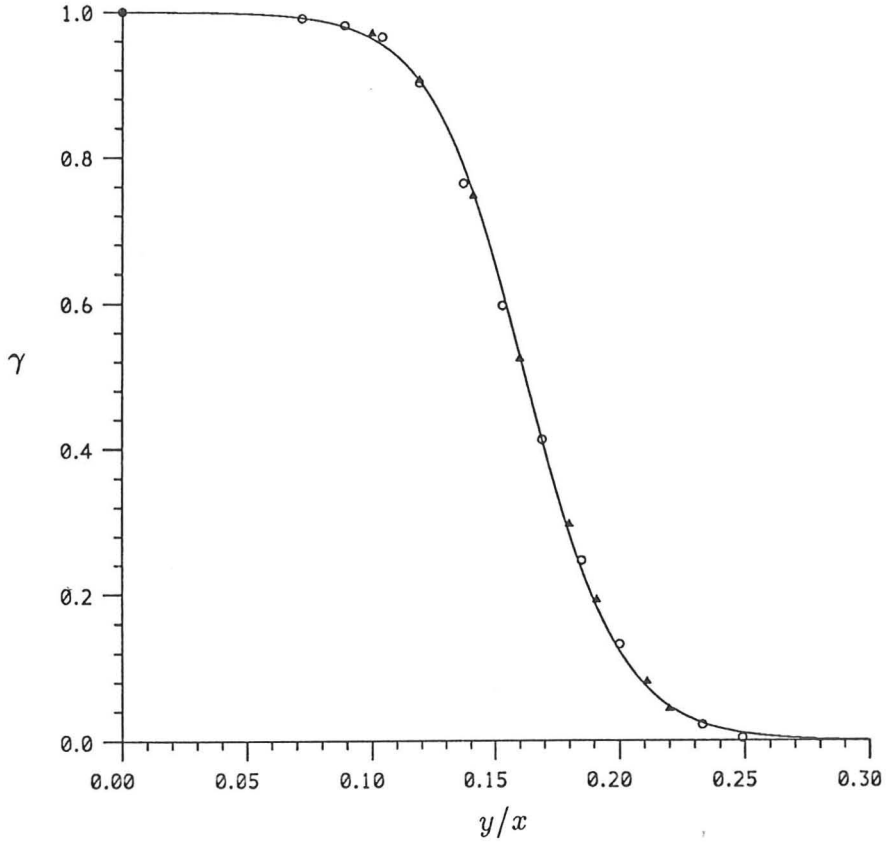

FIGURE 11. The behaviour of the intermittency factor, γ, in a circular jet (data from Wygnanski & Fielder 1969) and the fitted curve, equation (5.27).

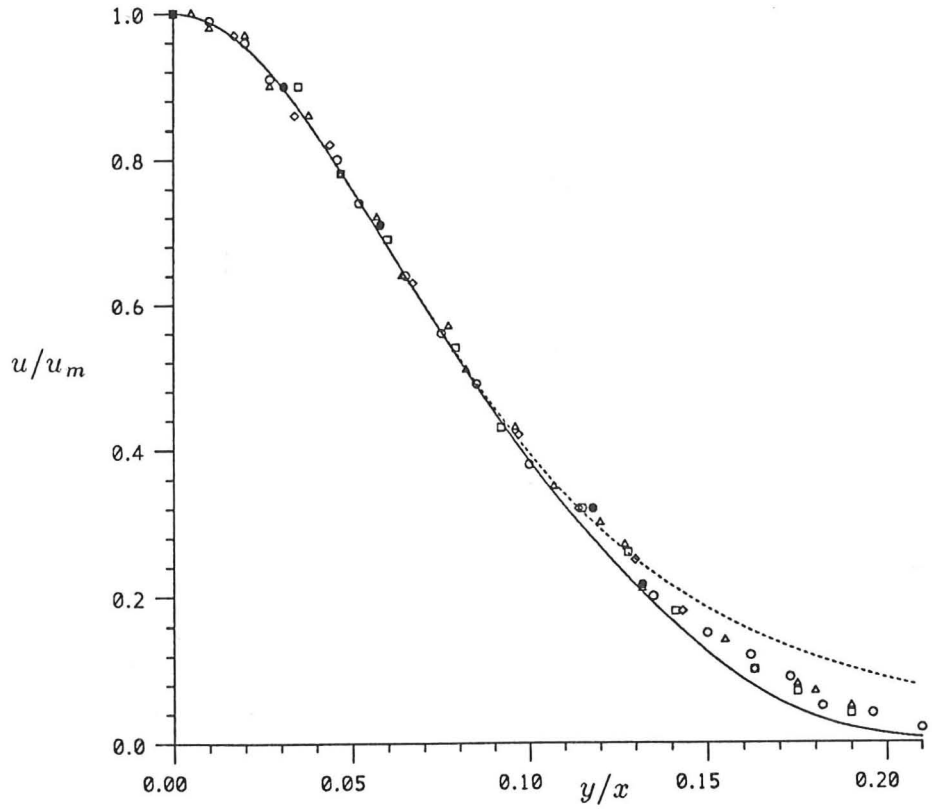

FIGURE 12. The solution to the first order equation of motion for a circular turbulent jet including variation of the intermittency factor, compared with experimental data (from Wygnanski & Fielder 1969).

—— Solution with intermittency variation; - - - - first order solution with constant intermittency.

6. Discussion and conclusions

The flow of buoyant fluid from a source is often modelled using the established theories of turbulent jets and plumes. The chapter started with definitions of these flows followed by a brief review of the well-known properties of jets and plumes obtained from experimental observations and simple dimensional analysis. Experimental measurements (see tables 1 and 3, and figure 2) have shown that, after an axial distance of about 6 nozzle diameters, the flow of a jet or plume reaches a fully turbulent, 'self-similar', state in which all of the flow variables are expressible in terms of a similarity variable proportional to y/x (for planar jets, r/x in axisymmetric jets). This fundamental observation was the basis of all of the theoretical analysis. The dimensional analysis, however, relied on the simple assumption that, for sufficiently large Reynolds numbers, the flow of a turbulent jet or plume is controlled by its initial (source) conditions namely the initial fluxes of mass, momentum and buoyancy. With this assumption the axial variations of the flow variables were deduced (see tables 2 and 4). In practice, however, it is most likely that a source will be one of both momentum and buoyancy - a 'buoyant jet'. It was shown that these flows undergo a transition between jet-like (initial) and plume-like (final) flow states. Consequently it is not possible to obtain expressions for the behaviour of the flow variables using simple dimensional analysis. A length scale which describes this jet-plume transition was constructed and is called the 'jet-length',

$$L_j = \frac{M_0^{\frac{3}{4}}}{B_0^{\frac{1}{2}}}.$$

It will become apparent in chapters 3 and 4 that this is an extremely important parameter, controlling and describing the flow produced by a buoyant source.

Having summarised the basic features of jets and plumes, the equations of incompressible fluid flow were then introduced and applied to jet flow. Similarity solutions were obtained by neglecting the smallest terms in the momentum equations, using either an eddy viscosity or a mixing length turbulence model. The solutions were used to predict the transverse/radial variation of the axial velocity, but for both planar and circular jets, neither solution was found to agree well with the experimental results over the whole jet cross-section. The possible causes of the disagreement were then investigated.

In general, the theoretical predictions were weakest near to the edge of the jet. This suggested that the poor agreement near the jet edge was possibly a result of neglecting the

smaller terms in the momentum equations which may be significant near to the edge of the jet. The analysis was then extended to include these terms. The resultant equations, (4.39), (4.44) and (5.26) show clearly that the modifications are of order of magnitude σ^2, i.e. about 1%. Consequently the numerical solutions showed little improvement on the first order solutions and so it was concluded that neglecting the second order terms was not the cause of the disagreement between the theoretical and numerical results. Note, however, that the predictions of the eddy viscosity model were poor when used to calculate the behaviour of the ($\overline{v'^2} - \overline{u'^2}$) turbulent term, with the experimental measurements being of much greater magnitude than the model predicts (see figure 4). It is possible that if this term could be modelled more accurately then the resulting solution could show a greater agreement with the experimental data.

The second effect investigated was variation of the intermittency factor over the jet cross-section. The form of the eddy viscosity model used in the first and second order term analysis (see equations (4.32) and (5.11)) did not allow for the possibility that the intermittency factor might not be constant over the whole jet cross-section. Measurements have shown (see figures 7 and 11) that the intermittency factor is approximately unity in the central region of the jet but falls to zero near to the edge. Including this variation modified the above equations to (4.45) and (5.28). Using these modified shear stresses and using experimental data to estimate the behaviour of the intermittency factor in the first order equations gave a significant improvement in the theoretical predictions. Near to the edge of the jet, where the difference between the theoretical predictions and experimental results was greatest, an improvement of about 45% for the planar jet and 76% for the circular jet was found. The solutions for the axial velocity were found to be approximately equal to the product of the first order solution and the intermittency factor, γ.

Notation

Below is a list of the symbols used in this chapter, provided for reference purposes.

$A, \tilde{A}, A_1$	Constants of integration
b_0	Nozzle radius
b	Length scale of the transverse/radial variation
$b_{u,w}$	Length scales of the transverse/radial variation of the axial velocity component in jets and plumes respectively
$b_{t,T}$	Length scales of the transverse/radial variation of the tracer and concentration in jets and plumes respectively
$B(_0)$	Local (initial) specific buoyancy flux
$C(_m)$	Concentration (maximum value)
c'	Concentration fluctuation
$c_i^{(')}$	Constants in the dimensional analysis of circular (planar) jets
$d_i^{(')}$	Constants in the dimensional analysis of circular (planar) plumes
f_i	Functions used in the dimensional analysis
F	Function used in the similarity analysis
g	Acceleration due to gravity
k	Constant used in the eddy viscosity
$K, \tilde{K}$	Constants of integration
l	Mixing length
ℓ	Ratio between the transverse and axial velocity scales
$L, \tilde{L}$	Constants of integration
L_{ax}	Axial length scale
L_j	'Jet-length' - the length scale of a buoyant jet
$M(_0)$	Local (initial) specific momentum flux
n	Parameter controlling the magnitude of the mean velocities
$p^{(')}$	Pressure (fluctuation)
$Q(_0)$	Local (initial) specific volume flux
r	Radial coordinate in circular jets
Re	Reynolds number
Ri	Richardson number

S	Integration area
u	Axial velocity component in jets
u'	Turbulent axial velocity in jets
u_m	The value of u on the axis of a jet (or the velocity scale)
u_0	Mean velocity at the source
v	Transverse/radial velocity component
v'	Turbulent transverse/radial velocity component
w	Axial (vertical) velocity component in pure plumes
w'	Turbulent axial velocity in pure plumes
w_m	The value of w on the axis of a plume (or the velocity scale)
x	Axial coordinate in jets
y	Transverse coordinate in planar jets
z	Axial (vertical) coordinate in plumes
α_j	Entrainment constant for a pure jet
β	Constant used in the mixing length model
γ	Intermittency factor
Δ	Variable used in the approximation of γ
ϵ	Eddy viscosity
ε	Ratio of scales between the turbulent velocity fluctuations and the mean axial velocity
η	Similarity variable used in the planar jet analysis
η_t	Constant used in the approximation of γ
κ	Constant used in the approximation of γ
$\lambda, \tilde{\lambda}$	Constants used in equations (4.39) and (5.26)
ν	Kinematic viscosity
ξ	Similarity variable used in the circular jet analysis
ξ_t	Constant used in the approximation of γ
ρ	Density
σ	Constant in the similarity variables
τ	Turbulent shear stress
ϕ	Azimuthal coordinate in circular jets
ψ	Streamfunction

Chapter Three

A Model of an Initially Horizontal Buoyant Jet with a Varying Entrainment Constant

The value of the entrainment constant is still not precisely known. However, it has been established that the value of the entrainment constant differs between jets and plumes and will consequently vary over the trajectory of a buoyant jet, which undergoes a transition from jet-like to plume-like states. A simple analysis of the motion of a buoyant jet in an unstratified environment is presented, which allows for this variability in entrainment constant.

The conservation equations for a buoyant jet are derived by integrating the time averaged, inviscid momentum equations, using the Boussinesq approximation. These are then examined analytically and numerically when applied to the case of an initially horizontal buoyant jet, using either of two contrasting, experimentally based assumptions to provide the variation in entrainment constant.

Particular attention is paid to the consequent behaviour of the centerline velocity components and the trajectory followed by the jet. Knowledge of the trajectory is of particular importance in confined jet flows as it shows whether or not the buoyant jet will impinge on the side boundaries of the container and hence whether or not the 'filling-box' model may be applied. It is found that the family of buoyant jet trajectories reduce to a single curve on scaling with the 'jet-length', L_j. The theoretical trajectories are compared with experimental observations.

---

1. Introduction

The theory of jets and plumes is well known and has been studied extensively (see, for example, Fischer *et al.* 1979, or chapter 2). However, in practice, the majority of sources are 'buoyant jets' (sometimes called 'forced plumes'), these being jets with an initial flux of both buoyancy and momentum. Vertical plumes have been studied theoretically by Morton, Taylor & Turner (1956) and vertical forced plumes by Morton (1959). Kotsovinos & List (1977) and Papanicolaou & List (1988) have made detailed experimental studies of the flow variables in vertically released buoyant jets. Germeles (1975) has numerically analysed the behaviour of non-vertical buoyant jets, but his equations break down in the horizontal limit. Lane-Serff, Linden & Hillel (1990) have also studied non-vertical buoyant jets. They assumed the standard laws of conservation of horizontal momentum flux and conservation of buoyancy flux. They also used the 'entrainment assumption' to give the variation in volume flux, assuming that the 'entrainment constant' takes some universal value. The 'entrainment assumption', first introduced by Taylor (1945, see Morton, Taylor & Turner 1956) states that if the flow is fully turbulent (i.e. independent of Reynolds number) then the entrainment velocity is proportional to the local velocity scale. The constant of proportionality, α, is the 'entrainment constant'. Experiments to determine the numerical value of this constant have proved inconclusive as α is thought to vary with source and environmental conditions. However, what has been established is that the entrainment rates vary substantially between pure jets and pure plumes. Fischer *et al.* (1979) quote $\alpha_{jet} = 0.0757$ and $\alpha_{plume} = 0.1178$ as mean values for circular jets and plumes from the results of many experiments, the difference being reflected by an increased dilution in a plume compared with a jet of equal local momentum flux. Priestly & Ball (1955) found that α varied linearly with the local Richardson number, Ri, of the jet, i.e.

$$\alpha = \alpha_{jet} + (\alpha_{plume} - \alpha_{jet})\left(\frac{Ri}{Ri_p}\right) \qquad \text{with} \qquad Ri = \frac{Q^2 B}{M^{\frac{5}{2}}}, \tag{1.1}$$

where Q, M, and B are the specific local fluxes of volume, momentum and buoyancy (defined in chapter 2 and below) and Ri_p is the plume Richardson number, i.e. the constant value of Ri for a pure plume. This result has been supported by Kotsovinos & List (1977). Kotsovinos (1976) also suggested that the even for a pure jet, the entrainment rate may increase with a large increase in the downstream distance although Bradshaw (1977) attributed this to draughts in the laboratory caused principally by the jet itself. It should also be noted that in

non-vertical buoyant jets, there may also be *detrainment* of fluid from the jet. This is a result of the instability of the upper surface of the jet which is lighter than the environmental fluid above it (in a negatively buoyant jet, the lower surface is unstable, being heavier than the environmental fluid below it). Small parcels of buoyant fluid may then convect away from the jet. In the following discussion, it will be assumed that the volume flux of fluid detrained from a buoyant jet is negligible compared to the volume entrained, so that the effects of detrainment can be neglected.

The behaviour of a buoyant jet is particularly interesting as it undergoes a transition from its early (jet-like) state, where the momentum forces dominate the buoyancy forces, to its final (plume-like) state where buoyancy dominates momentum. The length scale describing this transition is referred to as the 'jet-length' (see for example, Turner 1973 or chapter 2) given by

$$L_j = \frac{M_0^{\frac{3}{4}}}{B_0^{\frac{1}{2}}}, \tag{1.2}$$

where M_0 and B_0 are the initial specific momentum and buoyancy fluxes (defined in section 2 below). Since the value of the entrainment constant is different for pure jets and plumes, then there is clearly a change in the entrainment constant α between the early and final stages of buoyant jet flow. It is therefore not sufficient to assume that α is constant over the whole trajectory of the buoyant jet.

In the following analysis, this problem will be overcome by making one of two alternative experimentally based hypotheses, which will allow the entrainment constant to vary along the trajectory of the jet.

The first hypothesis assumes that the 'radius' or transverse length-scale, b, of the jet varies linearly with the arclength, s, or distance moved along the trajectory. This has been observed for plane vertical buoyant jets by Kotsovinos & List (1977) and experimentally in horizontal buoyant jets (Schatzmann 1976 and the author, see figure 1 - the experimental method will be detailed later). Thus this assumption is experimentally based, together with the knowledge that using the traditional entrainment theory (see Morton Taylor & Turner 1956), the theoretical solution for pure jets and vertical plumes implies a linear variation of radius with arclength.

The second hypothesis assumes the above linear relationship between the entrainment constant and the local Richardson number of the jet (equation (1.1)).

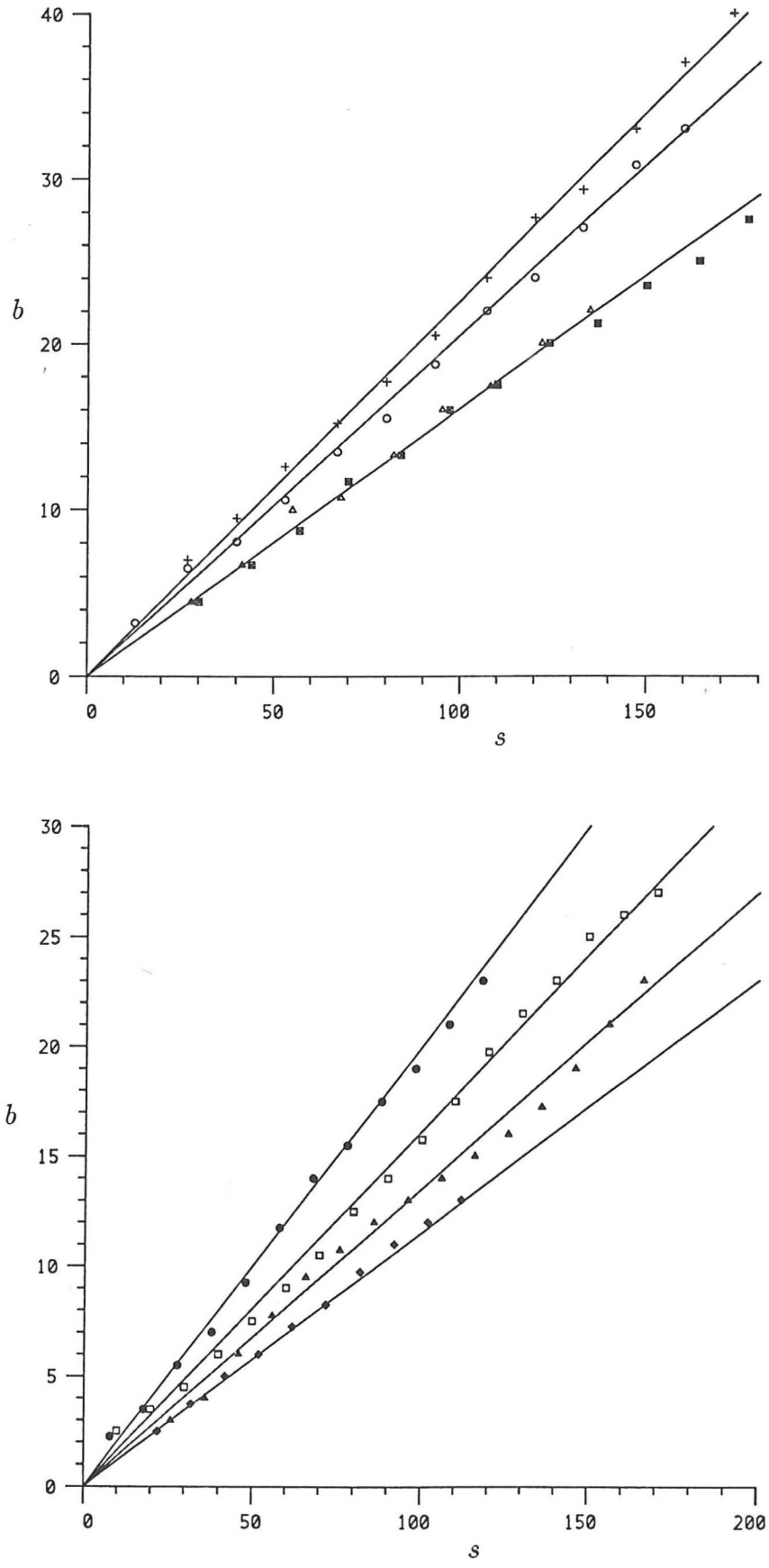

FIGURE 1. The variation of jet radius b with arclength s for a number of experiments.

+, o, •, □: Schatzmann/Fan (1976); △, ■, ▲, ♦: the author.

In order to calculate the conservation equations, the turbulent equations of motion are integrated across a cross-section of the jet, using the assumption that the contributions due to the turbulent transport and pressure gradients are small compared with those of the mean velocities. Although it is generally assumed that the velocity and density difference have approximately Gaussian profiles across a jet (for analytical simplicity - see chapter 2), it is satisfactory to use 'top-hat' profiles (see Lane-Serff 1989). This means that the velocity and density difference take constant values across the width of the jet. The entrainment assumption will then be used, assuming that the jet-induced flow outside of the jet has a magnitude proportional to the flow inside of the plume, with proportionality constant α, although α will be allowed to vary using one of the two hypotheses above. Terms of order α^2 will be neglected. Also, Kotsovinos & List (1977) found that the length scale over which the density difference spreads is larger than that over which velocity spreads (b). The density difference length scale will be denoted it by λb where Fischer *et al.* (1979) has calculated that $\lambda \simeq 1.19$ for circular jets, from the results of many experiments (see also chapter 2, section 2.1). The conservation equations obtained will then be applied to the case of an initially horizontal buoyant jet. Integral models for the flow of a buoyant jet have been presented before (see, for example, Morton 1959, Fan 1967 and Schatzmann 1979) but in this study the emphasis will be on derivation of simple analytical results from the conservation equations and differences in the effect of the two entrainment assumptions.

The horizontal and vertical limiting cases will be considered first and then the equations describing the intermediate behaviour will be considered analytically and numerically. Particular attention will be paid to the implied trajectory of the buoyant jet as this can be readily compared with experiment. The consequences of the first assumption that b varies linearly with s for the behaviour of the entrainment constant will be deduced.

This type of jet flow occurs in many physical situations, for example in a leak of a buoyant gas, or an outflow of sewage into a river. Detailed knowledge of the expected behaviour of buoyant jets can be used to predict the effect of such a flow more accurately. For example, it would be desirable to know the distance from the source that an outflow of sewage would travel before hitting the bottom of the sea, or whether or not an enclosed leak of natural gas will hit the wall of the container - which would then affect the subsequent build-up of gas concentration. Linden, Marshall & Cleaver (1991) have conducted experiments examining the flow resulting from an initially horizontal buoyant jet in a cubical container, with the source placed in the centre. They observed that the mixing of the fluid within the tank

only persists above the point of lowest penetration of the source fluid on the wall opposite the source. Thus in many cases, prior knowledge of the jet trajectory is important when attempting to predict the flow from a confined source.

2. Analysis

In this section the equations of motion are presented and are integrated across a cross-section of the buoyant jet in order to obtain the conservation equations. Before integrating over a general cross-section, the horizontal and vertical limiting cases will be considered.

2.1 Equations of motion

A schematic diagram of a horizontally directed buoyant jet is drawn in figure 2. The motion is assumed to be three dimensional, but effectively the jet centreline lies in the $x-z$ plane. The time averaged, inviscid momentum equations in the x and z directions are, using the Boussinesq approximation,

$$u\frac{\partial u}{\partial x}+w\frac{\partial u}{\partial z}=-\frac{1}{\rho_0}\frac{\partial p}{\partial x}-\frac{\partial}{\partial x}\overline{u'^2}-\frac{\partial}{\partial y}\overline{u'v'}-\frac{\partial}{\partial z}\overline{u'w'}, \tag{2.1}$$

$$u\frac{\partial w}{\partial x}+w\frac{\partial w}{\partial z}=-\frac{1}{\rho_0}\frac{\partial p}{\partial z}-\frac{\partial}{\partial x}\overline{u'w'}-\frac{\partial}{\partial y}\overline{v'w'}-\frac{\partial}{\partial z}\overline{w'^2}+\left(\frac{\rho_a-\rho}{\rho_0}\right)g, \tag{2.2}$$

where u, w, p, ρ are the time-averaged horizontal (x) and vertical (z) velocities, the mean pressure (including hydrostatic pressure), and the mean density within the buoyant jet, respectively. The density of the environment, ρ_a, is assumed to be constant and ρ_0 is a reference density. Use of the Boussinesq approximation assumes that the densities of the jet and environment not largely different from ρ_0. The primed variables are the turbulent fluctuations.

These equations may be rewritten using the continuity equation

$$\frac{\partial u}{\partial x}+\frac{\partial w}{\partial z}=0, \tag{2.3}$$

giving

$$\frac{\partial}{\partial x}\left(u^2+\overline{u'^2}+\frac{p}{\rho_0}\right)+\frac{\partial}{\partial y}(\overline{u'v'})+\frac{\partial}{\partial z}(uw+\overline{u'w'})=0, \tag{2.4}$$

$$\frac{\partial}{\partial x}(uw+\overline{u'w'})+\frac{\partial}{\partial y}(\overline{v'w'})+\frac{\partial}{\partial z}\left(w^2+\overline{w'^2}+\frac{p}{\rho_0}\right)=\left(\frac{\rho_a-\rho}{\rho_0}\right)g. \tag{2.5}$$

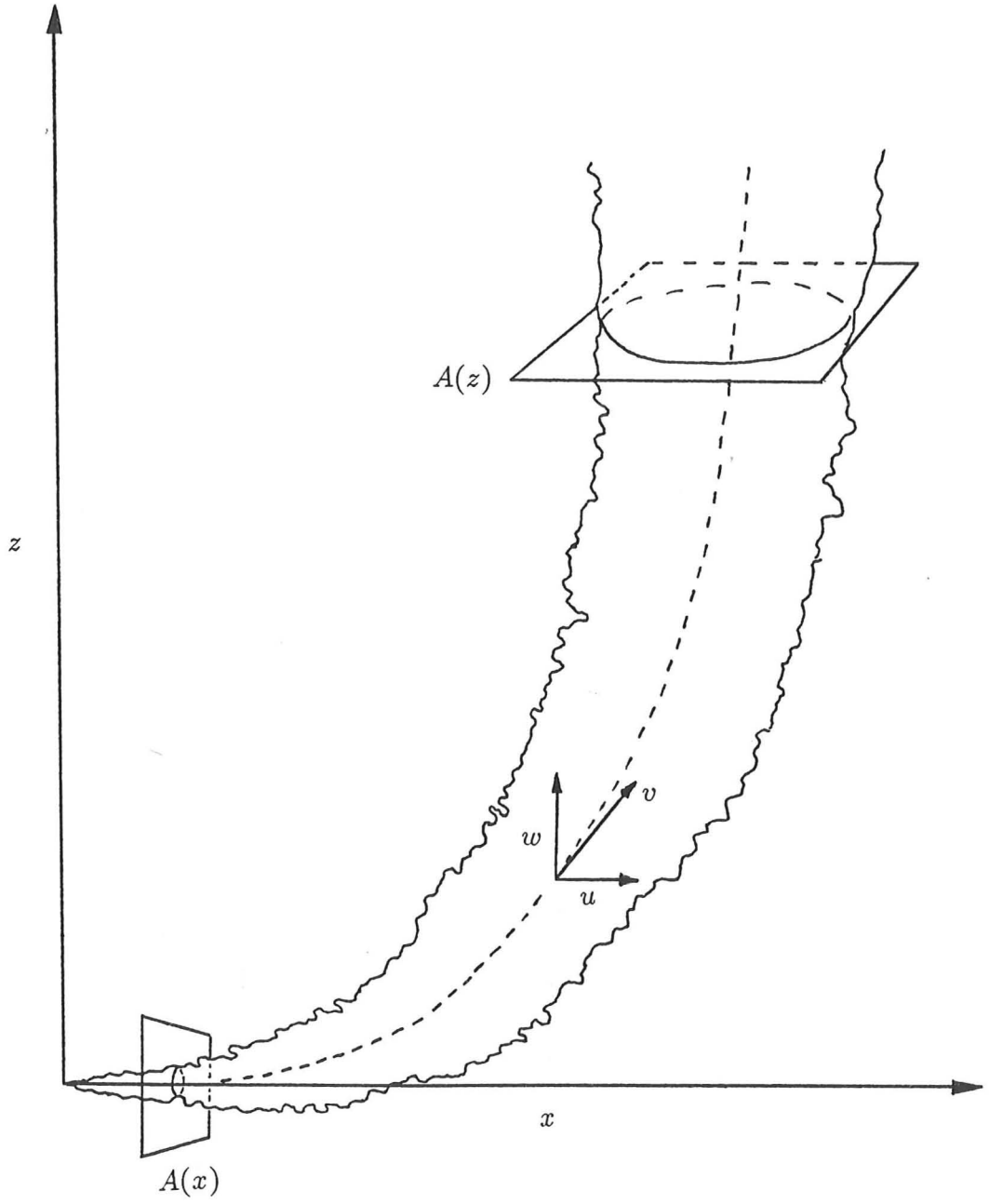

FIGURE 2. Schematic diagram of an initially horizontally directed buoyant jet.

Conservation of mass in unstratified surroundings gives

$$\frac{\partial}{\partial x}(u(\rho-\rho_a)+\overline{u'\rho'})+\frac{\partial}{\partial y}\overline{v'\rho'}+\frac{\partial}{\partial z}(w(\rho-\rho_a)+\overline{w'\rho'})=0. \tag{2.6}$$

In the following analysis it is assumed that within the jet, the velocity components and density difference have a 'top-hat' profile, i.e. constant value over a jet cross-section, with length scales (or 'radius' defining the region of non-zero value) $b(x)$ and $\lambda b(x)$, respectively. Outside of the jet the jet-induced flow has a magnitude proportional to the interior velocity scale with proportionality constant α. Terms of order α^2 will be neglected.

2.2 The horizontal limit

In order to consider the horizontal limit, the equations are integrated over a cross-section of the jet, $A(x)$ (see figure 2), defining the boundary of the area of integration, δA, to be sufficiently far from the axis of the jet so that the turbulent stresses can be neglected. The three conservation equations (2.4)-(2.6) then become

$$\int_{A(x)}\frac{\partial}{\partial x}\left(u^2+\overline{u'^2}+\frac{p}{\rho_0}\right)dydz=0, \tag{2.7}$$

$$\int_{A(x)}\frac{\partial}{\partial x}(uw+\overline{u'w'})\,dydz=\int_{A(x)}\left(\frac{\rho_a-\rho}{\rho_0}\right)g\,dydz, \tag{2.8}$$

$$\int_{A(x)}\frac{\partial}{\partial x}[u(\rho-\rho_a)+\overline{u'\rho'}]\,dydz=0, \tag{2.9}$$

where the y and z partial derivatives have been integrated, these terms vanishing since the turbulent stresses are zero on the boundary and the contributions due to the mean exterior velocities are neglected as they are of order α^2. If it is assumed that the contributions made by the turbulent velocities and pressure gradients are small, then (2.7)-(2.9) become

$$\frac{\partial}{\partial x}\int_{A(x)}u^2dydz=0, \tag{2.10}$$

$$\frac{\partial}{\partial x}\int_{A(x)}uw\,dydz=\int_{A(x)}\left(\frac{\rho_a-\rho}{\rho_0}\right)g\,dydz, \tag{2.11}$$

$$\frac{\partial}{\partial x}\int_{A(x)}u(\rho-\rho_a)\,dydz=0. \tag{2.12}$$

The flow variables u, w, and ρ have 'top-hat' profiles and so (2.10)-(2.12) imply that

$$\frac{d}{dx}(b^2u^2) = 0, \tag{2.13}$$

$$\frac{d}{dx}(b^2uw) = \lambda^2 b^2 g', \tag{2.14}$$

$$\frac{d}{dx}(b^2ug') = 0, \tag{2.15}$$

where

$$g' = \left(\frac{\rho_a - \rho}{\rho_0}\right) g,$$

is the reduced gravity. Equations (2.13) and (2.15) are the familiar equations stating conservation of momentum and buoyancy for a jet in unstratified surroundings. Equation (2.14) states that the rate of change of the horizontal flux of vertical momentum is equal to the vertical buoyancy force.

Either of the two hypotheses about the form of the entrainment constant may be easily applied at this point, giving the same solution. The solution using the first hypothesis, that the radius of the jet is proportional to the distance moved along the centreline, proceeds writing

$$b(x) = ks. \tag{2.16}$$

In the horizontal limit $s \simeq x$ and thus solving (2.13)-(2.15) gives the usual equations for a jet

$$u(x) = \frac{\sqrt{M_0}}{kx}, \qquad g'(x) = \frac{B_0}{\sqrt{M_0}kx}, \qquad b(x) = kx. \tag{2.17a}$$

Equation (2.14) gives

$$w(x) = \frac{\lambda^2 B_0}{2M_0}x, \tag{2.17b}$$

where M_0 and B_0 are the initial specific momentum and buoyancy fluxes

$$\pi M_0 = \int u_0^2 \, dS \qquad \text{and} \qquad \pi B_0 = \int u_0 g_0' \, dS, \tag{2.18}$$

where the zero subscript denotes evaluation (and integration) at the source. Both are constant from (2.13) and (2.15), respectively, with $M_0 = b^2u^2$ and $B_0 = b^2ug'$.

The analysis may be repeated using the second hypothesis, equation (1.1). In this horizontal limit, the Richardson number is approximately zero, $Ri \simeq 0$, and so from (1.1) the entrainment constant can be set to α_j, the entrainment constant for a pure jet. Hence the analysis will continue by integrating the continuity equation (2.3) over $A(x)$ obtaining

$$\frac{\partial}{\partial x}\int_{A(x)} u\,dydz + 2\pi b w_{\delta A} = 0.$$

However it is assumed that the exterior flow, $w_{\delta A}$, has magnitude proportional to the velocity scale of the interior flow, u, with $w_{\delta A} = -\alpha_j u$. Thus the familiar conservation of volume flux equation is obtained

$$\frac{d}{dx}(b^2 u) = 2\alpha_j b u. \tag{2.19}$$

The conservation equations can now be solved easily, again giving the familiar solution for jet flow

$$b(x) = 2\alpha_j x, \qquad u(x) = \frac{\sqrt{M_0}}{2\alpha_j x}, \qquad g'(x) = \frac{B_0}{2\alpha_j \sqrt{M_0} x},$$

and

$$w(x) = \frac{\lambda^2 B_0}{2M_0} x. \tag{2.20}$$

Comparing the two solutions (2.17) and (2.20), it is clear that they are equivalent if $k = 2\alpha_j$. For a pure jet $B_0 = 0$ and so $w = g' = 0$, i.e. the jet trajectory is horizontal.

2.3 The vertical limit

The vertical limit may be considered similarly by integrating across a cross-section $A(z)$ (see figure 2). Defining the boundary of the region of integration as before, integration gives

$$\frac{\partial}{\partial z}\int_{A(z)} uw\,dxdy = 0, \tag{2.21}$$

$$\frac{\partial}{\partial z}\int_{A(z)} w^2 dxdy = \int_{A(z)} g\left(\frac{\rho_a - \rho}{\rho_0}\right) dxdy, \tag{2.22}$$

$$\frac{\partial}{\partial z}\int_{A(z)} w(\rho_a - \rho)\,dxdy = 0. \tag{2.23}$$

Note here that the turbulent transport $\overline{w'\rho'}$ has been neglected, although experiments have shown (see chapter 2) this to be a poor supposition in a buoyancy dominated flow, as measurements of the mean tracer flux (Papanicolaou & List 1988) indicate that as much as 20% of the transport in plumes is by the turbulent flux.

Assuming 'top-hat' profiles as in the horizontal limit, the conservation equations

$$\frac{d}{dz}(b^2uw) = 0, \tag{2.24}$$

$$\frac{d}{dz}(b^2w^2) = \lambda^2 b^2 g', \tag{2.25}$$

$$\frac{d}{dz}(b^2wg') = 0, \tag{2.26}$$

are obtained. Equation (2.26) states that the vertical buoyancy flux is constant, (2.25) states that the change in the vertical momentum is equal to the vertical buoyancy force and (2.24) states that the vertical flux of horizontal momentum is constant in z.

Using the first hypothesis (2.16) it is assumed that

$$b = ks \simeq kz \qquad \text{(in the vertical limit).} \tag{2.27}$$

If the (constant) vertical buoyancy flux is equal to F and the vertical flux of horizontal momentum is equal to H, then equations (2.24)-(2.26) may be solved obtaining the solution

$$w(z) = \left(\frac{3\lambda^2 F}{4k^2}\right)^{\frac{1}{3}} z^{-\frac{1}{3}}, \qquad g'(z) = \left(\frac{4F^2}{3\lambda^2 k^4}\right)^{\frac{1}{3}} z^{-\frac{5}{3}}, \tag{2.28}$$

with (2.24) giving

$$u(z) = \left(\frac{4H^3}{3\lambda^2 F k^4}\right)^{\frac{1}{3}} z^{-\frac{5}{3}}. \tag{2.29}$$

This can be written in the usual form of the solution of Morton, Taylor & Turner (1956), (whom effectively use the second assumption with $Ri = Ri_p$ and so $\alpha = \alpha_p$, where α_p is the entrainment constant for a pure plume from equation (1.1)) by choosing

$$k = \frac{6}{5}\alpha_p. \tag{2.30}$$

This gives

$$b(z) = \frac{6\alpha_p}{5}z, \quad w(z) = \frac{5}{6\alpha_p}\left(\frac{9}{10}\lambda^2\alpha_p F\right)^{\frac{1}{3}} z^{-\frac{1}{3}}, \quad g'(z) = \frac{5F}{6\alpha_p}\left(\frac{9}{10}\lambda^2\alpha_p F\right)^{-\frac{1}{3}} z^{-\frac{5}{3}}$$

$$\text{and} \quad u(z) = \frac{5H}{6\alpha_p}\left(\frac{9}{10}\lambda^2\alpha_p F\right)^{-\frac{1}{3}} z^{-\frac{5}{3}}. \tag{2.31}$$

For a pure plume $H = 0$ and so $u = 0$, i.e. the trajectory is vertical.

2.4 Intermediate behaviour

The conservation equations will now be derived when the jet is in neither a jet-like nor a plume-like state and then analysed on application to the motion of an initially horizontally directed buoyant jet.

2.4.1 The conservation equations

The direction of the motion of the buoyant jet is now no longer horizontal or vertical and so the area of integration is not parallel to a coordinate axis (see figure 3).

As in sections 2.2 and 2.3, it is assumed that the profiles of velocity and reduced gravity are 'top-hat' over the area of integration with horizontal velocity component u and vertical velocity component w. The mean velocity *along* the axis is denoted by $v = \sqrt{u^2 + w^2}$.

In order to consider the motion at a point P on the trajectory, the equations are integrated across the cross-section at P. The coordinates (x, z) are rotated by an angle θ, equal to the angle between the tangent of the trajectory at P and the horizontal axis, so that the new coordinate x' is parallel to and along the tangent, and z' is perpendicular to it. The tangent angle θ is related to the velocity components with

$$\tan\theta = \frac{dz}{dx} = \frac{w}{u}, \quad \cos\theta = \frac{u}{v} \quad \text{and} \quad \sin\theta = \frac{w}{v}. \tag{2.32}$$

The equations of motion (2.4)-(2.6) then become

$$\left(\cos\theta\frac{\partial}{\partial x'} - \sin\theta\frac{\partial}{\partial z'}\right)u^2 + \left(\sin\theta\frac{\partial}{\partial x'} + \cos\theta\frac{\partial}{\partial z'}\right)(uw) = 0, \tag{2.33}$$

$$\left(\cos\theta\frac{\partial}{\partial x'} - \sin\theta\frac{\partial}{\partial z'}\right)(uw) + \left(\sin\theta\frac{\partial}{\partial x'} + \cos\theta\frac{\partial}{\partial z'}\right)w^2 = g', \tag{2.34}$$

$$\left(\cos\theta\frac{\partial}{\partial x'} - \sin\theta\frac{\partial}{\partial z'}\right)(ug') + \left(\sin\theta\frac{\partial}{\partial x'} + \cos\theta\frac{\partial}{\partial z'}\right)(wg') = 0, \tag{2.35}$$

where, for clarity, the turbulent terms have been left out as these will neglected later by suitable choice of the integration boundary. Substituting for $\cos\theta$ and $\sin\theta$ using (2.32) gives

$$\frac{u}{v}\frac{\partial}{\partial x'}(u^2) + \frac{u}{v}\frac{\partial}{\partial z'}(uw) - \frac{w}{v}\frac{\partial}{\partial z'}(u^2) + \frac{w}{v}\frac{\partial}{\partial x'}(uw) = 0, \tag{2.36}$$

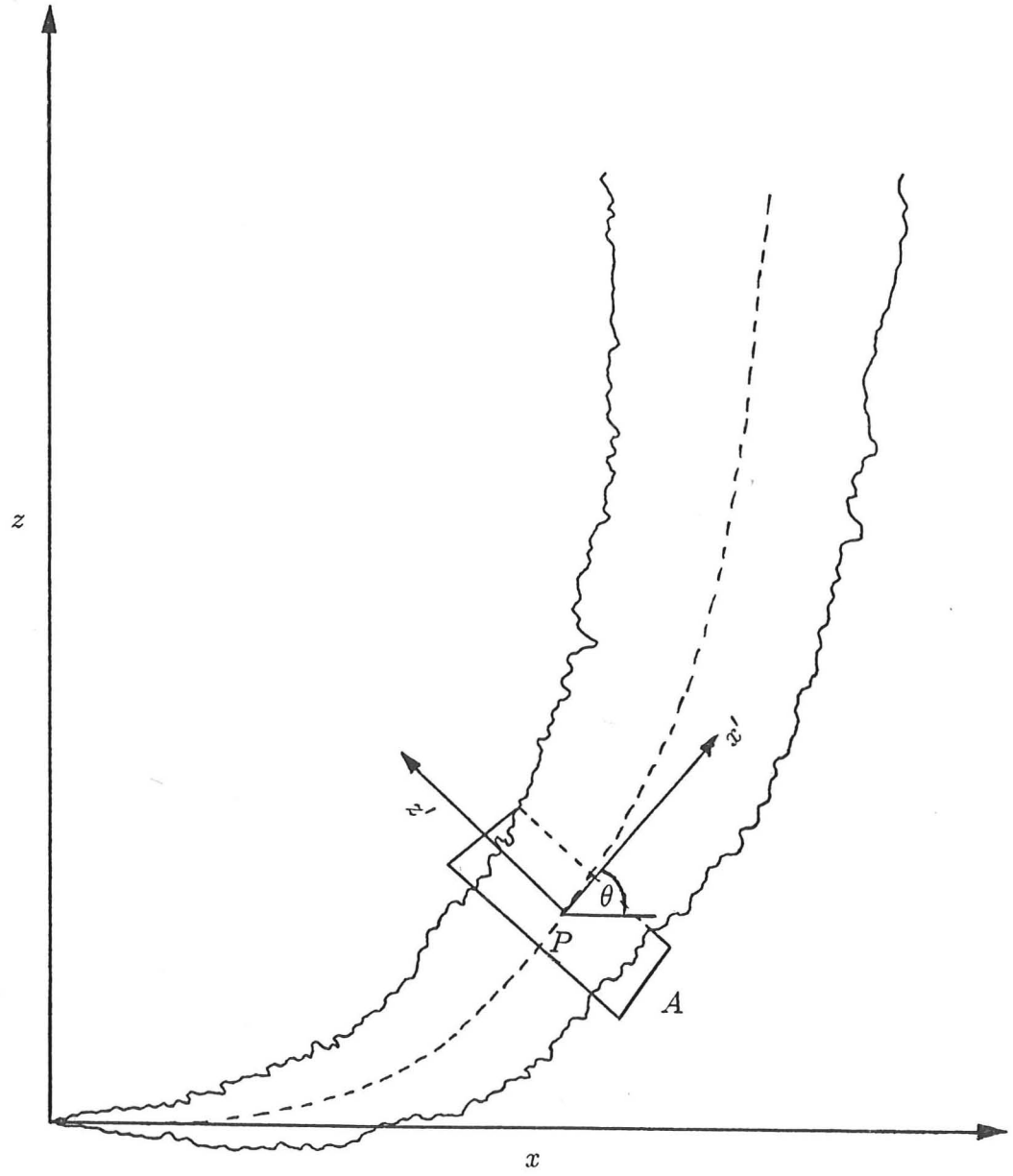

FIGURE 3. The rotated coordinate system, and plane of integration.

$$\frac{u}{v}\frac{\partial}{\partial x'}(uw) + \frac{u}{v}\frac{\partial}{\partial z'}(w^2) - \frac{w}{v}\frac{\partial}{\partial z'}(uw) + \frac{w}{v}\frac{\partial}{\partial x'}(w^2) = g', \tag{2.37}$$

$$\frac{u}{v}\frac{\partial}{\partial x'}(ug') + \frac{u}{v}\frac{\partial}{\partial z'}(wg') - \frac{w}{v}\frac{\partial}{\partial z'}(ug') + \frac{w}{v}\frac{\partial}{\partial x'}(wg') = 0. \tag{2.38}$$

These equations can be rewritten in the form

$$\frac{\partial}{\partial x'}(uv) + \cos\theta\frac{\partial}{\partial z'}(wu) - \sin\theta\frac{\partial}{\partial z'}(w^2) = 0, \tag{2.39}$$

$$\frac{\partial}{\partial x'}(wv) + \cos\theta\frac{\partial}{\partial z'}(w^2) - \sin\theta\frac{\partial}{\partial z'}(uw) = g', \tag{2.40}$$

$$\frac{\partial}{\partial x'}(g'v) + \cos\theta\frac{\partial}{\partial z'}(wg') - \sin\theta\frac{\partial}{\partial z'}(ug') = 0. \tag{2.41}$$

Equations (2.39)-(2.41) will now be integrated over a cross-section through the jet, $A(x')$, with respect to z' and y, with the boundary of the region of integration defined as before. Due to the curvature of the jet, it is possible that some integration regions may overlap. The contradictions that this implies for the 'top-hat' profiles will be ignored and the velocity contributions of order α^2 will be neglected. The integration gives

$$\frac{d}{dx'}(b^2uv) = 0, \tag{2.42}$$

$$\frac{d}{dx'}(b^2wv) = \lambda^2 b^2 g', \tag{2.43}$$

$$\frac{d}{dx'}(b^2vg') = 0. \tag{2.44}$$

Note that the arclength element

$$\begin{aligned} ds &= \sqrt{dx^2 + dz^2} = \sqrt{dx'^2 + dz'^2}, \\ &= \sqrt{1 + \left(\frac{w}{u}\right)^2}\,dx = \sqrt{1 + \left(\frac{dz'}{dx'}\right)^2}\,dx'. \end{aligned} \tag{2.45}$$

But $dz'/dx' = 0$ at P and so

$$ds = dx'. \tag{2.46}$$

Thus equations (2.42)-(2.44) can be written

$$\frac{d}{ds}(b^2uv) = 0, \tag{2.47}$$

$$\frac{d}{ds}(b^2 wv) = \lambda^2 b^2 g', \tag{2.48}$$

$$\frac{d}{ds}(b^2 vg') = 0. \tag{2.49}$$

This is the final form of the conservation equations; the variables u, v, w, b and g' are now considered as functions of the arclength $s(x)$. Before making any assumptions about the nature of the entrainment into the jet, the immediate implications of the above conservation equations will be examined.

2.4.2 Implications of the conservation equations

The implications of the above conservation equations (2.47)-(2.49) will now be considered, when applied to the case of an initially horizontal buoyant jet.

Equations (2.47) and (2.49) may be integrated immediately giving

$$b^2 uv = M_0, \tag{2.50}$$

$$b^2 vg' = B_0, \tag{2.51}$$

where the constants of integration have been calculated by considering the initial motion as follows. Initially, for small s the behaviour is jet-like. The vertical velocity is small compared with the horizontal velocity (w is zero at $s = 0$) and so $v \simeq u$. Hence initially $b^2 uv \simeq b^2 u^2 = M_0$ and $b^2 vg' \simeq b^2 ug' = B_0$ (see equation (2.18)). Consideration of the final motion (comparing with section 2.3) reveals that $H \equiv M_0$ and $F \equiv B_0$. Equations (2.50) and (2.51) state that the fluxes of buoyancy and horizontal momentum are constant over the whole trajectory of the buoyant jet flow. A further immediate consequence of (2.50) and (2.51) is that

$$g' = \frac{B_0}{M_0} u, \tag{2.52}$$

i.e. the reduced gravity g' is always proportional to the horizontal velocity u (as was the case in the solutions to the limiting cases above).

Eliminating g' from (2.48) gives

$$\frac{d}{ds}(b^2 wv) = \frac{\lambda^2 B_0}{v}, \tag{2.53}$$

and using (2.50) to substitute for $b^2 v$ gives

$$\frac{df}{ds} = \frac{\lambda^2 B_0}{M_0 v}, \qquad \text{where} \qquad f = \frac{w}{u}. \tag{2.54}$$

Hence using the fact that $v = u\sqrt{1+f^2}$, all the variables in the problem can be expressed in terms of the gradient, f and its derivative $f' = df/ds$

$$v(s) = \frac{\lambda^2 B_0}{M_0 f'}, \quad u(s) = \frac{\lambda^2 B_0}{M_0 f'\sqrt{1+f^2}}, \quad w(s) = \frac{\lambda^2 B_0 f}{M_0 f'\sqrt{1+f^2}},$$

$$b(s) = \frac{M_0^{\frac{3}{2}}}{\lambda^2 B_0} f'(1+f^2)^{\frac{1}{4}} \qquad \text{and} \qquad \frac{ds}{dx} = \sqrt{1+f^2}. \tag{2.55}$$

Each of the two hypotheses will now be used in turn to derive an equation in f and consequently solve the problem.

2.4.3 Hypothesis 1: The radius is proportional to the arclength

In this section the effect of making the first of the two hypotheses, namely that the radius of the jet varies linearly with the arclength

$$b = ks, \tag{2.56}$$

will be examined. As stated above this is based on experiments on horizontal buoyant jets presented by Schatzmann (1976) and the author (see figure 1 - experimental details given in section 4), and also experiments and theoretical analysis on vertical jets and plumes by Morton, Taylor & Turner (1956), Morton (1959) and Kotsovinos & List (1977). In order that the initial behaviour matches that of a pure jet (see equations (2.20)), it is assumed that the constant of proportionality $k = 2\alpha_j$.

Equations (2.50) and (2.51) may be rewritten as

$$s^2 uv = K \qquad \text{where} \qquad K = \frac{M_0}{k^2}, \tag{2.57}$$

and

$$s^2 vg' = \frac{J}{\lambda^2} \qquad \text{where} \qquad J = \frac{\lambda^2 B_0}{k^2}. \tag{2.58}$$

Thus, substituting for $b(s)$ in (2.55) above gives

$$s = \frac{K^{\frac{3}{2}}}{J} f'(1+f^2)^{\frac{1}{4}}, \tag{2.59}$$

which is the equation for the gradient f. Using $ds/dx = \sqrt{1+f^2}$, equation (2.59) may be written in the the alternative form

$$\frac{d^2 f}{dx^2} = \frac{f}{2(1+f^2)}\left(\frac{df}{dx}\right)^2 + \frac{J}{K^{\frac{3}{2}}}(1+f^2)^{\frac{3}{4}}. \tag{2.60}$$

It is convenient to non-dimensionalise the variables, scaling lengths [L] and time [T] with

$$[\mathrm{L}] = \frac{K^{\frac{3}{4}}}{J^{\frac{1}{2}}}[\mathrm{L}^*] \qquad \text{and} \qquad [\mathrm{T}] = \frac{K}{J}[\mathrm{T}^*]. \tag{2.61}$$

The problem then reduces to

$$u^* v^* s^{*2} = 1, \qquad g'^* v^* s^{*2} = \frac{1}{\lambda^2}, \qquad b^* = k s^*$$

with

$$\frac{df}{ds^*} = \frac{1}{v^*} = \frac{s^*}{(1+f^2)^{\frac{1}{4}}}. \tag{2.62}$$

Note also that $M_0^* = k^2$ and $B_0^* = k^2/\lambda^2$. Use of (2.57) and (2.58) above reveals that this length scaling is proportional to the 'jet-length' defined in section 1 above with

$$[\mathrm{L}] = \frac{1}{\sqrt{k}\lambda} L_j [\mathrm{L}^*]. \tag{2.63}$$

The numerical solution to equation (2.62) will be discussed in section 3, but it is possible to obtain approximate solutions in the limits of small and large f.

Small values of the gradient, f

The scaled version of (2.60) takes the form

$$\ddot{f} = \frac{f\dot{f}^2}{2(1+f^2)} + (1+f^2)^{\frac{3}{4}}, \tag{2.64}$$

where the dot denotes differentiation with respect to x^*. For small f, $\ddot{f} \simeq 1$ and so $f \simeq x^{*2}/2$. This approximation may be made more accurate by searching for a series solution of the form

$$f(x^*) = \frac{x^{*2}}{2} \sum_{i=0}^{\infty} a_i x^{*i}. \tag{2.65}$$

Substituting this into (2.64), expanding the powers of $(1+f^2)$ binomially, requires that all but the powers of x^{*4} have zero coefficient. The solution is

$$f(x^*) = \frac{x^{*2}}{2}\left(1 + \frac{7}{240}x^{*4} - \frac{49}{345600}x^{*8} + \cdots\right), \tag{2.66}$$

and integrating with respect to x^* gives the centreline trajectory

$$z^*(x^*) = \frac{x^{*3}}{6}\left(1 + \frac{1}{80}x^{*4} - \frac{49}{1267200}x^{*8} + \cdots\right). \tag{2.67}$$

This means that the initial trajectory follows a cubic course, which agrees with the result of Chan &, Kennedy (1975) in their analysis of the momentum dominated part of the flow.

A similar procedure may be applied to (2.62) giving

$$f(s^*) = \frac{s^{*2}}{2}\left(1 - \frac{1}{48}s^{*4} + \frac{19}{7680}s^{*8} + \cdots\right), \tag{2.68}$$

and the fifth of equations (2.55) may be used to calculate that

$$s^*(x^*) = x^*\left(1 + \frac{1}{40}x^{*4} - \frac{1}{17280}x^{*8} + \cdots\right). \tag{2.69}$$

The velocity components can also be found by using (2.55)

$$u^* = \frac{1}{s^*}\left(1 - \frac{1}{16}s^{*4} + \frac{19}{1536}s^{*8} + \cdots\right) = \frac{1}{x^*}\left(1 - \frac{7}{80}x^{*4} + \frac{2891}{345600}x^{*8} + \cdots\right), \tag{2.70}$$

$$w* = \frac{s^*}{2}\left(1 - \frac{1}{12}s^{*4} + \frac{31}{1920}s^{*8} + \cdots\right) = \frac{x^*}{2}\left(1 - \frac{7}{120}x^{*4} + \frac{49}{8640}x^{*8} + \cdots\right), \tag{2.71}$$

$$v* = \frac{1}{s^*}\left(1 + \frac{1}{16}s^{*4} - \frac{13}{1536}s^{*8} + \cdots\right) = \frac{1}{x^*}\left(1 + \frac{3}{80}x^{*4} - \frac{1069}{345600}x^{*8} + \cdots\right). \tag{2.72}$$

These series solutions may be used to give approximate values, whilst the gradient $f < 1$. In this case the corrective terms are generally small compared with the first terms in the series, indicating that the behaviour of the buoyant jet is like that of a pure jet even though the jet may have begun to divert from its horizontal course.

Large values of the gradient, f

The behaviour of the equations will now be considered for large values of the gradient f. Equation (2.62) now becomes

$$\frac{df}{ds^*} \simeq \frac{s^*}{\sqrt{f}}, \tag{2.73}$$

which may be integrated with respect to s^*, giving

$$f \simeq \left(\frac{3}{4}\right)^{\frac{2}{3}}(s^{*2} + s_0)^{\frac{2}{3}}, \tag{2.74}$$

where s_0 is a constant of integration. The arclength, s^*, may be chosen to be sufficiently large so that $s^{*2} \gg s_0$ and (2.74) then approximates to

$$f \simeq \left(\frac{3}{4}\right)^{\frac{2}{3}} s^{*\frac{4}{3}}. \tag{2.75}$$

Now for large f,

$$\frac{ds^*}{dx^*} \simeq f, \tag{2.76}$$

and so substituting for f from (2.75) and integrating gives

$$s^* = 48(x_m^* - x^*)^{-3}, \tag{2.77}$$

where x_m^* is a constant of integration. This is an important result, showing that the jet centreline can only reach a maximum horizontal displacement given by x_m^*. The values of s^*, z and b are infinite at this point, whereas the velocity components are zero. The value of x_m cannot be calculated analytically but it will be calculated from the numerical solution later.

Substituting (2.77) into (2.75) gives

$$f(x^*) = 144(x_m^* - x^*)^{-4}, \tag{2.78}$$

which may be integrated to give

$$z(x^*) = 48(x_m^* - x^*)^{-3} + z_0. \tag{2.79}$$

The velocity components can be found using (2.55) giving

$$u^* = \left(\frac{3}{4}\right)^{-\frac{1}{3}} s^{*-\frac{5}{3}} = \frac{1}{576}(x_m^* - x^*)^5, \tag{2.80}$$

$$w^* = \left(\frac{3}{4}\right)^{\frac{1}{3}} s^{*-\frac{1}{3}} = \frac{1}{4}(x_m^* - x^*), \tag{2.81}$$

$$v^* = \left(\frac{3}{4}\right)^{\frac{1}{3}} s^{*-\frac{1}{3}} = \frac{1}{4}(x_m^* - x^*). \tag{2.82}$$

As expected, in the limit of $s^* \to \infty$, $v^* \simeq w^*$ and substituting for $(x_m^* - x^*)$ using (2.79) and comparing with equations (2.31) shows that the velocity components have plume-like behaviour.

2.4.4 Hypothesis 2: The entrainment constant varies linearly with the local Richardson number

The implications of the second hypothesis will now be examined. In this case it is assumed that the entrainment constant varies linearly with the local Richardson number, Ri, of the jet

$$\alpha = \alpha_{jet} + (\alpha_{plume} - \alpha_{jet})\left(\frac{Ri}{Ri_p}\right) \qquad \text{with} \qquad Ri = \frac{Q^2 B}{M^{\frac{5}{2}}} = \frac{bg'}{v^2}, \tag{2.83}$$

where Q, B and M are the local fluxes of specific volume, buoyancy and momentum defined by

$$\pi Q = \int v\, dS, \qquad \pi B = \int v g'\, dS, \qquad \pi M = \int v^2\, dS, \tag{2.84}$$

dS denoting integration across the jet. This was first suggested by Priestly & Ball (1955) and has been supported by Kotsovinos & List (1977). Assuming that the solution tends to that of a pure plume as $s \to \infty$, equations (2.31) may be used to calculate Ri_p, giving

$$Ri_p = \frac{8\alpha_p}{5\lambda^2},$$

a constant, with value $R_p = 0.133$.

The analysis proceeds similarly to that of section 2.4.3. It is convenient to write (2.50) and (2.51) in the form

$$b^2 uv = M_0 = k^2 K \qquad \text{and} \qquad b^2 v g' = B_0 = \lambda^2 k^2 J, \tag{2.85}$$

where $k = 2\alpha_j$, for ease of comparison with the previous section. The continuity equation

$$\frac{\partial u}{\partial x} + \frac{\partial w}{\partial z} = 0, \tag{2.86}$$

must be integrated in order to obtain the equation defining f. In the rotated coordinate system of section 2.4.1, the continuity equation becomes

$$\left(\cos\theta \frac{\partial}{\partial x'} - \sin\theta \frac{\partial}{\partial z'}\right) u + \left(\sin\theta \frac{\partial}{\partial x'} + \cos\theta \frac{\partial}{\partial z'}\right) w = 0. \tag{2.87}$$

The terms in x' may be rewritten giving

$$\frac{\partial v}{\partial x'} - \sin\theta \frac{\partial u}{\partial z'} + \cos\theta \frac{\partial w}{\partial z'} = 0. \tag{2.88}$$

Integrating, making the same assumptions about the integration region as before, gives

$$\frac{d}{ds}(b^2 v) = 2b(u\sin\theta - w\cos\theta). \tag{2.89}$$

However $(w\cos\theta - u\sin\theta)$ is the exterior flow perpendicular to the jet axis, and so has magnitude proportional to the interior velocity scale, v. Hence

$$(u\sin\theta - w\cos\theta) = \alpha v, \tag{2.90}$$

and so

$$\frac{d}{ds}(b^2 v) = 2\alpha b v. \tag{2.91}$$

This is the conservation of volume equation that will be used to solve the problem when using the second hypothesis, recalling that α is dependent on the local Richardson number of the jet. Hence the problem is to solve (2.85), (2.91) and (2.54) with the hypothesis of (2.83).

The result of (2.55) still holds here, and substituting this into (2.91) with the hypothesis of (2.83), gives the equation for the gradient f

$$\frac{d}{ds}(\sqrt{1+f^2}f') = \frac{J}{K^{\frac{3}{2}}}(1+f^2)^{\frac{1}{4}} + \frac{5(\alpha_p - \alpha_j)f'^2}{4\alpha_p}. \tag{2.92}$$

By non-dimensionalising the variables as in section 2.4.3, (2.92) reduces to

$$\frac{d}{ds^*}\left(\sqrt{1+f^2}\frac{df}{ds^*}\right) = (1+f^2)^{\frac{1}{4}} + \frac{5(\alpha_p - \alpha_j)}{4\alpha_p}\left(\frac{df}{ds^*}\right)^2. \tag{2.93}$$

This is the equation for f that will be solved numerically later, but series solutions for small f, analogous to (2.66)-(2.72), may be found. These are

$$f(x^*) = \frac{x^{*2}}{2}\left(1 + \frac{\beta}{6}x^{*2} + 2\left[\frac{1}{40} + \frac{\beta^2}{45}\right]x^{*4} + \cdots\right), \tag{2.94}$$

$$z^*(x^*) = \frac{x^{*3}}{6}\left(1 + \frac{\beta}{10}x^{*2} + \frac{6}{7}\left[\frac{1}{40} + \frac{\beta^2}{45}\right]x^{*4} + \cdots\right), \tag{2.95}$$

$$f(s^*) = \frac{s^{*2}}{2}\left(1 + \frac{\beta}{6}s^{*2} + \frac{2\beta^2}{45}s^{*4} + \frac{17\beta^3}{1260}s^{*6} + \cdots\right), \tag{2.96}$$

$$s^*(x^*) = x^*\left(1 + \frac{1}{40}x^{*4} + \frac{\beta}{168}x^{*6} + \cdots\right), \tag{2.97}$$

$$u^* = \frac{1}{s^*}\left(1 - \frac{\beta}{3}s^{*2} - \left[\frac{\beta^2}{45} + \frac{1}{8}\right]s^{*4} + \cdots\right) = \frac{1}{x^*}\left(1 - \frac{\beta}{3}x^{*2} - \left[\frac{7}{90}\beta^2 + \frac{3}{20}\right]x^{*4} + \cdots\right), \tag{2.98}$$

$$w^* = \frac{s^*}{2}\left(1 - \frac{\beta}{6}s^{*2} - \left[\frac{\beta^2}{30} + \frac{1}{8}\right]s^{*4} + \cdots\right) = \frac{x^*}{2}\left(1 - \frac{\beta}{6}x^{*2} - \left[\frac{1}{10} + \frac{\beta^2}{45}\right]x^{*4} + \cdots\right), \tag{2.99}$$

$$v^* = \frac{1}{s^*}\left(1 - \frac{\beta}{3}s^{*2} - \frac{\beta^2}{45}s^{*4} + \cdots\right) = \frac{1}{x^*}\left(1 - \frac{\beta}{3}x^{*2} - \left[\frac{7}{90}\beta^2 + \frac{3}{20}\right]x^{*4} + \cdots\right), \tag{2.100}$$

where

$$\beta = \frac{5(\alpha_p - \alpha_j)}{4\alpha_p} \simeq 0.447 \qquad \text{with the values suggested above.}$$

Note that the series are now in x^{*2} rather than in x^{*4} as they were in (2.66)-(2.72).

The behaviour for large f is the same as that of the previous section, although the integration constants may be different.

2.5 The rate of entrainment

There is a fundamental difference between the two hypotheses - the second hypothesis defines the local rate of entrainment by defining the local entrainment constant in terms of the variables of the problem; whereas in the first hypothesis a simple experimentally based assumption is made, allowing this to determine the entrainment. However an *effective* local entrainment constant may be calculated when using the first hypothesis by defining

$$\alpha(s^*) = \frac{1}{2b^*v^*}\frac{d}{ds^*}(b^{*2}v^*), \tag{2.101}$$

(see equation (2.19)). Thus this is the from of the entrainment function that would have to be used to give a linear variation of radius with arclength. The numerical solution will be discussed later but the plume-like limit of α may be deduced when using the first hypothesis.

Since it is assumed that $b = ks$ with $k = 2\alpha_j$, by comparison with the pure jet solution (2.20), considering the solution for the plume-like limit (2.31) then

$$k = 2\alpha_j = \frac{6}{5}\alpha_p, \qquad \text{i.e.} \qquad \alpha_p = \frac{5}{3}\alpha_j. \tag{2.102}$$

So, using the value of α_j suggested by Fischer *et al.* (1979), $\alpha_j = 0.0757$, then (2.102) implies that $\alpha_p = 0.1261$, which compares favourably with the value $\alpha_p = 0.1178$ that they also suggest.

3. Numerical solutions

Equations (2.59) and (2.93) may be easily handled numerically, and (2.55) can be used to calculate all the other variables in the problem. For an initially horizontal jet, the initial conditions are that f, w, s, z, b, and x are zero. An off-horizontal jet could be considered by taking the initial value of $f = \tan\theta_0$ where θ_0 is the initial inclination of the jet to the horizontal. In both cases pure jet-like behaviour, $f \simeq s*^2/2 \simeq x^{*2}/2$, is expected initially.

The solutions, obtained using a NAG Fortran routine, are given in figures 4-9; variations with s^* are shown in figure 4, variations with x^* are shown in figure 5 and the variation of s^* with x^* is shown in figure 6. The behaviour of the Richardson number is shown in figures 7 and 8, and the effective entrainment constant in figure 9. The solid lines are the solution with the first hypothesis, $b = ks$, and the dotted lines are the solution with the second hypothesis, $\alpha = \alpha(Ri)$. The similarity between the two solutions is somewhat surprising. It is perhaps explained by the behaviour of $b^*(s^*)$ using the second hypothesis, shown in figure 4*f*. This graph shows that the second hypothesis, which makes no statement on the behaviour of the radius, b^*, gives a solution in which the radius varies almost linearly with s^* (which was assumed in the first hypothesis), although the effective spreading rate is slightly lower than that of the first hypothesis.

Figure 5*b* shows that the jet is still approximately horizontal at $x^* \simeq 1$, this being reflected by $s^* \simeq x^*$ in figure 7, with horizontal motion for $s^* \leqslant 1$ in figure 4*b*. The transition to plume-like behaviour can be considered to take place between $x^* = 1$ and $x^* = 3.5$, with the buoyant jet having almost vertical motion after $x^* = 3.5$. Notice the curious result that, to the degree of accuracy of the graphical plot, the two solutions are almost identical for $z^*(s^*)$, although they are different in real terms, as shown in figure 5*b*. Using either hypothesis, for $s^* \gtrsim 2$, z^* varies approximately linearly with s^*, with

$$z^* \simeq s^* - 1.25. \tag{3.1}$$

Figure 5*c* shows how the horizontal velocity, u^*, behaves initially as it would for a pure jet, decaying reciprocally with x^*, but as the transition to plume behaviour takes place ($x^* > 1$), u^* decreases more rapidly, eventually to zero at x^*_m.

The most interesting graphs are of the vertical velocity, w^*, in figures 4*d* and 5*d*. Initially w^* increases linearly during the jet-like phase (see equation (2.17)). As the upward velocity of a plume decreases with height, w^* must reach a maximum velocity and then decay. This

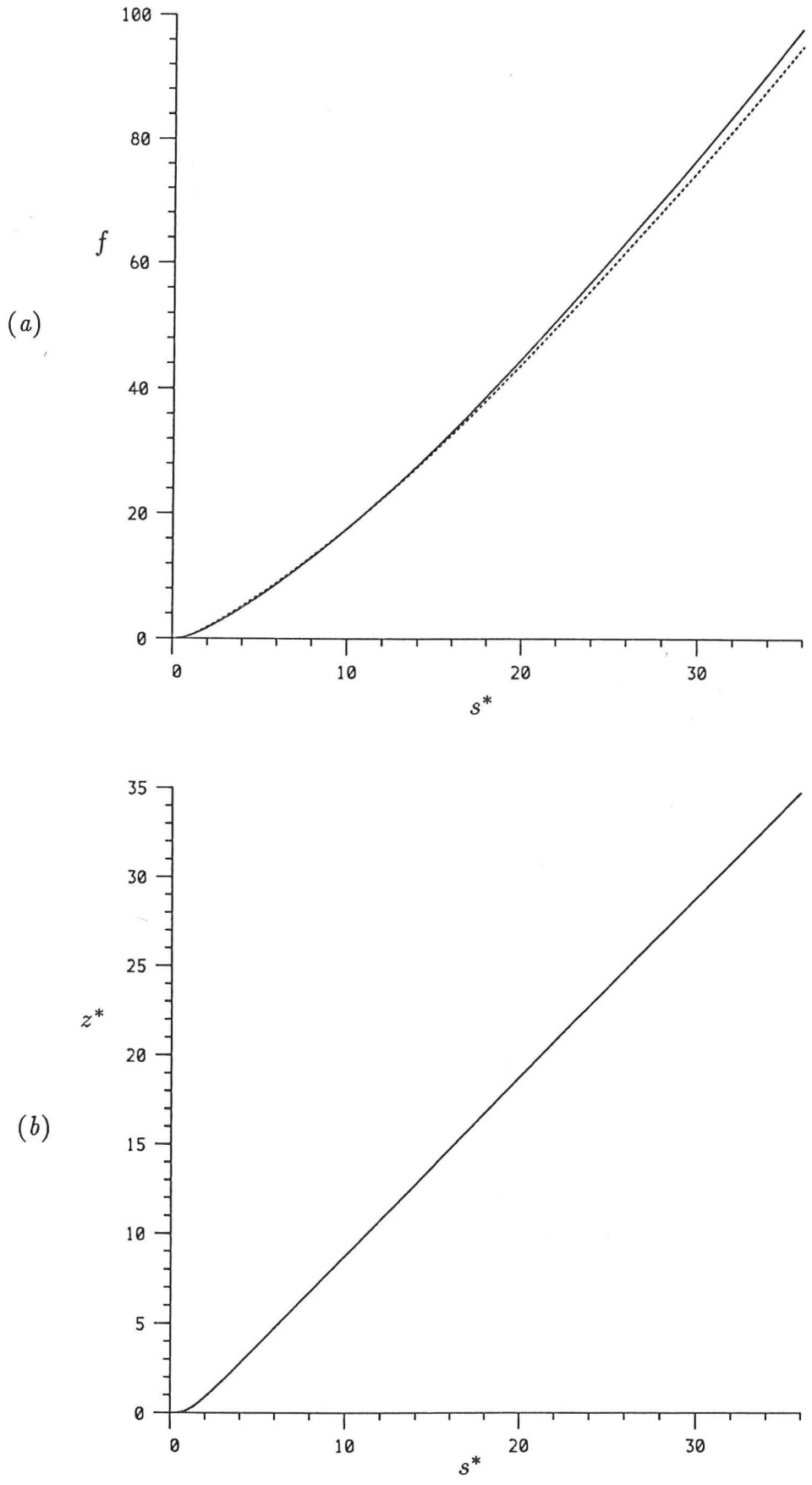

FIGURE 4. The numerical solutions showing variation with arclength s^*. (a) The gradient, f; (b) the elevation z^*; (c) the horizontal velocity component, u^*; (d) the vertical velocity component, w^*; (e) the centreline velocity, v^*; (f) the jet radius b^*.

——— First hypothesis: $b = ks$; ..... Second hypothesis: $\alpha = \alpha(Ri)$

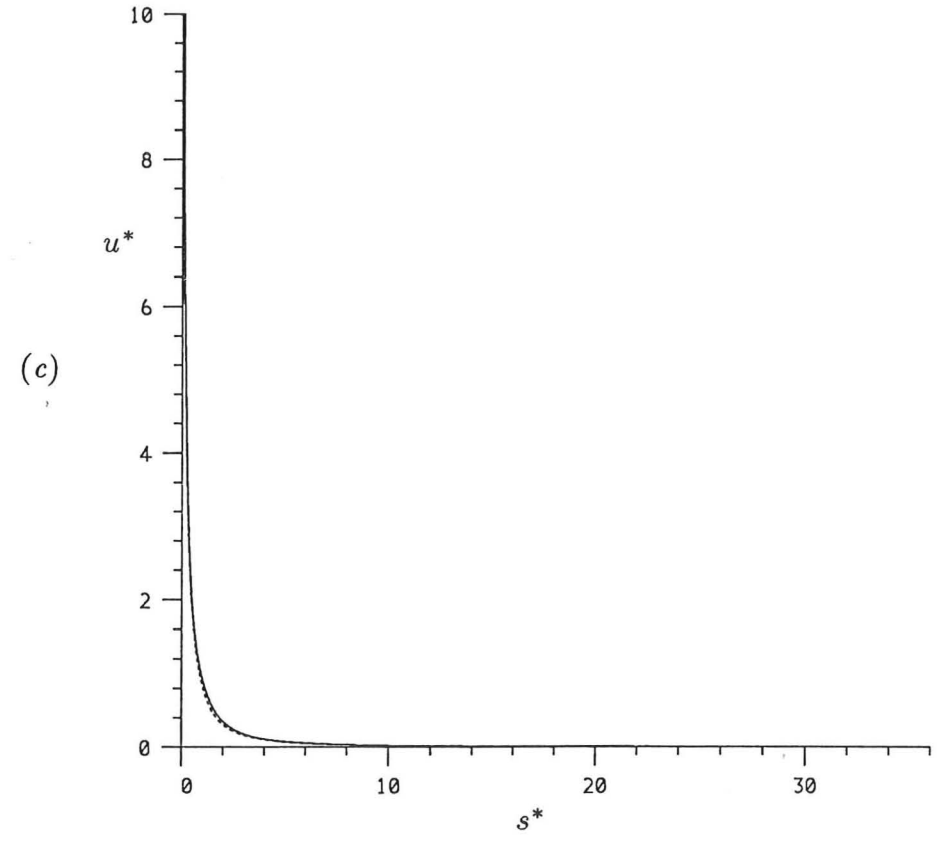

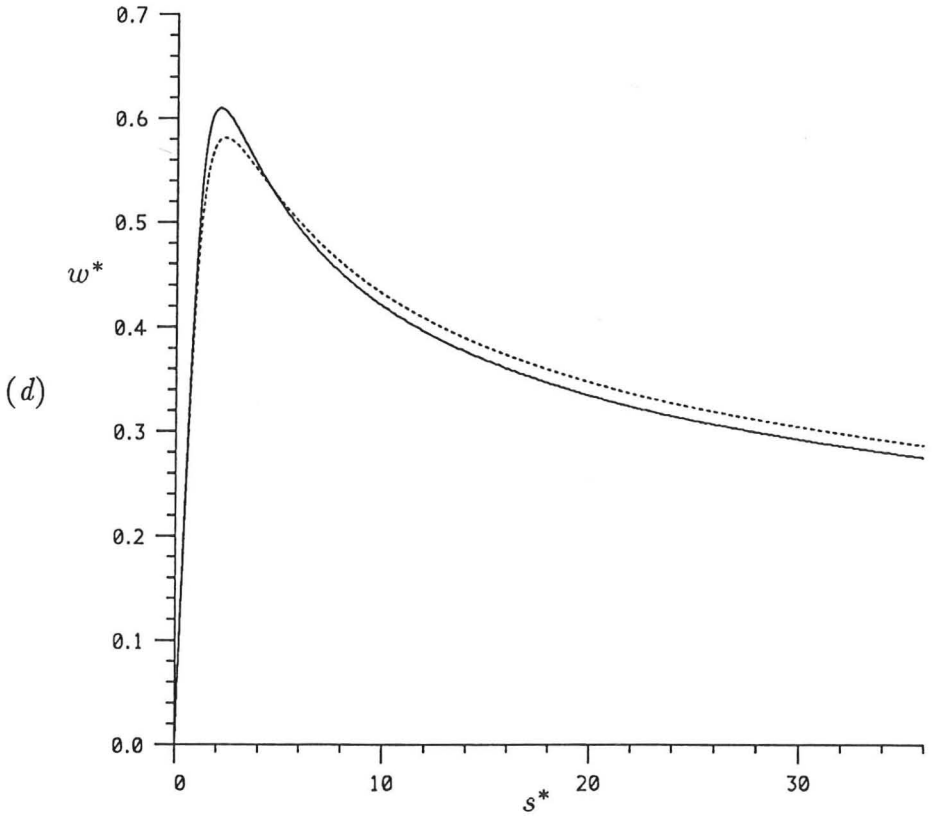

FIGURE 4 ct'd. The numerical solutions showing variation with arclength s^*. (c) The horizontal velocity component, u^*; (d) the vertical velocity component, w^*; (e) the centreline velocity, v^*; (f) the jet radius b.

——— First hypothesis: $b = ks$; ..... Second hypothesis: $\alpha = \alpha(Ri)$

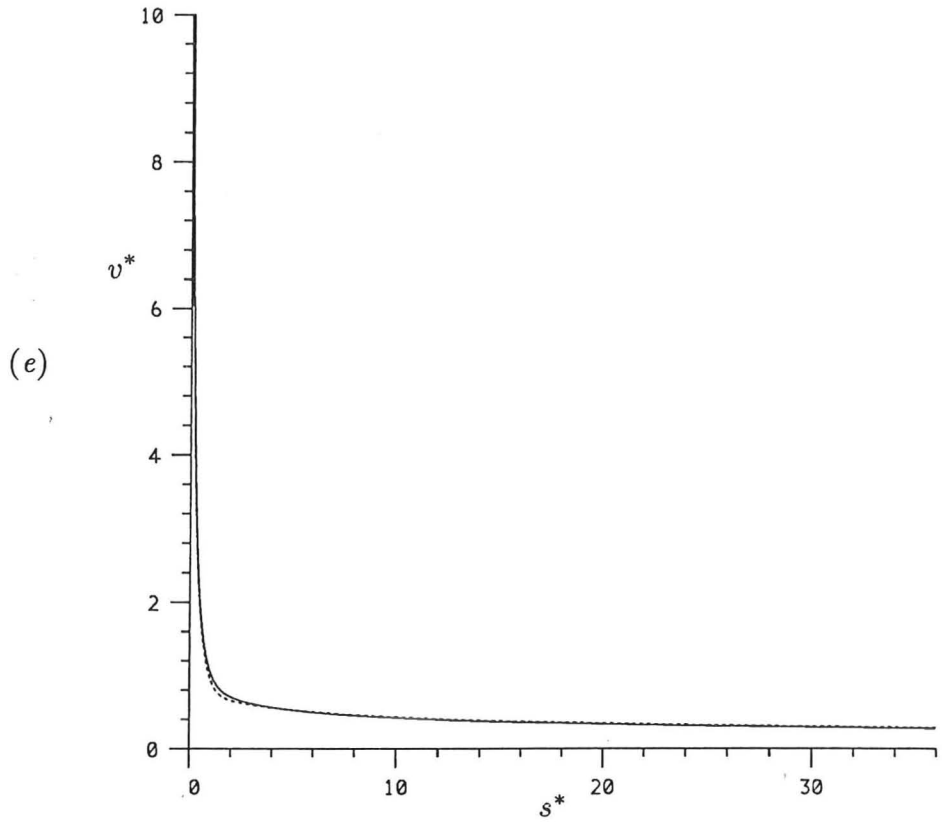

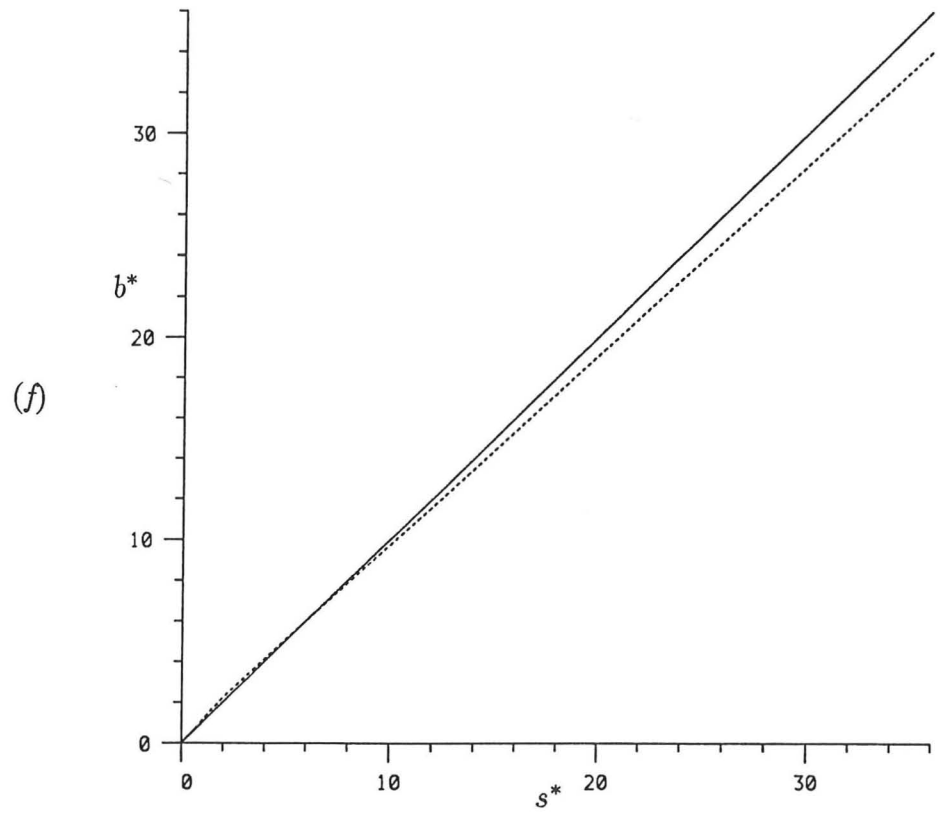

FIGURE 4 ct'd. The numerical solutions showing variation with arclength s^*.
(e) The centreline velocity, v^*; (f) the jet radius b^*.

——— First hypothesis: $b = ks$; ..... Second hypothesis: $\alpha = \alpha(Ri)$

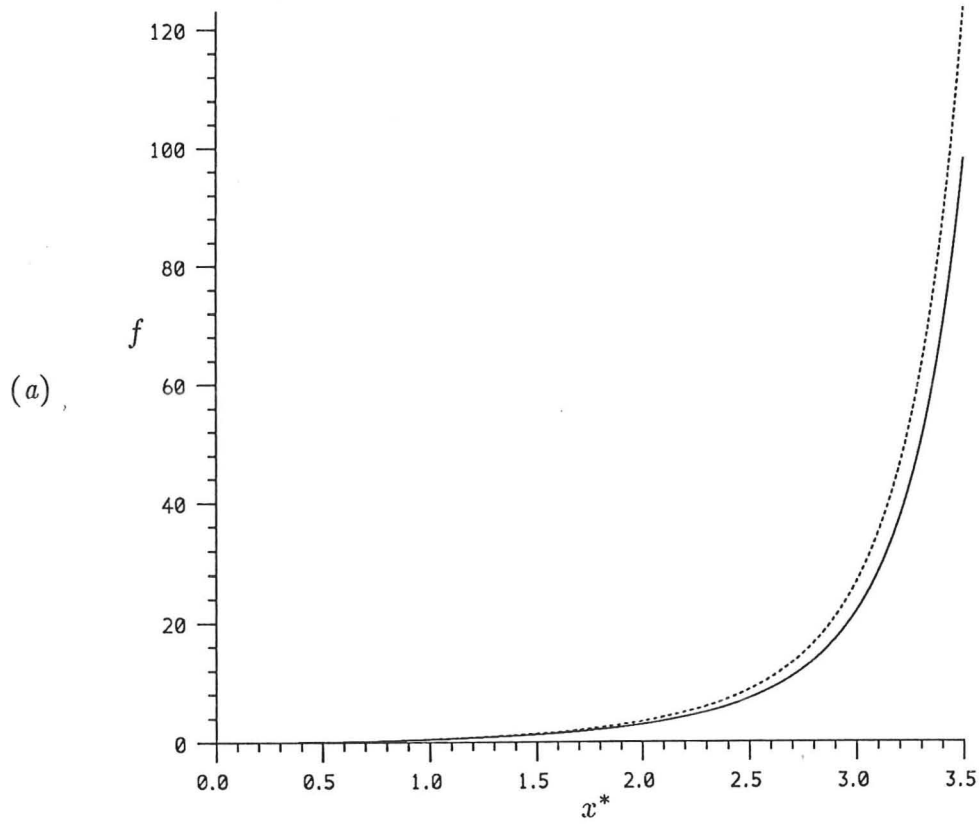

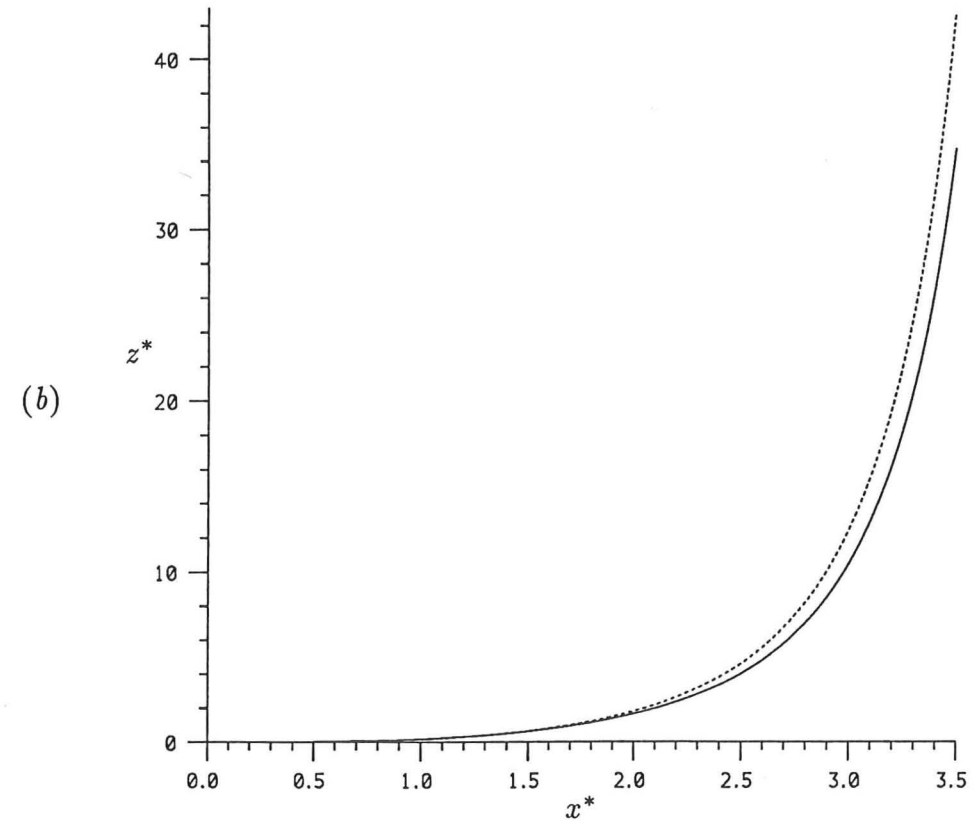

FIGURE 5. The numerical solutions showing variation with x^*. (a) The gradient, f; (b) the elevation, z^*; (c) the horizontal velocity component, u^*; (d) the vertical velocity component, w^*; (e) the centreline velocity, v^*; (f) the jet radius, b^*.

——— First hypothesis: $b = ks$; ..... Second hypothesis: $\alpha = \alpha(Ri)$

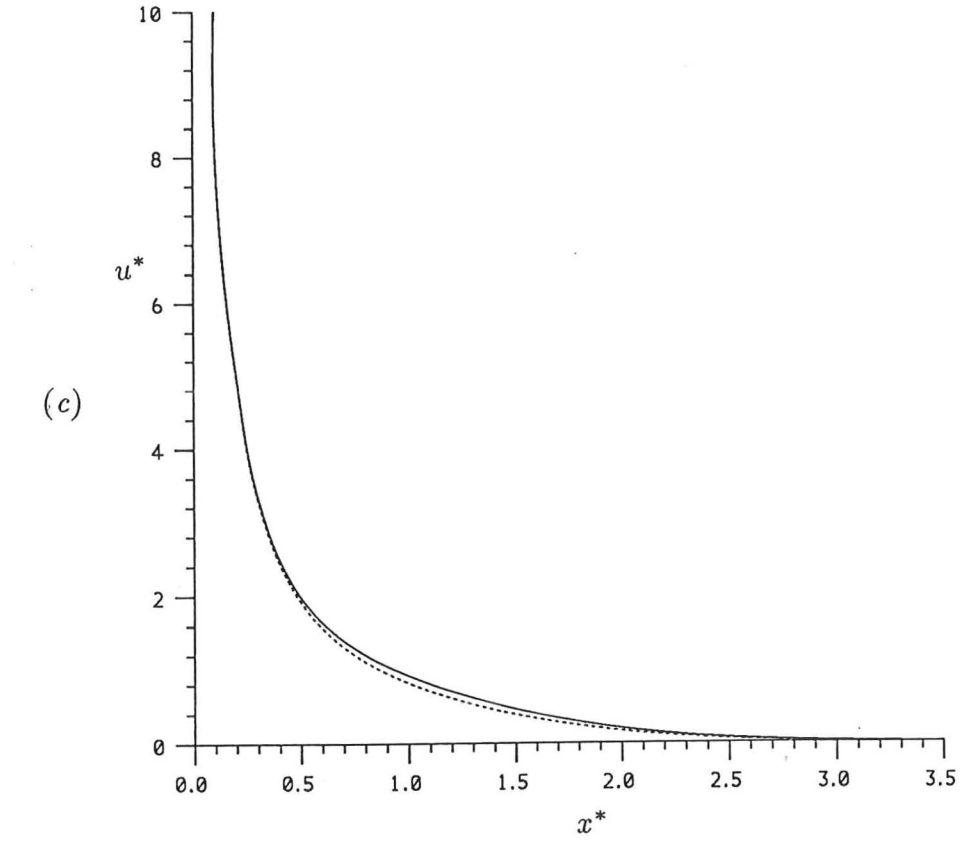

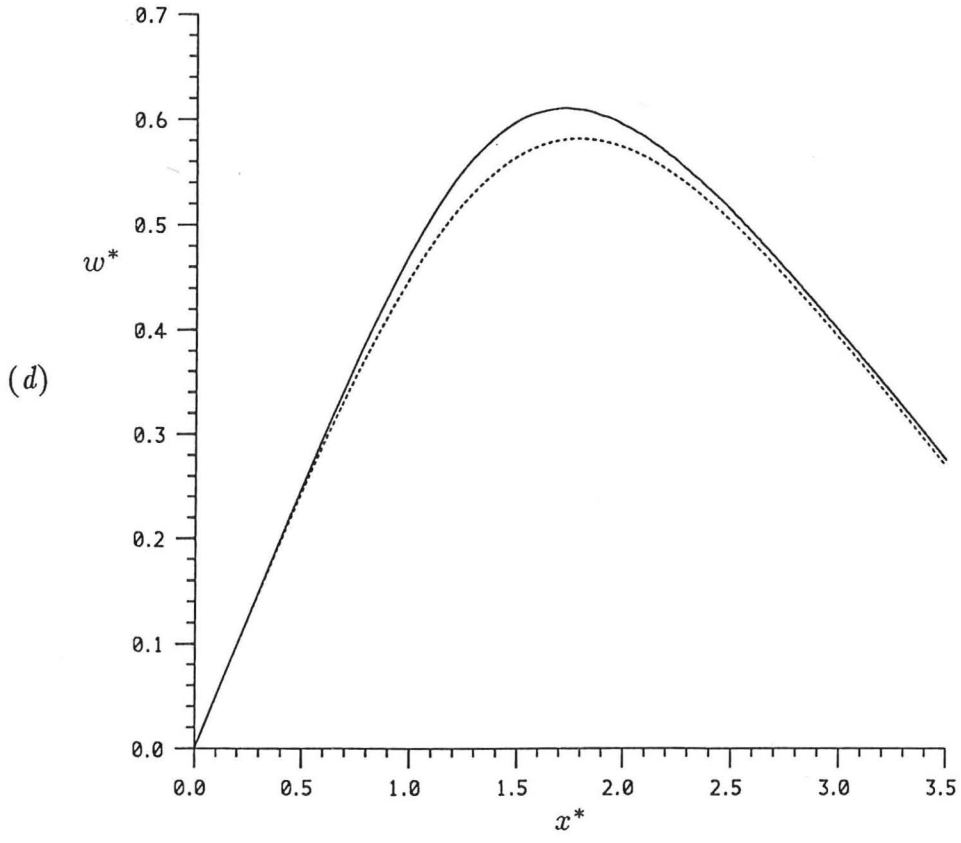

FIGURE 5. ct'd. The numerical solutions showing the variation with x^*. (c) The horizontal velocity component, u^*; (d) the vertical velocity component, w^*; (e) the centreline velocity, v^*; (f) the jet radius, b^*.

——— First hypothesis: $b = ks$; ..... Second hypothesis: $\alpha = \alpha(Ri)$

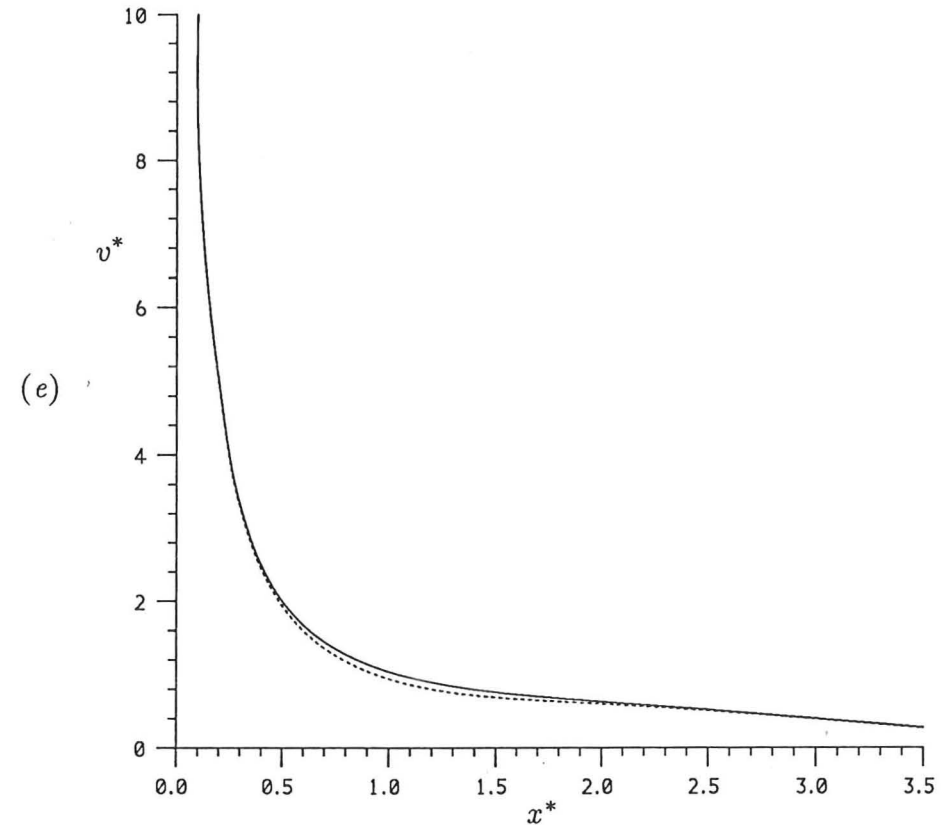

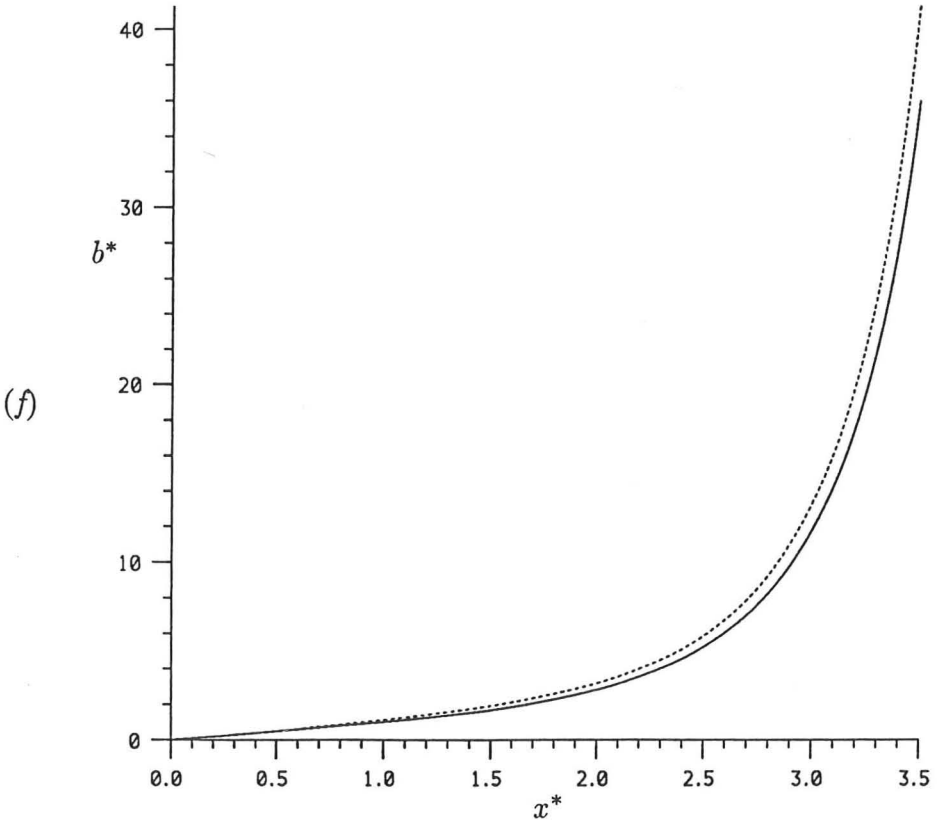

FIGURE 5. ct'd. The numerical solutions showing the variation with x^*. (e) The centreline velocity, v^*; (f) the jet radius, b^*.

———— First hypothesis: $b = ks$; ..... Second hypothesis: $\alpha = \alpha(Ri)$

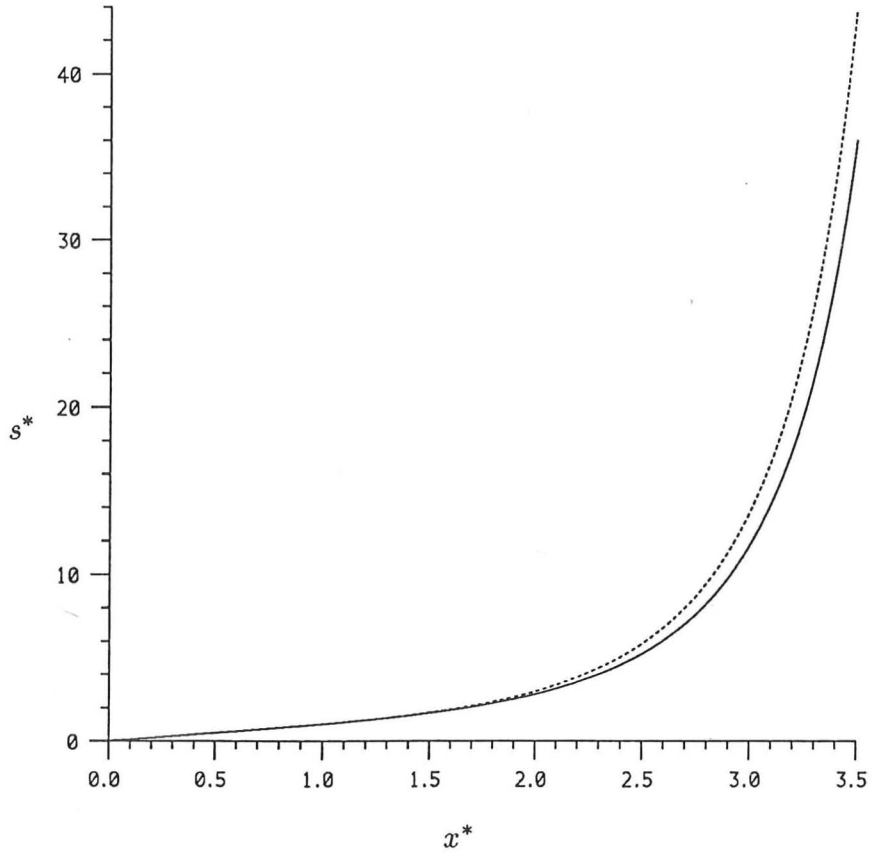

FIGURE 6. The numerical solutions showing $s^*(x^*)$.

——— First hypothesis: $b = ks$; ..... Second hypothesis: $\alpha = \alpha(Ri)$

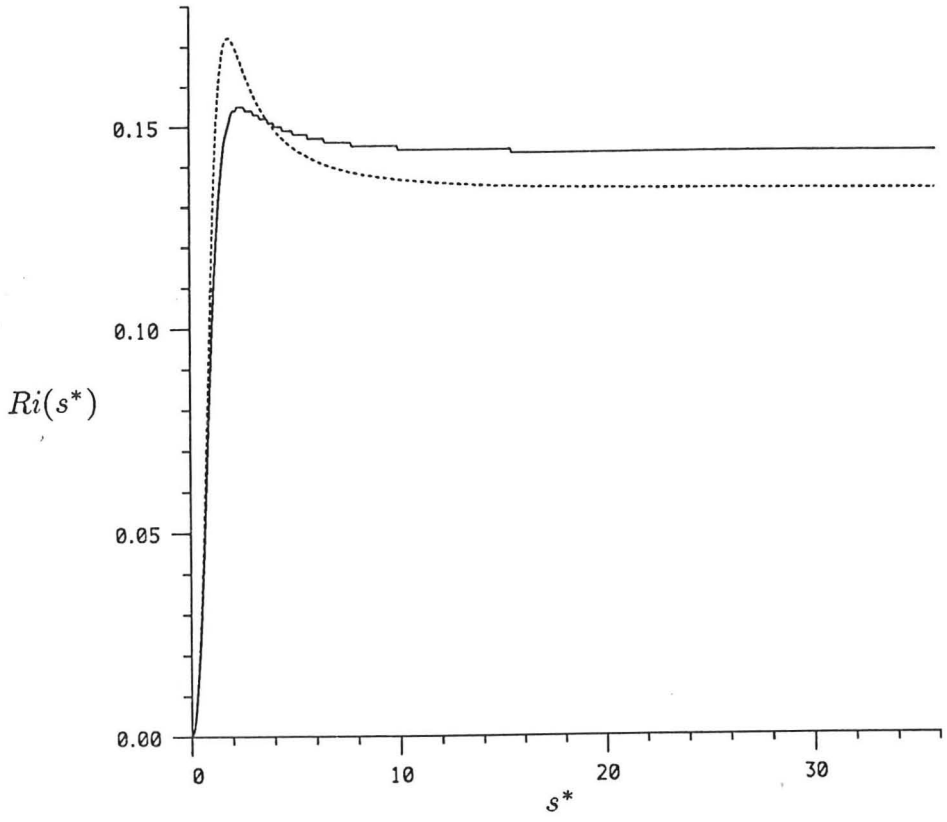

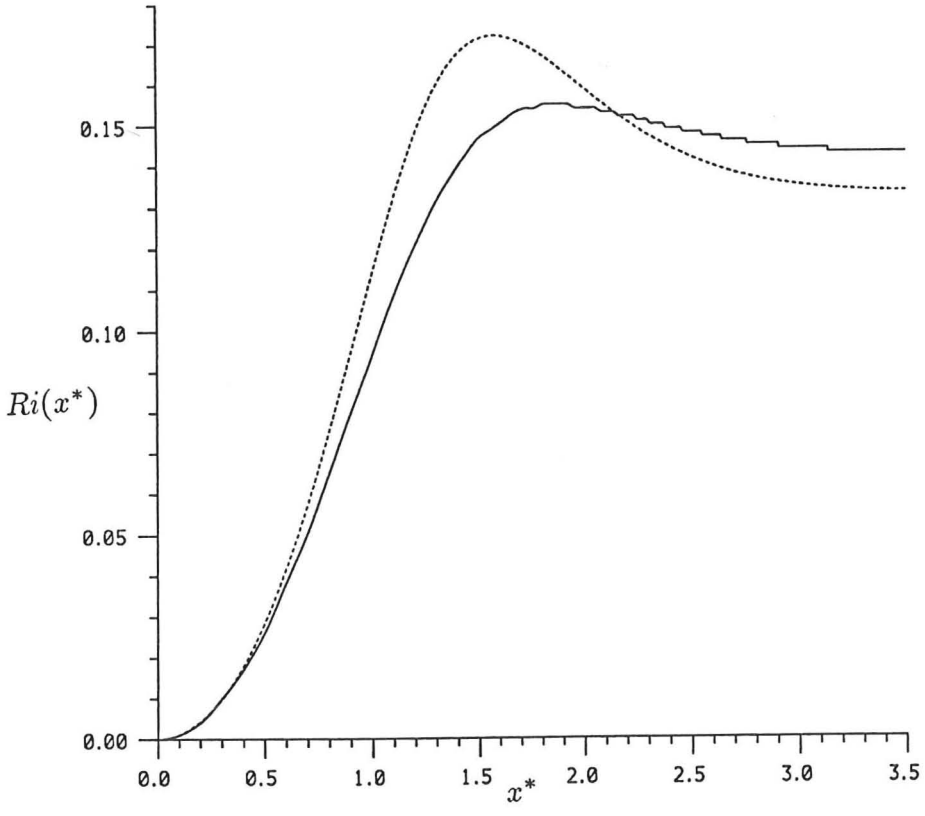

FIGURE 7. The numerical solutions showing the behaviour of the Richardson number.

——— First hypothesis: $b = ks$; ..... Second hypothesis: $\alpha = \alpha(Ri)$

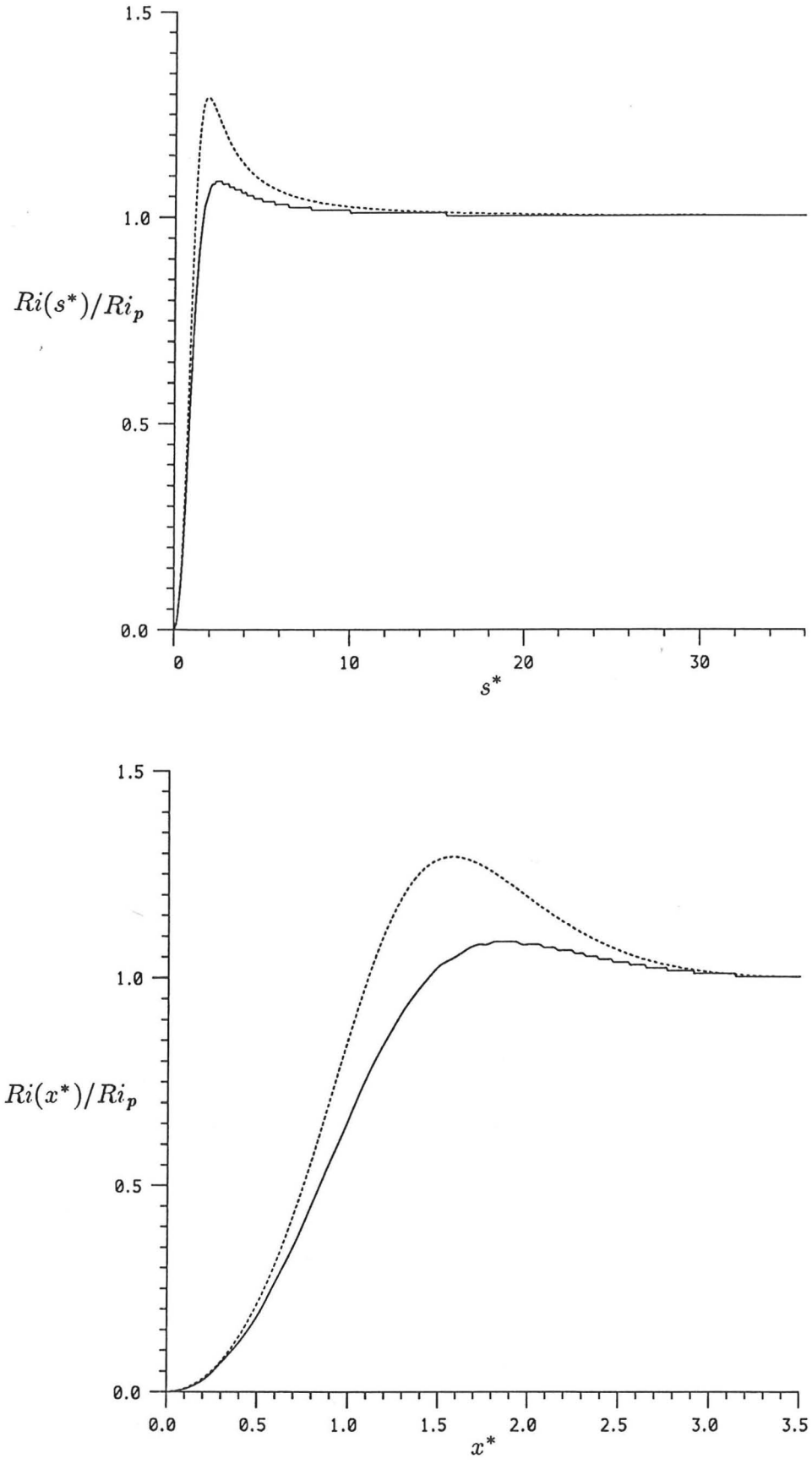

FIGURE 8. The numerical solution showing the behaviour of Ri/Ri_p

———— First hypothesis: $b = ks$; ..... Second hypothesis: $\alpha = \alpha(Ri)$

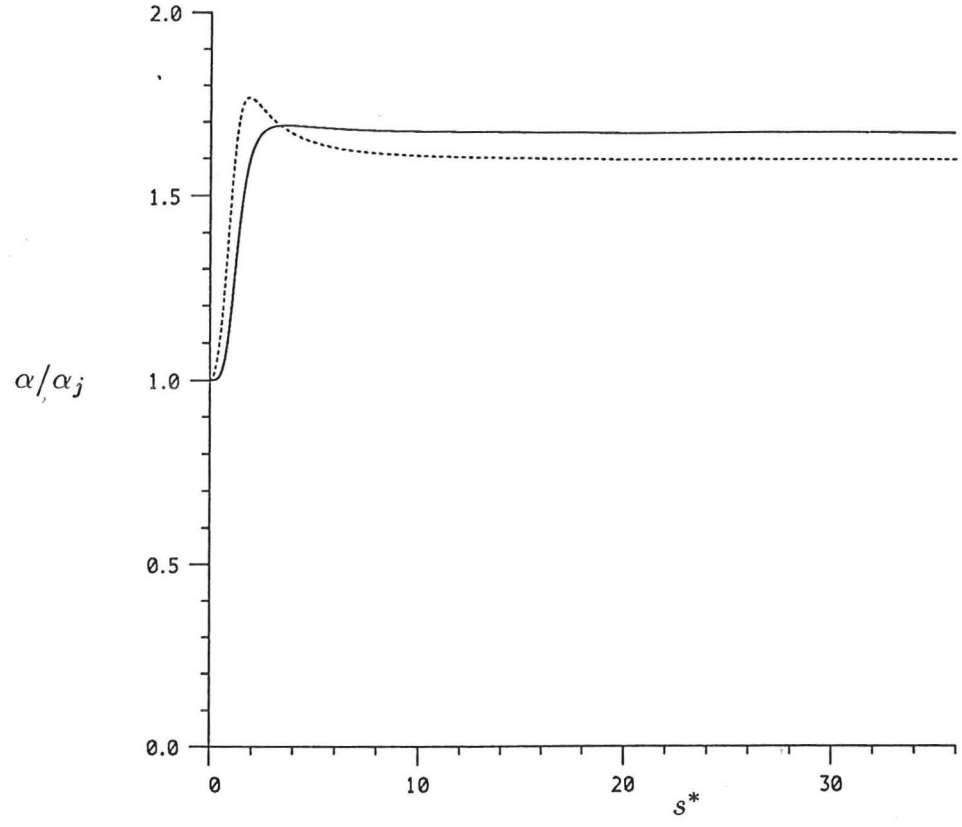

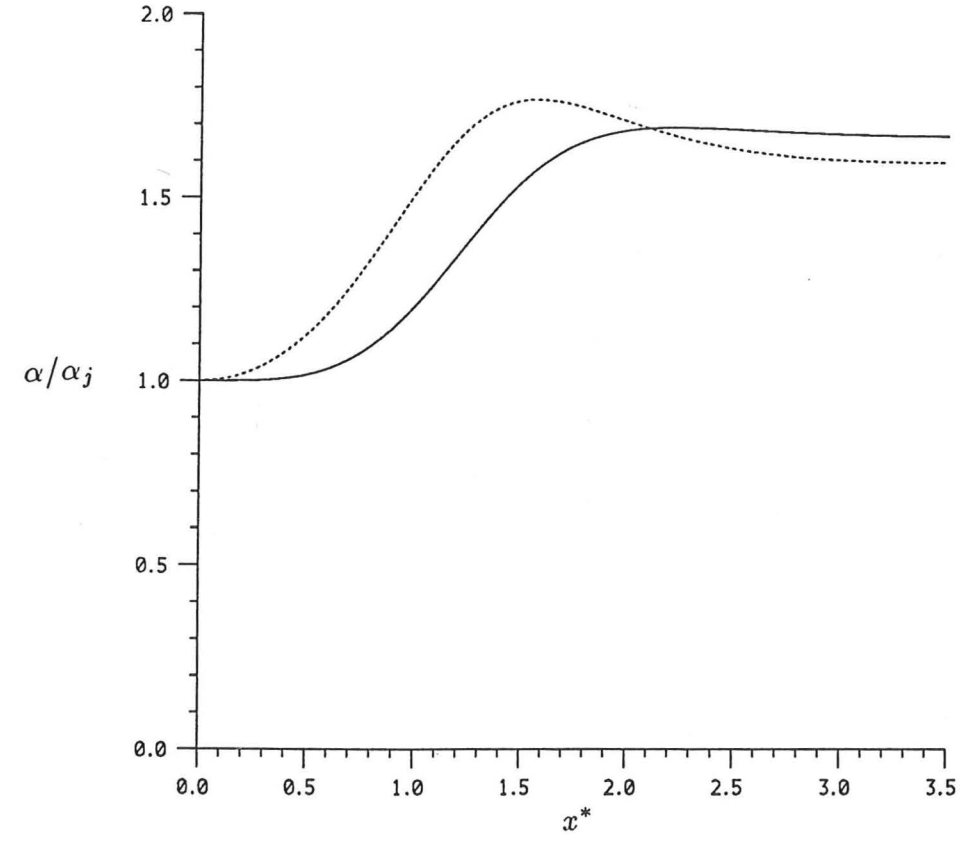

FIGURE 9. The numerical solution showing the change in effective entrainment constant.

———— First hypothesis: $b = ks$; ..... Second hypothesis: $\alpha = \alpha(Ri)$

is clear from the figures, with the maximum reached at about $x^* = 1.6$ in the first hypothesis solution, and $x^* = 1.7$ in the second hypothesis solution. The vertical velocity then decays, tending to the linear decay given by (2.81). The numerical solution may be used to compute the maximum value of x^* reached by the jet, and this is found to be

$$x^*_m = 4.6207 \qquad \text{using the first hypothesis,} \quad b = ks \tag{3.2}$$

and

$$x^*_m = 4.5824 \qquad \text{using the second hypothesis,} \quad \alpha = \alpha(Ri). \tag{3.3}$$

The graphs of the Richardson numbers, figures 7 and 8, show the greatest difference between the two solutions. In figure 7 the actual values of the Richardson number have been plotted against x^* and s^*, with Ri/Ri_p plotted in figure 8. Note that in figure 7, the curves tend to different limits for large x^* and s^* as they have different values of α_p. What can be immediately seen, is that for both hypotheses, the Richardson number is higher during the transition period than at its plume limit. This means that in the case of the second hypothesis (that the entrainment constant varies linearly with the Richardson number), the value of the local entrainment constant is higher during the transition period than at the plume limit, i.e. that the rate of entrainment into the jet is greatest during the transition phase.

Finally, in figure 9 the effective entrainment constant divided by its initial value, $\alpha(x^*)/\alpha_j$, has been plotted. The two solutions are surprisingly different here also, considering their similarity elsewhere. The first hypothesis solution (solid line) maintains its initial value until $x^* \simeq 0.6$, whereas the entrainment constant from the second solution increases more rapidly. Both solutions show maximum entrainment during the transition phase, although this is more noticeable in the solution obtained when using the second hypothesis.

4. Comparison with experiments

It is important to check theoretical results with those of practical experiments. The solutions for the horizontal and vertical limits have already been well documented (see Fischer 1979) with good experimental agreement for pure jets and plumes. For horizontal buoyant jets it is easiest to compare the theoretical prediction with the measured radii and trajectories.

Experiments were performed to do this by placing a jet of dyed salt solution in a large tank of fresh water, illuminated from behind. The flow rate of the source was varied, keeping the nozzle diameter of the jet and the reduced gravity of the buoyant source fluid constant (with $g_0' = 51.0 \pm 0.4\,\mathrm{cm\,s^{-2}}$). The flow was recorded on video tape. The radius of the jet at points along its axis can be measured directly from the video picture and the trajectory was found by eye, estimating the points mid-way between the boundaries of the jet along a line perpendicular to the axis of the jet. The video picture was also analysed digitally taking a time average of a succession of frames in order to obtain a clearer definition of the boundary of the jet.

Figure 1 shows the variation of the radius b with arclength s, where the results of radius measurements made here and some taken from Schatzmann (1976, who used the experiments of Fan 1967) have been plotted. A good linear agreement is seen in every case although the gradient of the line or 'spreading rate' varies between experiments. This linear relationship was used as the basis for the first hypothesis. A line through the points might have been expected to pass through a point on the negative s axis, rather than the origin. This is because the values of s measured in experiment are relative to the jet nozzle and not the point of zero radius (which should correspond to $s = 0$), the *virtual origin.* However, from the equation for $b(x)$ in (2.20), the distance between the virtual origin and the nozzle exit is expected to be proportional to the nozzle radius - which is very small ($\sim$ 0.25 mm) in these experiments. Thus any corrections required to compensate for the virtual origin/nozzle disparity are negligible and have been ignored.

A comparison between the theoretical and experimental trajectories, using both the experiments presented here and some of those listed by Schatzmann (1976), will now be made. Schatzmann (1976), however, only lists the Froude number for each experiment. The Froude number is proportional to the jet-length with constant of proportionality dependent on the nozzle radius, which is not known. Therefore, the theoretical scaling used in (2.61) for these experiments cannot be calculated and so the best fit between the experimental and theoretical centrelines is shown in figure 10. Figure 10*a* shows the actual trajectories observed experimentally (x and z have unknown units) and the scaled trajectories are shown in figure 10*b* - the curve is the theoretical solution obtained when using the first hypothesis. The agreement is excellent - however because the theoretical and best fit scalings cannot be compared, it is not possible to endorse the theoretical solution using this data.

The same procedure is carried out with the experiments described above. Now, however,

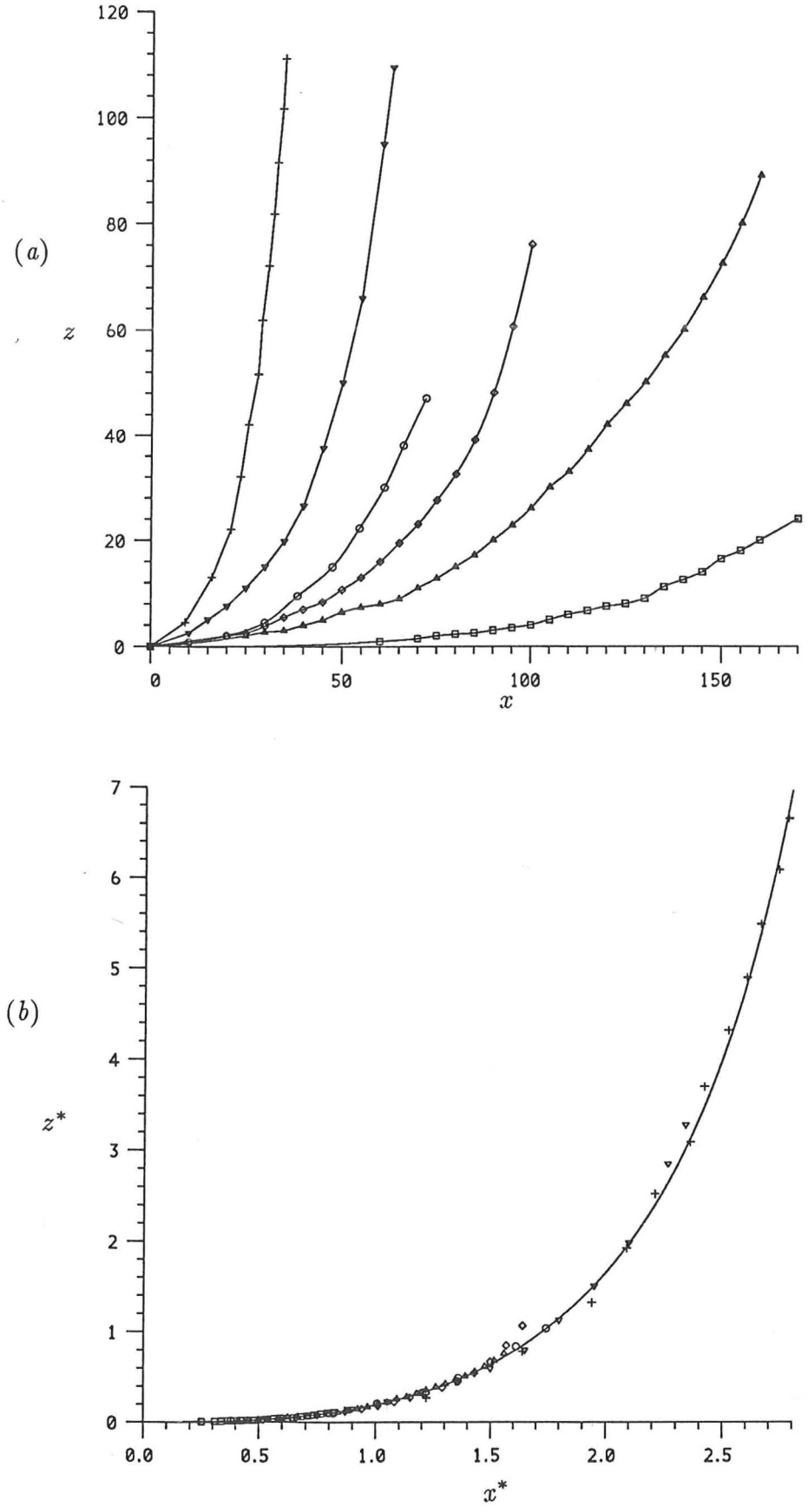

FIGURE 10. Comparison between the theoretical and experimental trajectories. Data from Schatzmann/Fan 1976. (*a*) The actual trajectories; (*b*) the best fit with the theoretical solution.

Symbol	Flow Rate (cm^3s^{-1})	Theoretical scale	Best fit scale
+	0.70	0.0583 ± 0.0087	0.0585
*	1.03	0.0396 ± 0.0059	0.0443
△	1.20	0.0340 ± 0.0051	0.0331
◇	1.50	0.0272 ± 0.0041	0.0284
□	1.57	0.0260 ± 0.0039	0.0232

TABLE 1. The theoretical and best fit scalings.

all of the data required to make a proper comparison is available, although the experimental errors in Q_0 and g_0', together with the uncertainty in α_j mean that the scaling can only be calculated to $\pm 15\%$. The experimental flow rates and theoretical scaling factors are given in table 1 (the scale given in the table is the scaling used to transform the experimental lengths into the theoretical starred variables) with figure 11*a* showing the actual observed jet trajectories. The theoretical and scaled experimental curves are shown in figure 11*b*. In this figure, the scaling which provides the best fit with the theoretical curve has been chosen, but in each case the 'best fit scale' is well within the degree of accuracy of the 'theoretical scale'. Again, the agreement between the theoretical and experimental jet trajectories is excellent, providing good support to the analysis above.

5. Discussion and Conclusions

The motion of a horizontally directed buoyant jet has been examined both analytically and numerically, comparing the theoretical predictions with experimental measurements. The conservation equations were derived by integrating over a cross-section of the jet, a technique initially illustrated by the consideration of the horizontal and vertical limiting cases, which have established solutions. The important feature of the analysis was that the entrainment constant was allowed to vary along the flow of the buoyant jet, as it changes from a jet-like to a plume-like state. This was achieved by using one of two hypotheses which have been detailed above.

Considering the analytical calculations first, it was found that for both hypotheses the reduced gravity was proportional to the horizontal velocity component (2.52) and that all

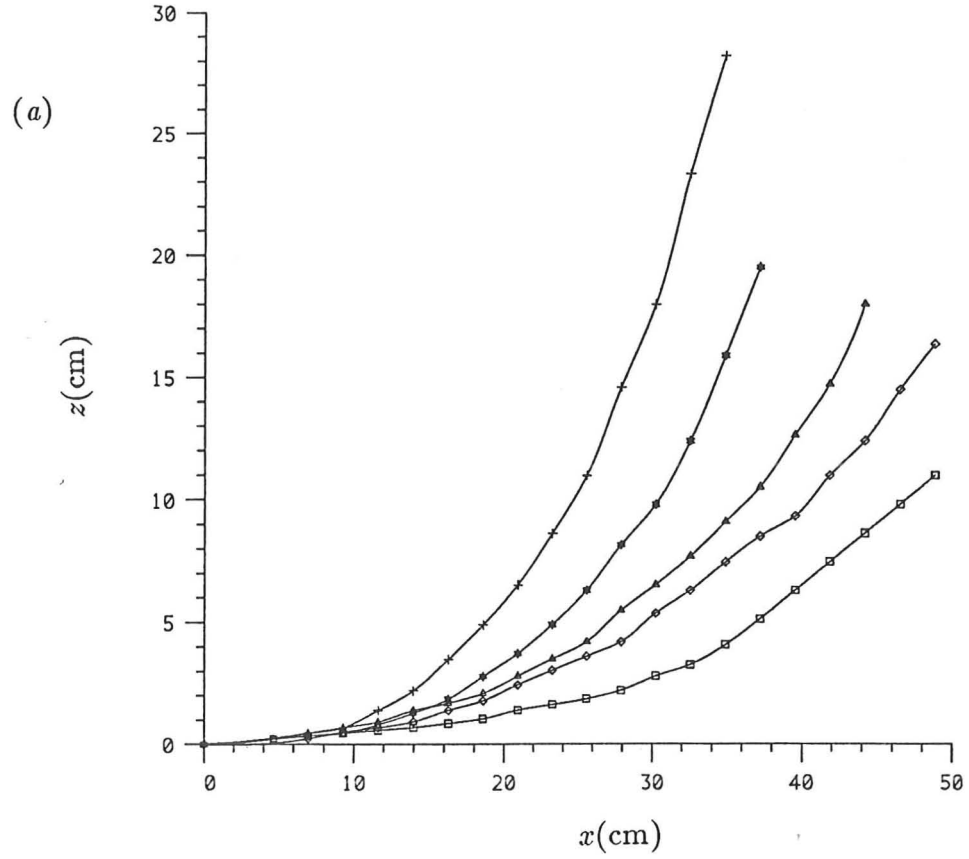

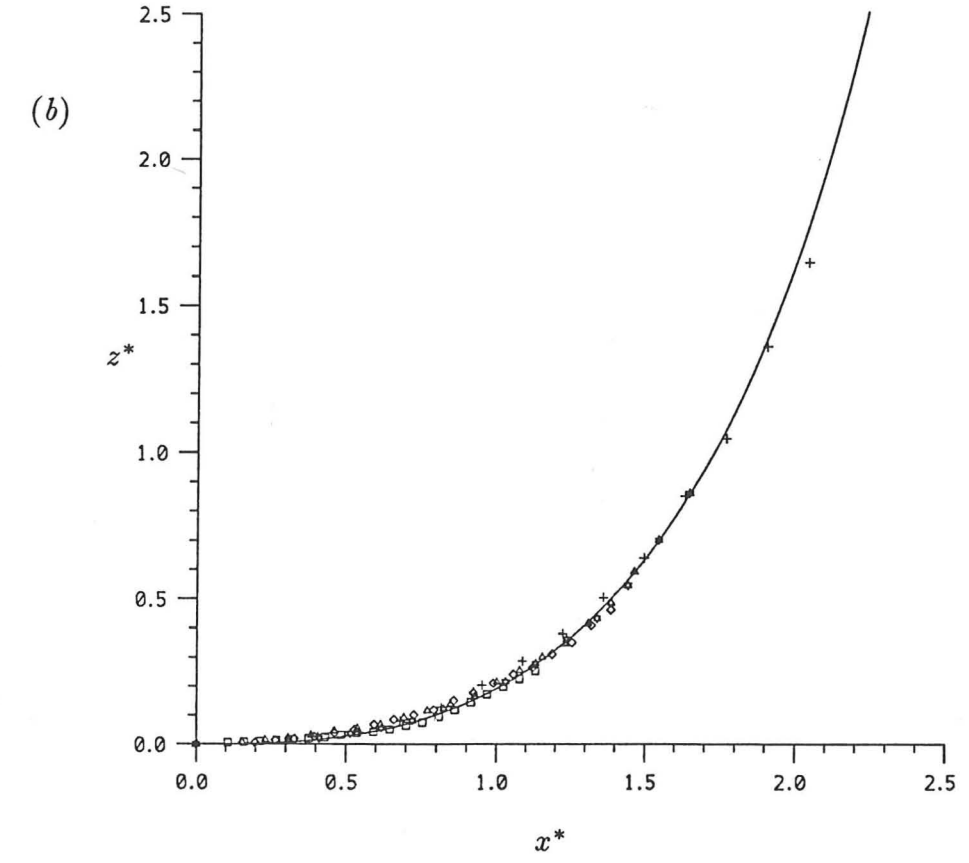

FIGURE 11. Comparison between the theoretical and experimental trajectories. (*a*) The actual trajectories; (*b*) the best fit with the theoretical solution (see table 1).

the variables in the problem could be expressed in terms of the gradient of the trajectory (2.55). It was also found that the equations governing the gradient (2.59) and (2.93) could be simplified by scaling the lengths by a factor proportional to the jet-length (2.63). These equations for f could not be integrated analytically and so they were considered for small and large values of the gradient in turn. Series expansions for small values of the gradient indicated that the behaviour of the velocity components remains pure jet-like, even though the jet may have begun to divert from its initially horizontal course. The analysis for large values of the gradient showed that the centreline axis of the jet reaches a maximum horizontal distance from the origin. At this point the velocity components are zero, and the gradient, vertical elevation and radius are infinite.

In order to examine the transition between the jet-like and plume-like states, equations (2.59) and (2.93) were integrated numerically to obtain the theoretical solution, using the two different hypotheses. The two solutions are generally similar in behaviour and were discussed in section 3. This similarity was explained by observing that the second hypothesis implies an almost linear variation of the radius with arclength and so will agree well with the solution of the first hypothesis which actually assumes that the radius varies linearly with the arclength. It was found that the transition between jet-like and plume-like states occurs between $x^* = 1$ and $x^* = 3.5$ approximately, the buoyant jet having almost vertical motion after $x^* = 3.5$. In terms of the original variables, the transition takes place between

$$x = \frac{L_j}{\lambda\sqrt{2\alpha_j}} \simeq 2.2L_j \qquad \text{and} \qquad x = \frac{3.5L_j}{\lambda\sqrt{2\alpha_j}} \simeq 7.6L_j.$$

This agrees well with the observations of Linden, Marshall & Cleaver (1991), who observed that the jet-plume transition appeared to take place from $x \simeq 2.6L_j$. The numerical solution was also used to determine the maximum horizontal distance travelled by the jet. This was found to be

$$x_m^* \simeq 4.6 \qquad \text{or} \qquad x_m = \frac{4.6L_j}{\lambda\sqrt{2\alpha_j}} \simeq 9.9L_j,$$

although at this point the radius is infinite. The greatest difference between the two solutions was seen in the behaviour of the Richardson number and the effective entrainment constant. With both solutions the values of the Richardson number and the effective entrainment constant become greater than their asymptotic plume values during the transition phase. This means that the entrainment into the buoyant jet is greatest during the transition phase, possibly a result of the high curvature of the jet there.

The theoretical predictions for the trajectory followed by the buoyant jet were then compared with experimental measurements, in order to endorse the theoretical results. The agreement was excellent, with the scaling providing the best fit to the theoretical curve being well within the experimental error of the theoretical scaling in each case. This provided suitable support of the analysis, although at this stage further measurements are required to decide which of the two hypotheses provides the best model for buoyant jet flow.

The theoretical calculations of the jet trajectory, reduced gravity and maximum distance reached (x_m) could have practical uses. For example, considering the horizontal discharge of a buoyant fluid into a container, it would be desirable to know if the jet will impinge on the side of the container or if it will reach a vertical plume-like state before reaching the boundary. If the container was closed, then in the latter case the 'filling-box' model (Baines & Turner 1969) could be used to describe the flow, whereas in the former case, the impingement may affect the subsequent concentration build-up inside the container (see Linden, Marshall & Cleaver 1991). Alternatively, consider the dumping of sewage or other negatively buoyant fluid from a horizontal pipe into the sea. If the flow in the region where the dumping took place was small compared with the buoyant jet flow, then the above analysis could be used to calculate the theoretical trajectory of the jet. This would give an indication of the distance from the pipe that the source material would travel before reaching the sea bed, and an estimate of the concentration level there (neglecting the effect of approaching the sea bed). The effects of stratification can be neglected near to the source if the density changes in the environment are small (over the length scale of the jet) compared with the buoyancy of the buoyant jet. A further use of the analysis could be to calculate the criterion for a buoyant jet to penetrate the interface between two fluids of different density (stably stratified). The buoyant jet will penetrate if, at the interface, it is more buoyant than the fluid into which it is trying to flow.

The analysis is also easily adaptable. Off-horizontal buoyant jets could be considered by simply changing the initial conditions of the numerical integration as outlined in section 3. Stratification of the environment could be included by adding the term $-w\frac{\partial \rho_a}{\partial z}$ to the right hand side of (2.6), assuming that density variations in the x and y directions are negligible. This modifies (2.49) to

$$\frac{d}{ds}(b^2 v g') = b^2 w N^2 \qquad \text{where} \qquad N^2 = -\frac{g}{\rho_0}\frac{\partial \rho_a}{\partial z},$$

and the analysis would proceed as before using one of the two hypotheses to solve the problem.

Notation

Below is a list of the symbols used in this chapter, provided for reference purposes.

b	Transverse length scale of the buoyant jet
$B_{(0)}$	(Initial) buoyancy flux
f	Gradient of the jet trajectory
F	Constant proportional to the buoyancy flux, used in the vertical limit
g'	Reduced gravity of the buoyant jet fluid
H	Vertical flux of horizontal momentum, used in the vertical limit
J	Constant proportional to the initial buoyancy flux
k	Constant of proportionality relating the jet radius and arclength in (2.56)
K	Constant proportional to the initial momentum flux
L	Length scale
L_j	Jet-length
$M_{(0)}$	(Initial) momentum flux
N^2	Buoyancy frequency
p	Pressure
Q	Local volume flux
Ri	Local Richardson number of the jet
Ri_p	Plume Richardson number
s	Arclength
T	Time scale
u	Horizontal velocity component
v	Mean centreline velocity
w	Vertical velocity component
x	Horizontal coordinate
x'	Rotated coordinate
x_m	Maximum horizontal displacement of the jet centreline
z	Vertical coordinate
z'	Rotated coordinate
$z(x)$	The centreline trajectory
$\alpha(x)$	Effective entrainment constant using the first hypothesis

$\alpha(Ri)$	Entrainment constant using the second hypothesis
$\alpha_{j,p}$	Entrainment constants for jets and plumes
β	Parameter in the series expansion using second hypothesis
λ	Factor by which length scale for the density difference is larger than that of the velocity
ρ	Density
ρ_a	Ambient density
ρ_0	Reference density
θ	The angle between the jet centreline and the horizontal axis
$*$	Denotes transformed variables using (2.61)

Chapter Four

The Flow of a Vertical Buoyant Jet with High Momentum in a Long, Ventilated Tunnel

The purpose of this chapter is to investigate and understand the flow resulting from the release of buoyant material within a long tunnel of rectangular cross section. The source is discharged through a nozzle of small radius with sufficiently high flow rate to ensure that the 'jet-length' is several times the depth of the tunnel, d. The ends of the tunnel may be either open or closed and a number of ventilation points may exist along it. Consideration of a source with high momentum is an important development in the study of confined jet flows, as most previous studies have assumed that the source has little or no initial momentum.

It is found that circulation cells are driven near to the source and that the concentration within them increases to a steady-state maximum. At a distance of about $2.5d$ from the source the buoyancy forces are then sufficiently strong to drive a two-layered stratified counterflow.

The steady state conservation equations are analysed in order to calculate the mean flow variables. The flow past a ventilation point and the characteristics of the secondary outflow are derived, enabling the calculation of total number of vents needed to vent the buoyant fluid. The time dependence of the mean concentration in the circulation cell near to the source is also deduced. This could be used to calculate time dependent solutions for the other mean flow variables. All the theoretical results are compared with experimental measurements.

---

1. Introduction

The dynamics of buoyant releases in confined regions were first examined by Baines & Turner (1969) who studied the behaviour of a vertical pure plume in a rectangular box (see chapter 1). Their 'filling-box' model makes the assumption that on reaching the upper surface of the box, the plume material immediately spreads out in a horizontal layer, slightly less buoyant than the preceding layer, so that stratification of the interior occurs. To ensure that the instantaneous spreading-out assumption is reasonably valid, Baines & Turner made a restriction on the aspect ratio of the box: height/width$\leqslant$1. In the present case, this ratio is satisfied, but the source has high momentum as well as buoyancy; the consequent overturning produced means that the assumption that the source fluid immediately spreads horizontally with no re-entrainment is not valid, i.e. the 'filling-box' model may not be applied in this situation.

Jirka & Harleman (1979) have investigated the stability and mixing of a vertical planar buoyant jet discharged in a long channel of rectangular cross-section, filled with a shallow layer of water with a free surface. They described two extreme steady-state flows which are outlined below.

i) Non-buoyant planar discharge

Jirka & Harleman (1979) observed that the source of momentum gave rise to circulation cells which extended over the full height of the channel (see figure 1). Up to two circulation cells on each side of the source were observed experimentally (in the planar case). Their experiments showed that the centre of the primary (first) circulation cell is approximately $1.5d$ from the source axis, which agreed with their estimated position. [Jirka & Harleman 1979 assumed that the jet holds the same geometric behaviour $b = 2\alpha s$, where b is the jet radius, α is the entrainment constant (see Morton, Taylor & Turner 1956) and s the distance from the source, after impingement. Using a value of $\alpha = 0.1$, then $b = d/2$ when $s = 5d/2$ or $x = 3d/2$, and the jet flow breaks down here as the magnitude of the walljet velocity is equal to the returning jet exterior entrainment flow velocity.] The flow reversal has characteristic radius $d/2$ and so the horizontal length of the primary cell can be estimated to be approximately $2d$. Using a circular source, assuming that the width ω of the channel is of a similar order to the depth d, then circulations will be inhibited in the $y - z$ plane.

ii) Strongly buoyant planar discharge

In this case the buoyancy forces are sufficiently strong to inhibit the formation of a cir-

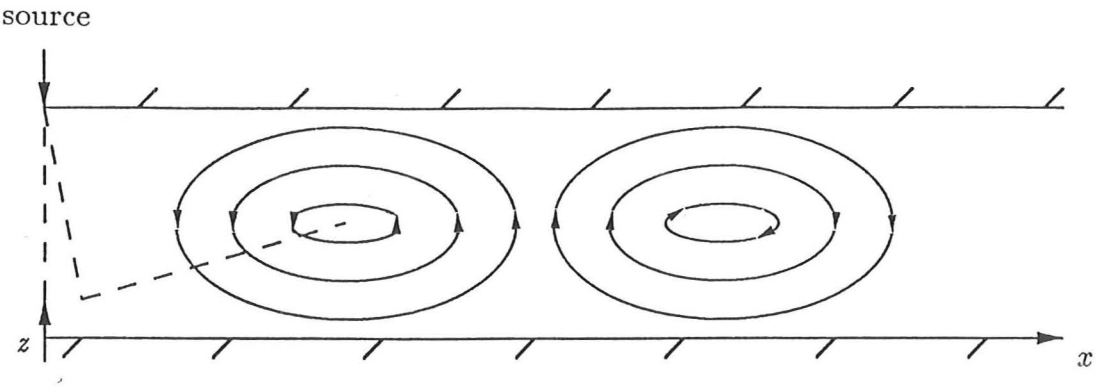

FIGURE 1. A schematic diagram of the flow produced by a plane, non-buoyant discharge into a tunnel.

(a)

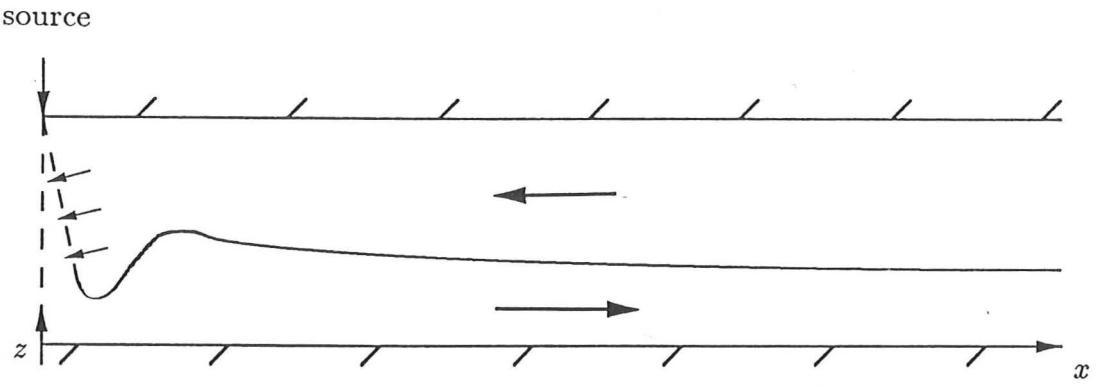

(b)

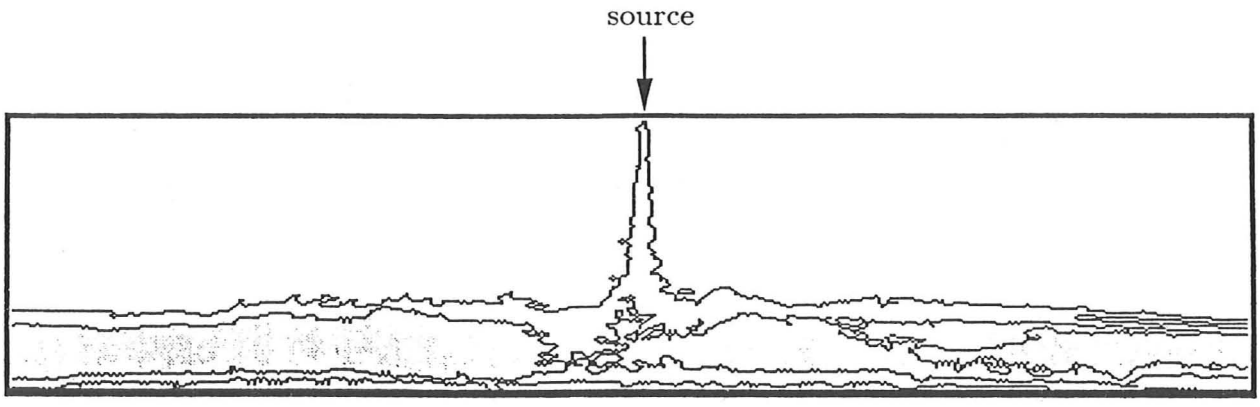

FIGURE 2. The flow produced by a strongly buoyant discharge into a tunnel; (*a*) a schematic diagram, and (*b*) an image taken from an experiment (in which a dyed, buoyant fluid was released from a circular nozzle in a perspex tunnel). The image was obtained by digital analysis of a video of the flow - the lines are contours of equal mean concentration (averaged through the tank).

culation cell and the jet spreads horizontally after impingement (see figure 2*a*). Figure 2*b* is an image from an actual experiment (in which a circular vertical source was used). The flow is dependent on both upstream and downstream conditions and can exhibit strong depth changes or gradual variations in thickness. All the entrainment into the flow takes place into the buoyant jet before it has impinged and is thus independent of the outflowing layer.

iii) The present case - buoyant discharge with high momentum from a circular source

In chapter 2 it was described how a buoyant jet is characterised by its initial specific momentum and buoyancy fluxes M_0 and B_0 (see chapter 2 for definitions). It was also shown that a length scale may be formed using these fluxes, called the 'jet-length' scale, L_j (see for example, Turner 1973 or chapter 2, equation (2.7)), which gives a measure of the length scale over which momentum forces will dominate buoyancy forces. In the situation considered here, L_j is several times the depth d, and so the effects of buoyancy are negligible before impingement.

The resulting flow, drawn schematically in figure 3*a*, is a combination of the above two extreme cases.

The buoyant jet, discharged vertically and driven mainly by its initial momentum, spreads out horizontally on impingement. The jet entrainment velocities are sufficiently high to drive a circulation cell near to the source (region 1) which is observed to be well mixed, with the concentration increasing to a steady state maximum. This increase in concentration is due to the re-entrainment of buoyant fluid into the jet itself (compare this with case (ii) in which only ambient fluid is entrained into the jet). The centre of the circulation is approximately $1.5d$ from the source axis, but due to the buoyancy of the source the centre is *less* than $0.5d$ from the impingement boundary. The buoyancy of the jet is sufficient to inhibit the formation of a secondary circulation cell, which was observed in the non-buoyant (planar) case above, but turbulent momentum transfer excites the fluid on the outer boundary of the primary cell (region 2), entraining ambient fluid and releasing buoyant fluid to the two-layer counterflow (region 3). The releasing region 3 may consist of an entrainment zone and a roller region (Wilkinson & Wood 1971). The inflow volume flux and hence the entrainment zone is controlled by the downstream conditions; so, for example, a restriction on the inflow volume flux will be accompanied by a decrease in the entrainment zone. The released fluid (from region 3) then flows horizontally in a stable buoyant layer with negligible entrainment across the interface (region 4). The depth of the buoyant layer may decrease slowly due to shear stresses. A typical 'freeze-frame' of the flow is given in figure 3*b*, demonstrating

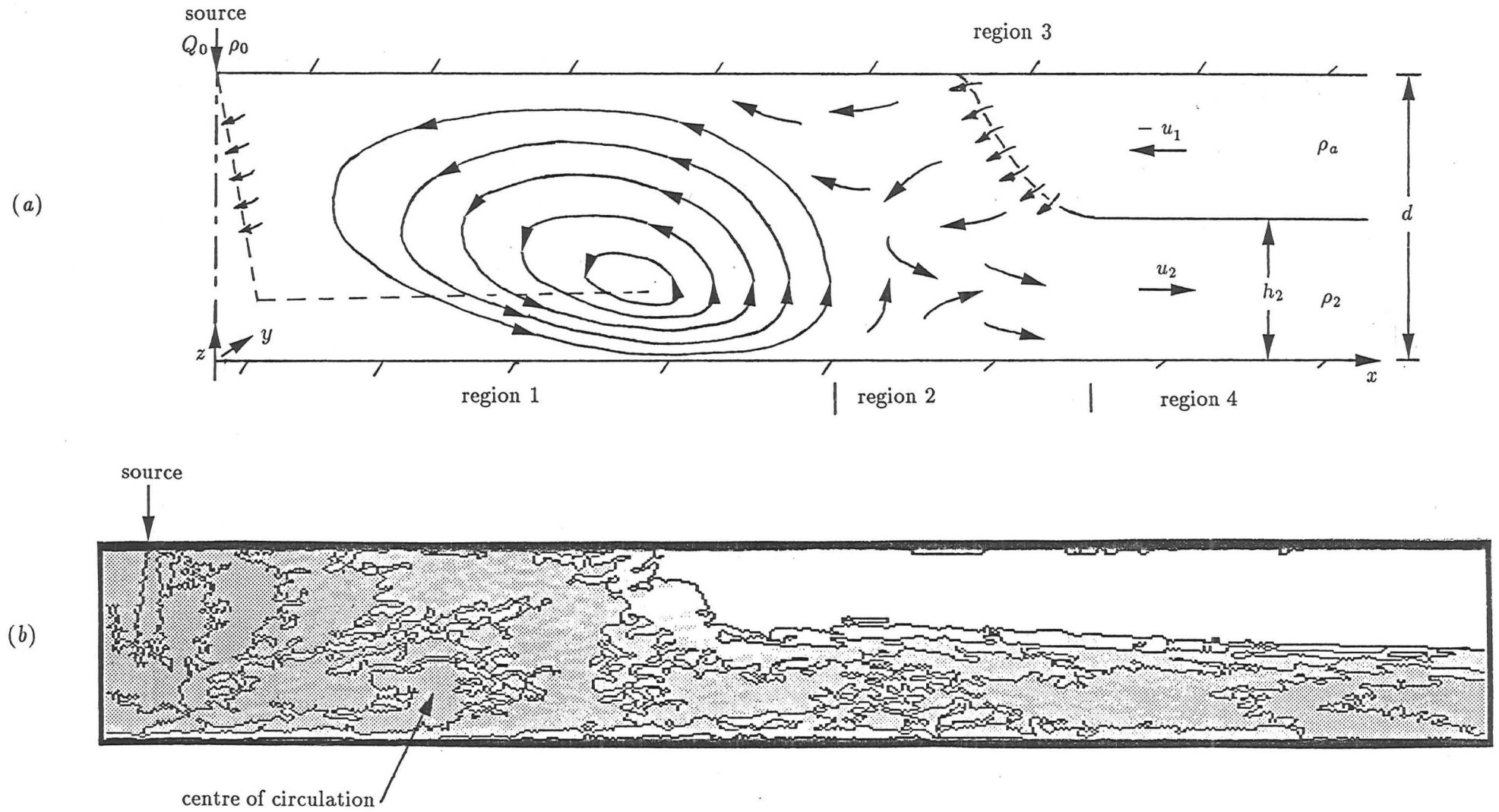

FIGURE 3. The flow produced by a buoyant source with high momentum; (a) schematic diagram, and (b) an image showing contours of dye concentration taken from an experiment.

all of the features mentioned above. This flow has been observed previously, by Lee (1980) and Andreopoulos *et al.* (1986) in experiments with vertical buoyant jets in shallow water, although they merely class the flow as 'unstable' and consider only the 'stable' buoyancy dominated flow described above (case (ii)).

One important aspect of this investigation, is the build-up of concentration within the tunnel and the dependence of the flow of buoyant fluid along it on the position, size and number of ventilation points. The counterflow with boundaries above and below will be considered as well as the flow over and through the ventilation points. A further objective is the study of the concentration build-up within the primary cell and the effect of a ventilation point within it.

2. Analysis

In the following analysis it is initially assumed that the ventilation points are situated symmetrically either side of the source, which is assumed to be negatively buoyant for ease of comparison with the experiments. Theoretically then, the flow should be symmetric about the source and so only one half is considered. An image, taken from an actual experiment, showing the symmetry of the flow is given in figure 4 - the shaded region contains source material. In practice it is observed that this type of (symmetric) configuration may become unstable, and any significant asymmetry in the flow forces acting on either side of the source will cause fluctuations in the outflow depth, which may unbalance the flow. Also, if the total out-vent area is too small, or the source is too close to a closed end then the outflowing buoyant fluid may contaminate the inflowing ambient fluid, thus affecting the flow. A ventilation point within the primary circulation cell region allows fluid from the environment to be 'sucked' in, due to the pressure drop associated with the circulating fluid - unless of course the edge of the vent is less than $2\alpha d$ from the source axis, in which case the overlapping jet fluid simply flows through the vent. A ventilation point overlapping the primary cell and the excited region adjacent to it (region 2 in figure 3*a*) may allow fluid to be sucked into the tunnel from the environment as mentioned above, but may also allow the fluid in region 2 to flow out. These effects will be considered later - initially it is assumed that all the ventilation points are outside of regions 1 and 2, and that there are sufficient vents to make no restriction on the inflow or outflow rates.

Suppose that the horizontal velocity is $u(x, y, z)$. Then, for a tunnel of depth d and width

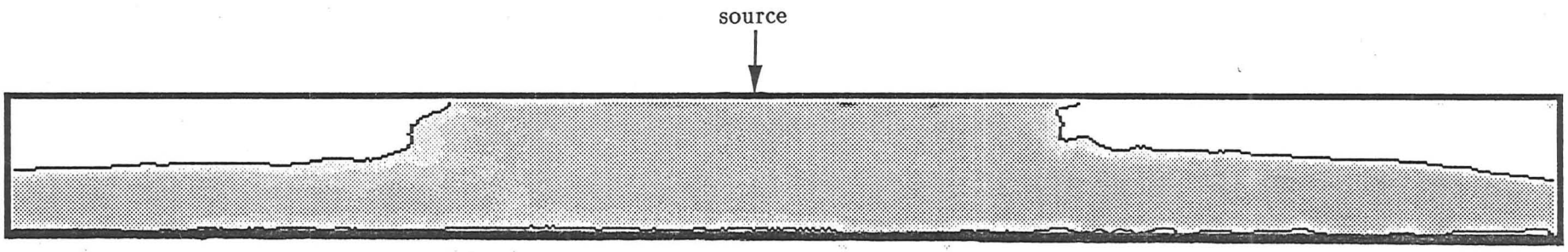

FIGURE 4. A typical image demonstrating the symmetry of the flow.

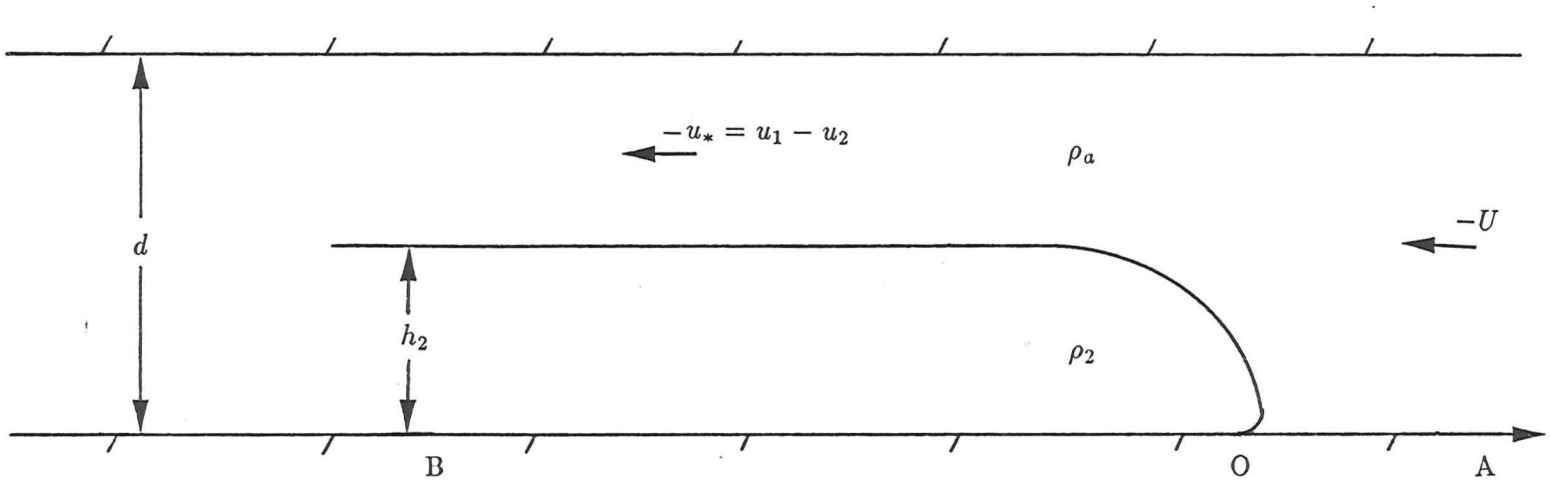

FIGURE 5 (a). Schematic diagram of the flow over the 'head'.

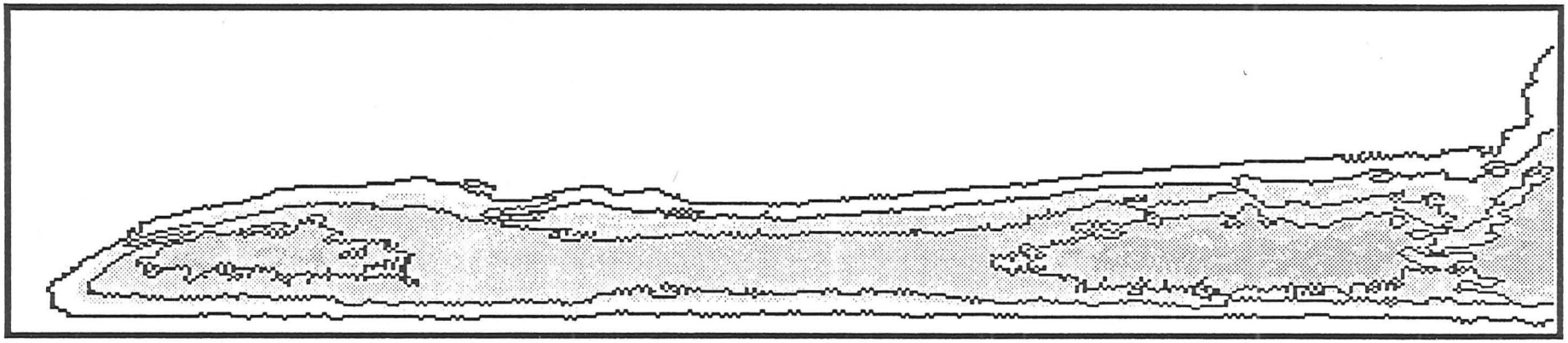

FIGURE 5 (b). An image taken from experiment of the flow over the 'head'.

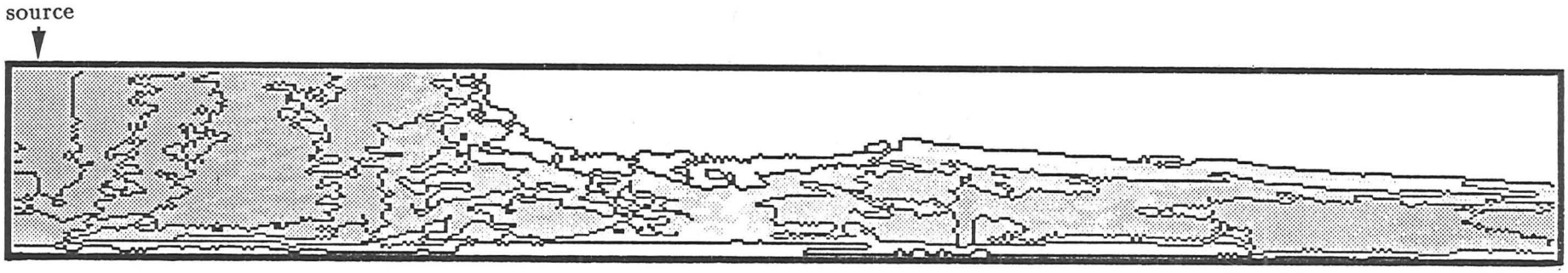

FIGURE 5 (c). A typical image taken from experiment showing that the outflowing buoyant layer occupies half the depth of the tunnel.

ω, conservation of volume implies that

$$\frac{Q_0}{2} = \int_0^d \int_0^\omega u(x,y,z)\, dydz, \tag{2.1}$$

for all $x > 0$, where Q_0 is the source volume flux.

2.1 Region 4: the stratified counterflow

The two dimensional flow of a buoyant layer has been previously studied by Ellison & Turner (1959), Wilkinson & Wood (1971) and Jirka & Harleman (1979), but only when the depth of the layer is small compared with the total depth and one layer has a free surface. The counterflow will now be re-examined when both layers are bounded by solid boundaries and the buoyant layer may have large depth.

The flow is analysed making the following assumptions:

i) the flow has reached a steady-state equilibrium;

ii) the flow is mainly two dimensional with vertical velocities sufficiently small for the flow to be considered horizontal with a hydrostatic pressure distribution;

iii) there is negligible entrainment across the interface; Ellison & Turner (1959) gave a lower limit on the Richardson number

$$Ri = \frac{g\Delta\rho\, d}{\rho_a(\Delta u)^2}, \tag{2.2}$$

where ρ_a is the ambient density, for entrainment across such an interface to be considered negligible, $Ri \simeq 0.8$ - this limit is generally satisfied in the experiments (the density difference and velocity shear may be calculated from the layer mean values);

iv) the flow force is constant along region 4 (see Benjamin 1968);

v) the shear stresses are related to the flow parameters; (see Jirka & Harleman 1979);

vi) at large distances from the tunnel the environmental fluid is still and of uniform density.

Let the height of the lower layer be $h_2(x,t)$, with density $\rho_2(t)$ (independent of x from (iii)) with mean velocity $u_2(x,t)$. The upper layer of in-flowing ambient fluid has mean velocity $u_1(x,t)$ and depth $h_1(x,t) = d - h_2(x,t)$.

Assuming a hydrostatic pressure distribution $p(x,z) = p_I - \rho g(z - h_2)$, where p_I is the pressure at the interface, then the equations of horizontal motion for the upper and lower layers are

$$\frac{\partial h_1}{\partial t} + \frac{\partial}{\partial x}(u_1 h_1) = 0, \tag{2.3}$$

$$\frac{\partial h_2}{\partial t} + \frac{\partial}{\partial x}(u_2 h_2) = 0, \tag{2.4}$$

$$\frac{\partial u_1}{\partial t} + u_1 \frac{\partial u_1}{\partial x} = -\frac{1}{\rho_a}\frac{\partial p_I}{\partial x} - g\frac{\partial h_2}{\partial x} - \frac{\partial}{\partial x}(\overline{u'^2}) - \frac{\partial}{\partial y}(\overline{u'v'}) - \frac{\partial}{\partial z}(\overline{u'w'}), \tag{2.5}$$

$$\frac{\partial u_2}{\partial t} + u_2 \frac{\partial u_2}{\partial x} = -\frac{1}{\rho_2}\frac{\partial p_I}{\partial x} - g\frac{\partial h_2}{\partial x} - \frac{\partial}{\partial x}(\overline{u'^2}) - \frac{\partial}{\partial y}(\overline{u'v'}) - \frac{\partial}{\partial z}(\overline{u'w'}), \tag{2.6}$$

where $\overline{u'^2}$ etc. are the shear stresses associated with the turbulent fluctuating velocities u', v', w' in the x, y and z directions respectively. Equations (2.3) and (2.4) are equations of volume conservation, and can be obtained by integrating the continuity equation over z.

2.1.1 Negligible shear stresses

In the following analysis, the steady state is considered initially, and as a first approximation it is assumed that the shear stresses are negligible. The equations then reduce to (substituting for $h_1(x)$)

$$\frac{d}{dx}(u_1(d - h_2)) = 0, \tag{2.7}$$

$$\frac{d}{dx}(u_2 h_2) = 0, \tag{2.8}$$

$$\frac{d}{dx}\left(\frac{u_1^2}{2} + \frac{p_I}{\rho_a} + g h_2\right) = 0, \tag{2.9}$$

$$\frac{d}{dx}\left(\frac{u_2^2}{2} + \frac{p_I}{\rho_2} + g h_2\right) = 0. \tag{2.10}$$

Integration of (2.8) and (2.7) with respect to x gives

$$Q_2 = \omega h_2(x) u_2(x) = \int_0^{h_2(x)} \int_0^{\omega} u(x, y, z)\, dydz, \tag{2.11}$$

where Q_2 is the constant volume flux of the lower layer, and

$$Q_1 = \omega(d - h_2(x)) u_1(x) = \int_{h_2(x)}^{d} \int_0^{\omega} u(x, y, z)\, dydz, \tag{2.12}$$

where Q_1 is the constant (negative) volume flux of the upper layer (of density ρ_a).

Thus in the steady-state, the equations of total volume and mass conservation over any vertical cross-section in the counterflow become

$$\frac{Q_0}{2} = \omega(u_2 h_2 + u_1(d - h_2)) = Q_2 + Q_1, \quad \text{and} \tag{2.13}$$

$$\frac{Q_0\rho_0}{2} = \omega(u_2\rho_2 h_2 + u_1\rho_a(d-h_2)) \quad \text{or} \quad \frac{Q_0 g_0'}{2} = Q_2 g_2', \tag{2.14}$$

where $g_2' = (\frac{\rho_2-\rho_a}{\rho_a})g$ is the reduced gravity of the buoyant layer.

The interface pressure can be eliminated from (2.9) and (2.10) giving

$$\frac{d}{dx}\left(\frac{u_1^2}{2} - \frac{\rho_2}{\rho_a}\frac{u_2^2}{2} - g_2' h_2\right) = 0, \tag{2.15}$$

and expanding this with the use of (2.11) and (2.12) gives

$$\left(\frac{u_1^2}{(d-h_2)} + \frac{\rho_2}{\rho_a}\frac{u_2^2}{h_2} - g_2'\right)\frac{dh_2}{dx} = 0. \tag{2.16}$$

This means that h_2, and consequently u_2 and u_1 must have constant values over the outflow region.

[The other alternative is that

$$\frac{u_1^2}{(d-h_2)} + \frac{\rho_2}{\rho_a}\frac{u_2^2}{h_2} - g_2' = 0.$$

In the Boussinesq limit this reduces to the critical Froude number condition

$$F_1^2 + F_2^2 = 1, \qquad \text{where} \qquad F_1^2 = \frac{u_1^2}{g_2'(d-h_2)} \qquad \text{and} \qquad F_2^2 = \frac{u_2^2}{g_2' h_2},$$

which corresponds to a jump in h_2. This is not observed experimentally (generally to obtain such jumps a controlling geometry, e.g. a ridge, is needed) and so this possibility is ignored.]

Hence the flow is governed by the three equations

$$\omega u_2 h_2 = Q_2, \tag{2.17}$$

$$Q_0 g_0' = 2Q_2 g_2', \tag{2.18}$$

$$u_1 = \frac{Q_0 - 2Q_2}{2\omega(d-h_2)}, \tag{2.19}$$

in the five unknowns u_1, u_2, h_2, g_2' and Q_2. A further two conditions must be obtained from the near-field and far-field conditions.

2.1.2 Balance of flow forces over the head

Definition of the flow force

Benjamin (1968) introduced the idea of a balance in the flow forces in his study of the flow over an air pocket. He defined the flow force F as the sum of the momentum flux and the pressure forces. Thus

$$F = \int_0^\omega \int_0^d (\rho_a + \Delta) u^2 \, dz dy + \int_0^\omega \int_0^d \int_z^d (\rho_a + \Delta) g \, dz' dz dy, \tag{2.20}$$

which, for the two-layered system above reduces to

$$\frac{F}{\omega \rho_a} = \frac{\rho_2}{\rho_a} u_2^2 h_2 + u_1^2 (d - h_2) + \frac{p_I}{\rho_a} d - \frac{1}{2} g d^2 + d h_2 g + \frac{1}{2} h_2^2 g_2'. \tag{2.21}$$

Balance of the flow forces over the head

Benjamin's analysis may be extended to the current situation. Consider the flow over the head of the outflowing layer (assuming that it has not met a ventilation hole) in a frame moving with the outflowing layer (see figure 5*a*). Figure 5*b* is an image of the head taken from an actual experiment.

The incoming ambient fluid has speed U and the speed of the fluid over the head (again, no mixing) is u_* with $u_* = u_1 - u_2$. The point O is a stagnation point, with pressure p_O.

Conservation of volume gives

$$U d = u_* (d - h_2). \tag{2.22}$$

The Bernoulli theorem may be applied along OA to find the pressure at A, p_A

$$p_A = p_O - \frac{\rho_a}{2} U^2. \tag{2.23}$$

Hence the flow force per unit width of the incoming fluid is

$$F_{in} = p_O d + \frac{1}{2} \rho_a d U^2 - \frac{1}{2} g \rho_a d^2. \tag{2.24}$$

Applying the Bernoulli theorem along OI gives

$$p_O = p_I + \frac{1}{2} \rho_a u_*^2 + g \rho_a h_2, \tag{2.25}$$

where p_I is the interface pressure. Now, again by Bernoulli, the pressure at B, p_B is equal to that at O; but also $p_B = p_I + g \rho_2 h_2$ and so

$$g \rho_2 h_2 = \frac{1}{2} \rho_a u_*^2 + g \rho_a h_2, \tag{2.26}$$

or

$$u_*^2 = 2h_2 g_2'. \tag{2.27}$$

Equation (2.25) will now be used to calculate the flow force per unit width of the outgoing fluid

$$F_{out} = \rho_a u_*^2 (d - h_2) + (p_O - \frac{1}{2} u_*^2 \rho_a) d - \frac{1}{2} g \rho_a (d^2 + h_2^2) + \frac{1}{2} g \rho_2 h_2^2. \tag{2.28}$$

Equating the flow forces and using (2.22) and (2.27) yields

$$\frac{h_2}{d}(d - h_2)^2 g_2' = 2\left(\frac{d}{2} - h_2\right) h_2 g_2' + \frac{1}{2} g_2' h_2^2. \tag{2.29}$$

Hence ignoring the uninteresting possibility of $g_2' = 0$, equation (2.29) gives two solutions for h_2: $h_2 = 0$ and

$$h_2 = \frac{d}{2}, \tag{2.30}$$

i.e. the buoyant layer occupies half the depth of the tunnel, which is analogous to the solution obtained by Benjamin (1968) in his application to the flow over an air pocket.

Whilst moving in a frame at the propagation velocity of the density current, the hydrostatic pressure assumption is exact. Moncrieff and So (1989) presented a theory including the effect of vorticity in the density current on its far-field behaviour. The pressure in the density current is then not hydrostatic except in the far-field where the flow is horizontal. By allowing the density current to have an inflow speed far from the head, they found that there is partial cancellation in the corrective terms to (2.27), and so the above solution is more accurate than might otherwise be expected.

Moncrieff & So (1989) also found that for constant vorticity in the head, $h_2/d \in [\frac{1}{2}, \frac{2}{3}]$. This solution comes from an equation representing the conservation of mass, momentum and energy, and the solution $h_2 = 2d/3$ is the special case where the fluids have the same density. However, in their analysis, there is a large circulating flow at the head which is not observed in experiment, and so the above solution, (2.30) is considered to be more appropriate here.

The above analysis will only apply before the head has met a vent; however it is observed experimentally that the outflow continues to maintain this half-tunnel depth even after the head has flown through or over a vent (see for example, figure 5c which shows a typical flow).

2.1.3 Implications for the flow

Making the assumption that the previously obtained result (2.30) holds between the start of the counterflow region and the first ventilation point, then the flow variables, Q_2, u_2 and g_2' may be calculated.

Eliminating u_2 and Q_2 from (2.17), (2.18) and (2.19), and substituting for h_2 and u_1 using (2.27), (2.30) and $u_* = u_1 - u_2$, gives an equation for g_2'

$$dg_2' = \left(\frac{Q_0}{d\omega}\right)^2 \left(\frac{2g_0'}{g_2'} - 1\right)^2. \tag{2.31}$$

Writing $g_2'/g_0' = \gamma_2$ then (2.31) may be rewritten

$$\gamma_2^3 - \frac{B^3}{4}(2 - \gamma_2)^2 = 0, \tag{2.32}$$

where

$$B^3 = \frac{4Q_0^2}{d^3\omega^2 g_0'}. \tag{2.33}$$

Equation (2.32) could be solved numerically, but a good approximation to the solution, for small B, is given by

$$\gamma_2 = B - \frac{B^2}{3}. \tag{2.34}$$

The corresponding approximate solutions for u_2, u_1, Q_2 and g_2, including the term of order B^2 in (2.34), are

$$u_2 = \frac{1}{2}\sqrt{dg_0'}B^{\frac{1}{2}}(1 + \frac{B}{3}) \simeq \frac{1}{\sqrt{2}}\sqrt{h_2 g_2'}, \tag{2.35}$$

$$u_1 = -\frac{1}{2}\sqrt{dg_0'}B^{\frac{1}{2}}(1 - \frac{2B}{3}) \simeq -\frac{1}{\sqrt{2}}\sqrt{h_2 g_2'}, \tag{2.36}$$

$$Q_2 = \frac{1}{2}\frac{Q_0}{B}(1 + \frac{B}{3}), \tag{2.37}$$

$$g_2' = g_0' B(1 - \frac{B}{3}). \tag{2.38}$$

Generally B is small and so the terms of order B^2 could be neglected. In this case, note also that the total volume flux of the outflowing buoyant layers, $2Q_2$, is considerably larger than that of the source. The reduced gravity of the buoyant outflow will be lower than that of the source by an equal factor (see equation (2.18)). As an illustrative example, with

typical experimental values $d = \omega = 10\,\text{cm}$, $Q_0 = 6.5\,\text{cm}^3\text{s}^{-1}$ and $g_0' = 63\,\text{cm}\,\text{s}^{-2}$, then the above solution gives $B = 0.03$, $Q_2 = 109.6\,\text{cm}^3\text{s}^{-1}$, $g_2' = 1.9\,\text{cm}\,\text{s}^{-2}$, $u_2 = 2.2\,\text{cm}\,\text{s}^{-1}$ and $u_1 = -2.1\,\text{cm}\,\text{s}^{-1}$ all of which are consistent with experimental measurements.

It should be pointed out that (2.35) and (2.36) are the dependencies that would be obtained in a simple dimensional analysis, but note that (2.37) and (2.38) imply that $Q_2 \sim Q_0^{\frac{1}{3}}$ and $g_2' \sim g_0'^{\frac{2}{3}}$ - the former in particular indicating that the variation in outflow characteristics is smaller than an appropriate variation in the source. Note also that the solution implies that the Richardson number (see equation (2.2)) has a value of approximately unity and is approximately independent of the source conditions. This would explain why negligible entrainment between the layers is observed in the experiments.

In the above solution, (2.35)-(2.38), it was assumed that the value of the parameter B is small. This is generally the case (in the experiments described in section 3, $B \ll 1$), however the behaviour of the solution to (2.32) for large B may also be considered.

The value of B may be increased (equivalent to increasing the flow rate or decreasing the reduced gravity of the source) and the value of the solution (2.32), γ_2, increases correspondingly. However when $B^3 = 4$ then the solution to (2.32) is $\gamma_2 = 1$, i.e. the reduced gravity of the buoyant outflow is equal to that of the source. In this case $Q_2 = Q_0/2$, $u_2 = Q_0/\omega d$ and $u_1 = 0$. Thus when $B^3 = 4$ the solution implies that there is zero entrainment into the primary cell. This is clearly a physically unrealistic situation, as $B^3 = 4$ is equivalent to having an enormous value for the jet-length ($B^3 = 4$ implies that $L_j = 8000d$ with the above typical experimental values, also assuming that the nozzle radius, $b_0 = 0.025\,\text{cm}$), and under such circumstances there would be considerable entrainment.

Increasing B further yields $\gamma_2 > 1$, a physically impossible result. It must therefore be concluded that the model may be applied to situations in which $B \ll 1$. Physically this states that the volume flux of the buoyant layer is sufficiently small to be easily transported as a gravity current (i.e. the model is appropriate). For large values of B, tests (Marshall & Cleaver 1991) with a source of natural gas in air have shown that the source fluid forms a 'plug', driving the air from the tunnel.

2.1.4 Flow with energy loss at the head

Benjamin (1968) extended his analysis to include the possibility of energy loss or supply. Equation (2.27) may be modified by including the head loss, ζ, giving

$$u_*^2 = 2g_2'(h_2 - \zeta). \tag{2.39}$$

The balance of flow forces is unaffected by the energy loss, so equating (2.24) and (2.28) gives

$$u_*^2 = dg_2', \tag{2.40}$$

and so

$$h_2 = \frac{d}{2} + \zeta. \tag{2.41}$$

Hence a flow with $h_2 > \frac{1}{2}d$ is possible with an energy loss ($\zeta > 0$) and a flow with $h_2 < \frac{1}{2}d$ implies an energy supply to the counterflow ($\zeta < 0$). The previous solutions for u_2, u_1, Q_2 and g_2' are modified accordingly. Equation (2.32) is modified to

$$\gamma_2^3 - \frac{B'^3}{4}[2 - \gamma_2(1 + 2\frac{\zeta}{d})]^2, \quad \text{where} \quad B' = \left(\frac{4Q_0^2 d}{(d^2 - 4\zeta^2)^2 w^2 g_0'}\right)^{\frac{1}{3}}. \tag{2.42}$$

Neglecting all but the largest terms, the modified approximate solutions are

$$u_2 = \frac{1}{2}\sqrt{dg_0'}B'^{\frac{1}{2}}(1 - 2\frac{\zeta}{d}),$$

$$u_1 = -\frac{1}{2}\sqrt{g_0' d}B'^{\frac{1}{2}}(1 + 2\frac{\zeta}{d}),$$

$$Q_2 = \frac{1}{2}\frac{Q_0}{B'},$$

$$g_2' = B' g_0'. \tag{2.43}$$

Note that $B' \geqslant B$ for all ζ and if the flow is not energy conserving, the flow rate Q_2 will be less than its value in (2.37) whereas the reduced gravity g_2' will be greater than in (2.38).

2.1.5 The effect of shear stresses

It was shown in section 2.1.1 by equation (2.16) that neglecting the shear stresses meant that the values of h_2, u_2 and u_1 remained constant over the length of the counterflow. By integrating the equations of motion (2.5) and (2.6) over each layer the effects of including the stresses (see Jirka & Harleman 1979 for the case with a free upper surface) may be determined.

Integrating (2.5) over the upper layer $\int_0^\omega dy \int_{h_2}^d dz$, and using (2.12) to substitute for u_1 gives

$$\frac{Q_1^2}{\omega^2(d - h_2)^3}\frac{dh_2}{dx} = -\frac{1}{\rho_a}\frac{dp_I}{dx} - g\frac{dh_2}{dx} - \frac{2\tau_{w_1}}{\omega\rho_a} - \frac{(\tau_i - \tau_t)}{(d - h_2)\rho_a} - \frac{\partial}{\partial x}(\overline{u'^2}), \tag{2.44}$$

where τ_i, τ_t and τ_{w_1} are the stresses at the channel interface, top and upper wall given by

$$\tau_i = -\rho_a \overline{u'w'} \mid_{z=h_2},$$

$$\tau_t = -\rho_a \overline{u'w'} \mid_{z=d},$$

$$\tau_{w_1} = -\rho_a \overline{u'v'} \mid_{y=0, z>h_2} .$$

Similarly integrating (2.6) across the lower layer $\int_0^{\omega} dy \int_0^{h_2} dz$, and using (2.11) to substitute for u_2 gives

$$-\frac{Q_2^2}{\omega^2 h_2^3}\frac{dh_2}{dx} = -\frac{1}{\rho_2}\frac{dp_I}{dx} - g\frac{dh_2}{dx} - \frac{2\tau_{w_2}}{\omega\rho_a} - \frac{(\tau_b - \tau_i)}{h_2\rho_a} - \frac{\partial}{\partial x}(\overline{u'^2}), \tag{2.45}$$

where τ_b and τ_{w_2} are the stresses at the channel bottom and lower wall given by

$$\tau_b = -\rho_a \overline{u'w'} \mid_{z=0},$$

$$\tau_{w_2} = -\rho_a \overline{u'v'} \mid_{y=0, z<h_2} .$$

Eliminating the interface pressure and using the Boussinesq approximation gives

$$\left(\frac{Q_2^2}{\omega^2 h_2^3} + \frac{Q_1^2}{\omega^2 (d-h_2)^3} - g_2'\right)\frac{dh_2}{dx} = \frac{1}{\rho_a}\left(\frac{(\tau_b - \tau_i)}{h_2} - \frac{(\tau_i - \tau_t)}{d-h_2} + \frac{2}{\omega}(\tau_{w_2} - \tau_{w_1})\right). \tag{2.46}$$

Thus (2.46) shows explicitly that the downstream change in h_2 is controlled by the shear stresses. Following Jirka & Harleman (1979), the shear stresses can be related to the mean flow quantities through the relationships

$$\tau_t = \frac{1}{8} f_t \rho_a u_1 \mid u_1 \mid, \quad \tau_i = \frac{1}{8} f_i \rho_a (u_2 - u_1) \mid u_2 - u_1 \mid, \quad \tau_b = \frac{1}{8} f_b \rho_a u_2 \mid u_2 \mid,$$

$$\tau_{w_1} = \frac{1}{8} f_{w1} \rho_a u_1 \mid u_1 \mid, \quad \tau_{w_2} = \frac{1}{8} f_{w2} \rho_a u_2 \mid u_2 \mid, \tag{2.47}$$

in which f_t, f_i, f_b, f_{w1} and f_{w2} are the Darcy-Weisbach friction coefficients which are independent of x.

The friction coefficients can be related to the Reynolds number, Re, with $f \sim Re^{-\frac{1}{4}}$, and so using the results of section 2.1.3, it may be estimated that $\mid dh_2/dx \mid = O(10^{-4})$. This is supported by experiment, with the observation that in an unventilated tunnel the depth h_2 remains almost constant (see figure 5*c*) along the length of the duct (except at the ends). Thus for all of the subsequent analysis it will be assumed that the effect of shear stresses (and consequent variations in h_2) can be ignored.

2.2 Counterflow with ventilation points

A typical ventilation system is shown schematically in figure 6*a*. The N ventilation points have area A_i ($i = 1...N$). Without the presence of a 'head' the analysis of 2.1.2 and 2.1.3 cannot be used and so it is assumed here that the flow has pre-set initial values for the flow variables h_2 etc.. In practice though, it is observed that the outflow maintains its initial depth of $d/2 + \zeta$ long after the fluid has flowed through a vent (or vents). Figures 6*b* and 6*c* are images from actual experiments showing the flow over a vent and the flow through a vent.

2.2.1 The volume flux through the vent

It has been shown (Linden, Lane-Serff & Smeed 1990) that the exchange flow Q of a buoyant fluid through a hole in a closed box containing buoyant fluid takes the form

$$Q \simeq kA\sqrt{g'h}, \tag{2.48}$$

where A is the area of the hole, g' is the reduced gravity, h is the depth of the buoyant fluid and k is a constant dependent on the shape and orientation of the hole. For a vertical square hole the value of k is approximately $k = 0.25$ with equal flow in and out of the hole. It is assumed that a similar relation holds in the present situation with the flow out of the first ventilation hole $q_{(1)}$ given by

$$q_{(1)} = k_1 A_1 \sqrt{g_2' h_{2(0)}}, \tag{2.49}$$

where k_1 is a constant and $h_{2(0)}$ denotes the initial value of h_2. As there is only outflow through the ventilation point it might be expected that the volume flux through it is double that for the separated flow, i.e. $k_1 \simeq 0.5$.

2.2.2 The flow over the vent

The flow over a ventilation hole is drawn schematically in figure 7 (compare with figure 6*b*). It is assumed that the fluid flowing past the hole has height $h_{2(1)}$ and reduced gravity g_2', i.e. that no mixing has taken place, and that the velocities of the lower and upper layers are $u_{2(1)}$ and $u_{1(1)}$ respectively.

Continuity of volume in the upper and lower layers then gives

$$\omega u_{1(0)}(d - h_{2(0)}) = \omega u_{1(1)}(d - h_{2(1)}), \tag{2.50}$$

$$\omega u_{2(0)} h_{2(0)} - q_{(1)} = \omega u_{2(1)} h_{2(1)}. \tag{2.51}$$

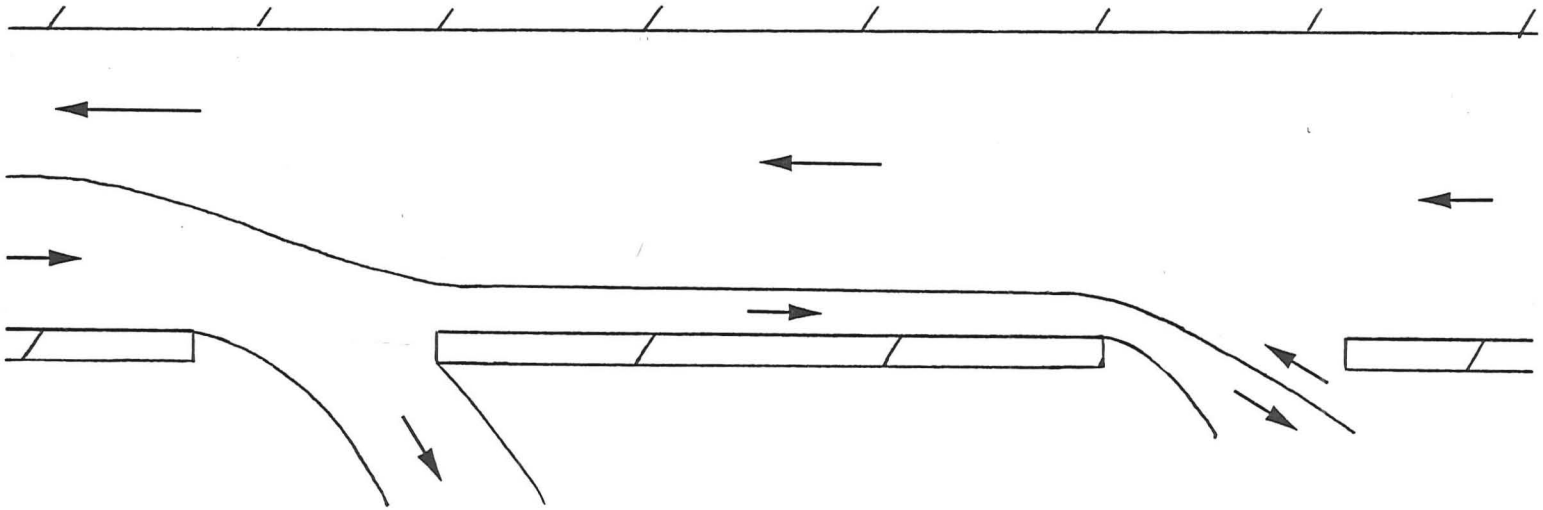

FIGURE 6 (*a*). A schematic diagram of a typical flow with ventilation points.

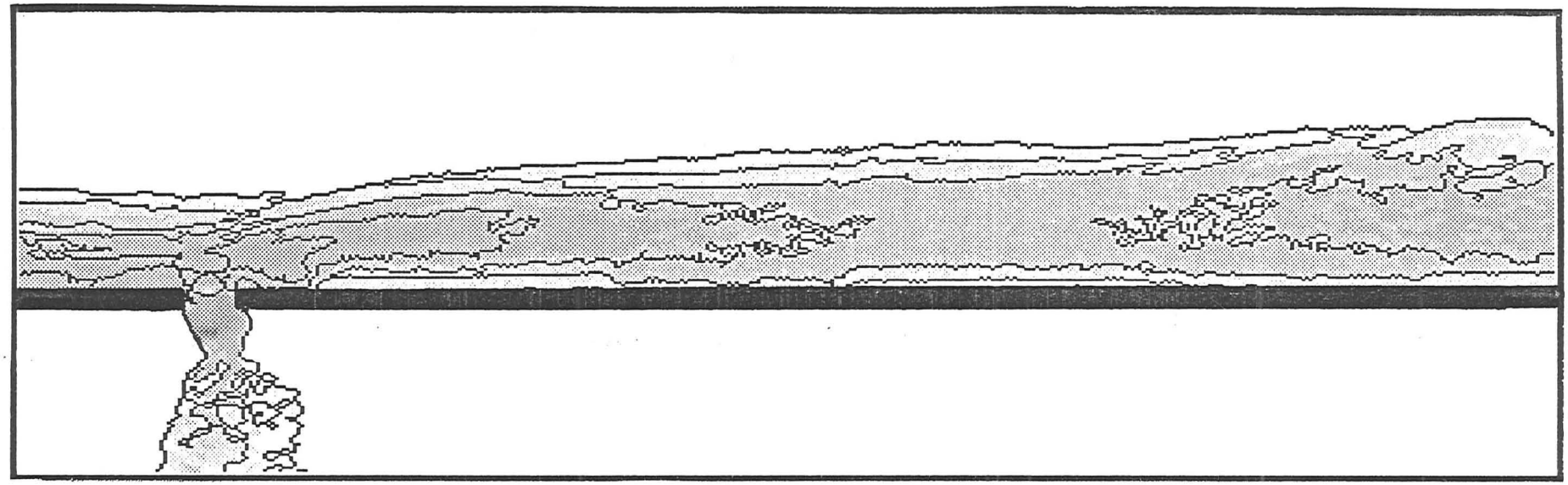

FIGURE 6 (*b*). An image taken from experiment showing the flow over a vent.

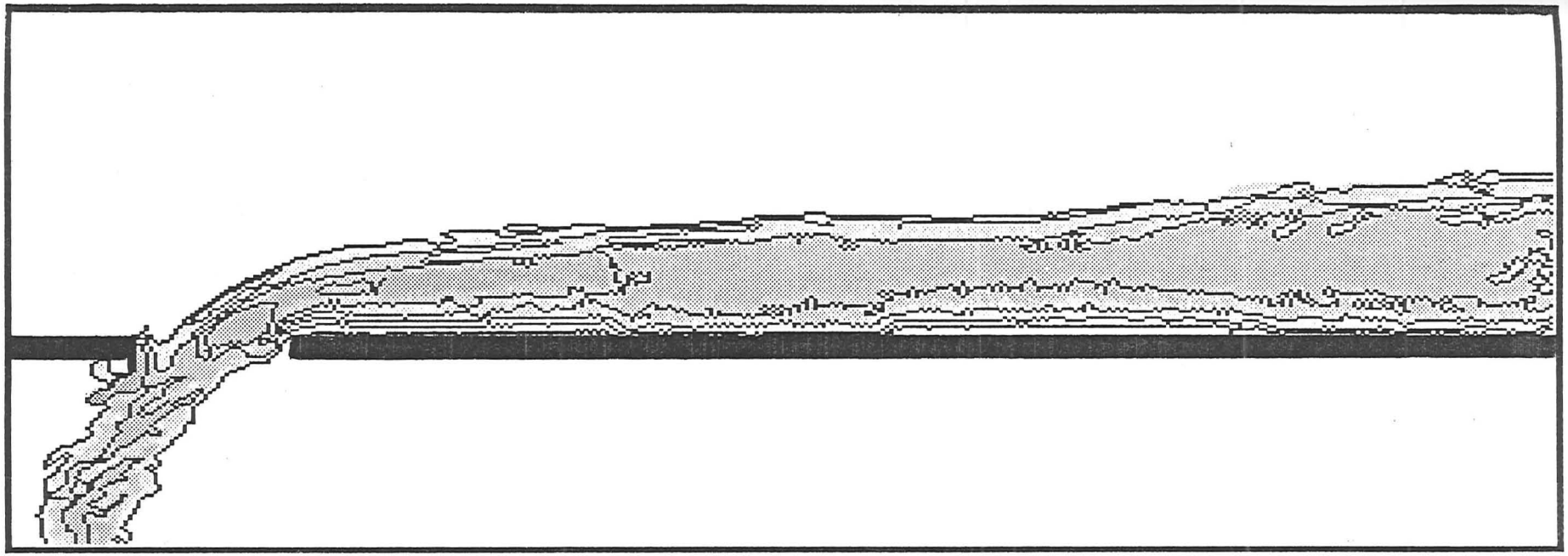

FIGURE 6 (c). An image taken from experiment showing the flow through a vent.

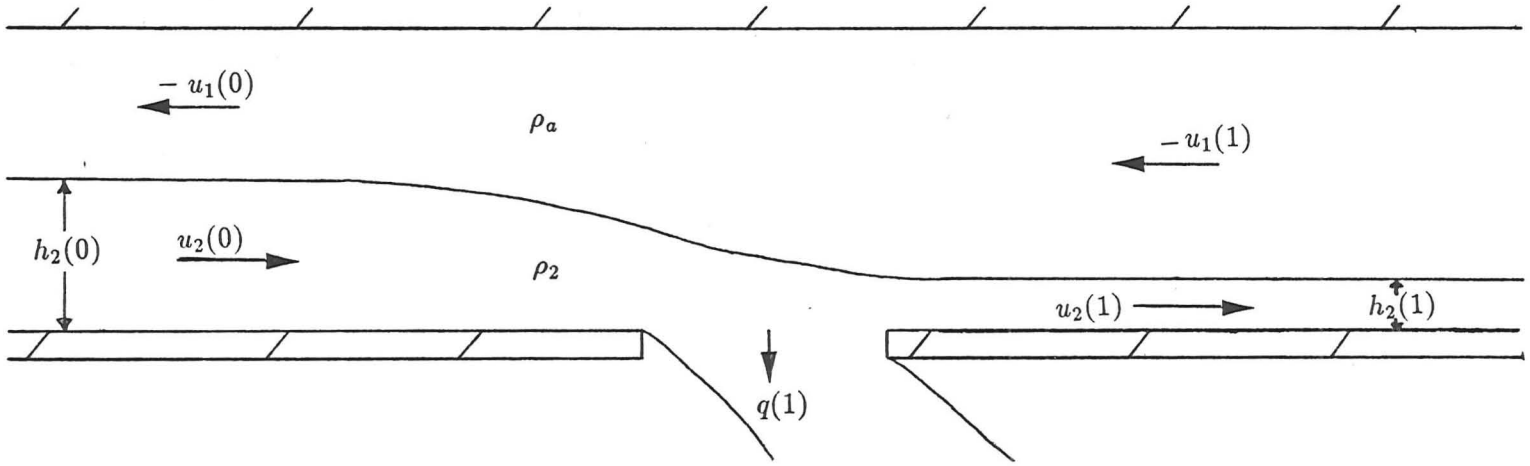

FIGURE 7. A schematic diagram of the flow over a vent.

Equation (2.15) may also be applied, giving

$$(u_{1(0)}^2 - u_{1(1)}^2) - \frac{\rho_2}{\rho_a}(u_{2(0)}^2 - u_{2(1)}^2) - 2g_2'(h_{2(0)} - h_{2(1)}) = 0. \tag{2.52}$$

Hence $u_{1(1)}$ and $u_{2(1)}$ may be eliminated giving an equation for $h_{2(1)}$,

$$u_{1(0)}^2 \left[\left(\frac{d - h_{2(0)}}{d - h_{2(1)}}\right)^2 - 1\right] = \frac{\rho_2}{\rho_a}\left[\left(\frac{\omega u_{2(0)} h_{2(0)} - k_1 A_1 \sqrt{g_2' h_{2(0)}}}{\omega h_{2(1)}}\right)^2 - u_{2(0)}^2\right] - 2g_2'[h_{2(0)} - h_{2(1)}]. \tag{2.53}$$

As an example, using the values obtained from the previous solution (2.43) with $\zeta = 0$ (i.e. no energy loss), $k_1 = 1/2$ and $A_1 = 64\,\mathrm{cm}^2$, equation (2.53) implies that $h_{2(1)} = 0.5\,\mathrm{cm}$, $u_{2(1)} = 4.3\,\mathrm{cm\,s^{-1}}$, $Q_{2(1)} = 2.2\,\mathrm{cm^3 s^{-1}}$ and $u_{1(1)} = -1.1\,\mathrm{cm\,s^{-1}}$. These values may be used to compute the maximum flow through the second vent (of the same area), $q_{(2)} = k_2 A_2 \sqrt{g_2' h_{2(1)}}$, which gives (if $k_2 = k_1$) $q_{(2)} = 28.0\,\mathrm{cm^3 s^{-1}}$. Since $q_{(2)} > Q_{2(1)}$, then with these values, only the first two ventilation points are needed to vent the buoyant fluid. So repeated application of (2.53) represents a method with which the number of ventilation points required for total ventilation of the buoyant layer can be calculated.

Equation (2.53) may be rewritten making use of the solution obtained in section 2.1.4 (2.43) for small ζ and the Boussinesq approximation giving

$$\left[\frac{(1 - 4\zeta'^2)}{1 - h_{2(1)}'}\right]^2 = \left[\frac{(1 - 4\zeta'^2) - 2\sqrt{2}k_1 A_1'(1 + 2\zeta')^{\frac{1}{2}}}{h_{2(1)}'}\right]^2 - 16[1 - 2h_{2(1)}'], \tag{2.54}$$

where

$$A_1' = \frac{A_1}{\omega d}, \quad h_{2(1)}' = \frac{h_{2(1)}}{d}, \quad \zeta' = \frac{\zeta}{d}. \tag{2.55}$$

This final equation shows that for a given inflow depth $h_{2(0)}$ (set by ζ'), the secondary outflow height $h_{2(1)}$ is dependent (to first order in B') only on the area of the opening. (Note that the secondary height is considered here rather than the secondary volume flux as it is easier to measure $h_{2(1)}$ in experiment.)

2.2.3 A ventilation point in the primary cell

It was mentioned earlier that a ventilation point in the primary cell region allows environmental fluid to be 'sucked' into the tunnel due to the drop in pressure associated with the

circulation. This flow is drawn schematically in figure 8*a*. Figure 8*b* is taken from experiment, the contour lines clearly showing the flow through the vent close to the source. If the volume flux of the inflowing environmental fluid into the primary cell is Q_p, then the equations of conservation of volume and mass flux become

$$\frac{1}{2}Q_0 + Q_p = Q_1 + Q_2, \tag{2.56}$$

$$\frac{1}{2}Q_0 g_0' = Q_2 g_2'. \tag{2.57}$$

It is expected that the velocity of the inflowing fluid is proportional to the exit velocity of the source. Thus an expression for Q_p may take the form

$$Q_p = k_p A_p \frac{M_0}{Q_0} f(\frac{x_p}{d}, \frac{g_c'}{g_0'}), \tag{2.58}$$

where A_p is the area of the opening, k_p is a constant, and $f(\frac{x_p}{d}, \frac{g_c'}{g_0'})$ is the functional dependence on the distance of the centre of the vent x_p from the source axis and on the mean reduced gravity within the primary circulation cell, g_c'.

Because of the increased volume flux entering the primary cell, the volume flux of the outflow is expected to increase similarly.

Adopting the solution given by (2.39)-(2.41) and using the new conservation equations above it is possible to derive an equation analogous to (2.32)

$$\gamma_2^3 = \frac{B'^3}{4}(2 - P\gamma_2)^2, \qquad \text{where} \qquad P = (1 + 2\frac{Q_p}{Q_0})(1 + 2\zeta'). \tag{2.59}$$

The value of $P \geqslant 1$ can be large which makes it hard to find a general approximate solution to (2.59) but a satisfactory approximation (a quadratic fit) is given by

$$\gamma_2 = B'\left[1 - \frac{5}{16}PB' + \frac{2}{41}P^2B'^2 + \cdots\right] \qquad \text{for} \qquad 0 \leqslant PB' \leqslant 2 \qquad \text{with} \qquad g_2' = \gamma_2 g_0'. \tag{2.60}$$

Of more significance to the problem of venting the buoyant fluid is the new value of the outflow rate. This is given by

$$Q_2 = \frac{Q_0}{2\gamma_2} \simeq \frac{Q_0}{2B'}\left[1 + \frac{5}{16}PB' + \cdots\right], \tag{2.61}$$

and the velocities are given by

$$u_2 = \frac{1}{2}\sqrt{dg_0'}B'^{\frac{1}{2}}(1 - 2\zeta')\left[1 + \frac{5}{16}PB' + \cdots\right], \tag{2.62}$$

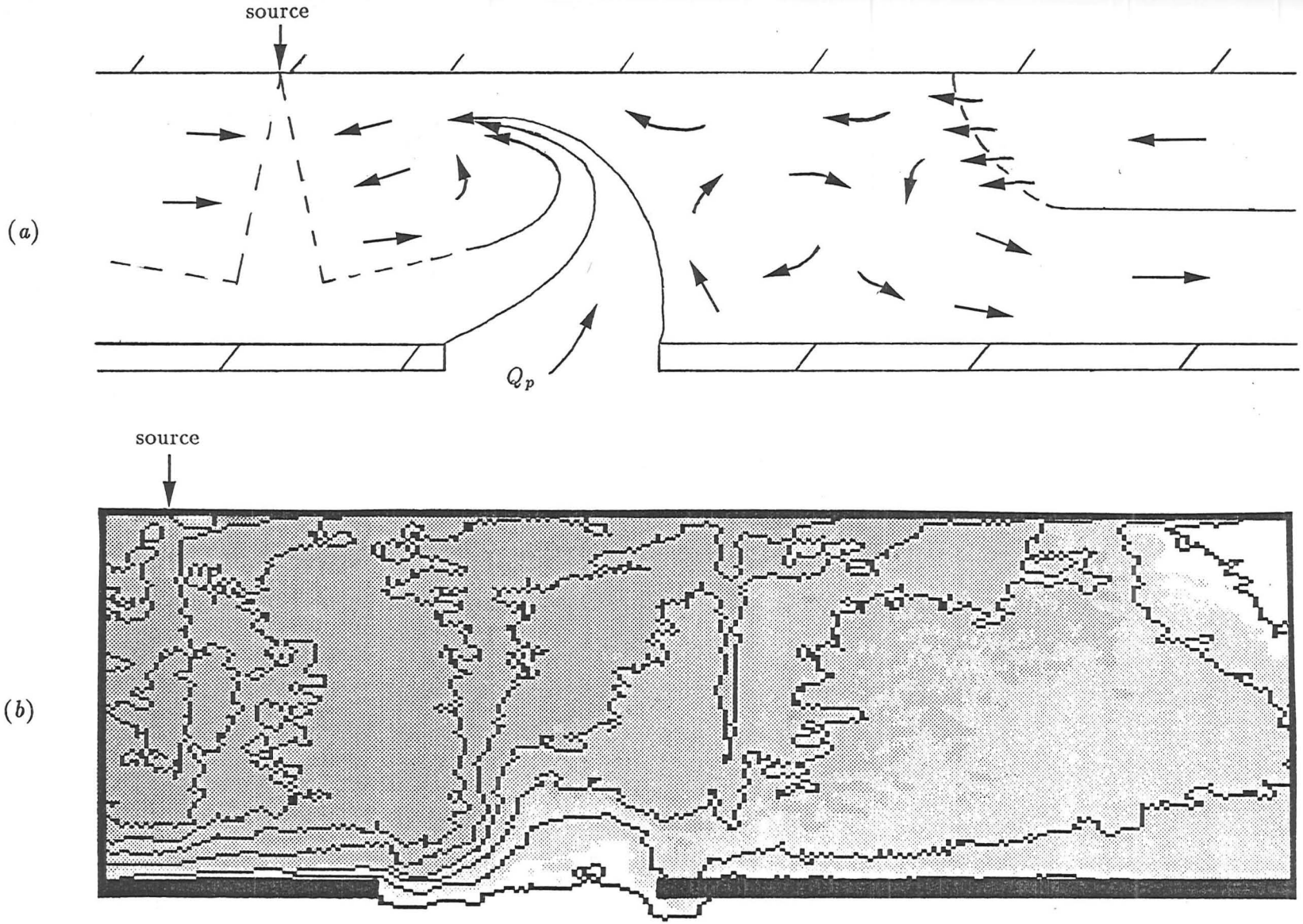

FIGURE 8. The flow with a vent in the primary cell; (a) a schematic diagram, and (b) an image taken from experiment.

$$u_1 = -\frac{1}{2}\sqrt{dg_0'}B'^{\frac{1}{2}}(1+2\zeta')\left[1+\left(\frac{5}{16}-\frac{15}{16(1+2\zeta')}\right)PB'+\cdots\right]. \qquad (2.63)$$

From these expressions it can be seen that the inflow Q_p is not merely reflected in an equal increase in the outflow Q_2, but that Q_2 increases by approximately $5Q_p/16$ only (for large Q_p), with the inflowing velocity u_1 decreasing significantly to compensate. Thus the system is able to adjust to cope with relatively large volumes of environmental fluid being sucked into the primary cell, with quantitatively smaller changes to Q_2, g_2' and u_2. Following the example values of section 2.1.3, with an inflow $Q_p = 100\,\mathrm{cm^3 s^{-1}}$ and taking $\zeta' = 0$, the solution above gives $Q_2 = 145.4\,\mathrm{cm^3 s^{-1}}$ - an increase of about 33%. The reduced gravity decreases to $g_2' = 1.4\,\mathrm{cm\,s^{-2}}$, and the layer velocities are now $u_2 = 2.9\,\mathrm{cm\,s^{-1}}$ and $u_1 = -0.9\,\mathrm{cm\,s^{-1}}$. The increase in Q_2, and the decrease in g_2', may mean that a larger number of vents are needed to vent the buoyant layer. This is observed in experiment.

2.2.4 A ventilation point in region 2

This is probably the most complex problem resulting from ventilation because a vent in the mixing region 2 will allow fluid to flow both in and out of the tunnel.

Initially there is little buoyancy of the fluid inside the tunnel and so environmental fluid may be sucked in by the circulating fluid in the primary cell. However with increasing time the buoyancy of the fluid inside the tunnel increases causing an increasing resistance to the outflow. Eventually the buoyancy forces may become larger than the suction forces and buoyant fluid will flow out of the ventilation point.

2.3 The concentration build-up in the primary cell

It has already been stated that the concentration within the primary cell increases to a steady state maximum, this being due to the re-entrainment of buoyant fluid into the jet and the eventual balance between the buoyancy forces of the mixed region and the opposing inertial and frictional forces of the counterflow system.

Recall that in the central region there may be both outflowing buoyant fluid and inflowing ambient fluid as well as the source. The high 'jet length' of the source means that the source fluid and any inflowing environmental fluid are very rapidly mixed throughout the primary cell, and so it is not inappropriate to consider the *mean* reduced gravity g_c' of the fluid within the primary cell, which is assumed to have length l.

Suppose the buoyant fluid layer has volume flux $Q_2(g_c')$. The equation for conservation of

volume flux (2.13) will still apply, but the equation for conservation of mass (2.18) is modified to

$$\frac{dg_c'}{dt} = \frac{1}{l\omega d}\left(\frac{1}{2}Q_0 g_0' - Q_2(g_c')g_c'\right), \tag{2.64}$$

and hence (2.18) is satisfied when $dg_c'/dt = 0$. This is the equation governing the concentration build-up within the primary cell, clearly dependent on the nature of the function $Q_2(g_c')$.

A first order form for $Q_2(g_c')$ may be found by observing that (2.43) and (2.17) imply that

$$Q_2(g_c') \sim \sqrt{g_c'}. \tag{2.65}$$

Writing

$$Q_2(g_c') = \frac{1}{2}Q_0 g_0' \beta g_c'^{\frac{1}{2}}, \tag{2.66}$$

for convenience, equation (2.64) then becomes

$$\frac{dg_c'}{dt} = \frac{Q_0 g_0'}{2l\omega d}(1 - \beta g_c'^{\frac{3}{2}}). \tag{2.67}$$

Also, assuming that in the limit $t \to \infty$ then $g_c' \to g_2'$, then the parameter β may be found using (2.60)-(2.63)

$$\beta = \frac{\omega d^{\frac{3}{2}}(1 - 4\zeta'^2)}{2g_0' Q_0}\left[1 + \frac{15}{32}PB' + \cdots\right], \tag{2.68}$$

recalling that $P = 1$ if there is no vent in the primary cell, and that B' is small (as long as ζ' is small). With the typical experimental values given in section 2.1.3, $\beta = 0.39$. Equation (2.67) has solution

$$-\frac{1}{3}\ln\left(\frac{(1-\eta)^2}{1+\eta+\eta^2}\right) - \frac{2}{\sqrt{3}}\arctan\left(\frac{2\eta+1}{\sqrt{3}}\right) + \frac{2\pi}{6\sqrt{3}} = \frac{Q_0 g_0' \beta^{\frac{2}{3}}}{2l\omega d}t, \quad \text{where } \eta = \beta^{\frac{1}{3}} g_c'^{\frac{1}{2}}, \tag{2.69}$$

which will be compared with experiment.

In practice, however, it is observed that in the steady state $g_c' > g_2'$ due to the dilution of the mixed fluid in region 2 by the incoming ambient fluid. Thus the above analysis must be modified appropriately, writing

$$g_2'(t) = \kappa g_c'(t) \qquad \text{and} \tag{2.70}$$

$$\frac{dg_c'}{dt} = \frac{1}{l\omega d}\left(\frac{1}{2}Q_0 g_0' - Q_2(g_2'(t))g_2'(t)\right), \tag{2.71}$$

where the notation $g_2'(t)$ is used to denote the mean reduced gravity of the outflow before the steady state value given in equation (2.60) has been reached. The constant $\kappa \leqslant 1$ is representative of the increased dilution of the buoyant outflow compared with the mean concentration of the central region. Equation (2.66) must also be modified, with Q_2 now dependent on g_2' rather than g_c' and so

$$Q_2(g_2') = \frac{1}{2}Q_0 g_0' \beta g_2'^{\frac{1}{2}} = \frac{1}{2}Q_0 g_0' \beta \kappa^{\frac{1}{2}} g_c'^{\frac{1}{2}}. \tag{2.72}$$

Hence the time dependence of g_c' is now given by

$$\frac{dg_c'}{dt} = \frac{Q_0 g_0'}{2l\omega d}(1 - \beta\kappa^{\frac{3}{2}} g_c'^{\frac{3}{2}}). \tag{2.73}$$

The exact solution is the same as before, (2.69), except that now $\eta = (\kappa^{\frac{3}{2}}\beta)^{\frac{1}{3}} g_c'^{\frac{1}{2}}$. This will be compared with experiment measuring the mean primary cell concentration and the mean outflow concentration to compute κ. Equation (2.73) can be written in the form

$$\frac{d\tilde{g}_c'}{d\tilde{t}} = \kappa(1 - \tilde{g}_c'^{\frac{3}{2}}), \tag{2.74}$$

where

$$\tilde{g}_c' = (\beta^{\frac{2}{3}}\kappa) g_c' \qquad \text{and} \qquad \tilde{t} = \beta^{\frac{2}{3}} \frac{Q_0 g_0'}{2l\omega d} t. \tag{2.75}$$

Equations (2.74) and (2.75) are the form of (2.73) that will be used in the comparison with experimental data as it is easier to obtain $\tilde{g}_c'$ than g_c' using digital video analysis. Note that the maximum value of $g_c'(t)$ is given by

$$g_c' = \frac{1}{\kappa\beta^{\frac{2}{3}}}. \tag{2.76}$$

The time dependent solution for g_c', (2.69), and the corresponding solution for g_2', (2.70), could be used to calculate time dependencies for all of the other flow variables (by using (2.72),(2.17) and (2.19)). However, it will be shown that the steady state is reached rapidly in practice and thus the steady state solution, (2.35)-(2.38), is likely to be of greater use.

3. Experiments

The experiments were carried out in a Perspex tunnel of width and depth 10 cm and length 210 cm (see figure 9*a*). The base of the tunnel consisted of seven slats of length 30 cm in which there were either one or two ventilation holes of area 64 cm^2 in which stoppers could

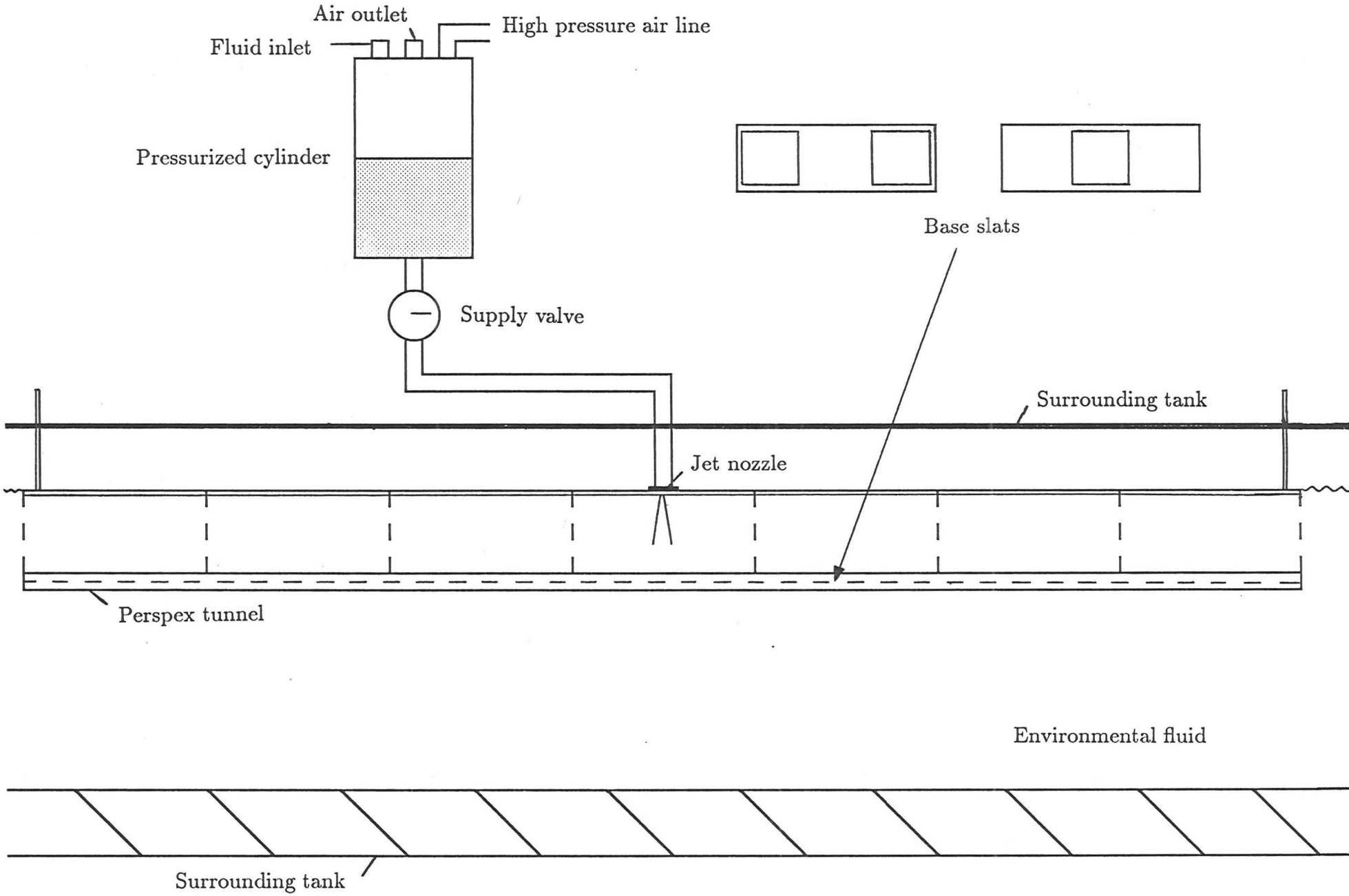

FIGURE 9(*a*). The experimental apparatus.

be placed. Vertical aluminium dividers could be used to vary the length of the tunnel, or to open or close the ends. Except when examining the effect of ventilation points, all the vents were closed and the ends of the tunnel were open. The Perspex tunnel was placed in a tank of length 9.4 m, depth 47 cm and width 26 cm. The tank was then filled with water until the surface was at the same height as the top of the tunnel. The water was allowed to settle for at least an hour before each experiment.

The outflow of buoyant fluid was represented by a solution of salt water. A small amount of dye (food colouring) was added to the salt solution and the flow visualised using the shadowgraph technique (see chapter 1). The dyed salt solution was introduced into the tunnel using a fine circular nozzle of radius 0.25 mm supplied by a brass cylinder which was constantly connected to a high pressure air supply, ensuring steady flow rates of up to 7.5 cm^3s^{-1}. Source reduced gravities of up to 65 cm^2s^{-1} were used.

The primary objectives of the experiments were:

i) to observe the flow and check the solution (2.43), testing the dependence of Q_2 and g_2' on the source flow rate, Q_0;

ii) to measure the increase of the concentration in the primary cell with time;

iii) to measure the variation in the secondary outflow height $h_{2(1)}$ with vent area A_1 in order to check equation (2.54);

iv) to measure the increase in Q_2 and the decrease in g_2' and g_c' with a vent in the primary cell.

3.1 Video Analysis

By recording the experiments on video tape, digital video analysis can be used to calculate mean source concentrations along lines perpendicular to the walls of the tunnel. This is a satisfactory way of measuring concentrations in this problem as the flow is two dimensional in the counterflow, and in the primary cell only mean values are needed for comparison with the theory.

It was explained in chapter 1 that the video picture is divided up into a grid of pixels each with an intensity (from 0, black to 255, white) dependent on the dye concentration. An image of the initial state of the apparatus is removed by division to allow for variations in the background illumination. An experiment was performed to investigate the variation of pixel intensity value with dye concentration in which a small quantity of dye was progressively

added to a perspex box of initially fresh water. The box was placed in the same surrounding tank that held the model of the tunnel and was illuminated in the same way. The average digital intensity over the whole box was measured using video analysis after each addition of dye and the measurements are plotted in figure 9*b*. This experiment confirms that the dye/intensity relationship is linear for sufficiently low dye concentrations. So by making one density measurement at a specific point in the flow from a fluid sample (using the Paar density meter) and comparing it to the intensity value there, it is easy to calculate the density/intensity relationship.

The intensity corresponding to zero dye is 255 and so if the intensity at the test point is I_t, and the test density is ρ_t then the density at a given point with intensity I is given by

$$\rho = \frac{255 - I}{255 - I_t}\rho_t. \tag{3.1}$$

In practice several measurements were made by hand, periodically taking samples from the flow, and were compared with the digitally calculated values to check the reliability of the video analysis measurements. Good consistency was found in all cases.

4. Results

Four sets of experiments were carried out, with the objectives described in section 3. The experiments are described first, and then the theoretical predictions are compared with the observations.

4.1 The flow and its dependence on the source flow rate

The flow was initially observed using the shadowgraph technique. Figures 10*a*-10*f* show the time development of a typical, unventilated run. Notice particularly the development of the gravity current, with the outflow occupying approximately half the depth of the tunnel.

In general, the flow was symmetric for symmetric configurations of vents (see figure 4) and in such 'perfect' conditions, the outflow occupied half the depth of the tunnel, in agreement with (2.30) (to $\pm 0.05d$). As was pointed out in section 2, this type of situation appears to be unstable and occasionally the flow became permanently asymmetric, with the outflow on one side of the source occupying a much larger depth and the outflow on the other side occupying a lesser depth. These cases were in the minority however, and are thought to be the result of initial imbalances in the temperature between the ends of the tunnel, producing a slight bias

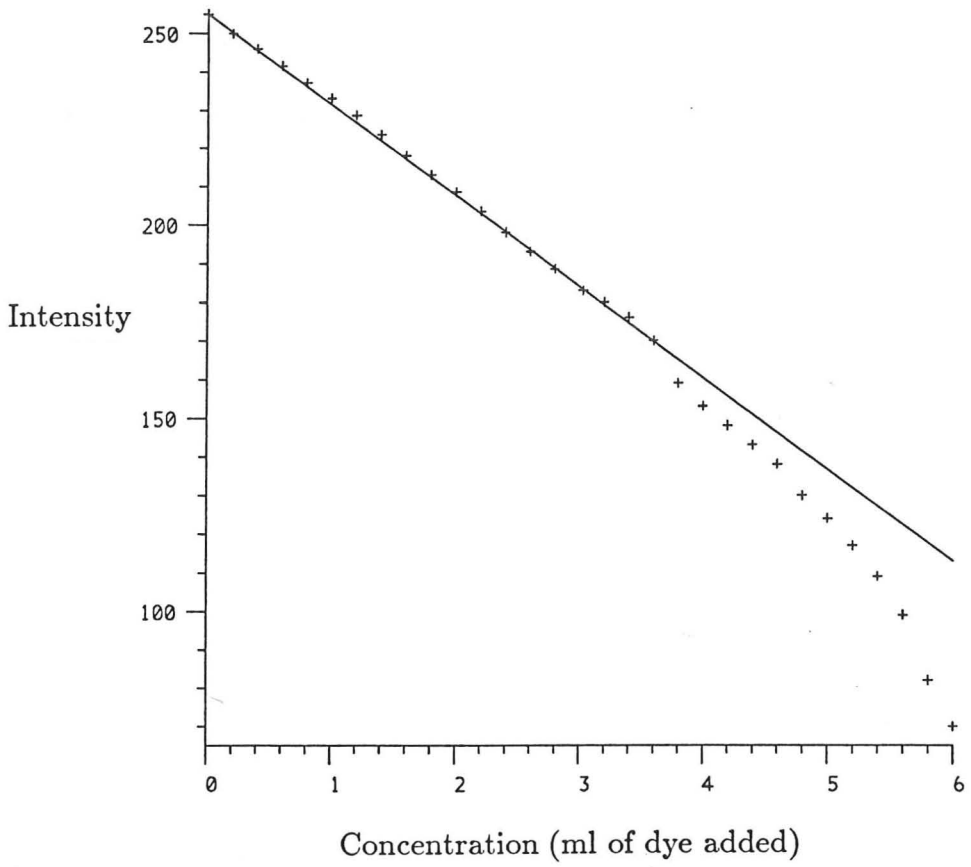

FIGURE 9(*b*). The variation of the average intensity with the dye concentration in a calibration experiment. Mean pixel intensities were measured by digital analysis of a video tape of an experiment in which dye was slowly added to a perspex box filled with initially fresh water.

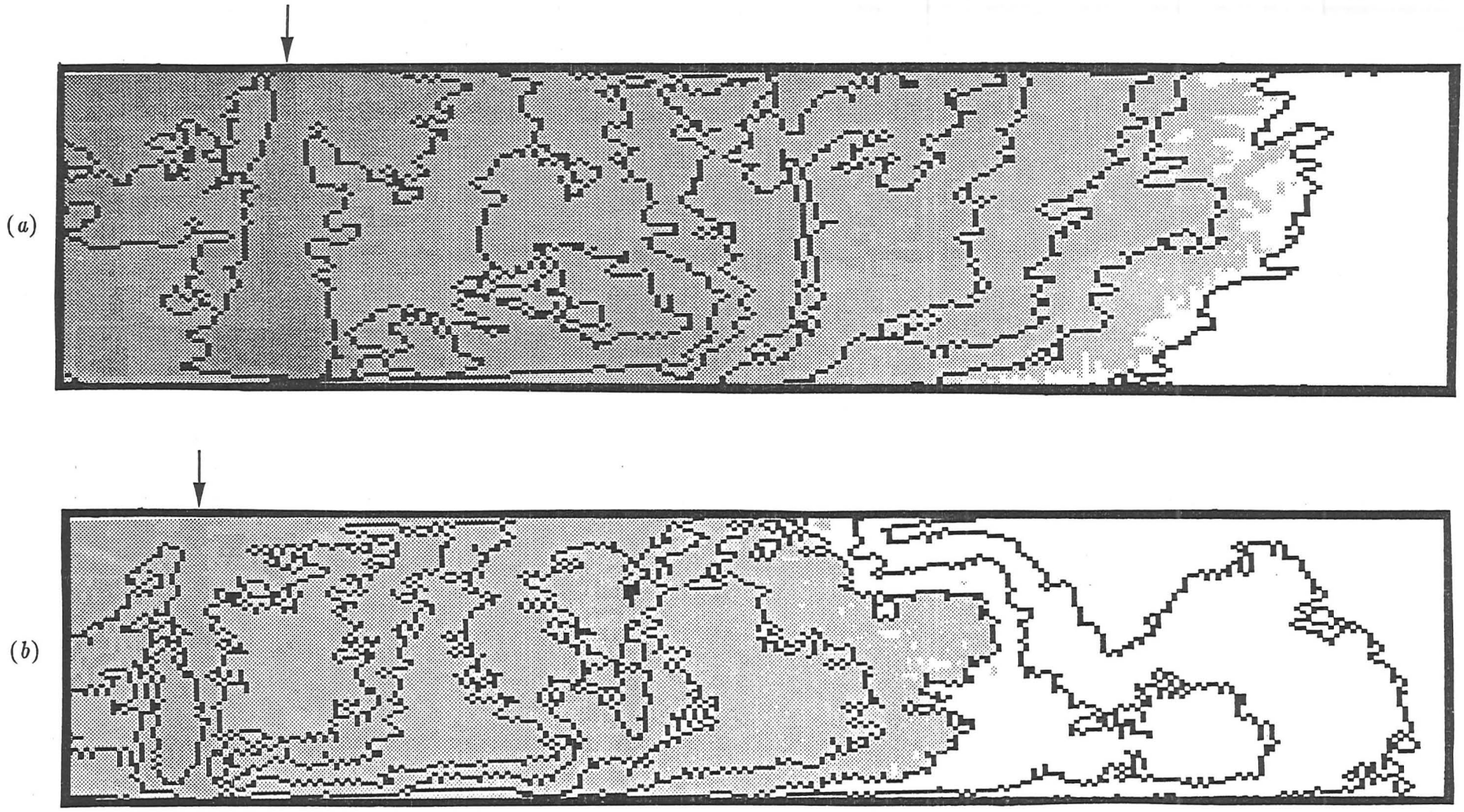

FIGURE 10. Images showing the initial development of the flow: (*a*) $t = 10s$, (*b*) $t = 20s$, (*c*) $t = 30s$, (*d*) $t = 40s$, (*e*) $t = 50s$ and (*f*) $t = 100s$.

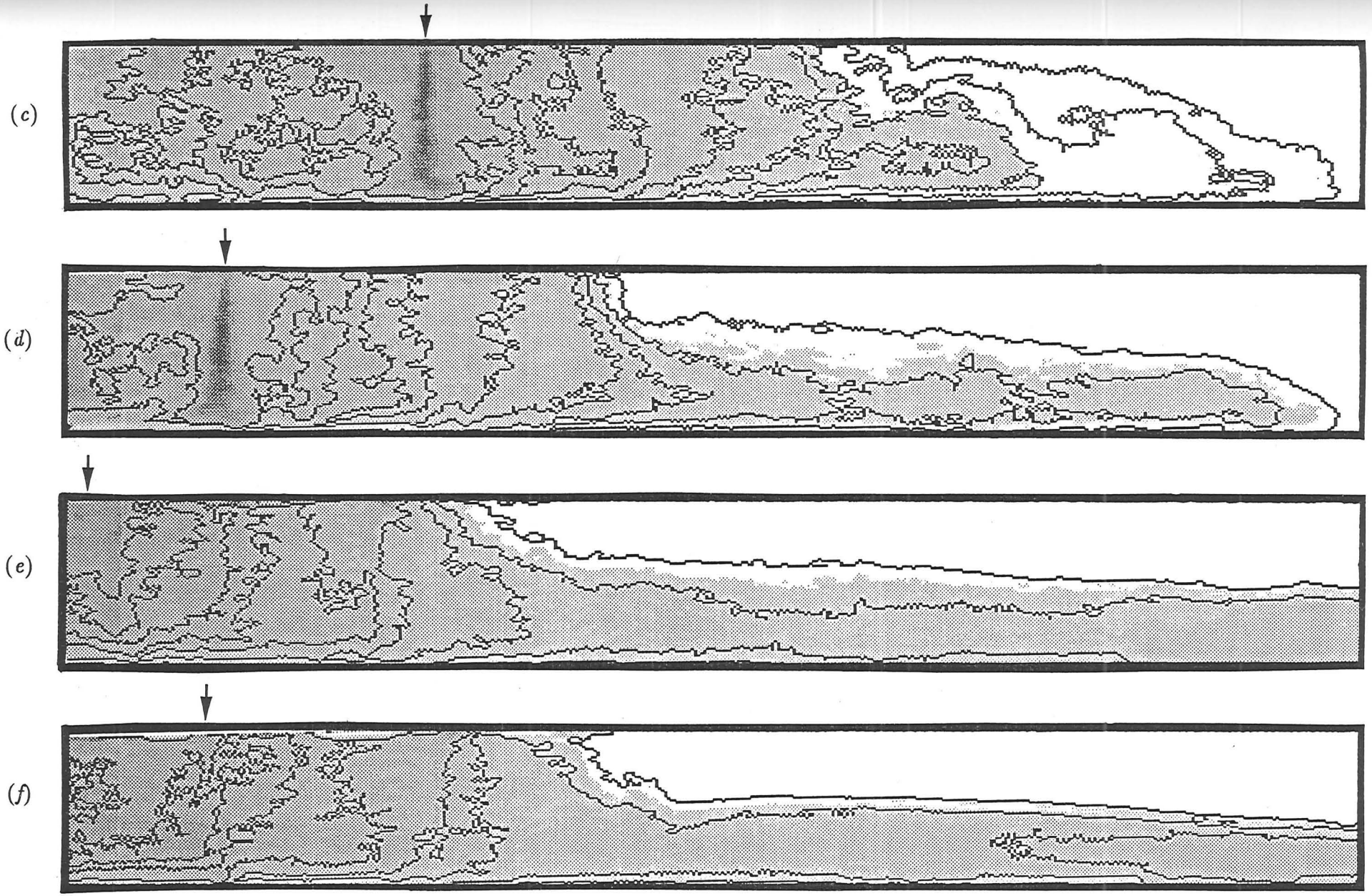

FIGURE 10 ct'd. Images showing the initial development of the flow: (*c*) $t = 30s$, (*d*) $t = 40s$, and (*e*) $t = 50s$, (*f*) $t = 100s$.

on the flow within it. After large time periods this initial small asymmetry may be amplified producing a larger asymmetry in the flow. Under good conditions, then, the predictions for the bulk flow can be checked.

Experiments were carried out to test the dependence of u_2 and g_2' on the source flow rate Q_0. The source flow was altered by changing the pressure in the brass chamber, the valve on which ensures constant pressure and hence constant flow rate. For each setting of the pressure, the flow was allowed to develop to a steady state before measurements were taken. The value of g_0' was kept constant.

It was found that a minimum source flow rate was required to maintain the flow system of section 2, i.e. the input of momentum below this threshold was insufficient to mix the fluid to the extent assumed in the analysis. At the threshold it was found that the ratio of jet length to tunnel depth, δ, was

$$\delta = \frac{L_j}{d} = 2.9,$$

i.e, although $\delta > 1$ in all of the experiments, for the system to contain a well mixed recirculating central region, $\delta \geqslant 2.9$ is required.

The outflow velocities were measured by injecting a small volume of green dye into the outflow and measuring the time taken for the dye patch to travel a distance of 30 cm along the tunnel. There was little mixing within the buoyant outflow and so the dispersion of the dye patch was minimal, particularly for the lower source rates. The measurements were taken some distance away from the point of injection so that then the patch was moving at the same speed as the outflow. Samples were also taken from the outflow, each time from the same place in the flow.

For each experiment the velocity was measured several times for each source flow rate. The average velocity values for each experiment and source flow are plotted in figure 11*a* and the average of the averages in figure 11*b*. Equation (2.62) predicts that $u_2 \sim Q_0^{\frac{1}{3}}$ and so u_2^3 is plotted against Q_0 here. A good linear relationship is seen in figure 11*b*. It should be pointed out that the theory of section 2 is concerned with an *average* velocity over the whole depth of the outflow. However, in practice it was observed that the velocity of the fluid decreases near to the interface. Thus, as the *fastest* moving fluid was generally measured in the experiments, it is expected that the experimental values will be higher than the theoretical ones. This is indeed the case, the experimental values being approximately 16% higher.

The values of g_2' were calculated from the samples using a Paar density meter (see chap-

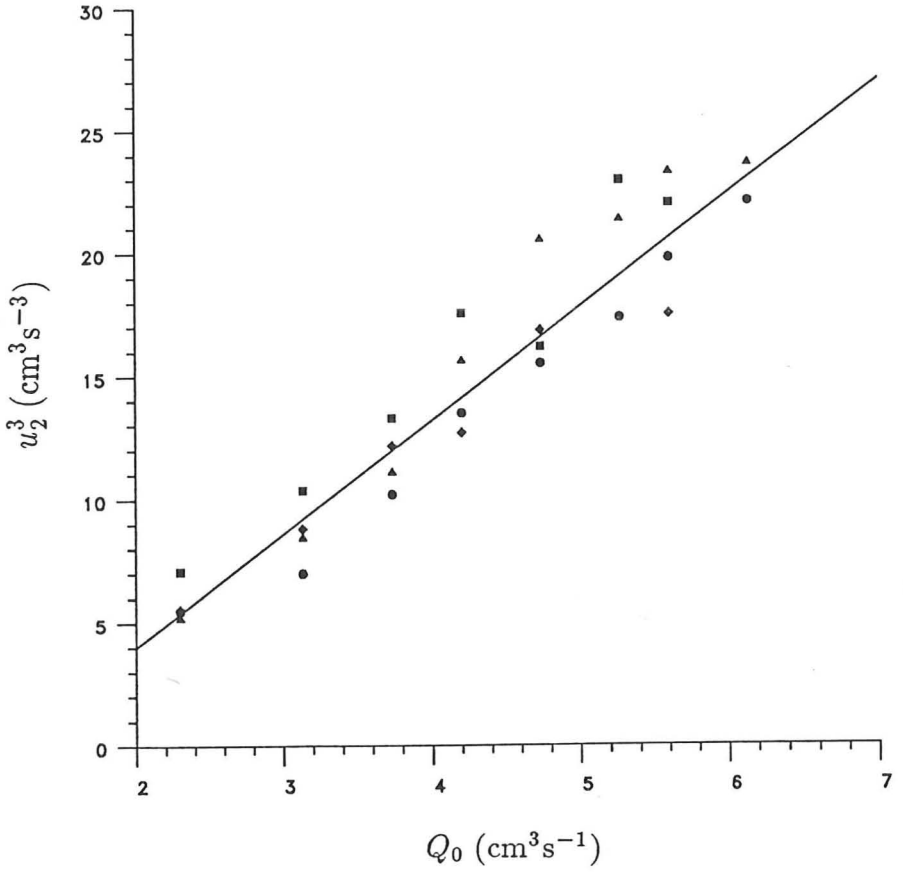

FIGURE 11*a*. The variation of the outflow velocity u_2 with source flow rate Q_0.

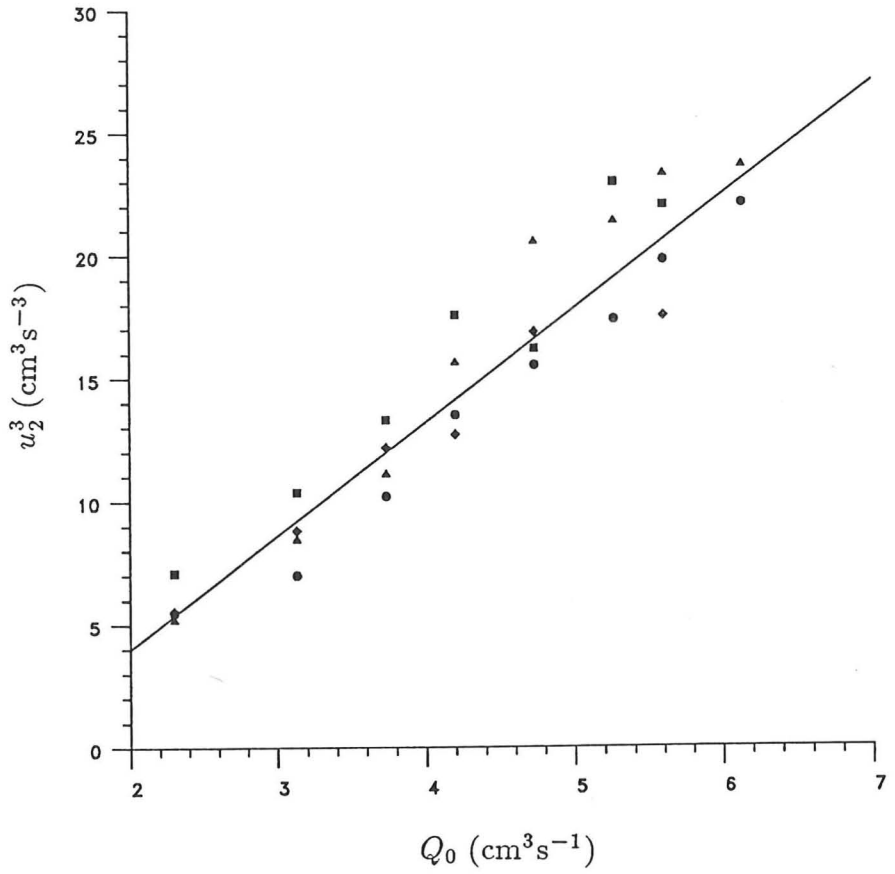

FIGURE 11*a*. The variation of the outflow velocity u_2 with source flow rate Q_0.

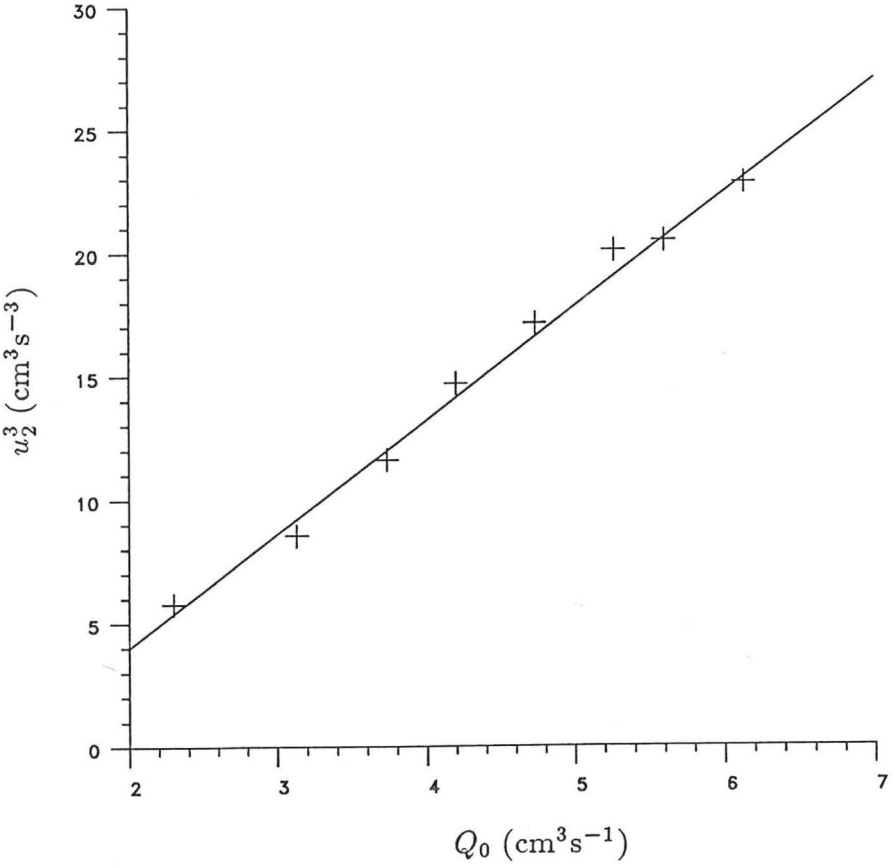

FIGURE 11*b*. The variation of the outflow velocity u_2 with source flow rate Q_0 - mean values.

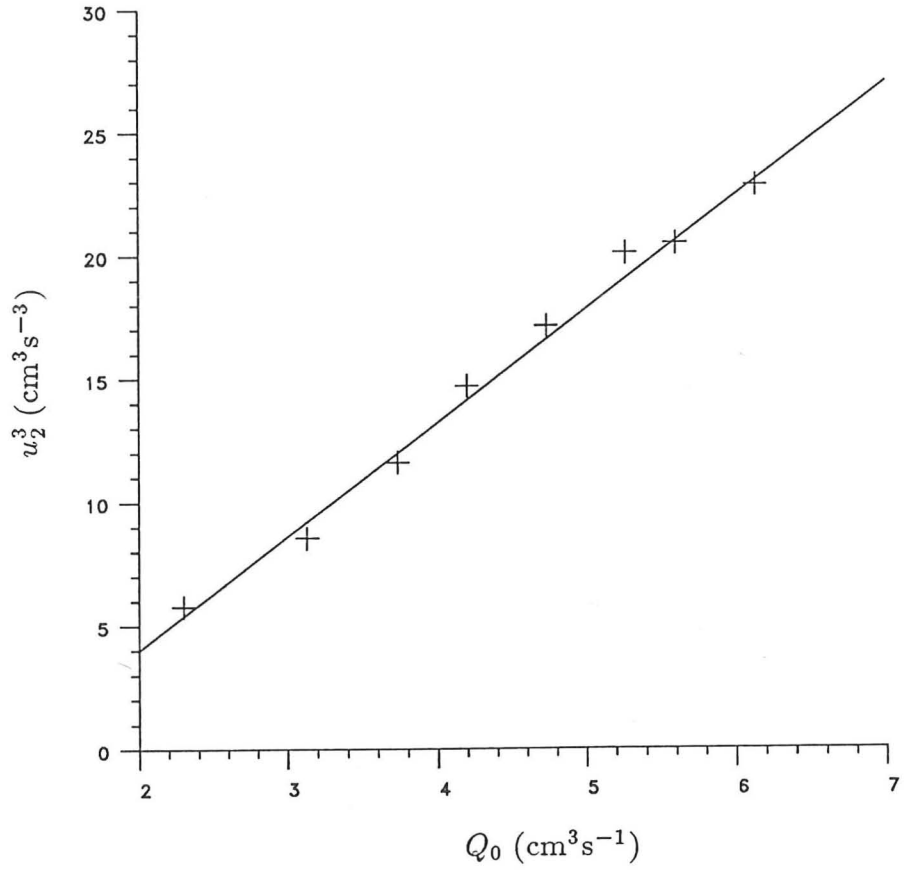

FIGURE 11*b*. The variation of the outflow velocity u_2 with source flow rate Q_0 - mean values.

ter 1). The theory predicts that $g_2' \sim Q_0^{\frac{2}{3}}$ and so in figure 12, $g_2'^{\frac{3}{2}}$ has been plotted against Q_0. Again a good linear relationship is observed although there is some variation in values between experiments. This may be due to slight variations in the depth of the outflow, or the position at which measurements were taken within it.

4.2 The concentration of the primary cell

Figure 10*d* is a typical freeze-frame of the flow, showing concentration contours. The contour gradients are small close to the source, indicating that this region is well mixed with the gradient steepening with distance through the turbulent mixing region in the range $1.5d - 2.5d$ from the source, the fluid becoming more diluted by the incoming environmental fluid. Compare this with figure 8*b* which is the flow observed when there is a vent within the primary cell. The environmental fluid being sucked in is clearly visible in figure 8*b*, as shown by the accompanying distortion in the contours.

To analyse the flow, frames were taken from the video every 10 s, the background removed, and the dye intensities calculated by digital analysis. The mean primary cell concentration was calculated by averaging the intensities over a section of the tunnel of length $l = 2.5d$, with one edge on the axis of the source, the same section being used for each experiment. The data was put into the appropriate form and compared with equation (2.74).

The data and the solution to (2.74) with $\kappa = 0.9$ are plotted in figure 13. The agreement with the theoretical curve is excellent although there is some scatter about the equilibrium state, possibly due to fluctuations in the entrainment flow of the ambient layer into the primary cell. This choice of κ is reasonable, agreeing with initial test measurements of g_2' and g_c' from which κ may be calculated using (2.70). The transition to equilibrium takes place over a relatively short time, usually within two minutes in these experiments.

4.3 The flow over a vent

The third objective of the experimental study was to measure the dependence of the secondary outflow height following flow over a vent, on the area of the vent. In this section, the experimental investigation is limited to vents at a sufficiently large distance away from the source so that they are in the counterflow region.

The source was switched on and the flow allowed to reach equilibrium. A large vent far from the source was then made by sliding one of the base slats along to make a vent of

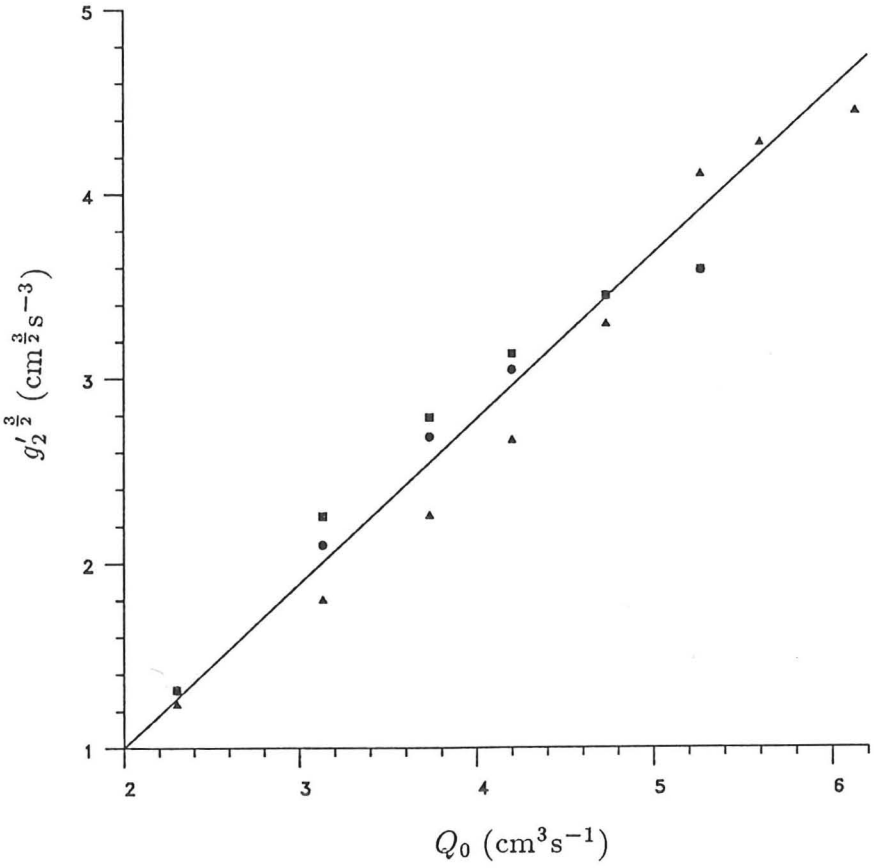

FIGURE 12. The variation of g_2' with Q_0.

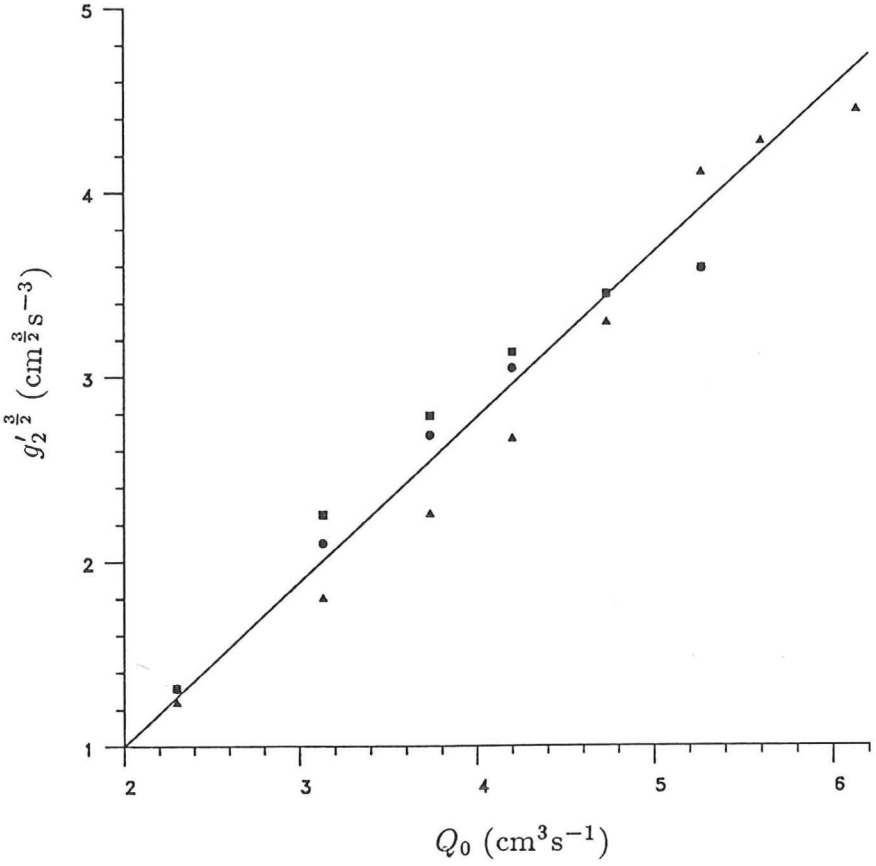

FIGURE 12. The variation of g_2' with Q_0.

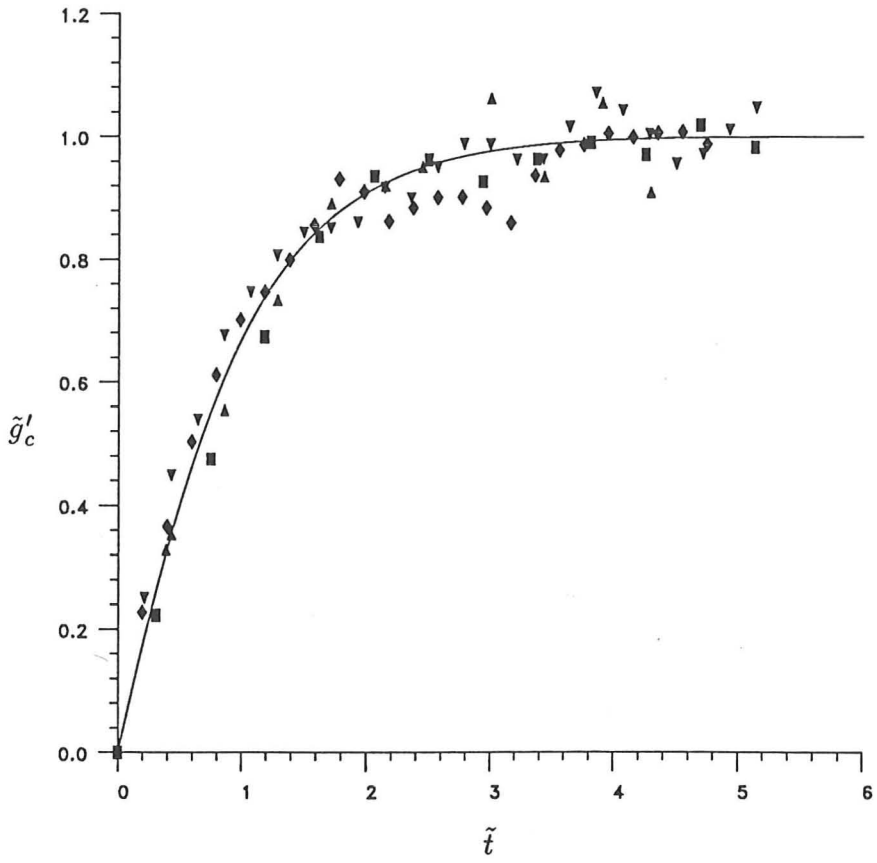

FIGURE 13. The time dependence of the primary cell concentration. Comparison between the experimental data, and the theoretical curve of (2.74) with $\kappa = 0.9$.

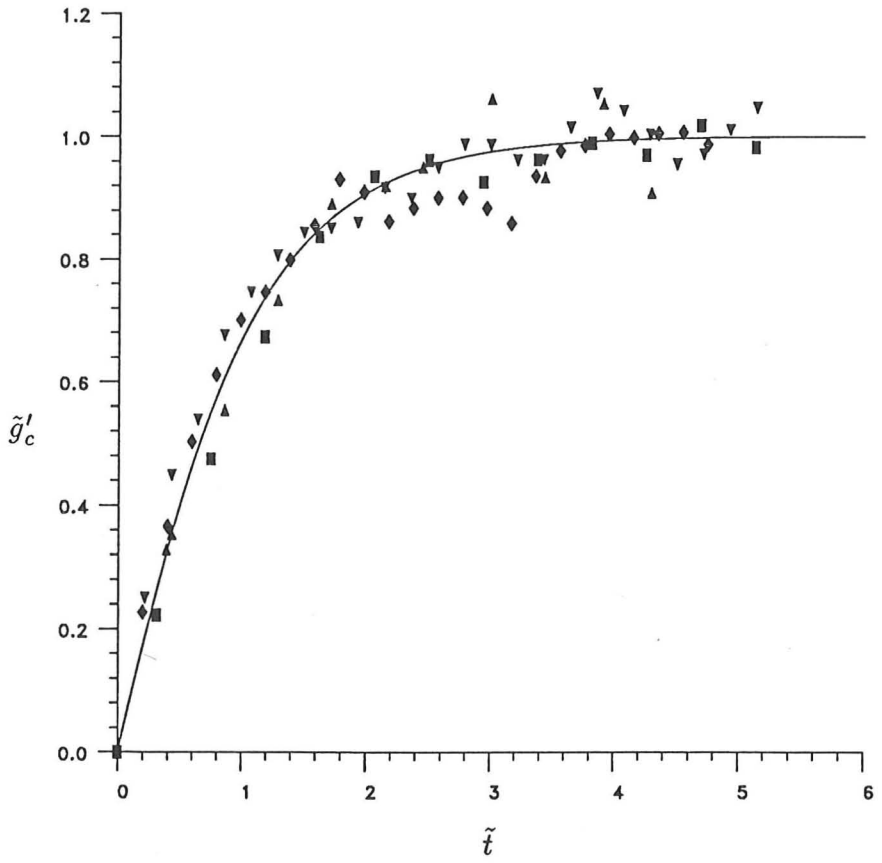

FIGURE 13. The time dependence of the primary cell concentration. Comparison between the experimental data, and the theoretical curve of (2.74) with $\kappa = 0.9$.

sufficiently large area for all the outflow to be easily vented by this single hole.

The vent was then closed by slowly pushing the slat back to its original position in small steps, recording the secondary outflow height at each stage. Of particular importance is the minimum size of hole required to vent all the fluid - this will enable the calculation of the constant k in (2.54). In practice the measurement of $h_{2(1)}$ proved difficult due to the presence of a layer of mixed fluid between the outflowing layer and the inflowing environmental fluid. This layer was formed as a result of random fluctuations in the outflow overshooting and undershooting the vent when calculating k. Hence the secondary outflow height measured was that of *moving* fluid only.

The data is plotted in dimensionless form in figure 14, together with the theoretical curve of (2.54). The agreement is good although there is some degree of scatter with the large error bars reflecting the difficulty of measurement, particularly for vents of larger areas.

The mean value of k measured using the above method was found to be $k = 0.51 \pm 0.03$, in good agreement with the prediction of section 2.2.1.

4.4 The effect of a vent in the primary cell

The final set of experiments were carried out with a single vent placed symmetrically either side of the source, and close to it, together with a vent some distance from the source so that the effect of the large inflow of environmental fluid sucked in through the near vents could be calculated.

It was predicted in section 2.2.3 that the outflow rate Q_2 would rise by a value of approximately $21Q_p/62$, where Q_p is the volume flux sucked in through each vent: the changes in u_2, u_1 and g_2' are given in equations (2.62), (2.63) and (2.60). From (2.48) it can be seen that the minimum value of area A_m required to vent all the outflow is given by

$$k\sqrt{h_2 g_2'} A_m = Q_2. \tag{4.1}$$

Applying the results of section 2.1.3 shows that in an unventilated tunnel A_m is approximately constant with value

$$A_m = \frac{d\omega(1 - 4\zeta'^2)}{\sqrt{8(1 + 2\zeta')k}}. \tag{4.2}$$

With the experimental values used here, this has a value of $A_m = 69.1\,\mathrm{cm}^2$ which explains why two vents (of area $64\,\mathrm{cm}^2$) were needed to vent all the buoyant outflow even with the

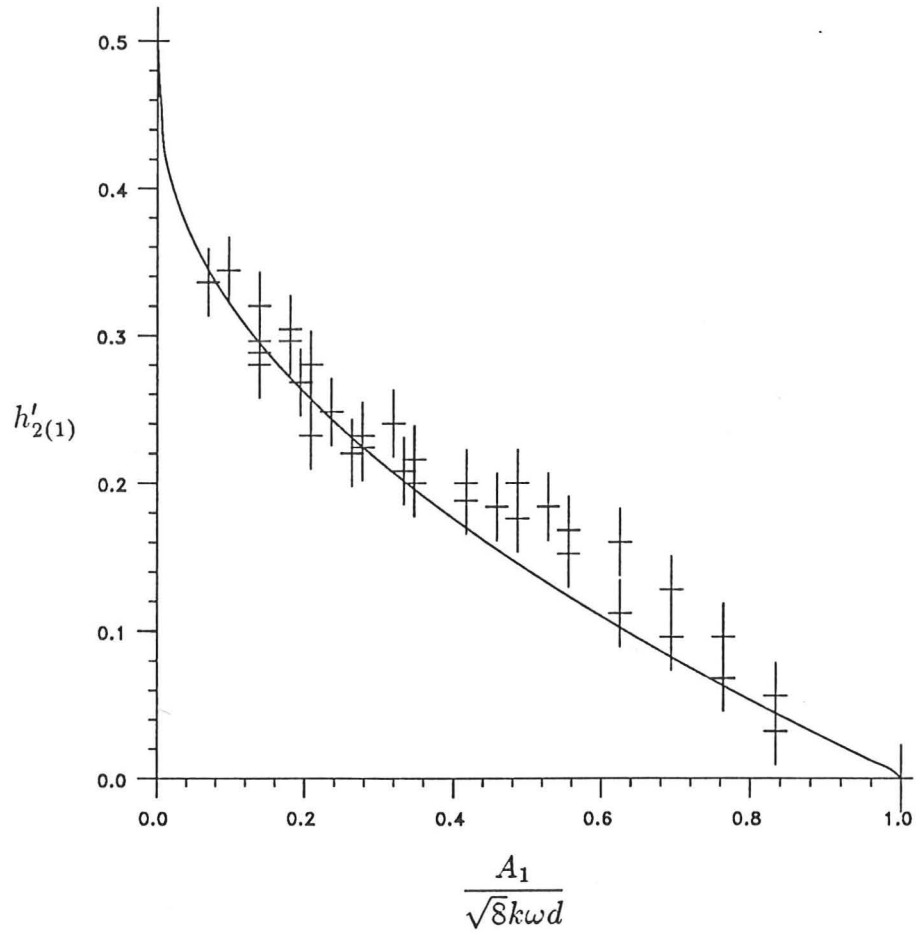

FIGURE 14. The variation of the secondary outflow height with vent area. Comparison between the experimental data and the theoretical curve of (2.54).

lowest source flow rates. However, with a vent in the primary cell this is modified to

$$A_m = \frac{d\omega(1-4\zeta'^2)}{\sqrt{8(1+2\zeta')k}}\left[1+\frac{15}{32}PB'+\cdots\right], \tag{4.3}$$

from (2.60) and (2.61). Equations (2.59) and (2.42) may be used to calculate A_m, finding that now A_m is greater than before. The *increase* in A_m as a result of opening the vent in the primary cell is approximately given by (assuming that $Q_p \gg Q_0$)

$$A_{increase} = \frac{15Q_p\omega^{\frac{1}{3}}}{2^{\frac{29}{6}}kQ_0^{\frac{1}{3}}g_0'^{\frac{1}{3}}}. \tag{4.4}$$

Hence by measuring the increase in A_m, the value of the primary cell inflow Q_p may be calculated. This is assuming that the analysis of 2.2.3 is correct, of course.

It can be checked, however, by testing its implications. As supposed in equation (2.58) it is expected that Q_p is proportional to the velocity of the impinging jet fluid flowing over the vent, and this in turn is expected to be proportional to the exit velocity of the source. Thus it is expected that $Q_p \sim Q_0$ and the increase in A_m will vary as $A_{increase} \sim Q_0^{\frac{2}{3}}$.

Experiments were performed to test this result using a single vent either side of the source. The source flow rate was increased in intervals whilst keeping the area of the vents near to the source constant. A further vent at a large distance from the source was then opened to a large extent by sliding the base slats apart. The slats were then slowly closed until a point was reached at which further closure would mean that not all the buoyant layer was vented by that single vent. The area of the vent is then A_m.

The experimental data points for several experiments are plotted in figure 15, and exhibit the linear relationship between $A_{increase}$ and $Q_0^{\frac{2}{3}}$ described above. This provides satisfactory evidence that the theory and assumptions of section 2.2.3 are valid, although further research is required to test the dependence on the source velocity in equation (2.58), and to determine the nature of the function $f(x_p, g_c')$ (although the dependence on x_p could be estimated by analysis of an impinging jet flow).

4.5 Further experimental observations

In addition to the experiments performed to make the measurements described above, some further experiments were also carried out in a general investigation of other factors (which have not been discussed previously) that might affect the flow.

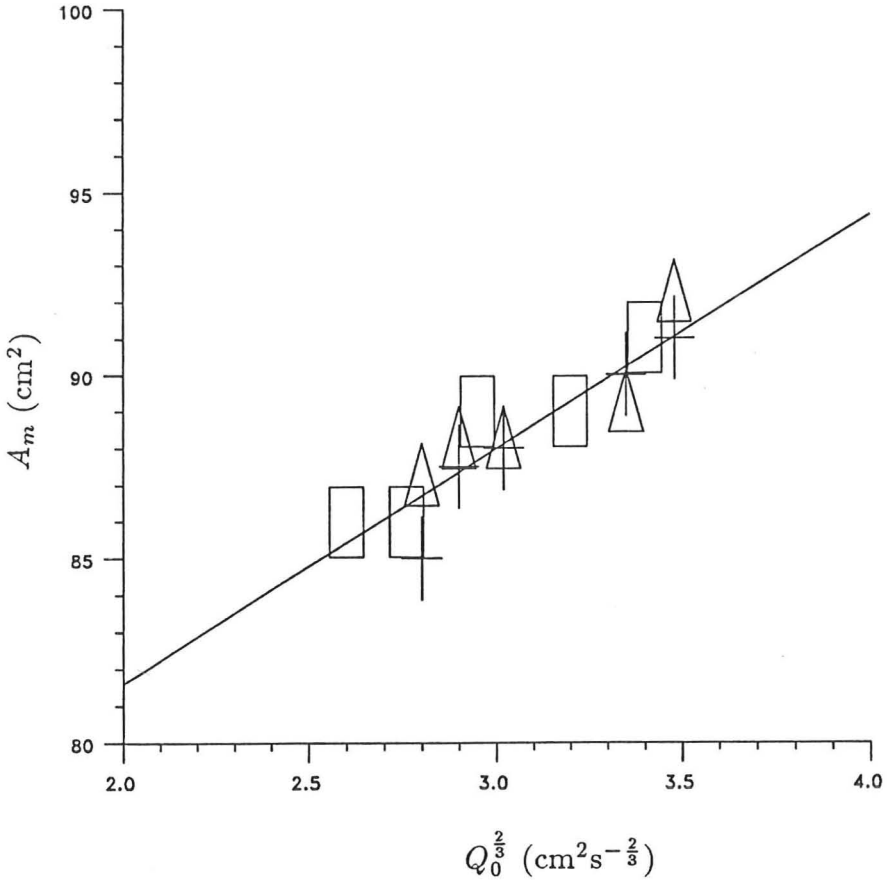

FIGURE 15. The variation of A_m with Q_0.

4.5.1 The effect of closing the ends of the tunnel

All of the above experiments were performed with the ends of the tunnel open. Some investigative experiments were conducted in order to examine the effect of closing the ends on the flow.

Closing the ends of the tunnel was observed to have negligible effect except when:

i) there were only a small number of vents or

ii) the source was near to an end of the tunnel.

In the former case, there may not be sufficient vent area to vent the buoyant layer and also allow unrestricted flow into the tunnel from the environment. The buoyant layer may not then be fully vented before it reaches the ends of the tunnel. However, the ends of the tunnel are closed and so fluid entering the tunnel from the environment flows through the vents furthest from the source (rather than through the ends as before). Thus there is competition for these far vents between the remaining buoyant layer fluid (which wants to flow out) and the environmental fluid (which wants to flow in). The buoyant layer is continuously supplied by the central mixed region which is also continuously entraining uncontaminated fluid from the environment. In practice some of the buoyant layer escapes through the furthest vent but the remainder mixes with the incoming environmental fluid, contaminating the inflow layer (see figure 16*a*).

In the latter case there may be little or no ventilation between the source and the nearest closed end. The concentrations within this region and the primary cell will now reach higher values than before as now all of the buoyant fluid flows out in a single buoyant layer (see figure 16*b*). In the equilibrium state this flow should be analytically equivalent to that of section 2 with a source of volume flux $2Q_0$.

4.5.2 Asymmetric vent configurations

In the analysis of section 2 and the experiments above the vents were assumed to be symmetrically placed about the source. Some experiments were conducted with the vents asymmetrically placed.

Vent asymmetry was observed to be of little importance when all of the vents are outside of the central mixed region: the positions of the vents in the counterflow has no effect on the central region and so the volume flux of the buoyant layer is the same on either side of the source (see figure 17*a*). However, if there is a vent in the primary cell on one side of the source but not on the other, then there is an increased volume flux into the former side (due

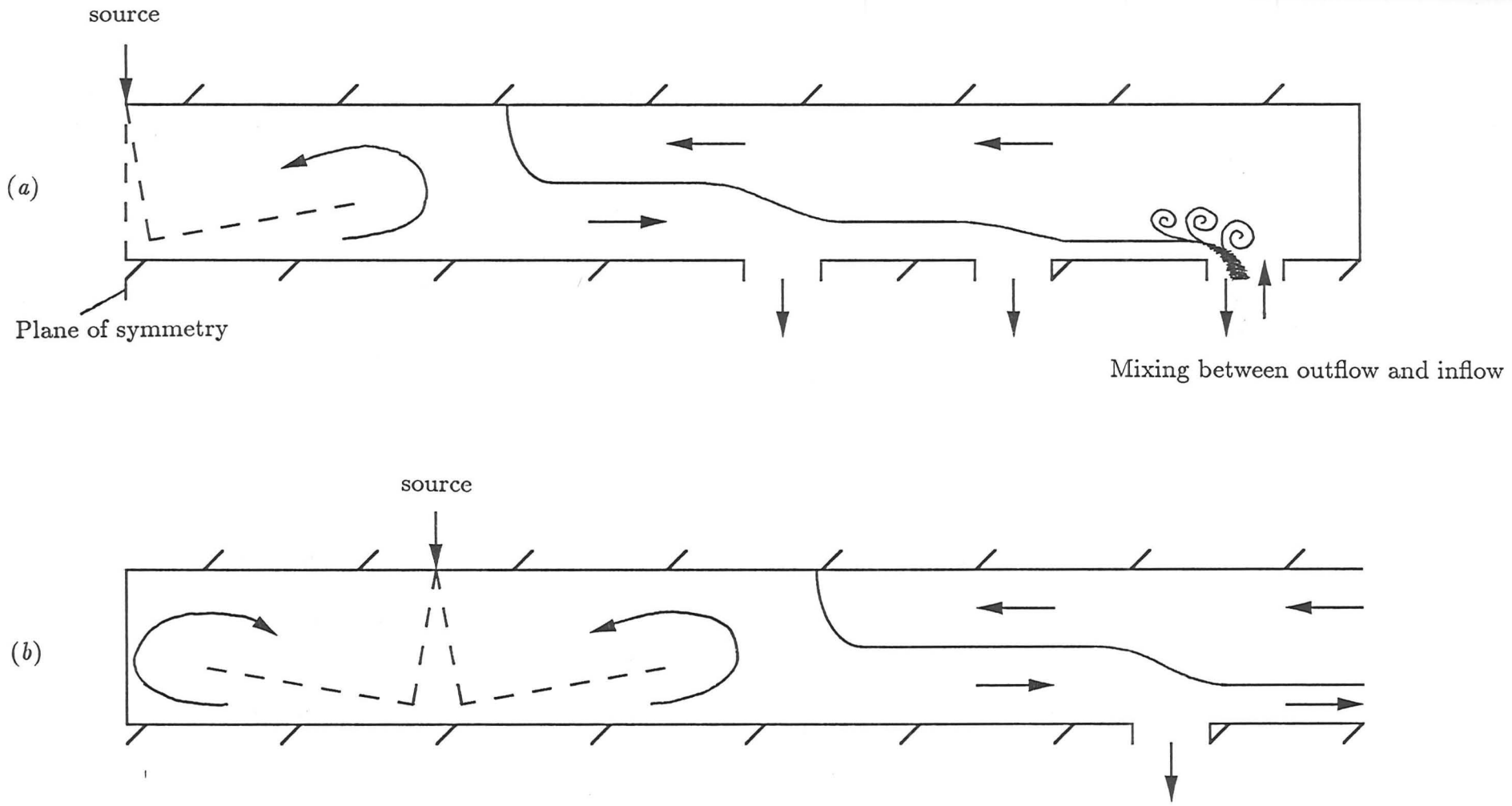

FIGURE 16. The effect of closing the ends of the tunnel on the flow; (*a*) the flow when there is insufficient vent area; (*b*) the flow when the source is near to an end of the tunnel.

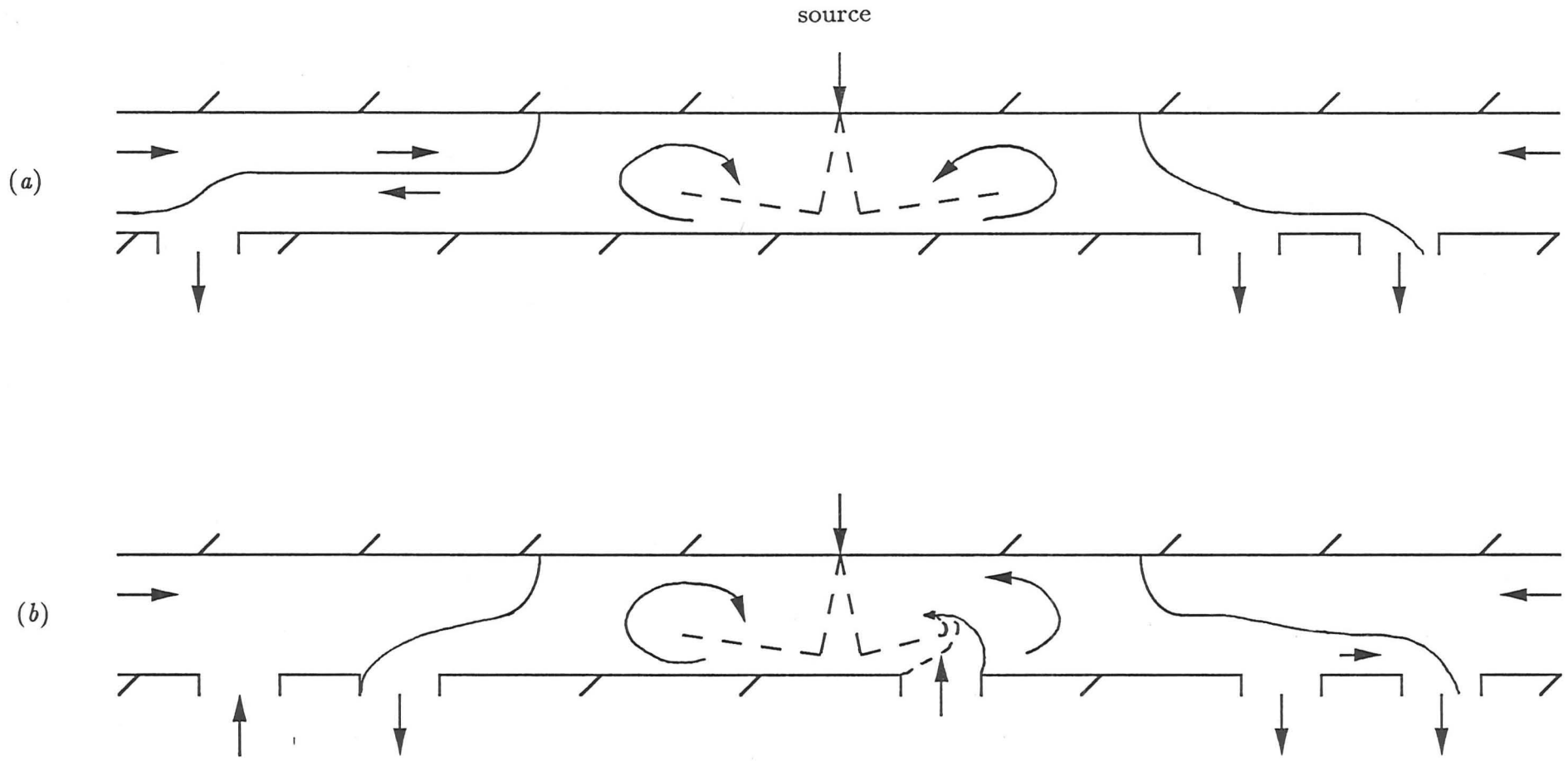

FIGURE 17. The effect of vent asymmetry on the flow; (*a*) the flow when all the vents are outside of the central mixed region; (*b*) the flow when there is a vent in the primary cell region on one side of the source only.

to the environmental fluid sucked in). In practice, this has been observed to unbalance the flow (see figure 17*b*).

4.5.3 Angled tunnels

Some experiments were also conducted to examine the effect of placing the tunnel at a small angle to the horizontal (up to 15°). The equilibrium flow is drawn schematically in figure 18.

Initially the recirculation develops as before with a buoyant layer flowing out on either side of the source. However, the buoyancy of the fluid decelerates the buoyant fluid flowing uphill which then flows back into the mixing region. The high momentum of the source maintains the recirculating flow on both sides of the source but there is little further flow of buoyant fluid uphill, although fluid is still entrained into the primary cell on this side of the source. On the downhill side of the source there is a component of gravity acting to pull the buoyant fluid in the mixing region down the tunnel. This results in a breakdown in the counterflow system with fluid from the primary cell moving slowly down the tunnel occupying nearly the entire depth. There appears to be little entrainment on the downhill side of the source - all the entrainment takes place on the uphill side. This flow appeared to develop for all but very small angles, although further experiments are required to determine the relationship between the minimum angle required to breakdown the counterflow system and the source characteristics.

5. Discussion and conclusions

The dynamics of a vertical, buoyant jet of high momentum in a long, possibly ventilated tunnel have been investigated using a mathematical model and laboratory experiments. The analysis was developed assuming that the vents were symmetrically placed about the source and that the ends of the tunnel were open. The jet-length L_j was several times the depth of the tunnel d, i.e. $\delta = L_j/d \gg 1$.

The flow is driven by the effects of both momentum and buoyancy, although in different regions. Close to the source the high momentum of the jet is important: a recirculating cell centered at a distance of $1.5d$ from the source axis is maintained and the fluid further down the tunnel is excited by turbulent momentum transfer. The buoyancy of the source fluid then drives the stratified counterflow and ventilation system (see figure 3). The excellent

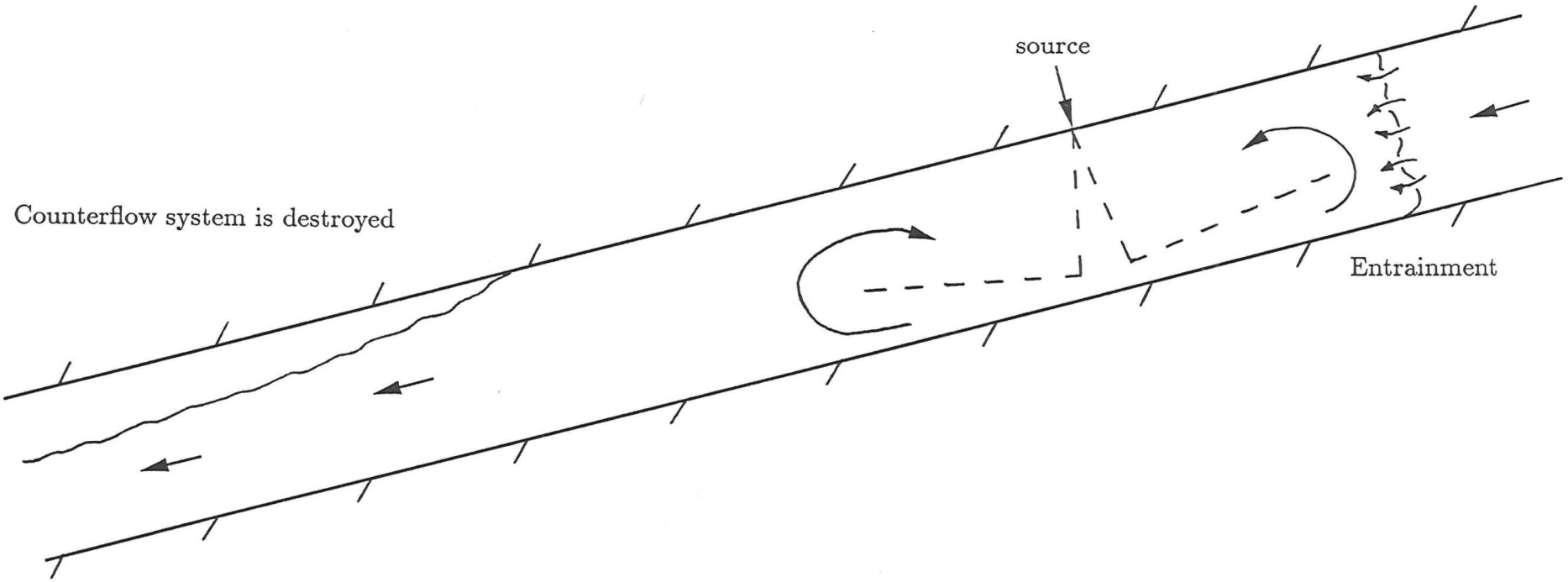

FIGURE 18. The flow of a vertical buoyant jet of high momentum in an angled tunnel.

agreement between the predictions of the theory and the experimental results indicates that the model gives a good description of the flow. For the main features of the model to be valid, it was found that $\delta \geqslant 2.9$ was required and so all the experiments were carried out under this condition. For all source values used within this range, the central mixed region near to the source had the same mean length of approximately $2.5d$. It must therefore be concluded that the effect of high source momentum in tanks of length $\lesssim 5d$, will be to mix the whole tank (provided that the source is vertical and centrally placed, $\delta \geqslant 2.9$ and that the length of the tank is not too small - see chapter 5).

Following Benjamin's (1968) analysis of the flow over the 'head' of an air pocket, it was deduced that the buoyant outflow occupies half the depth of the tunnel

$$h_2 = \frac{d}{2}.$$

This result was supported by almost all of the experiments, as are the consequent dependencies of the outflow velocity and reduced gravity on the source flow rate: $u_2 \sim Q_0^{\frac{1}{3}}$ and $g_2' \sim Q_0^{\frac{2}{3}}$. Occasionally the flow was asymmetric with a larger flow on one side of the source than on the other, but these cases were assumed to be the result of initial imbalances in the temperature between the ends of the tunnel. It should also be noted that the total volume flux of the outflowing buoyant fluid, $2Q_2$, is very much greater than that of the source; with the values suggested in section 2.1.3, $2Q_2 > 33Q_0$ - hence a relatively small volume input will produce a much larger volume motion within the tunnel. The reduced gravity of the outflow is lower than that of the source by an equal factor. This solution (2.35)-(2.38) was used as the basis for the subsequent analysis of the flows over vents and the concentration build-up within the primary cell.

The model was tested further when calculating the time dependence of the central mixing region concentration. In the analysis it was assumed that the volume flux of the buoyant outflow is dependent only on the mean concentration of the central region. The excellent agreement between the theory and experiment (figure 13) indicated the validity of this assumption. As suggested, it was found that the mean concentration of the central region, g_c' is slightly higher than that of the outflow, g_2' with $g_2'/g_c' = \kappa \simeq 0.9$. This is because a large fraction of the buoyant outflow originates in the inflowing environmental fluid, which becomes contaminated and more buoyant as it enters and mixes in regions 2 and 3 (figure 3*a*). Tests with dye patches indicate that most of this fluid will then flow out again in the buoyant layer, and that the more dense fluid from the source may remain in the circulating cell for longer

periods of time. The time dependent solution for the mean primary cell concentration could be used to calculate time dependent solution for the other mean flow variables. Once the steady-state is reached, which was within two minutes in all of the experiments, g_2' appears to fluctuate by up to approximately 8% about its mean, maximum value.

The other aspect considered was the effect of ventilation points along the tunnel. There are four possible ventilation modes (which may occur in combination) depending on the position of the vent relative to the source.

Firstly, if all or part of the vent is within $\simeq 2\alpha d$ of the source axis, then the overlapping jet fluid will flow straight out of the vent. The jet fluid impinging between the vent and the source axis may still recirculate, but the flow system of figure 3 may not now apply. This situation has not been studied.

Secondly, if the vent is within the primary cell region, but is not sufficiently close to the source to allow the jet to flow straight out of the vent, then the pressure drop associated with the recirculating fluid causes environmental fluid to be 'sucked' into the recirculating cell. This results in an increase in the volume flux entering the primary cell and hence the volume flux of the buoyant outflow increases. The analysis showed that this increase in volume flux is about a third of the volume flux of the environmental fluid being sucked into the primary cell. The analysis was modified in section 2.2.3 to allow for the presence of a vent in the primary cell, and the predictions for the increase in area required to vent the outflow agreed well with experimental measurements (figure 15). The environmental fluid sucked in also acts to dilute the buoyant fluid, and so the concentration values are lowered.

Thirdly, if the vent is between the primary cell and the counterflow regions, then initially the recirculating fluid will suck in environmental fluid through it as in the case above. However as the concentration of the central region increases to the steady state, the increasing buoyancy of the fluid above the vent increasingly opposes the weak inflow until the inflow is stopped and the buoyant fluid flows out.

Finally there may be vents in the counterflow region. Here, the flow is governed by buoyancy forces and some or all of the buoyant outflow will flow through a vent in its path. The volume flux through such a vent has been considered by Linden, Lane-Serff & Smeed (1990), and in section 2.2.2 a simple analysis of the flow over a vent was developed. The importance of this analysis is that the volume flux and depth of any 'secondary' buoyant layer may be calculated. The analysis may then be applied repeatedly for successive outflow layers until all of the initial buoyant fluid layer has been vented. Thus this provides a method

for calculating the total number of vents required to remove the buoyant outflow from the tunnel. The validity of the analysis was tested experimentally by measuring the variation of the secondary outflow depth with vent area. The value of k in (2.48) was found to be $k \simeq 0.51$ although this may vary for vents which are not rectangular, or do not span the whole width of the duct.

As mentioned above, all the experiments were carried out with the vents symmetrically placed and the ends of the duct open. The openness of the ends is effectively a control on the inflow of environmental fluid. If the volume flux of the buoyant outflow is so great that the volume flux of the inflow Q_1 required to satisfy (2.13) or (2.56) cannot be accommodated by the available openings, then the depth of the buoyant outflowing layer increases to compensate (by reducing the 'entrainment zone' - region 3 in figure 3). This was observed in preliminary experiments using a shorter tunnel with closed ends. If the buoyant layer can still not be vented, then buoyant fluid may become mixed with inflowing environmental fluid (as the buoyant fluid tries to flow out of the tunnel) and the counterflow system may break down as the buoyancy forces that drive it are reduced. This was also observed when the source was placed near to one end of the tunnel. The effect of asymmetry of the vents was found to be significant only if the vents are not symmetric near to the source. This is because the volume fluxes of the fluid entering and leaving the primary cells on either side of the source may no longer be equal (as there may be fluid sucked in on one side but not on the other). Consequently the buoyant layer may need more vents to vent it on one side than on the other.

This work has obvious practical applications to leakages of buoyant gases (for example, natural gas) from pipes in ducts or tunnels. Such gas is often under high pressure and unless the leak is significantly non-vertical the flow described here may be set up. It would be advantageous to know under what circumstances the concentration levels of gas pass required safety limits, and what configurations of vents would be most effective in venting the gas. Assuming that the density of the gas in the pipe was known, then, using the results presented here, it would be possible to calculate the minimum area required to vent the buoyant outflow created by a leak (see section 4.4) using a single vent - assuming also that the leak was not so near to a vent so that environmental fluid was sucked in. The spacing between the vents should be high so that the probability of the source being near to a vent is small, although if this were the case the maximum concentrations reached would be lower. Ideally, the ends of the tunnel should be open and if the ends are closed, the tunnel should extend some distance beyond the length of the gas pipe.

Notation

Below is a list of the symbols used in this chapter, provided for reference purposes.

A_i	Area of a vent
A_m	Minimum vent area needed to vent all of the fluid in the buoyant layer
A_p	Area of a vent in the primary cell
b	Radius of the jet
b_0	Nozzle radius
$B^{(\prime)}$	Parameter given in equations (2.33) and (2.42)
B_0	Initial source buoyancy flux
d	Depth of the tunnel
f	Darcy-Weisbach friction coefficients
F	Flow Force
$F_{1,2}$	Froude numbers
$g'_{0,2,c}$	Reduced gravities of source, buoyant layer and central region
$h_{1,2}$	Depth of the layers in the counterflow system
k	Constant controlling the flow through a vent in equation (2.48) and (2.58)
l	Half-length of the central mixing region
L_j	Jet-length
M_0	Initial source momentum flux
N	Number of vents in a system
p	Pressure
P	Parameter in equation (2.59)
$q_{(i)}$	The volume flux through the ith vent
$Q_{0,1,2,p}$	Flow rate of the source, outflow layers or through a vent in the primary cell
s	Axial distance from the source in the impinging jet flow
t	Time
u	Horizontal velocity
w	Vertical velocity
x	Horizontal coordinate
z	Vertical coordinate
α	Entrainment constant

β	Parameter in equation (2.68)
γ_2	Ratio of the outflow to source reduced gravities
δ	Ratio of the jet-length to depth of tunnel
Δ	Density difference
ζ	Energy loss at the 'head'
η	Parameter in equation (2.69)
κ	Ratio of the mean primary cell concentration to outflow concentration
$\rho_{0,2,a}$	Densities of the source, buoyant layer and environment
τ	Shear stresses
ω	Tunnel width

Chapter Five

Buoyant Convection from a Source in a Tall Chamber

The flow of a vertical plume in a confined space of low height to width ratio has been well studied, primarily by using or developing the 'filling-box' model. This model is, however, restricted to cases where the height, H, is less than or equal to the container width, R. Consequently flows in tall or thin chambers have been relatively neglected.

In this chapter flows with aspect ratio $a = H/R \geqslant 1$ are considered, placing particular emphasis on the concentration field that develops within the chamber.

It is shown that there exists a singularity in the gradient of the vertical momentum flux at a distance $z \simeq 5.8R$ from the nozzle, and that the plume behaviour breaks down there. As a result, two types of flow are produced depending on whether H is smaller or greater than the threshold depth $z \simeq 5.8R$.

When $H < 5.8R$ this threshold point is not reached and the behaviour of the mean flow variables may be modelled adequately using modified versions of the standard confined plume equations. In taller chambers the breakdown in plume behaviour gives rise to a region of unstable stratification at $z \gtrsim 5.8R$. This unstable density gradient drives mixing of the fluid further from the source. In this region, the behaviour of the mean density is modelled using a turbulent diffusion equation; a simple hypothesis is then used to connect the plume and convective regions of the flow.

Experiments have been carried out to compare the theoretical and numerical results using aspect ratios up to $H/R = 27$.

---

1. Introduction

Most work in the field of convection from a confined source has been developed from the 'filling-box' model of Baines & Turner (1969). This model has already been described in chapter 1, but before proceeding it is important to recall some of the assumptions on which it is based.

Firstly, it was assumed that plume fluid reaching the base† of the enclosure immediately spreads out forming a horizontal layer with a discontinuity (or front) above it; secondly, it was assumed that in any horizontal cross-section of the container, the area occupied by the plume is a small fraction of the total area at any level; and thirdly, in their asymptotic analysis Baines & Turner (1969) assumed that the concentration of the fluid in the environment (exterior) of the plume increased linearly in time, a result supported by experimental measurements.

Baines & Turner (1969) also investigated the possibility that a large scale vertical circulation may be set up, mixing the environment. Carrying out experiments in tanks with aspect ratio, a up to $a = H/R = 2.5$, where H is the height of the tank and R is the radius of a circle with equal area to a cross-section of the tank (the 'effective' radius), they observed increasing levels of over-turning motion when $a > 1$. Consequently Baines & Turner (1969) restricted their model to cases when $a \leqslant 1$.

In the following, the behaviour of the flow will be discussed when $a > 1$, a case relatively neglected because of the restriction on the filling-box model above. Flows of this type could arise in real physical situations, for example a leak of natural gas at the bottom of a lift, mine shaft, or tower, or in a building with an enclosed tall atrium. In these cases the behaviour of the concentrations of the plume and environmental fluid is of particular interest. The main effect of the over-turning observed by Baines & Turner (1969) is to produce non-uniformities in the density and velocity distributions on horizontal levels in the environment of the plume. In the analysis these effects will be neglected, considering mean values (over horizontal levels) only. Comparison with experimental measurements will show whether this simplification has a significant effect on the accuracy of the predictions of the analytical model. However, the area of the plume may approach that of the container and so must be included in the analysis.

The flow becomes more complicated when the aspect ratio is very large ($H/R \gtrsim 6$). The

† The description here, and the following analysis will be presented under the assumption that the fluid is negatively buoyant and the direction of the plume is *downwards* for ease of comparison with the experiments.

radius and the volume flux of the plume increase with distance from the source, and so the upward velocity of the environment increases correspondingly. Eventually, the upward environmental flow is sufficient to break down the downward plume flow, giving rise to a mixed region at the base of the plume. There is then a region of unstable stratification there, as the mixed fluid is more dense than the fluid below it. Some of this buoyant fluid flows upwards into the environment of the plume to be re-entrained but the remainder mixes with the fluid in the lower part of the chamber by turbulent convection. There are now two different dynamical regions which are coupled together: the initial confined plume flow, and the turbulent convection region with an unstable density gradient and concentration increasing in time. The latter region has similarities with convection flows produced by cooling a tall cylinder from above (or heating from below). Again the majority of work on this problem has been concerned with low aspect ratios, investigating the effect of Rayleigh number (defined below) on the formation and number of convection cells. Some, mainly two-dimensional, numerical work has been carried out (see, for example, Liang *et al.* 1969; Olsen & Rosenberger 1979; Neumann 1990), with small to moderate aspect ratios, attempting to model the eddy behaviour. In the large aspect ratio cases considered here, the flow is non-axisymmetric making numerical simulation complex; however, what is of relevant interest here is the interaction between the two regions of the flow, i.e. the driving of the convective region by the plume. With this in mind, the details of the eddy behaviour are of lesser importance and so it will suffice to consider the mean density over horizontal levels only.

2. Experimental Observations

Before analysing the problem theoretically, some experimental observations and measurements are now examined. These show how the flow develops and how the concentration behaviour varies in the different regions of the overall flow.

2.1 Experimental technique and apparatus

In all of the experiments the plume flow was modelled by pumping dyed salt solution from a reservoir into a tall, vertical tank, initially containing still fresh water. The dyed salt solution was injected vertically downwards from the top of the tank through a nozzle at a sufficiently slow, steady rate to ensure that the 'jet-length' (see chapter 2) was small compared with the width of the tank. The effects of the initial momentum flux of the source

are then negligible. The buoyancy flux of the source could be varied by changing the salt concentration of the reservoir fluid or the source flow rate.

In the experiments with the lower aspect ratios ($H/R \lesssim 5$) a perspex container of height 40 cm and square cross-section, with side 12.6 cm (equivalent in area to a cylinder of radius $R = 7.1$ cm), was used. For practical reasons, in order to study the effects of higher aspect ratios, a cylindrical perspex tube of radius 4.5 cm and height 131 cm was used. Both containers were closed at one end. Containers with other effective radii were also used in preliminary experiments, in which it was observed that the flows produced were independent of radius as long as the aspect ratio remained the same.

The experiments were recorded on video tape, which was analysed digitally to obtain the concentration profiles. The digital video analysis technique calculates the mean dye colour intensities along lines through the apparatus in the direction of the video camera. Experiments (see chapter 4) have shown that for small dye concentrations, the dye intensity measured varies linearly with the concentration. In all of the experiments carried out, this relationship was checked in the range of dye intensities obtained in the experiments; i.e. the intensity readings were carefully calibrated against known concentrations. Any nonlinearities due to high dye concentrations could then be taken into account. It is also important to note that the dye intensity varies linearly (for low dye concentrations) with the thickness of the dyed fluid (i.e., if the fluid has reduced gravity g' and depth d, then the intensity measured varies linearly with $g'd$). Thus if the intensities were measured through the vertical cylindrical tube filled with uniformly concentrated fluid, a variation in the intensity reading would be observed across any horizontal level of the tube, as the thickness of the dyed fluid varies (because the chordal distance through the tube varies). This will be unimportant when the concentration can be considered to be uniformly distributed across a horizontal cross-section of the flow, as the mean intensity measured over a horizontal plane will still be proportional to the mean intensity that would be measured using a container of uniform thickness. However, if the fluid cannot be considered to be uniformly mixed over a given horizontal plane, then this technique cannot be used to compare concentrations in parts of the flow in which the fluid has different thicknesses. To make sure that the results are not distorted by the above effect when using the cylindrical tube, the use of digital analysis will be restricted to thin vertical slices down the centre of the tube so that the thickness variation is negligible.

The relevant features of the flow observed experimentally will now be described.

2.2 Lower aspect ratios

In this section the flow observed using the shorter of the two tanks is described. This tank allows aspect ratios in the range $0 \lesssim H/R \lesssim 5$ to be investigated.

Figure 1 shows the time variation of mean, equally spaced concentration contours in the case when $a = 4.8$, measured by digital analysis of the video tape, at time intervals of one minute (where $t = 0$ is defined to be when the plume reaches the base of the container). It should be stressed again that these are mean concentrations along a line through the tank perpendicular to its front face. The concentrations shown here are then not only varying with the axial distance from the source and the approximately Gaussian radial dependence, but also with the variation of the thickness of the plume. Hence the concentrations shown here are effectively averages of an integration along a chord of the plume, together with the environmental fluid exterior to the plume. For comparison, the contours for the confined 'starting-plume' at $t = 0$, are shown in figure 2*a*. In this case the environment is unstratified and the form of these contours may be predicted analytically, neglecting the effect of the box boundaries.

In an infinite unstratified environment it can be shown that the reduced gravity g' of a plume is of the form

$$g'(x, y, z) \sim z^{-\frac{5}{3}} e^{-(x^2+y^2)/\sigma^2 z^2}, \tag{2.1}$$

(Morton, Taylor & Turner 1956), where x, y and z are cartesian coordinates scaled on the effective radius of the chamber, with the z-axis vertical, through the centre of the plume and σ is a constant controlling the radial variation. The radial variation of the reduced gravity has been assumed to be approximately Gaussian. For comparison with the experimental contours this must be integrated through the plume assuming that the plume material extends over a distance equal to its length scale

$$b = \frac{6\alpha_p z}{5}, \tag{2.2}$$

where α_p is the entrainment constant for a plume (see chapter 3). Integrating (2.1) along a chord through the plume, gives an intensity function

$$I(x, z) = \frac{2\sqrt{\pi}\sigma e^{-x^2/\sigma^2 z^2}}{z^{\frac{2}{3}}} \operatorname{erf}\left(\frac{\sqrt{b^2 - x^2}}{\sigma z}\right). \tag{2.3}$$

Equally spaced contours, (not chosen to match the experimental contours) of the form $I(x, z) =$ constant are shown in figure 2*b*, for $\sigma = 0.125$, a value typical of experimental

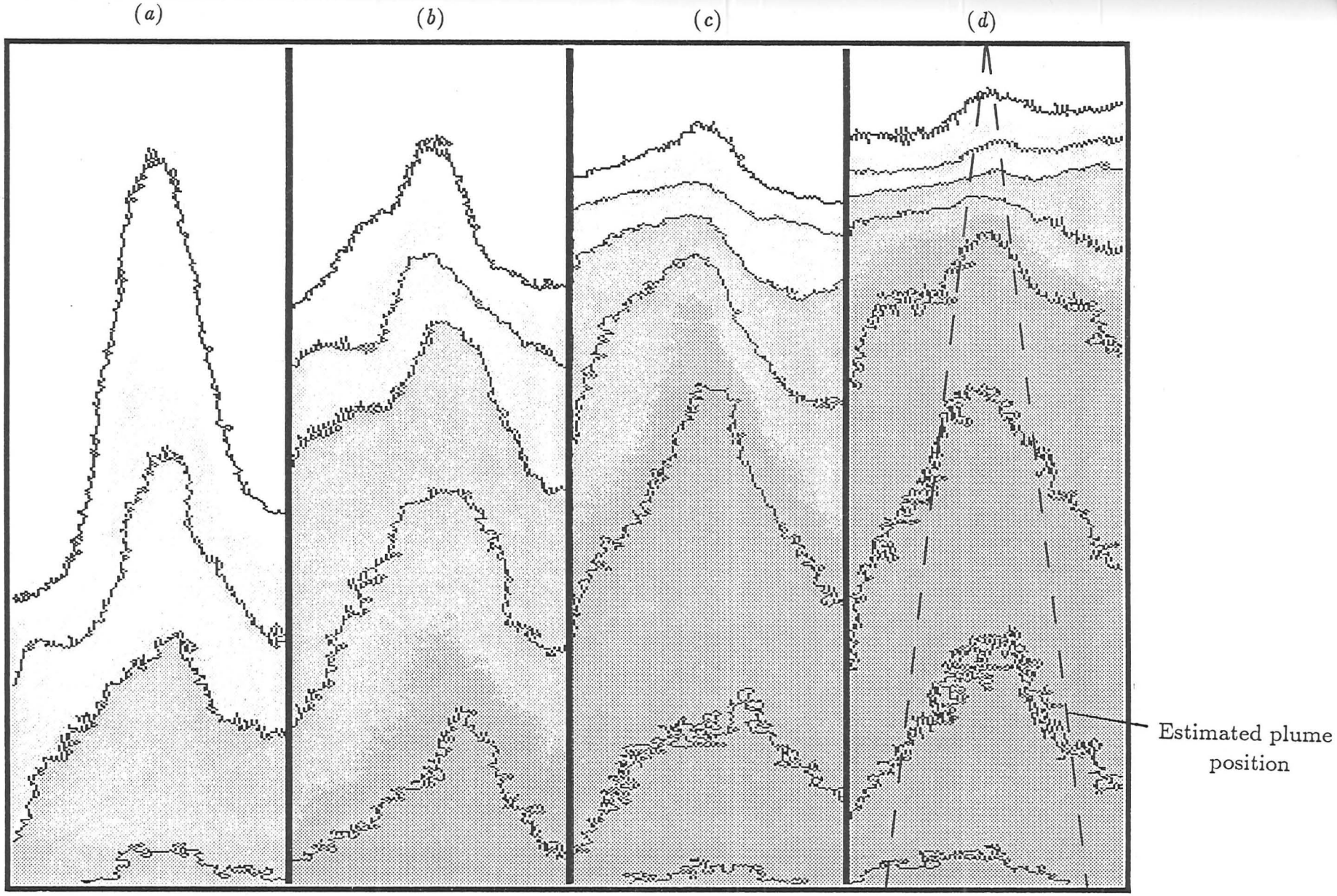

FIGURE 1. The mean concentration contours obtained in an experiment using a square container, with $a = 4.8$. (*a*) $t = 60$s; (*b*) $t = 120$s; (*c*) $t = 180$s; (*d*) $t = 240$s; (*e*) $t = 300$s; (*f*) $t = 360$s; (*g*) $t = 420$s; (*h*) $t = 480$s.

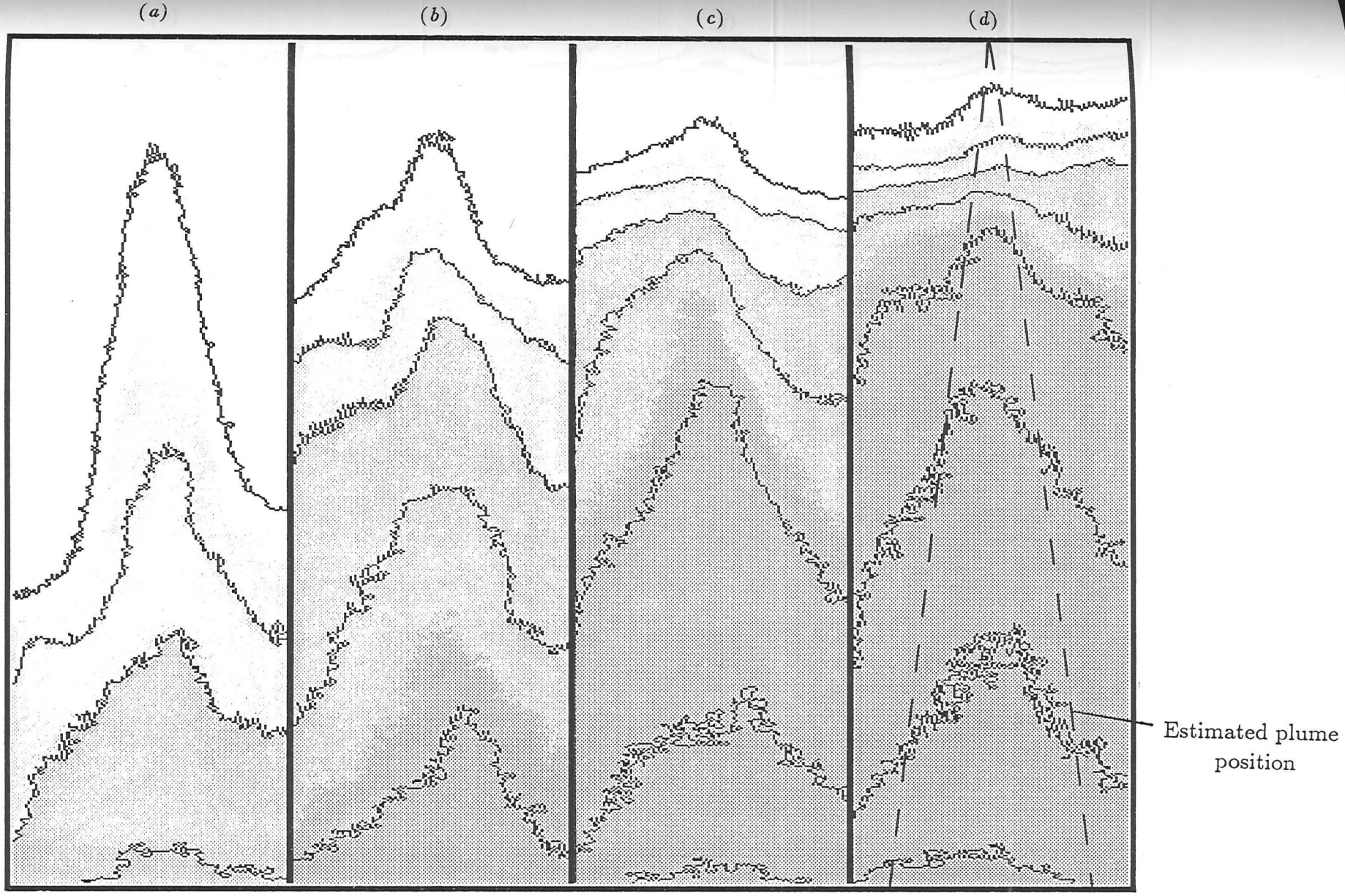

FIGURE 1. The mean concentration contours obtained in an experiment using a square container, with $a = 4.8$. (*a*) $t = 60$s; (*b*) $t = 120$s; (*c*) $t = 180$s; (*d*) $t = 240$s; (*e*) $t = 300$s; (*f*) $t = 360$s; (*g*) $t = 420$s; (*h*) $t = 480$s.

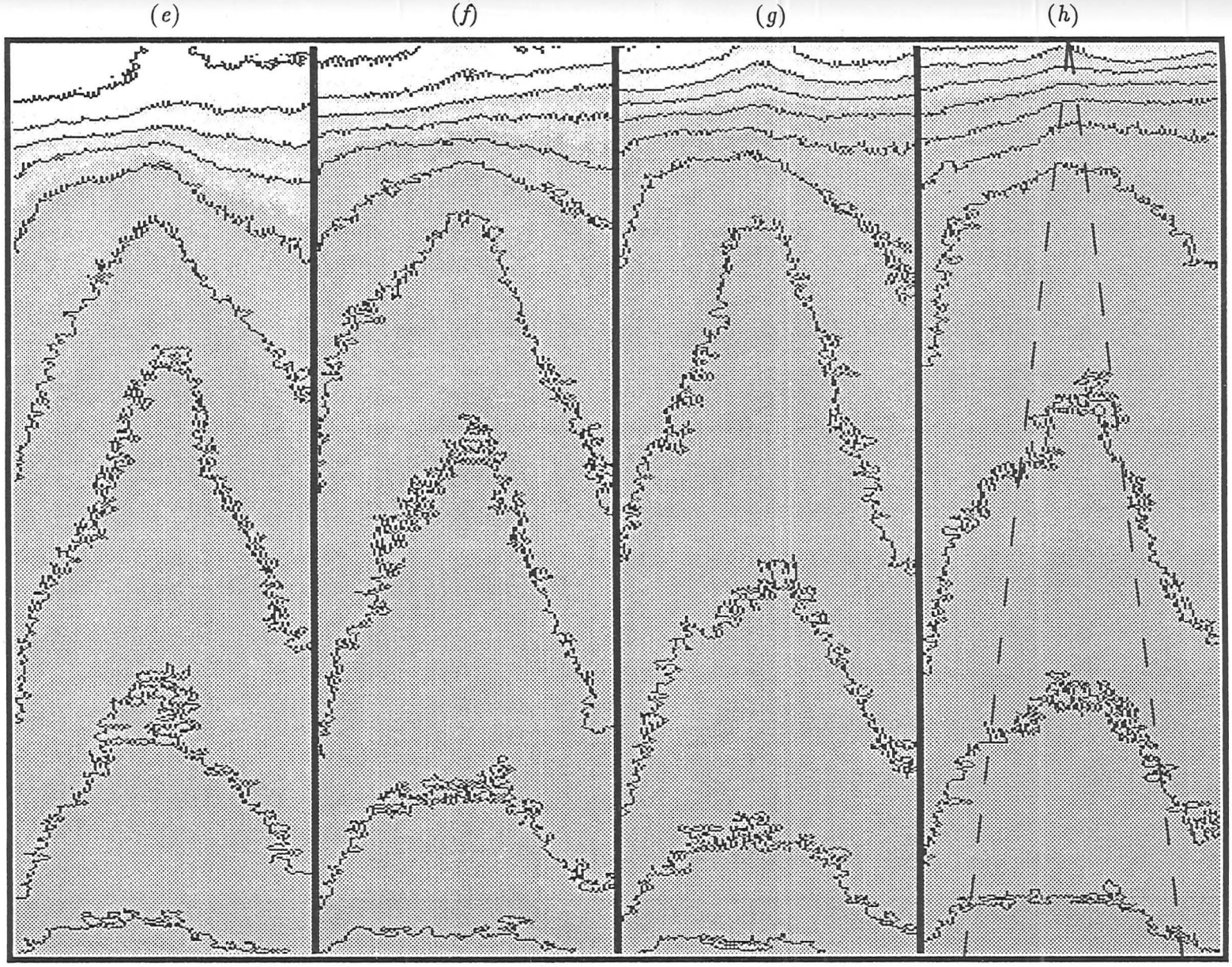

FIGURE 1 ct'd. For caption see previous page.

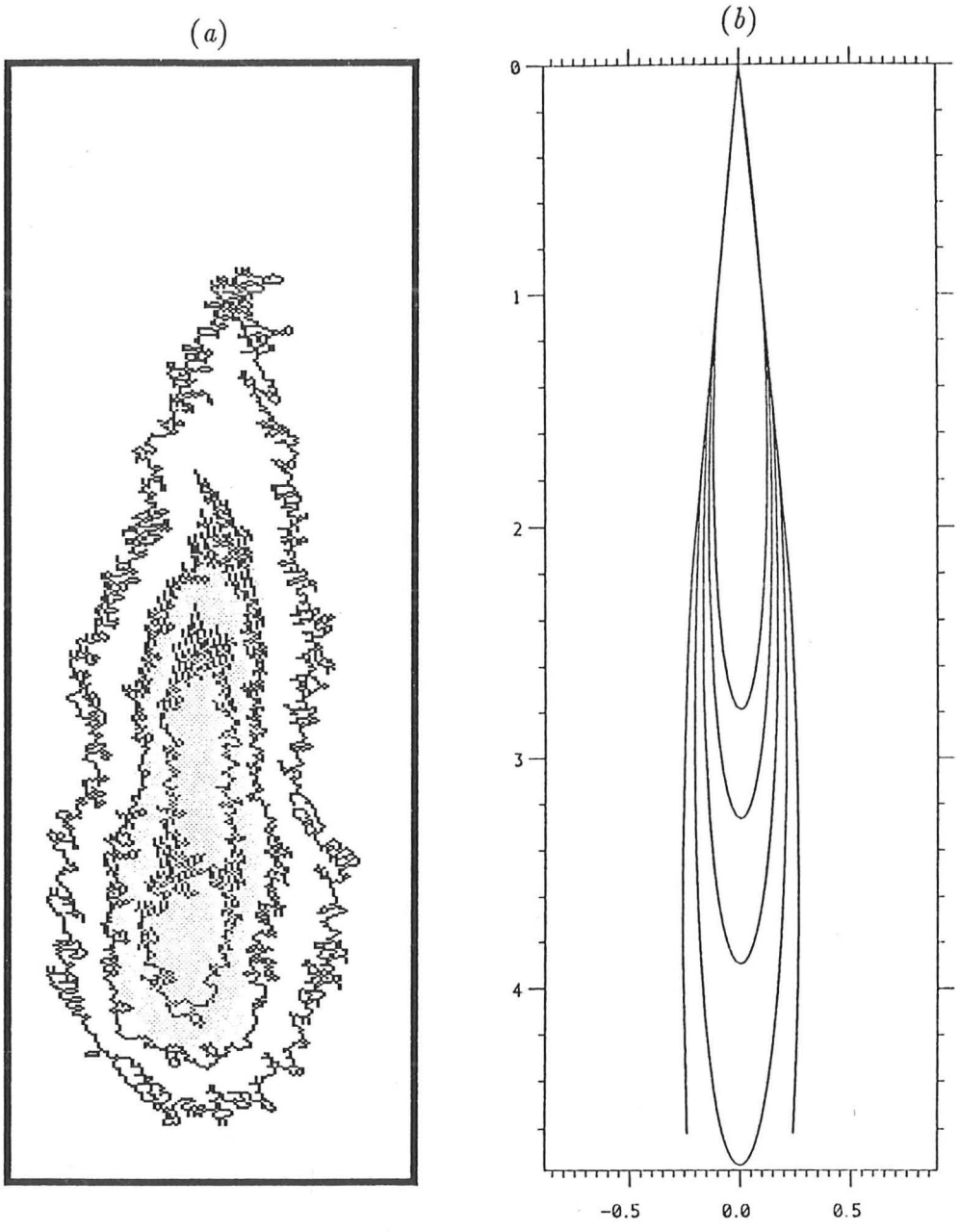

FIGURE 2. (*a*) The initial mean concentration contours for the experiment shown in figure 1; (*b*) the theoretical contours that should be observed through a plume in an infinite, unstratified fluid.

results (see Fischer *et al.* 1979). The contours essentially take the same form as is observed experimentally - this comparison serves as a useful check on the video analysis technique, but it also indicates that the plume material mixes over a much larger region than that given by its length scale or 'radius' b above. This is probably due to the horizontal confinement of the plume - the above calculation assumes an environment of infinite extent and plumes released near to boundaries have a tendency to 'stick' to them. The experimental contours are inaccurate near to the source as the plume radius is comparable to the digital pixel resolution.

Returning to figure 1, the movement of the first front, i.e. the fluid in the environment that originated from the first plume material to reach the tank base, can be clearly seen by following the topmost contour (which in each case corresponds to a concentration of 0.4%) as it moves up the box. Notice also that the contours near to the source are approximately horizontal, indicating uniform concentration over horizontal planes. This is effectively the type of flow considered by Baines & Turner (1969): there is little interaction between the plume and the environment other than horizontal entrainment. Recall that the contours shown here are of the mean concentration through the tank; thus near to the source the radius of the plume is small and so the mean value measured is dominated by the environment fluid. This explains why the horizontal contours of the environment are dominant, the characteristic upturned 'V' shaped contours associated with the plume (see figure 2) being hardly apparent. Further from the source the plume contours become more obvious although distorted by the exterior flow. Outside of the plume (the mean position of the plume may be estimated using traditional plume theory, see chapter 3, and is indicated by the dashed lines on figures 1*d,h*), there is a horizontal concentration gradient as well as the vertical stable stratification. This is a result of the increased interaction between the plume and the environment as the radius of the plume increases with distance from the source. (This is also reminiscent of the 'overturning' observed by Baines & Turner 1969.) As the plume radius increases, the downward plume motion and its induced entrainment velocity have an increasing effect on the motion of the fluid exterior to the plume. When the radius of the plume is small, the bulk of the exterior fluid is free to flow vertically, resulting in approximately uniform profiles of velocity and density on horizontal levels. However, when the plume radius is large, a much higher proportion of the exterior fluid must have a significant radial component of velocity which results in non-uniformities in the profiles of velocity and density on horizontal levels.

Digital video analysis may also be used to measure the time dependence of the mean concentration at a given point, outside of the plume. Figure 3 shows measurements, taken

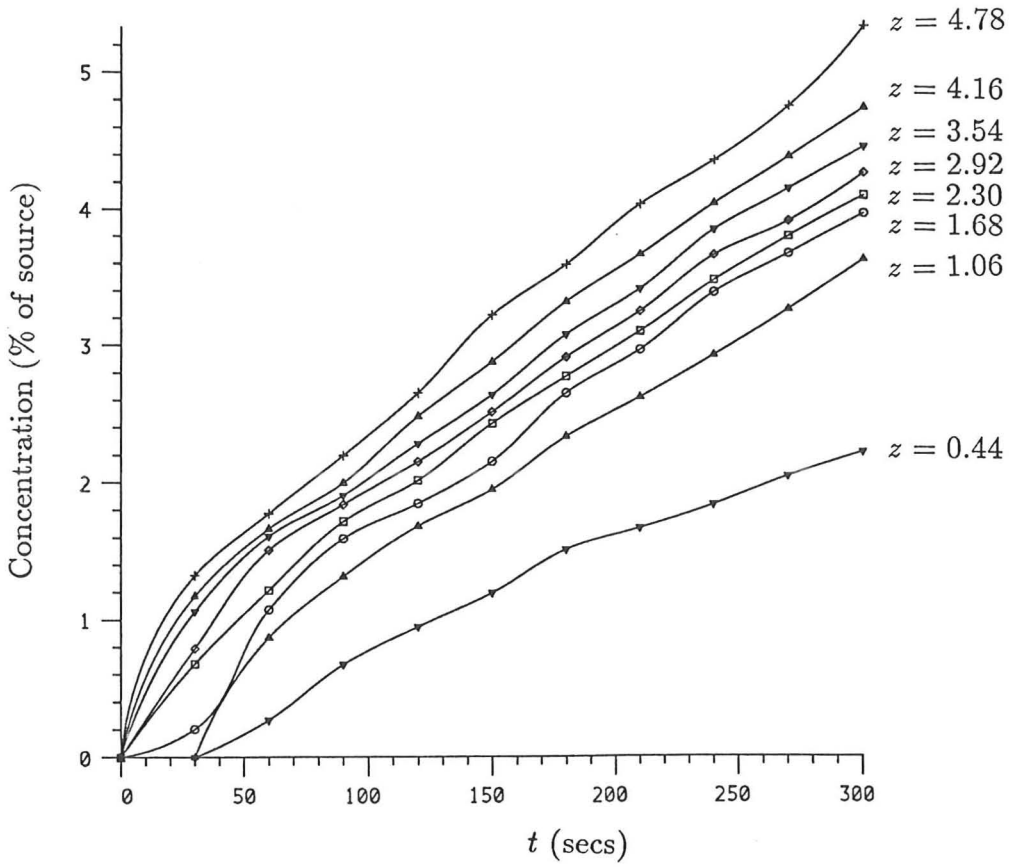

FIGURE 3. The time variation of the mean concentration at various depths in the fluid exterior to the plume, at a distance $0.2R$ from the left hand boundary (taken from the experiment shown in figure 1).

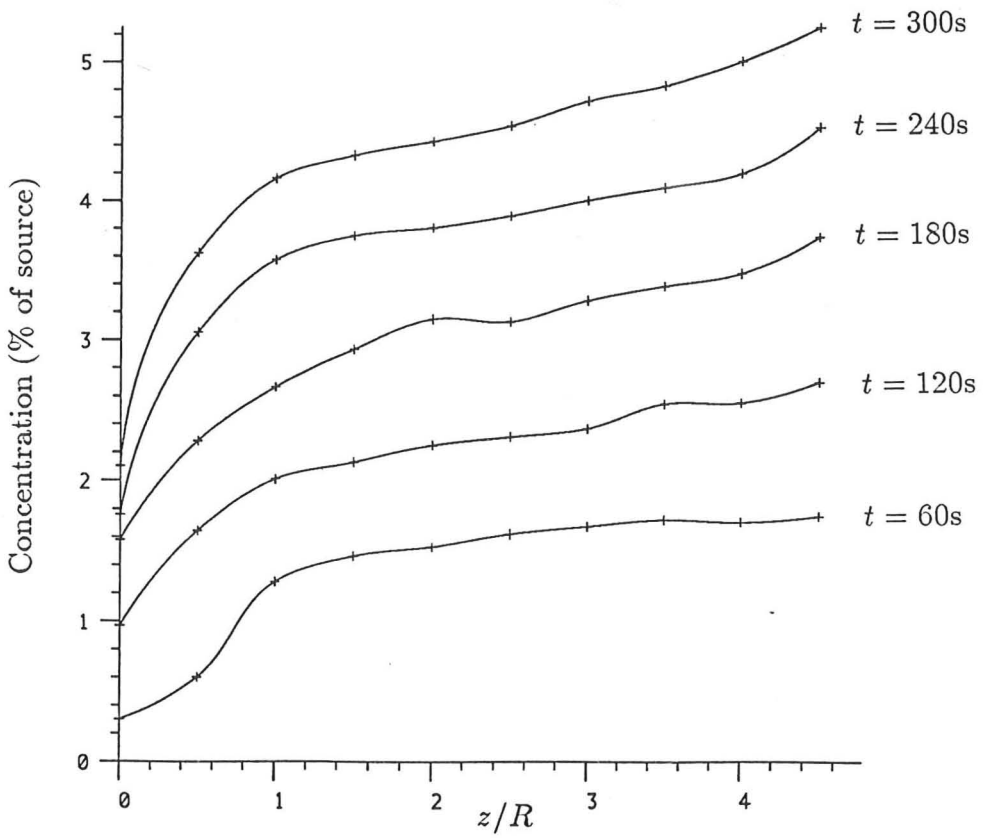

FIGURE 4. The mean concentration along a vertical slice through the centre of the chamber, (from the experiment shown in figure 1), plotted after successive time intervals of one minute.

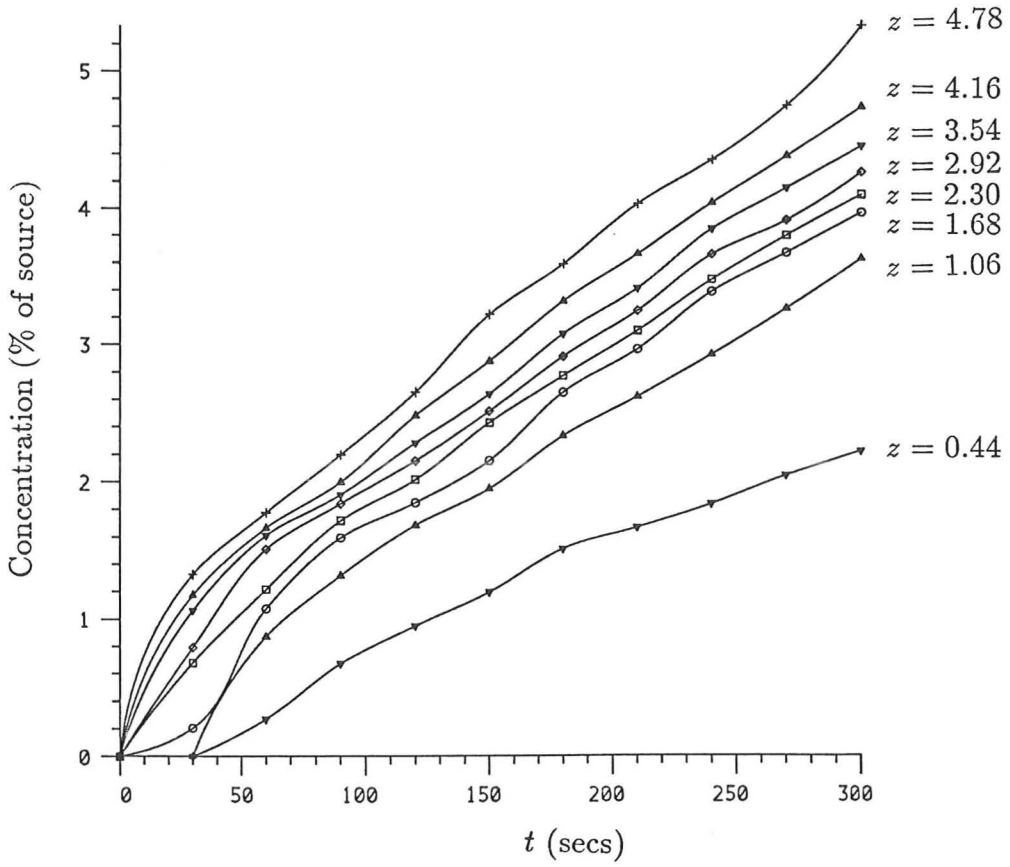

FIGURE 3. The time variation of the mean concentration at various depths in the fluid exterior to the plume, at a distance $0.2R$ from the left hand boundary (taken from the experiment shown in figure 1).

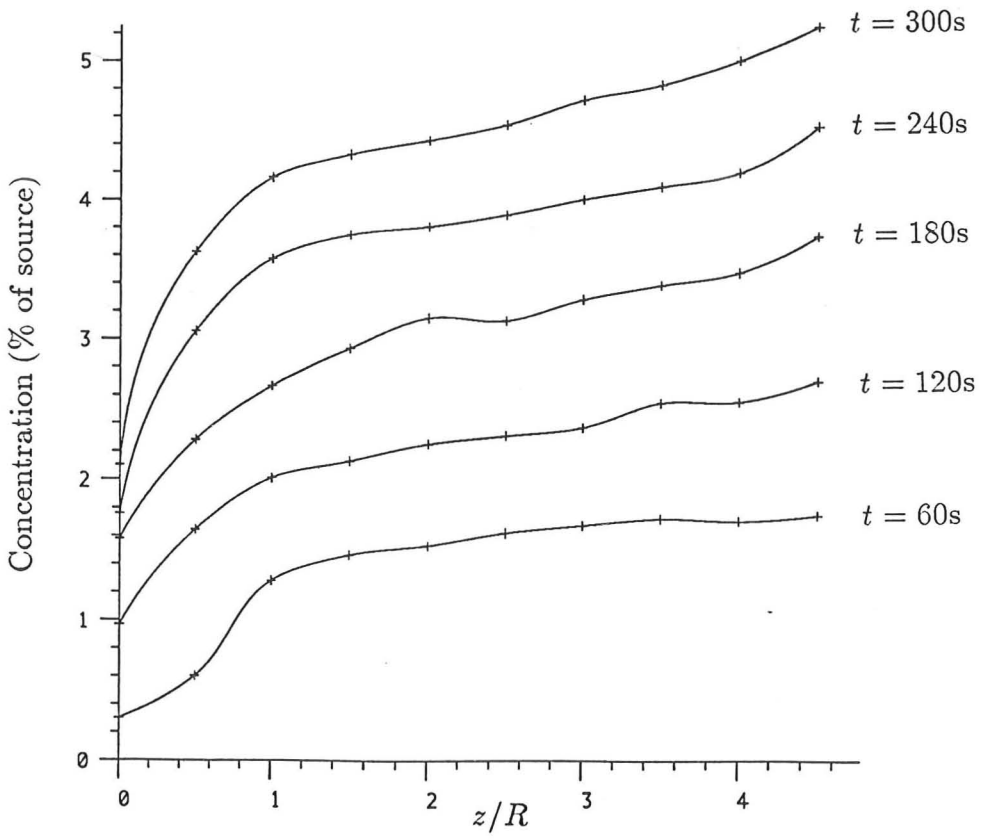

FIGURE 4. The mean concentration along a vertical slice through the centre of the chamber, (from the experiment shown in figure 1), plotted after successive time intervals of one minute.

during the experiment shown in figure 1, of the concentrations at various vertical heights at points a horizontal distance of $0.2R$ from the left hand boundary. It can be seen from this figure that after a sufficiently large time (which varies according to vertical distance from the source), the concentration increases approximately linearly in time. This is in agreement with the time dependence assumed by Baines & Turner (1969) in their asymptotic theory.

For future comparison with the taller cylinder, the mean concentrations along a thin slice through the centre of the box have also been measured. These measurements are shown in figure 4 in which the 'centre-slice' concentration is plotted against depth, after successive time intervals of one minute. The roughly equal spacing between the lines again illustrates the linear time dependence.

2.3 Higher aspect ratios

A schematic diagram of the flow observed using a tank of higher aspect ratio is given in figure 5. The flow comprises three regions, which are referred to as the plume, mixing and convective regions.

The first region, of height h_1 and nearest to the source, contains the downward plume flow and the upwardly flowing exterior fluid, and is similar to the low aspect ratio case. The radius and volume flux increase with axial distance from the source, z. Therefore, conservation of volume on any horizontal plane in this region implies that the mean vertical speed of the environmental fluid must also increase with z. The increasing shear increases the mixing between plume and exterior fluid to a point at which the downward plume flow is no longer defined. This is the second region of the flow, of height h_2, where the plume fluid is mixed with the ambient. At the division between these first two regions the downward volume flux of the plume must be balanced by that of the up-flowing environment (by conservation of volume on this horizontal plane), but the buoyancy flux of the environment is less than that of the plume. This difference in the buoyancy fluxes implies an increase in the concentration of the mixing region. However, the fluid in region 2 is now more dense than that of the fluid below it. This unstable stratification drives mixing between the second and third regions.

In the third region the dense fluid supplied by region 2 is eventually mixed over its whole length by convection. The mixing is three dimensional with no observable ordered structure, although occasionally eddies can be observed with dimensions on the same scale as the tank effective diameter. The density gradients are small and so this mixing process takes place on

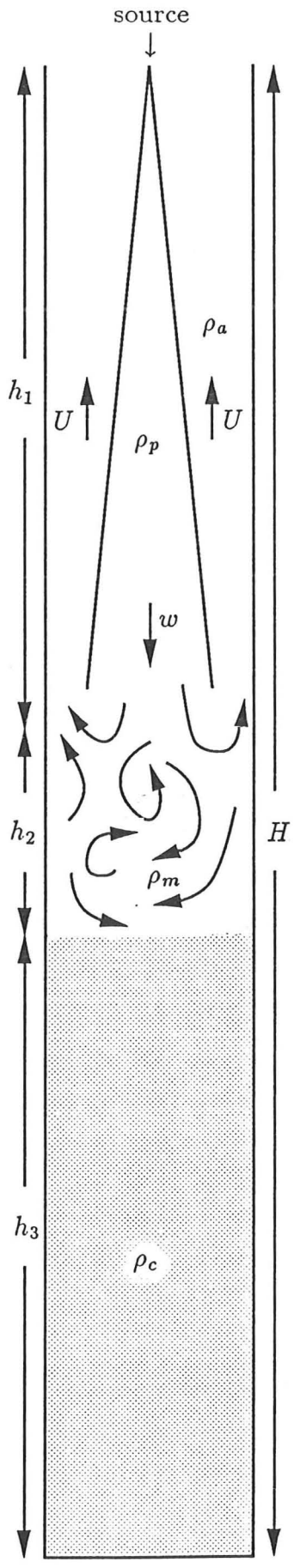

FIGURE 5. A schematic diagram of the flow observed for very large aspect ratios.

a large time scale. Estimation of the Rayleigh number (see Turner 1973),

$$Ra = \frac{g\Delta\rho h_3^3}{\rho_0 \kappa \nu}, \tag{2.4}$$

where h_3 is the length of region 3, separating a density difference $\Delta\rho$, κ is the thermal diffusivity, and ν is the kinematic viscosity, shows that the convective threshold ($Ra \sim O(10^3)$) will be reached easily (generally $Ra \gtrsim 10^7$ here) and that the mixing is expected to be turbulent and described by a turbulent diffusion equation.

Mean concentrations through a 'centre slice' of the tube are shown in figure 6, taken from an experiment in which $H/R = 27$, with plots at successive time intervals of one minute. The concentrations are obtained from an average of three video frames and represent a time average over a period of two seconds. For values of $z/R \lesssim 5$ the plume flow is well defined and these contours can be compared with those of figure 4. Notice that the spacing between the curves tends to decrease with time, whereas for the shorter chambers the lines were approximately equally spaced. Between $z/R \simeq 5$ and $z/R \simeq 6$ the plume flow deteriorates (so this may be regarded as being the mixing region 2 above), with a fairly rapid decrease in mean concentration over this region. For larger values of z/R, the concentration gradients are smaller: the convective mixing here results from the unstable stratification rather than the momentum of the plume. This is the turbulent convective region 3. The mean concentrations decrease slowly from top to bottom (the very bottom of the tank is not shown here), but the mean concentration at a given depth increases monotonically with time.

3. Chambers with moderate aspect ratios

It was stated above that the flow of the plume breaks down as the upward velocity of the environment becomes comparable to that of the downward plume. It will now be shown that there is a singularity in the momentum flux of the plume at that point. The flow in chambers with aspect ratio sufficiently small such that this point is not reached will then be considered.

3.1 The breakdown of the plume flow

Figure 7 shows a schematic diagram of the enclosed plume part of the flow. All velocity and density profiles are assumed to be 'top-hat', i.e. constant in horizontal planes over the area in which they apply. At an axial distance z from the source the plume has mean axial

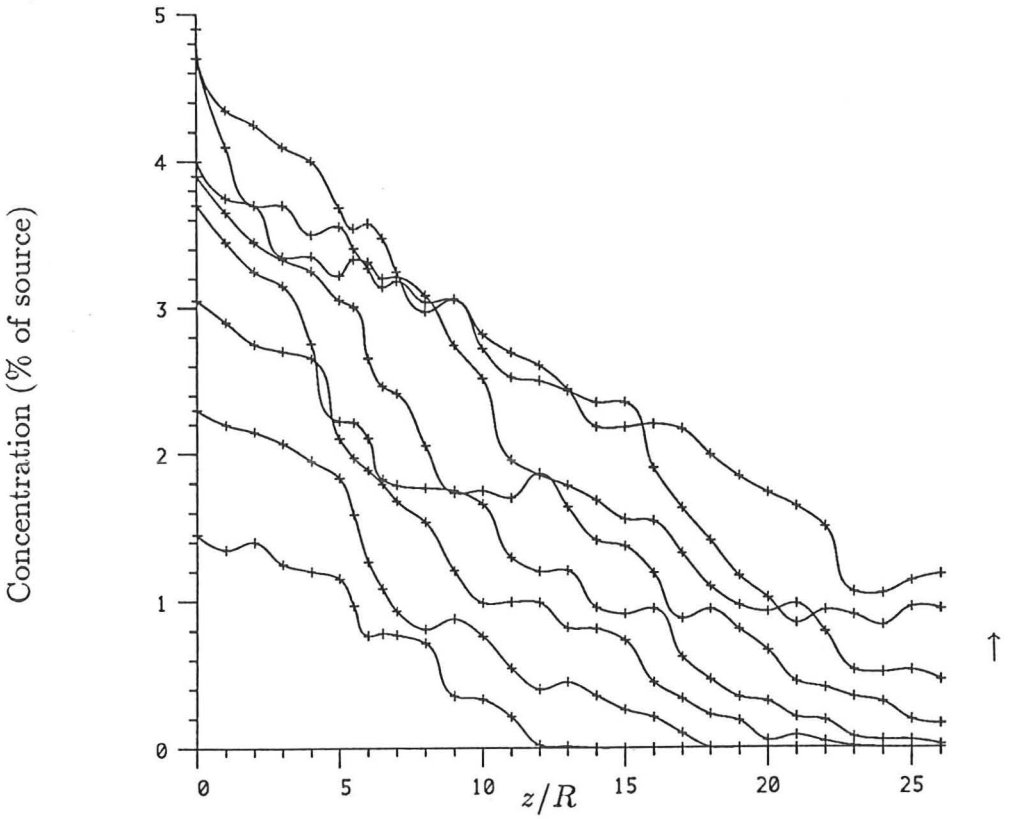

FIGURE 6. The mean concentration along a vertical slice through the centre of the chamber, from an experiment in which $a = 27$, $B_0 = 5.62\,\mathrm{cm^4 s^{-3}}$, plotted after successive time intervals of one minute.

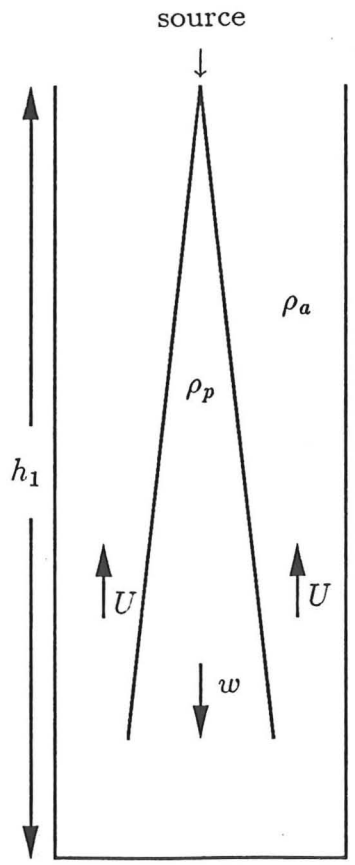

FIGURE 7. A schematic diagram of the plume region of the flow.

velocity $w(z,t)$, length-scale or 'radius' $b(z,t)$ and mean reduced gravity (relative to the environment) $g_1'(z,t) = (\rho_p - \rho_a)g/\rho_0$, where $\rho_p(z,t)$ is the mean density of the plume fluid, $\rho_a(z,t)$ is the mean density of the fluid exterior to the plume and ρ_0 is a reference density equal to that of ambient fluid. The mean velocity of the exterior fluid is $U(z,t)$. The initial flow of the plume, when the environment is uncontaminated by the source fluid, is considered first.

The conservation equations for a plume confined to a chamber of small aspect ratio have been presented by Baines & Turner (1969) (see also chapter 3, equations (2.91), (2.25) and (2.26)). Here, however, the aspect ratio is large and the plume radius must be included in the conservation of momentum equation and the equation in which the volume flux of the plume flow is equated with the volume flux of the upward environmental fluid. The variables may be non-dimensionalised using the 'effective radius', R, (the radius of a circle with the same area as a cross-section of the chamber) and the buoyancy flux of the source, B_0. Thus if the star denotes a dimensionless scale then

$$[L]^* = R^{-1}[L], \qquad [T]^* = B_0^{\frac{1}{3}} R^{-\frac{4}{3}}[T],$$

where $[L]$ and $[T]$ are the scales of length and time respectively. Thus the conservation equations for a plume in an unstratified environment in non-dimensionalised variables, dropping the stars, are

$$\frac{d}{dz}(b^2 w) = 2\alpha_p b w, \tag{3.1}$$

$$\frac{d}{dz}(b^2 w^2 + (1-b^2)U^2) = b^2 g_1', \tag{3.2}$$

$$\frac{d}{dz}(b^2 w g_1') = 0, \tag{3.3}$$

and continuity on horizontal planes gives

$$(b^2 - 1)U = b^2 w. \tag{3.4}$$

Writing $Q = b^2 w$ and $M = b^2 w^2$, the local fluxes of specific volume and momentum of the plume respectively, and substituting for U, gives

$$\frac{dQ}{dz} = 2\alpha_p M^{\frac{1}{2}}, \tag{3.5}$$

$$M\frac{d}{dz}\left(\frac{M^2}{M-Q^2}\right) = QB, \tag{3.6}$$

where $B = b^2 w g_1'$ is the specific buoyancy flux of the plume (constant if the environment is unstratified and so it maintains its initial value, B_0, which is unity in dimensionless variables). Equation (3.6) can then be rewritten in the form

$$\frac{dM}{dz} = \frac{Q[(M-Q^2)^2 - 4\alpha_p M^{\frac{7}{2}}]}{M^2(M-2Q^2)}. \tag{3.7}$$

Clearly dM/dz has a singularity when $M - 2Q^2 = 0$ or $2b^2 = 1$, i.e. when $b \simeq 0.71$. From (3.4) above it can be seen that at this point $w = -U$, i.e. the speed of the plume fluid is equal to that of the exterior flow. Also, at this point the momentum fluxes of the plume and environment are equal (as $b^2 = 1/2$), which gives a physical interpretation to the singularity: the net vertical momentum force is zero and so the plume flow is expected to collapse.

The above equations have proved impossible to solve analytically, but are easy to solve numerically. The numerical solution is shown in figure 8, obtained using a NAG Fortran routine. The erratic behaviour beyond the point at which the singularity is reached is included here to graphically illustrate the breakdown of the confined plume equations.

Figure 8*a* shows the behaviour of the plume radius b. In an infinite environment the plume radius increases linearly with z (the dotted line) and from this figure it may be seen that this is still the case whilst $z \lesssim 4$, but for larger values of z the plume radius increases more rapidly to the threshold value at $z \simeq 5.78 \pm 0.01$. Figure 8*b* shows the plume and environmental velocities w and $-U$ clearly indicating that the plume breakdown occurs when the mean velocities of the plume and environment are equal.

The position of this threshold point will depend on the value of the entrainment constant used in the analysis ($\alpha_p = 0.1178$ here - see chapter 2) but the position $z \simeq 5.8$ is consistent with experimental observations and will used throughout the rest of this chapter.

In practice, for aspect ratios $a < 5.8$ the above singularity will not be reached, and the continuing flow of the plume will stratify the environment. However if the aspect ratio $a \gtrsim 5.8$ then the plume behaviour will break down at $z \simeq 5.8$, as shown above. Some of the dense fluid at this level will flow up into the environment of the plume, but the remainder will mix with fluid further down the chamber.

In either case the environment of the plume will become contaminated by the source fluid (which may alter the position of the singularity) and the fully time dependent equations for a plume in a stratified environment must be studied.

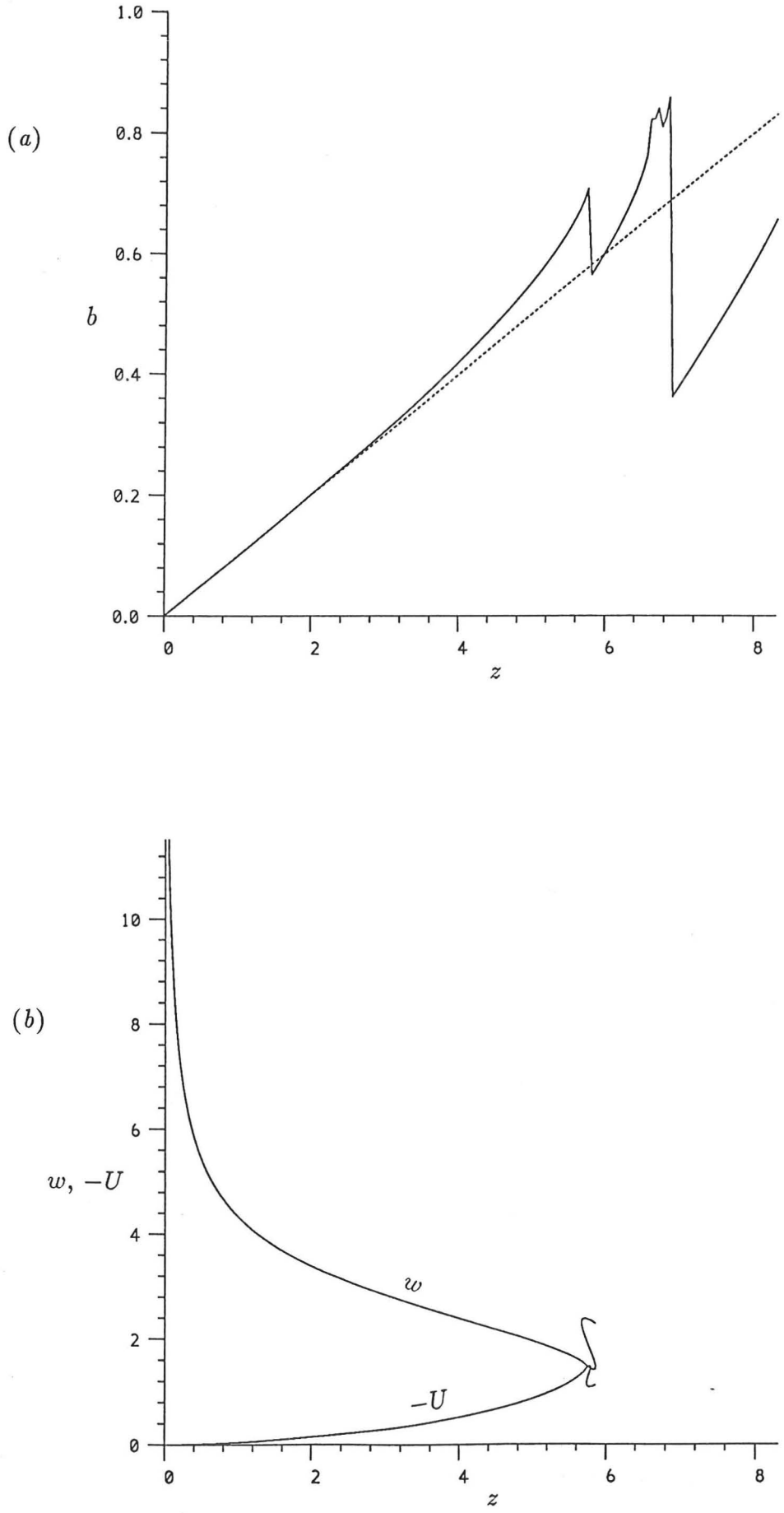

FIGURE 8. The numerical solution for the confined plume equations (3.1)-(3.4); (*a*) the plume radius b; (*b*) the mean plume velocity w, and the mean velocity of the fluid in the environment of the plume U.

3.2 Time dependent analysis and numerical solution

The time-dependent conservation equations for a confined plume will now be considered assuming that the aspect ratio of the container is sufficiently small so that the above singularity is not reached. The height of the tank is h_1, and it is assumed that $h_1 < 5.78$.

The conservation of volume and momentum equations, (3.1) and (3.2) remain unchanged, as does the continuity equation (3.4). However stratification of the environment must be included in equation (3.3) which then becomes

$$\frac{d}{dz}(b^2 w g_1') = -\frac{b^2 w g}{\rho_0}\frac{\partial \rho_a}{\partial z}. \tag{3.8}$$

Finally the stratification of the environment is given by the equation

$$\frac{\partial \rho_a}{\partial t} = -U\frac{\partial \rho_a}{\partial z}, \tag{3.9}$$

(see Baines & Turner 1969).

These equations can be solved numerically, integrating equation (3.9) over each time-step to obtain the behaviour of ρ_a and using the solution for a pure plume (see Morton, Taylor & Turner 1956) at the source. This integration method assumes that the time-variation of the variables is small compared with the spatial variation. It is also assumed that on reaching the base of the tank, the plume fluid immediately flows out into a horizontal layer, i.e. that at the base of the tank ($z = h_1$),

$$\rho_a(h_1, t + \delta t) = \rho_p(h_1, t). \tag{3.10}$$

Also, it is necessary that the volume of exterior fluid flowing upwards in the time-step δt must be less than that enclosed by the vertical step δz, i.e. that

$$-U(h_1, t)\delta t \ll \delta z. \tag{3.11}$$

The numerical solution for a tank with $a = 4.78$ is shown in figures 9*a-c*, the curves showing the solution after equally spaced steps in t (the arrows indicating increasing t). Figure 9*a* shows the behaviour of the mean plume and environmental velocities w and $-U$ with distance from the source z. The velocities appear to approach the limiting profiles quickly. At the tank base the values of w and $-U$ appear to meet although in fact the numerical value of

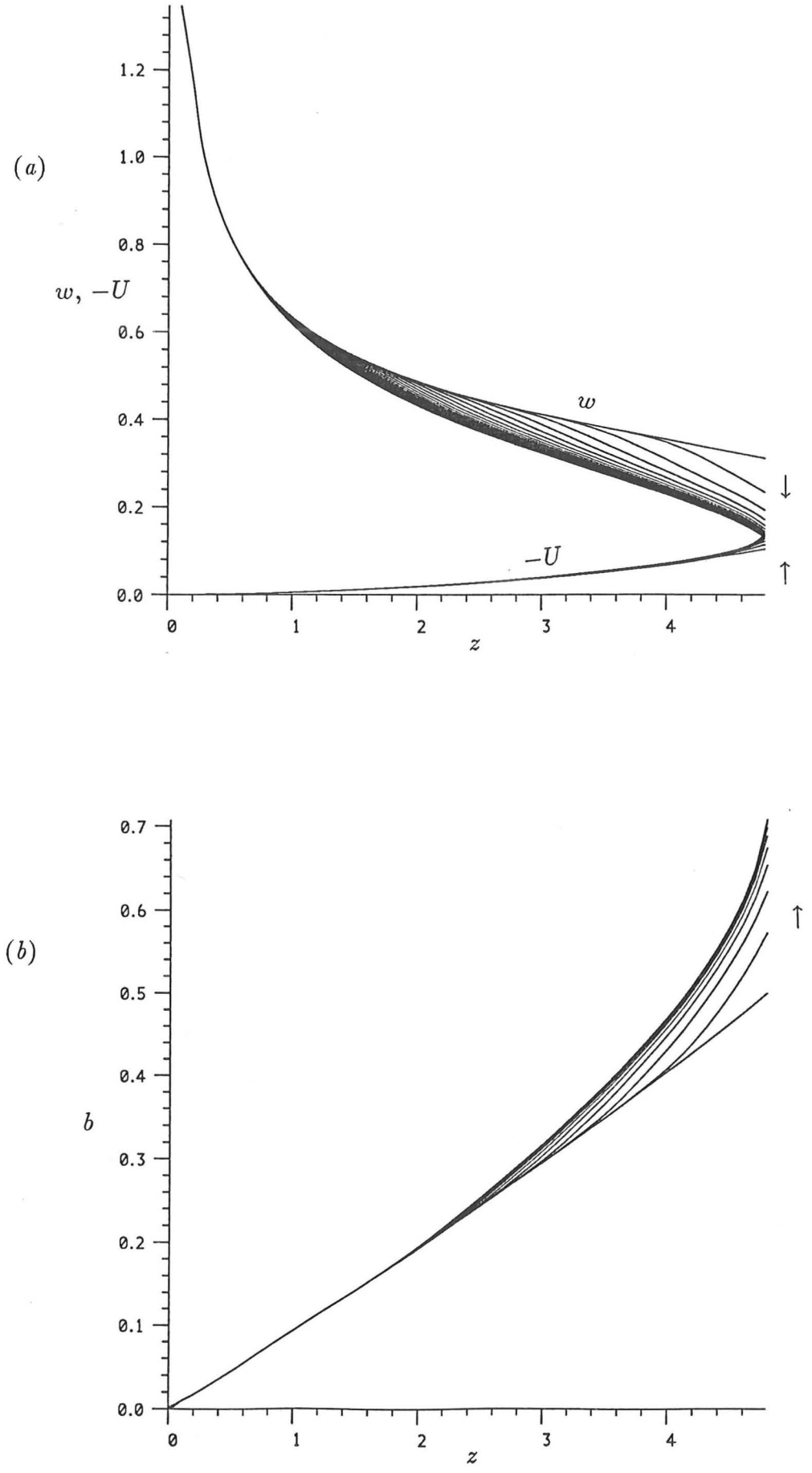

FIGURE 9. A numerical solution of the time-dependent filling-box problem for containers of moderate aspect ratio ($a = 4.8$ here); (a) the mean plume and plume environment velocities w and U; (b) the plume radius b; (c) the reduced gravities of the plume and environment fluids (g'_p and g'_a respectively).

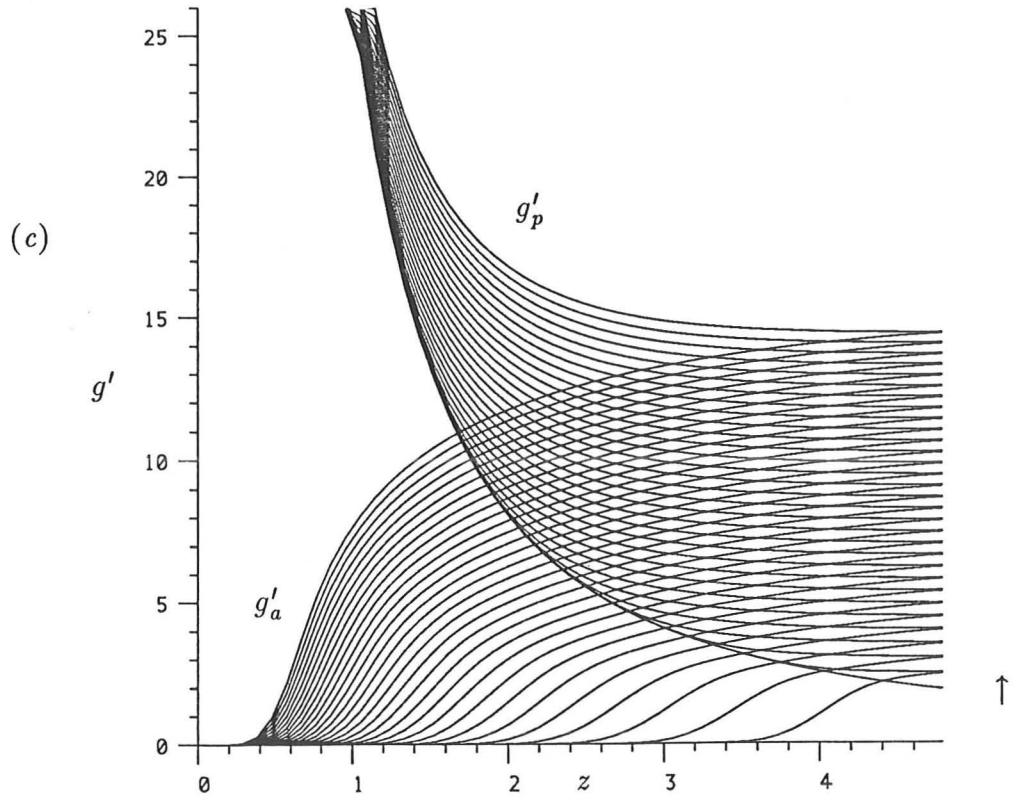

FIGURE 9. ct'd. (c). The reduced gravities of the plume and environment fluids (g'_p and g'_a respectively).

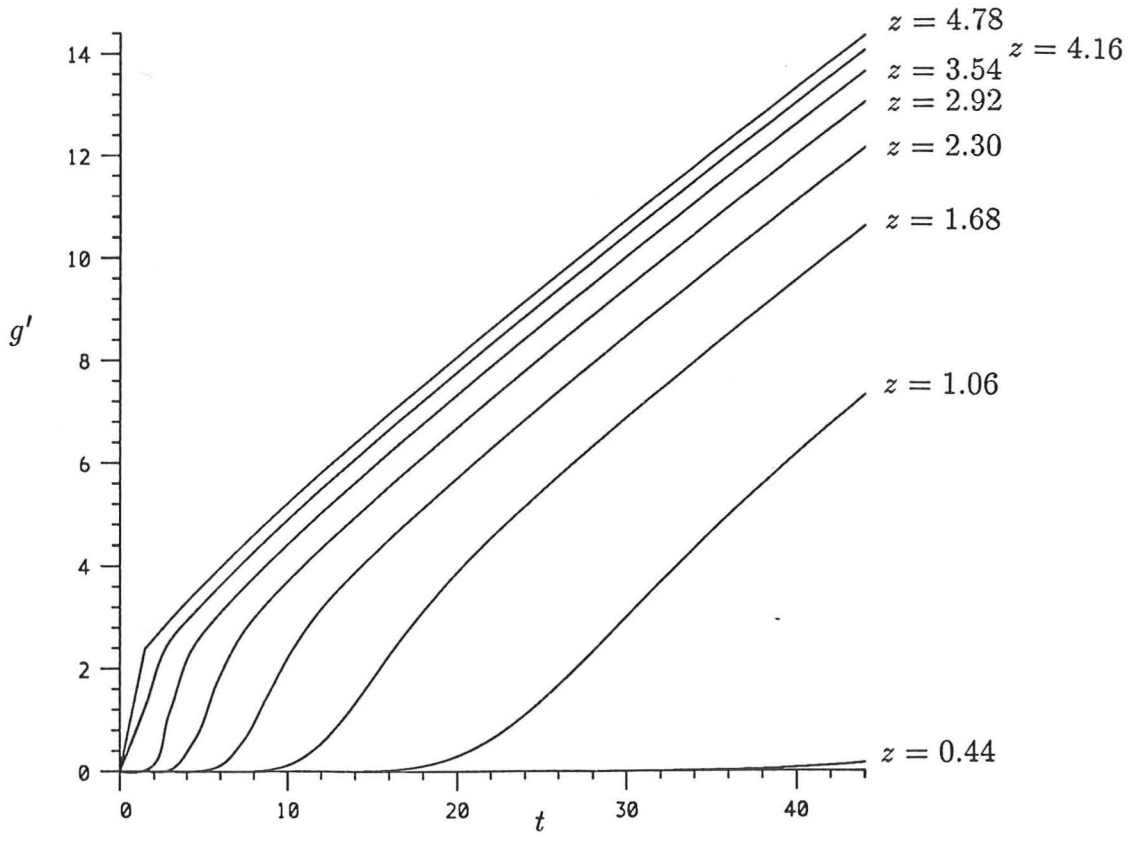

FIGURE 10. The numerical behaviour of the reduced gravity of the fluid in the exterior of the plume at various depths (see figure 3).

$-U$ is still less than that of w. Eventually, however, it might be expected that the threshold condition described in section (3.1) above will be reached, with consequent breakdown in the plume behaviour. In practice though, there is a flow of fluid from the plume forming a thin layer at the base of the tank. This means that the numerical solution shown here is not really applicable for $z \gtrsim 4.78 - \delta h_1$, where δh_1 is the layer thickness. The velocities at this point ($z \simeq 4.78 - \delta h_1$) are then still significantly unequal, so that the plume breakdown threshold is not expected to be reached, except possibly for very large t. Thus the effect of the increasing stratification of the environmental fluid is to decrease the distance between the singularity and the source.

The behaviour of the plume radius, b, is shown in figure $9b$, in which it can be seen that the variation of b with z becomes progressively more nonlinear as t increases, with $b(H,t)$ approaching its threshold value $b \simeq 0.71$.

Finally, the plume and environment reduced gravities are shown in figure $9c$, $g'_p(z,t)$ and $g'_a(z,t)$ respectively (defined relative to the reference density ρ_0). It can be easily seen that at a given height, after a sufficiently large time, both reduced gravities increase linearly with t, and that the reduced gravity of the environment approaches that of the plume.

3.3 Comparison with experiment

The validity of the above simplified model may be tested by comparing the predictions of the numerical solution with concentration measurements from experiments in which a tank of the same aspect ratio is used.

Firstly, the prediction for the concentration behaviour of the fluid exterior to the plume is compared with experimental data. In section 2.2 the concentrations at various heights at a distance of $0.2R$ from the tank wall were discussed (see figure 3). The equivalent numerical solution is given in figure 10. The numerical solution exhibits the same linear time dependence for sufficiently large t, although in the experiments the concentrations seem to increase more rapidly near to the source. This is due to the horizontal non-uniformities of the vertical velocity and density profiles which exist in practice (whereas the analysis assumes uniform profiles) - in particular, the vertical environment velocity is greater near to the walls of the tank than near to the plume. Thus fluid from the plume will reach a given height in the environment (at $x = 0.2R$) more rapidly in practice than the model will predict. Nevertheless, the actual values predicted by the theoretical model agree very well with the

experimental measurements, particularly at points near to the base of the tank.

As a second comparison, it is possible to compare the numerical prediction of the mean reduced gravity averaged along a line through the axis of the plume, perpendicular to the tank walls (a 'centre-slice'), with the experimental values measured using digital video analysis described above. The numerical values are shown in figure 11*a* plotting the 'centre-slice' mean reduced gravity at t intervals $\Delta t = 1.46$. (the solid lines are intervals of $\Delta t = 8.75$). The experimental points discussed in section 2.2 are plotted in figure 11*b* (the experimental time intervals are of one minute), together with the corresponding theoretical prediction from figure 11*a*. The agreement is good, particularly near to the tank base, although again the reduced gravity increases faster near to the source than the numerical solution predicts for the reason given above.

In conclusion, the comparison between this simple numerical model and the experimental results shows that in spite of neglecting the effects of the additional mixing and the horizontal non-uniformity of the velocities and density profiles, the confined plume equations still describe and predict the mean reduced gravities observed in practice to a good degree of accuracy.

When considering taller chambers in the next section, it will become apparent that when connecting the plume and convective regions, the greatest accuracy is required at the base of the plume. It is clear from figure 11*b* that this has been achieved.

4. Chambers with high aspect ratios

Having shown that the modified filling-box equations may still be used to model the behaviour of the mean variables in chambers of moderate aspect ratio $a < 5.8$, chambers of high aspect ratio $a \gtrsim 5.8$ will now be considered. It has already been described how the plume behaviour breaks down near $z \simeq 5.78$ giving rise to a mixed region at the plume base and that the resultant unstable stratification drives mixing of the fluid further away from the source by turbulent convection (see figure 5).

The mixing in this latter region will be studied first, comparing theoretical with experimental mean concentration contours. A simple hypothesis will then be used to connect the plume and convective regions, re-stating the overall equations of motion and comparing their numerical solution with experimental measurements.

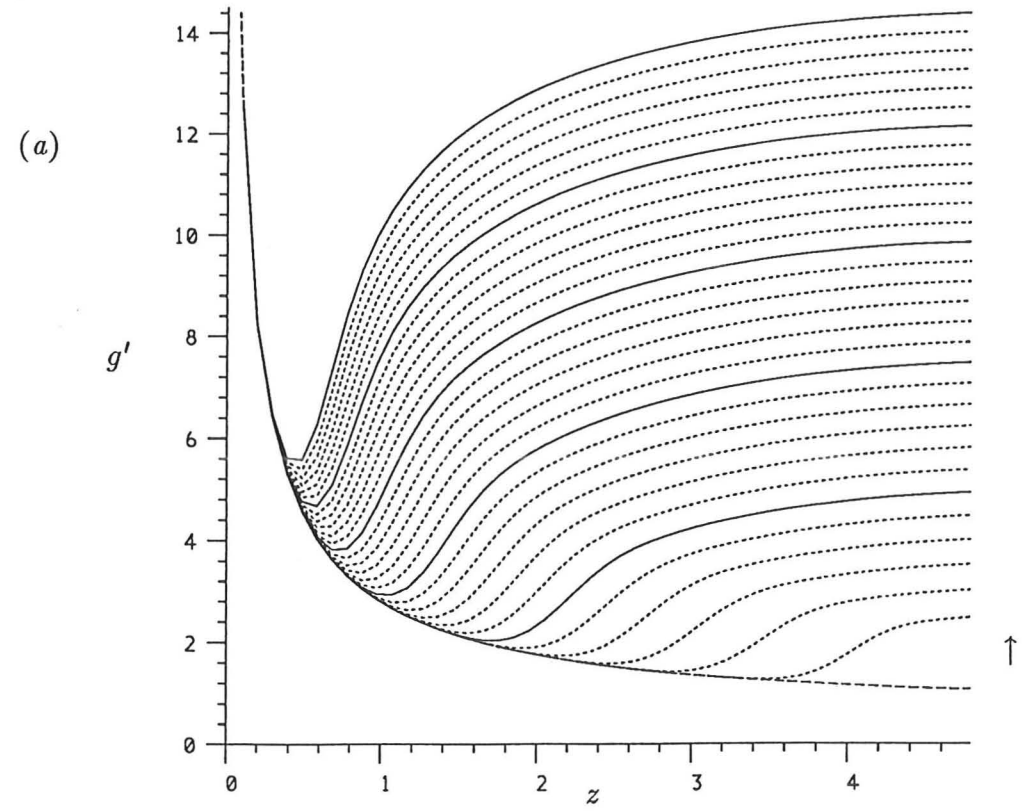

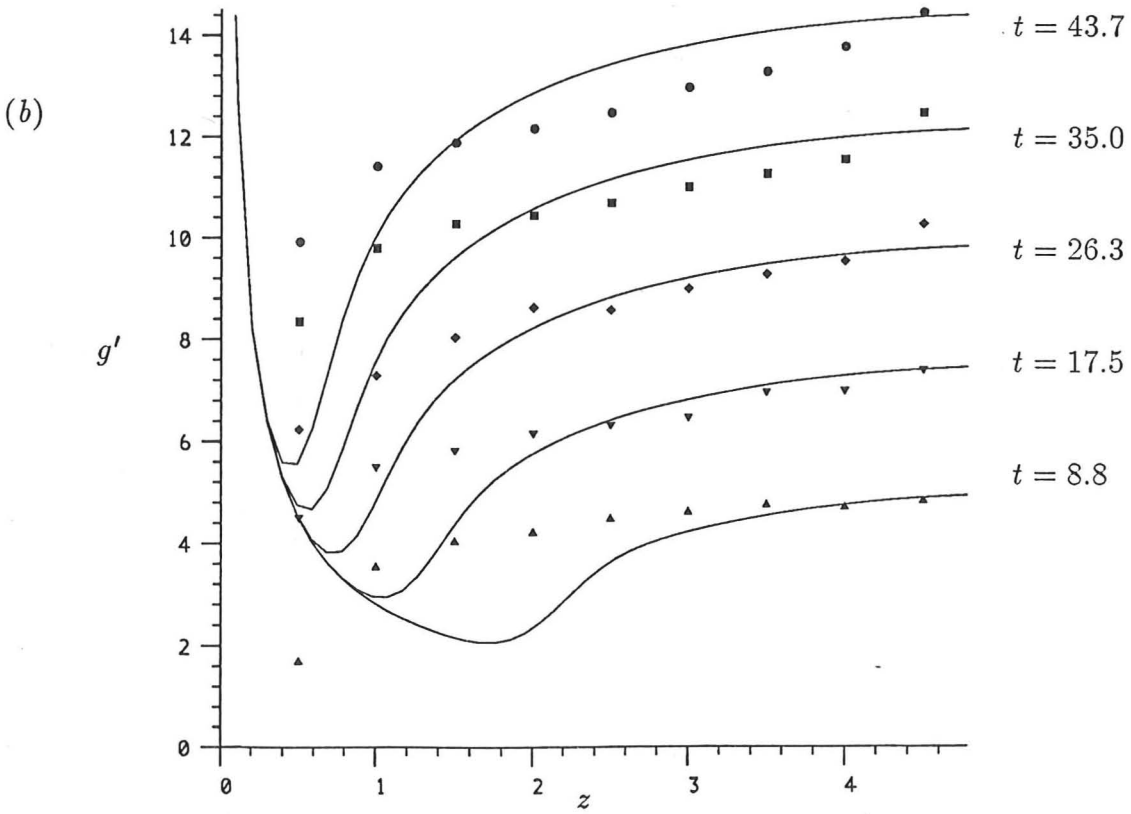

FIGURE 11. (*a*) The numerical behaviour of the mean reduced gravity along a vertical slice through the centre of the chamber after equally spaced t intervals, $\Delta t = 1.46$; (*b*) a comparison between the numerical solution and the experimental results after t intervals, $\Delta t = 8.75$ (which correspond to real-time intervals of one minute in the experiment).

4.1 The convective region

In this section the behaviour of the mean reduced gravity in the convective region is considered. The density distribution is assumed to have been averaged over horizontal planes in the convective region, which has length h_3. In this section, the vertical coordinate z' will refer to the distance along the axis of the container relative to the start of the convective region. The container is closed at the bottom ($z' = h_3$) and so the mean vertical velocity across any horizontal plane is zero. The horizontally averaged density is ρ_c, with reduced gravity $g_3'(z',t) = (\rho_c - \rho_0)g/\rho_0$. Initially the tank is filled with ambient fluid ($g_3' = 0$), and the reduced gravity at $z' = 0$ is $\gamma(t) \equiv g_3'(0,t)$ which in practice will be given by the plume behaviour, although in the following analysis it will be assumed to be a given function.

The one-dimensional equation describing the convection of the buoyant fluid is (see Fischer *et al.* 1979)

$$\frac{\partial g_3'}{\partial t} = \frac{\partial}{\partial z'}\left(\kappa_S \frac{\partial g_3'}{\partial z'}\right), \tag{4.1}$$

where κ_S is the eddy diffusivity. The boundary conditions are

$$\begin{aligned} g_3'(z',0) &= 0, \\ g_3'(0,t) &= \gamma(t), \\ \frac{\partial g_3'}{\partial z'} &= 0 \quad \text{at} \quad z' = h_3, \end{aligned} \tag{4.2}$$

this last condition stating that the buoyancy flux through the base of the container is zero.

The eddy diffusivity κ_S may vary with $\partial\rho_c/\partial z'$ but an analytical solution to the above problem exists when κ_S is constant

$$g_3'(0,t) = \gamma(t), \tag{4.3a}$$

$$g_3'(z' > 0,t) = \frac{\kappa_S \pi}{h_3^2}\int_0^t \gamma(\tau)\sum_{n=0}^{\infty}(2n+1)\exp\left[\frac{\kappa_S}{4h_3^2}(2n+1)^2\pi^2(\tau - t)\right]\sin(n+\frac{1}{2})\frac{\pi z'}{h_3}d\tau. \tag{4.3b}$$

Experimental results may be used to estimate $\gamma(t)$ and an estimate for κ_S may be obtained by comparing the solution given by (4.3) (using this estimate of γ) with experimental measurements.

Figure 12*a* shows the profiles of mean (on horizontal levels) reduced gravity obtained in an experiment in which $a = 27$, with measurements taken at real-time intervals of 30 seconds.

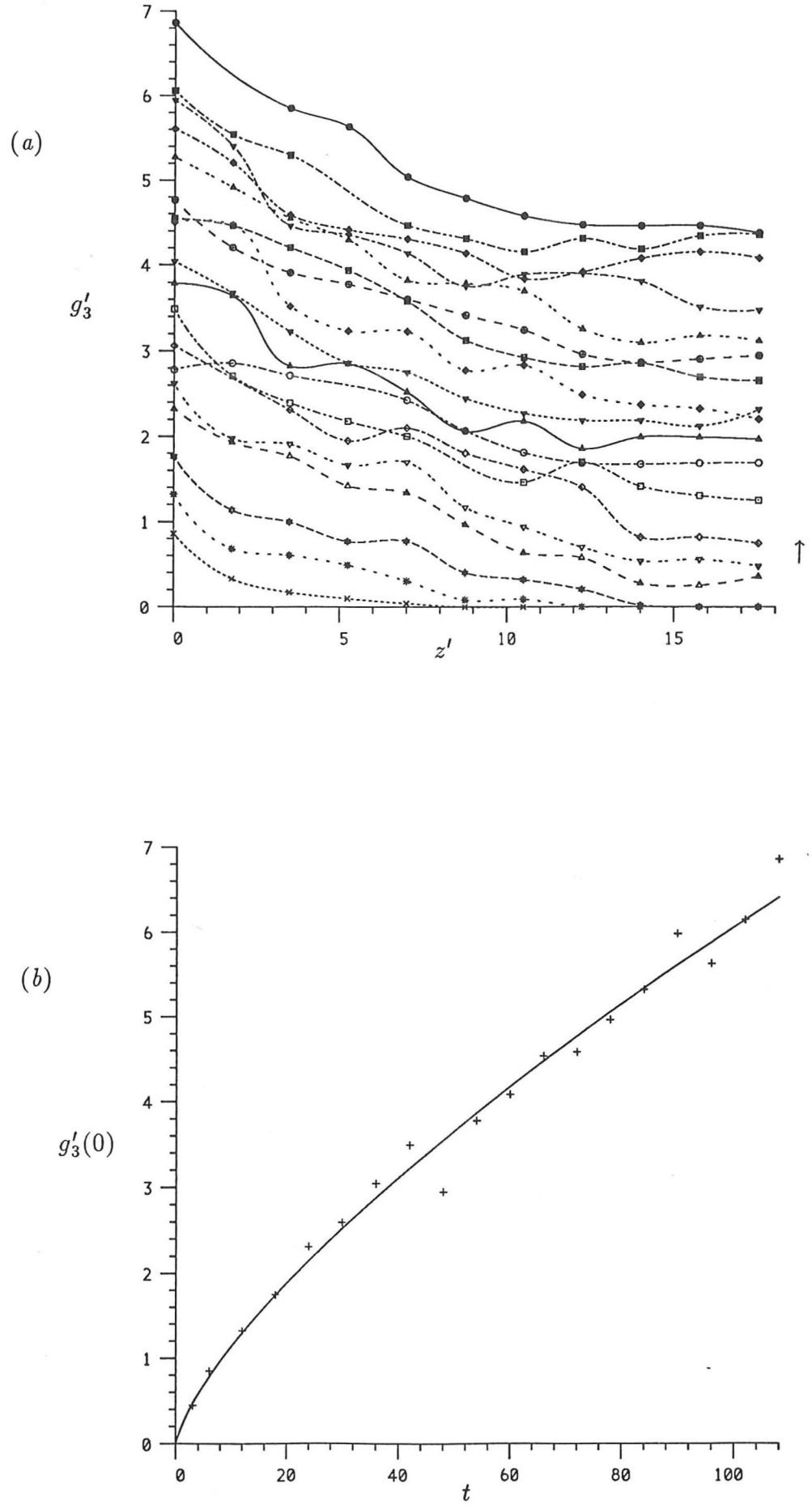

FIGURE 12. (a) The profiles of reduced gravity in the convective region, measured after successive t intervals, $\Delta t = 6.0$ (which correspond to real-time intervals of 30 seconds), in an experiment in which $a = 27$; (b) the behaviour of $g_3'(0) \equiv \gamma(t)$, fitted to a power law.

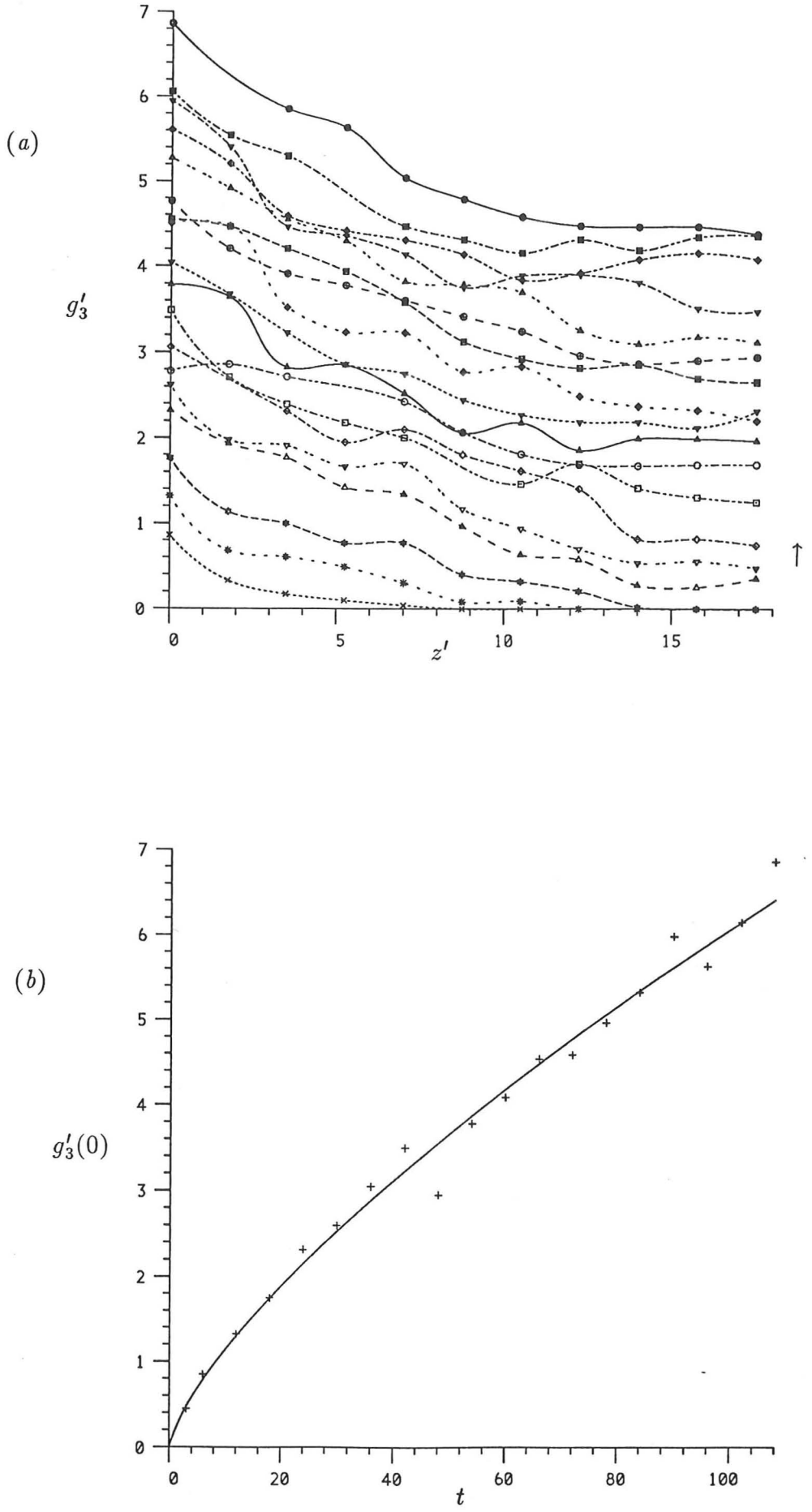

FIGURE 12. (a) The profiles of reduced gravity in the convective region, measured after successive t intervals, $\Delta t = 6.0$ (which correspond to real-time intervals of 30 seconds), in an experiment in which $a = 27$; (b) the behaviour of $g_3'(0) \equiv \gamma(t)$, fitted to a power law.

(c)

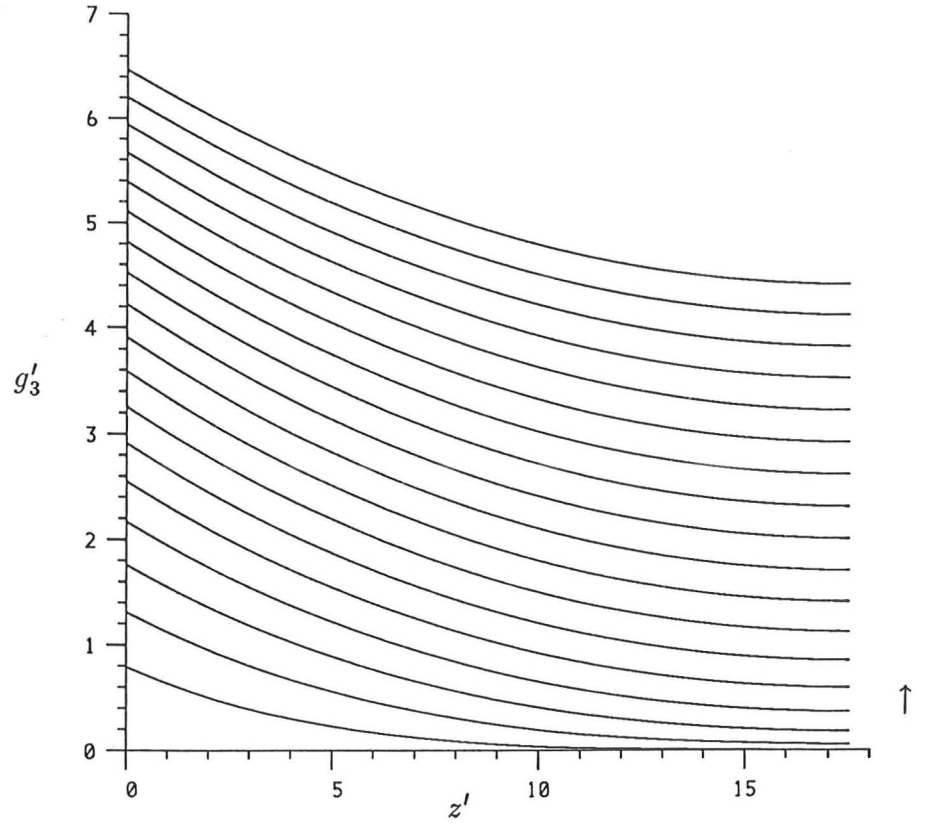

(d)

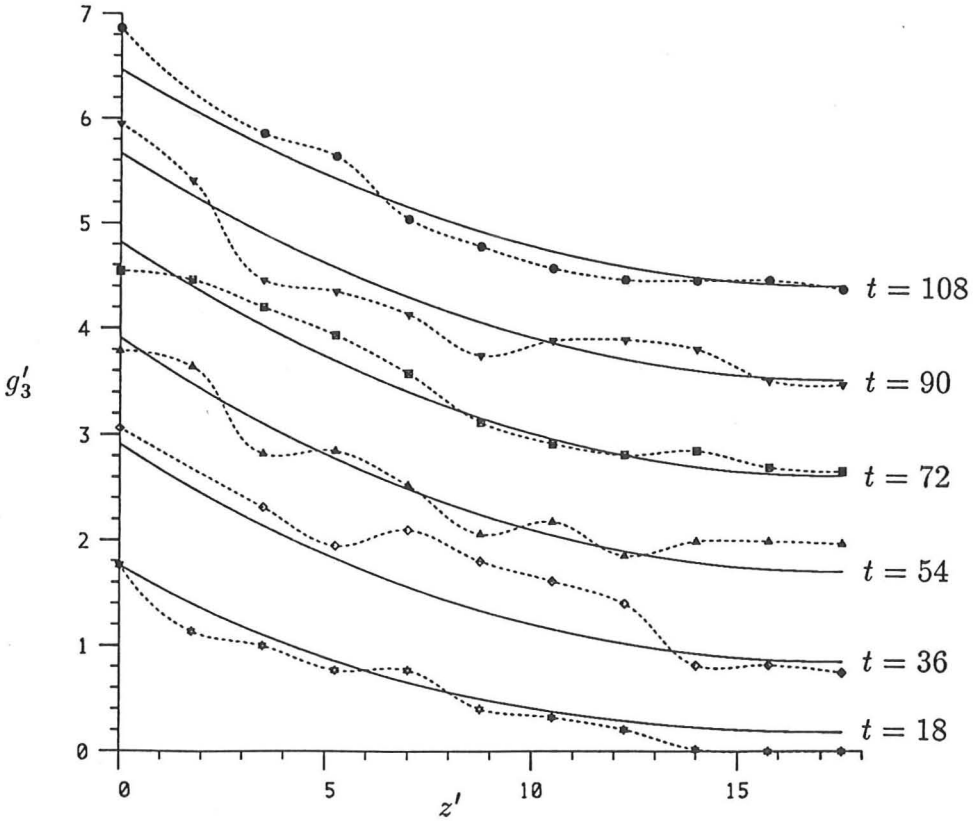

FIGURE 12. ct'd. (c) The analytical solution of (4.3) calculated using the power law expression for $\gamma(t)$ obtained from the data of figure 12b; (d) a comparison between the theoretical and experimental profiles at selected values of t.

The convective region *only* is shown over the range $9 < z < 27$. The reduced gravity at $z = 9$ (or $z' = 0$), i.e. the top of the convective region that is considered here, is plotted against t in figure 12*b* and a least-squares fit (the solid line) was used to estimate that $\gamma(t) \propto t^{0.726}$. Using this expression in the analytical solution above, a value of the eddy diffusivity providing the best fit may be found. The analytical solution with $\kappa_S = 1.50$ is shown in figure 12*c* and a comparison between the experimental data and theoretical solution is shown in figure 12*d*. The theoretical solution provides a good prediction of the mean values, although there is some fluctuation of the experimental data about the theoretical profiles (as expected, given the underlying eddy nature of the mixing process). Repeating this process with three further experiments gave a mean value of the eddy diffusivity, $\kappa_S = 1.52 \pm 0.03$, which will be used in the overall model later.

In the above analytical solution it was assumed that the value of κ_S is constant although in practice κ_S could vary with $\partial\rho_c/\partial z'$. Since the local density gradients are small (in the previous solution $\partial g_3'/\partial z'$ has a maximum absolute value in the time period shown of about 0.1), for variable κ_S an expansion of the form

$$\kappa_S\left(\frac{1}{\rho_0}\frac{\partial\rho_c}{\partial z'}\right) \simeq \epsilon_0\left[1 + \epsilon_1\frac{1}{\rho_0}\frac{\partial\rho_c}{\partial z'} + \epsilon_2\left(\frac{1}{\rho_0}\frac{\partial\rho_c}{\partial z'}\right)^2 + \cdots\right], \tag{4.4}$$

where ϵ_i are constant expansion coefficients, could be assumed. The effect of including first and second order terms is shown in figure 13 to be negligible for all but very large values of ϵ_1 and ϵ_2. In figure 13*a* the effect of a non-zero ϵ_1 on the solution is shown, plotting the numerical solution of (4.1) (solved using a NAG Fortran library routine), using the above form for $\gamma(t)$. The positive values of ϵ_1 decrease the concentration values and vice-versa. Figure 13*b* shows the lesser effect of a non-zero ϵ_2, where in this case positive values increase the concentration values and vice-versa.

The theoretical solution (4.3) will be used in the formulation of the whole problem, with the above discussion showing that it is sufficient to assume that κ_S is constant.

4.2 The mixing region

The first and last regions of the flow observed in containers of large aspect ratio, namely the plume and convective regions, have now been formulated. In practice these regions are not distinct, and both effect the behaviour of each other. The rate at which the mixing takes place in the convective region depends on the density gradients achieved at the base of the

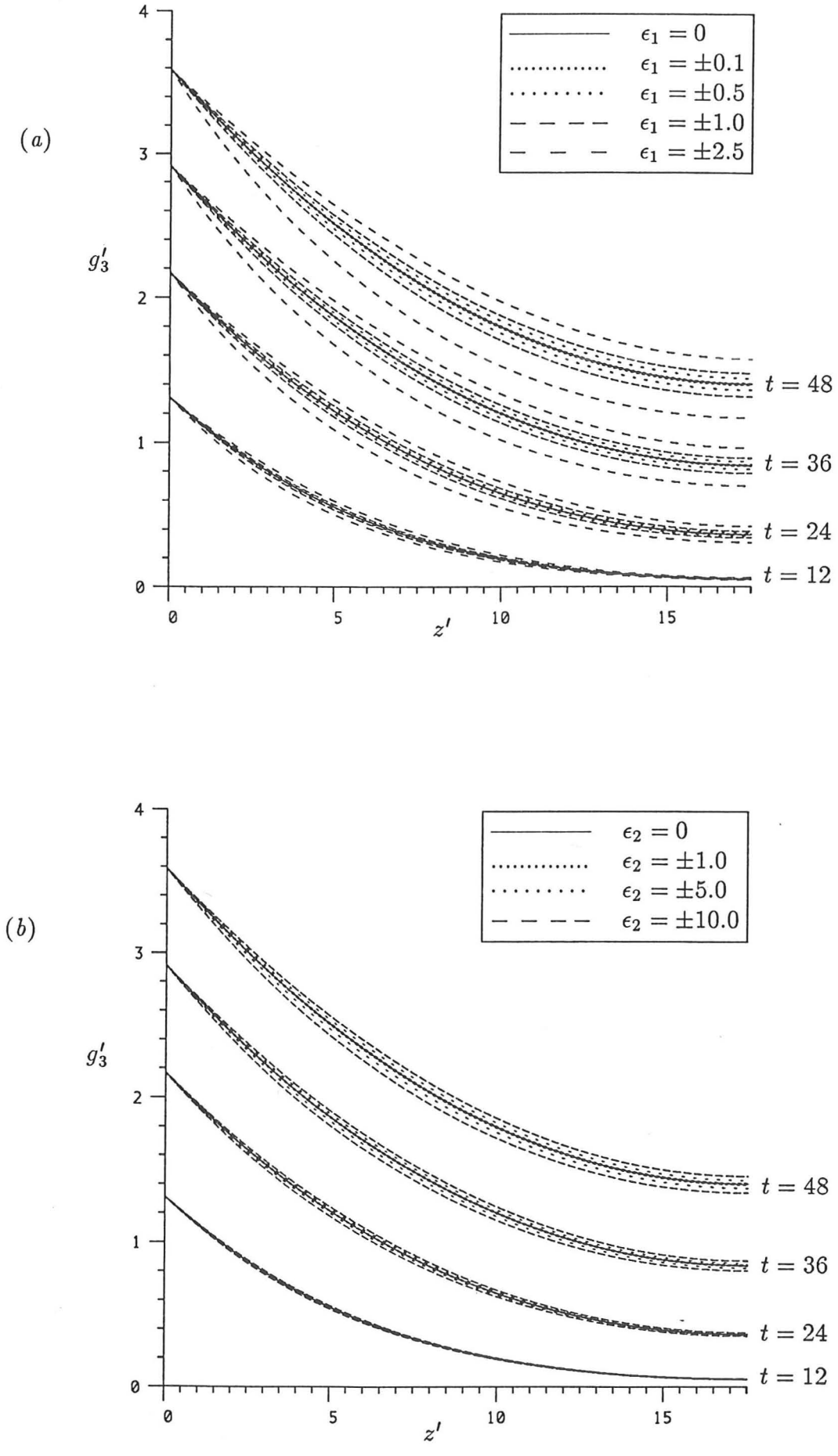

FIGURE 13. The effect of first and second order terms in κ_S on the theoretical solution; (*a*) $\epsilon_1 \neq 0$, $\epsilon_2 = 0$; (*b*) $\epsilon_1 = 0$, $\epsilon_2 \neq 0$.

plume, but conversely the rate at which dense fluid is mixed into the convective region affects the concentration of the fluid that is re-entrained into the plume - and so on.

This interaction is modelled by supposing the existence of a mixed region of constant length h_2 at the base of the plume. It is assumed that dense fluid from the plume at $z = h_1$ is instantaneously mixed with that of the mixed region, which has density $\rho_m(t)$ and reduced gravity $g_2'(t) = (\rho_m - \rho_0)g/\rho_0$. In practice this mixing is driven by the opposing velocities of the plume and environmental fluids. The mixed region forms a negatively buoyant layer above (for a negatively buoyant source) the less buoyant convective region and so some of the buoyant fluid from the mixed region mixes with that of the convective region. This results in a flux of buoyancy from the mixing region into the convective region, by an amount which will be determined by the density gradient at the top of the convective region. At the same time fluid from the mixed region flows into the environment of the plume. Thus an equation for conservation of buoyancy in the mixed region can be derived as follows.

Firstly the total buoyancy input from the plume in time δt is given by

$$\pi Q(h_1, t) \left(\frac{\rho_p(h_1, t) - \rho_0}{\rho_0} \right) g \, \delta t, \tag{4.5}$$

(recall that $Q(z,t) = b^2 w$ is the plume volume flux) which will be mixed over the length h_2 of the mixing region. Secondly, the total buoyancy of the convective region, $\mathcal{G}$, can be obtained by integrating (4.3) above

$$\mathcal{G} = \int_0^{h_3} \pi g_3'(z', t) \, dz', \quad \text{where} \quad z' = z - h_1 - h_2. \tag{4.6}$$

Thus the buoyancy flux into the convective region, $\lambda(t)$, is given by

$$\lambda(t) = \frac{d\mathcal{G}}{dt}. \tag{4.7}$$

Thirdly there is the buoyancy flux of the fluid flowing from the mixed region into the plume environment. This flow must have the same volume flux as that of the fluid flowing into the mixed region from the plume (by continuity).

Finally the dependence of $\gamma(t)$ and $\rho_a(h_1, t)$ on the reduced gravity of the mixed region, g_2', must be determined. The most simple assumption that can be made is that

$$\gamma(t) \equiv g_3'(0,t) = g_2'(t) \quad \text{and} \quad \left(\frac{\rho_a(h_1, t) - \rho_0}{\rho_0} \right) g = g_2'(t), \tag{4.8}$$

i.e. that the reduced gravities of the fluid at the top of the convective region and the fluid flowing from the mixed region into the environment of the plume are the same as that of the mixed region. Thus conservation of buoyancy within the mixing region is given by the equation

$$[g_2'(t+\delta t) - g_2'(t)]h_2 = \left[Q(h_1,t)\left(\frac{\rho_p(h_1,t)-\rho_0}{\rho_0}\right)g - Q(h_1,t)g_2'(t) - \lambda(t)\right]\delta t, \qquad (4.9)$$

or in the limit $\delta t \to 0$,

$$\frac{dg_2'}{dt} = \frac{1}{h_2}\left(Q(h_1,t)g_1'(h_1,t) - \frac{d\mathcal{G}}{dt}\right). \qquad (4.10)$$

4.3 The combined model

The formulation of the whole flow in high aspect ratio chambers will now be restated briefly before considering and comparing the numerical solution and experimental measurements.

The flow is divided into three regions, namely the plume, mixing and convective regions, of heights h_1, h_2 and $h_3 = H - h_1 - h_2$, respectively. The first region contains the source of the motion, a plume whose motion satisfies the equations given in section 3. The third region is a convective region with horizontally averaged reduced gravity $g_3'(z,t)$, described in section 4.1. The second region is a mixing region which connects the plume and convective regions and has been described in section 4.2 above. The length and time scales have been non-dimensionalised using the effective radius R and the source initial buoyancy flux, B_0. Thus the equations of motion for the whole flow may be summarised in non-dimensionalised form as follows

$$\left.\begin{aligned}
\frac{d}{dz}(b^2w) &= 2\alpha_p bw,\\
\frac{d}{dz}(b^2w^2 + (1-b^2)U^2) &= b^2g_1',\\
\frac{d}{dz}(b^2wg_1') &= -\frac{gb^2w}{\rho_0}\frac{\partial\rho_a}{\partial z},\\
(b^2-1)U &= b^2w,\\
\frac{\partial\rho_a}{\partial t} &= -U\frac{\partial\rho_a}{\partial z},\\
\left(\frac{\rho_a(h_1,t)-\rho_0}{\rho_0}\right)g &= g_2'(t),\\
\text{with}\qquad b(0,t) = U(0,t) &= 0 \quad\text{and}\quad [b^2wg_1'](0,t) = 1,
\end{aligned}\right\} \; 0 \leqslant z \leqslant h_1, \qquad (4.11)$$

$$\left.\begin{aligned} \frac{dg_2'}{dt} &= \frac{1}{h_2}\left(Q(h_1,t)g_1'(h_1,t) - \frac{d}{dt}\int_0^{h_3} g_3'(z',t)dz'\right), \end{aligned}\right\} \quad h_1 \leqslant z \leqslant h_1 + h_2, \tag{4.12}$$

$$\left.\begin{aligned} \frac{\partial g_3'}{\partial t} &= \kappa_S \frac{\partial^2 g_3'}{\partial z'^2}, \\ g_3'(z'=0,t) &= g_2'(t), \\ \frac{\partial g_3'}{\partial z'} = 0 \quad \text{at} \quad z = H \quad \text{or} \quad z' &= h_3, \end{aligned}\right\} \quad h_1 + h_2 \leqslant z \leqslant H \quad \text{or} \quad 0 \leqslant z' \leqslant h_3, \tag{4.13}$$

$$\text{with initial values} \qquad \left(g_a'(z,0) \equiv \frac{\rho_a(z,0) - \rho_0}{\rho_0}\right) g = g_2'(0) = g_3'(z',0) = 0. \tag{4.14}$$

The choices of H, h_1, h_2 and κ_S define the numerical solution, although clearly H is set by the comparative experiment (as are the non-dimensionalising quantities R and B_0), and h_1 and κ_S have been estimated in sections 3.1 and 4.1 above. Note that, whereas in section 4.1 an artificial function $\gamma(t)$ was used to specify the reduced gravity at the top of the convective region, now this boundary condition is determined by the reduced gravity of the mixed region, which in turn is determined by the plume flow.

4.4 The numerical solution and comparison with experiments

The system of equations above was integrated numerically to obtain the solution. At each time step the solutions to (4.11) and (4.13) were calculated (using NAG Fortran routines). The plume exterior density ρ_a and mixing region density ρ_m were then updated before the next iteration.

A numerical solution with $H = 27$, $h_1 = 5.5$, $h_2 = 2$ and $\kappa_S = 1.52$ is shown in figure 14*a*, with profiles plotted after equally spaced t intervals. This is then compared with measurements from an experiment, with the same value of H/R, in figure 14*b* (see also figure 6). The mean reduced gravity at points along a 'centre-slice' are shown in the figures as this was measured in the experiments for reasons explained in section 2.1 above. The part of the profile joining the plume region to the mixing region is drawn with a dashed line.

The numerical solution is well behaved and exhibits the main features of the experimental results. Firstly in the plume region, $0 \leqslant z \lesssim 5.5$, the profiles take the same form that

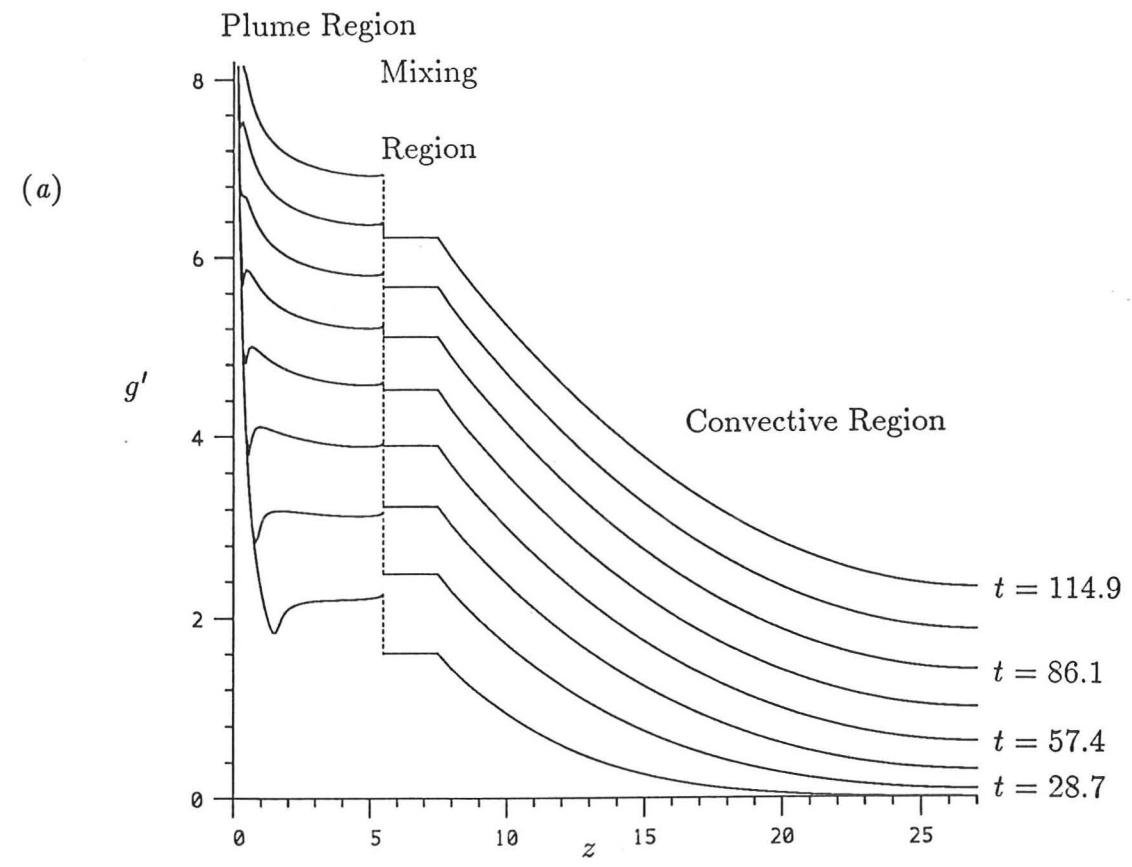

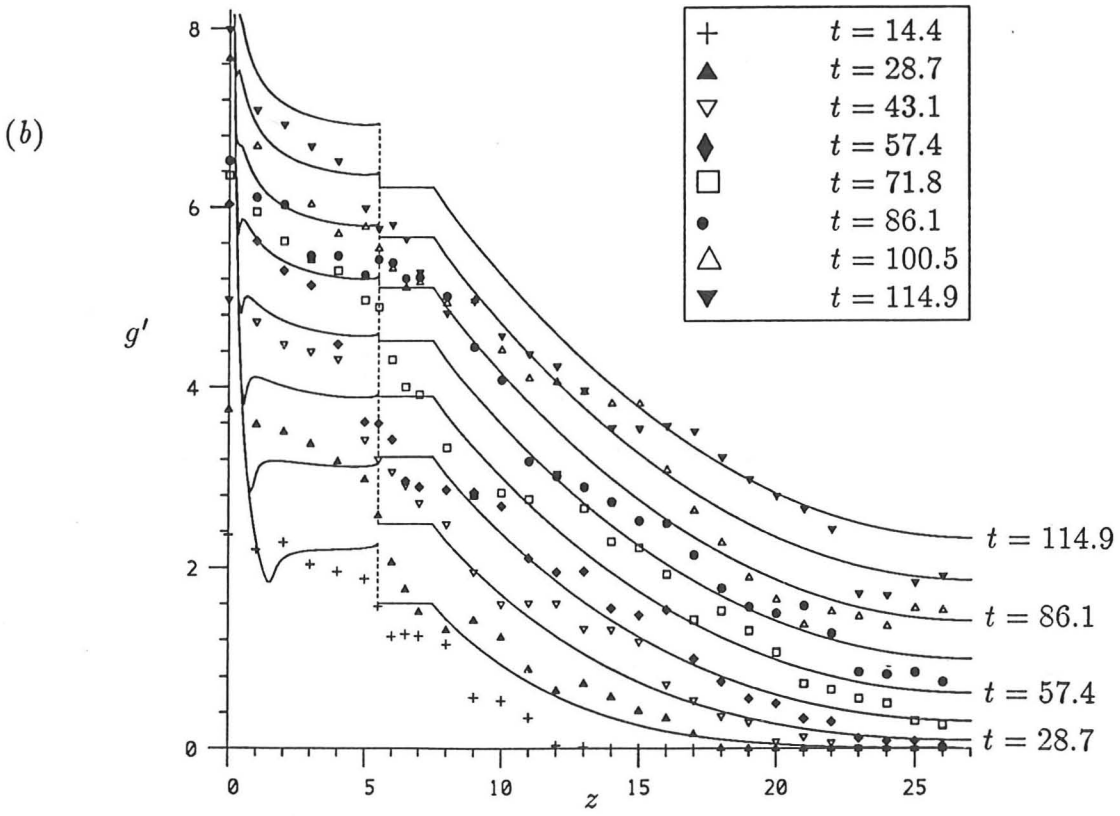

FIGURE 14. (*a*) The numerical solution of the model for large aspect ratios ($a = 27.1$ here), plotting the solution after equally spaced t intervals, $\Delta t = 14.35$, for comparison with (*b*) an experiment in which $a = 27.1$ (the real-time intervals are of one minute in the experiment).

has been illustrated earlier (see figures 4 and 11), although now the spacing between the curves decreases with time (as pointed out in section 2.3 following figure 6), whereas for lower aspect ratio containers the concentration increased linearly in time. This is a direct result of the loss of buoyancy from the plume to the mixing and convective regions. The nonlinear time-dependence in the plume region shown by the numerical solution agrees quite well with its comparative experiment, indicating that the mixing region hypothesis used above approximates the buoyancy transfer from the plume to convective regions reasonably.

The steps observed in the numerical solution at $z = h_1$ are a consequence of the assumption that the density is constant over the whole length of the mixing region. The mixing region concentration should not exceed that of the fluid at the base of the plume and this is clearly the case in the numerical solution, resulting in a jump in the 'centre-slice' reduced gravity between the fluid at the plume base and that at the top of the convective region. This drop in concentration value is also observed in some of the experimental contours (see figures 6 and 14*b*). The theoretical mixing region concentration is found to vary approximately as $g_2' \sim t^{0.68}$ which is in good agreement with the experimentally obtained approximation used in section 4.1 ($\gamma(t)$ there).

Finally the prediction for the behaviour of the convective region may be compared with the experimental results. There is a large degree of scatter in the experimental results, due to the eddy nature of the mixing process, and so no numerical solution will ever agree perfectly with them. However, the numerical solution models the general behaviour reasonably well, particularly for larger times, although overall the numerical concentration values tend to be slightly higher than the experimental. This may be due to inaccuracies in the measurement of the buoyancy flux in the experiment, which mean that the theoretical values are accurate to about $\pm 4\%$. The dependence of the solution on h_2 is weak, and in order to obtain significantly better agreement with the experimental values, the value of h_2 must be increased beyond what can be considered to be a physically realistic value.

The above comparison has been made between a single experiment and the numerical solution. This is because the degree of scatter in the experimental data is such that using more than one set of experimental results would have made the figure much more confusing. However, it is possible to compare more than one experiment with the numerical solution by taking measurements at a specific value of t. Figure 15 shows measurements from three experiments (all with $a = 27$) at $t = 71.8$. The agreement is good although again there is considerable scatter between each set of experimental measurements.

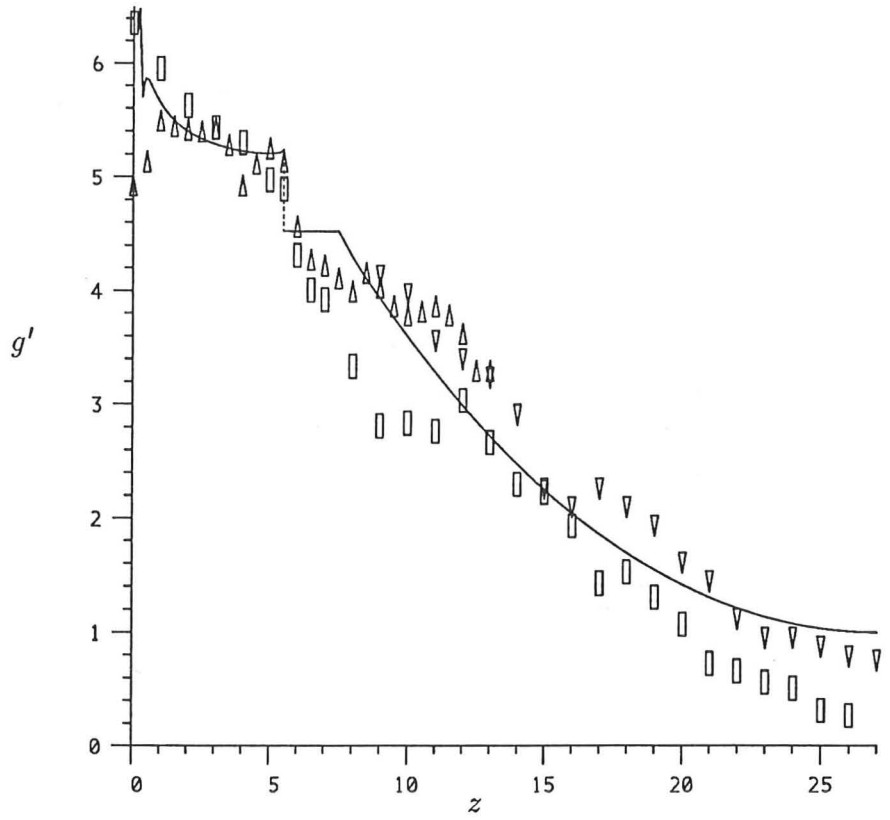

FIGURE 15. A comparison between the concentration values obtained from three experiments and the numerical solution at $t = 71.84$.

5. Discussion and conclusions

In this chapter, the flow and concentration field produced by a buoyant convection from a source in a vertical tank of initially still, uniform fluid with aspect ratio, $a > 1$, has been investigated experimentally and theoretically. When $a \leqslant 1$, the flow can be described well by the 'filling-box' theory of Baines & Turner (1969).

It was shown that the behaviour of a plume confined to a container of large depth will eventually break down at $z \simeq 5.78$, with the plume flow becoming undefined. Flows in containers of general aspect ratio can thus be divided into two types: those in which the plume breakdown does not occur, ($a < 5.8$) and those for which it does ($a \geqslant 5.8$).

For containers of moderate aspect ratio ($1 \leqslant a < 5.8$) it was found that the behaviour of the mean flow variables can still be modelled well by the confined plume equations (3.1), (3.2), (3.4), (3.8) and (3.9) - the numerical solution agreed well with experimental data. The numerical solution predicted that the concentrations will increase linearly in time after sufficiently large times, which was observed experimentally. This is also in agreement with the assumption that Baines & Turner (1969) used in their asymptotic theory for low aspect ratio containers. The numerical solution also predicted that the point at which plume breakdown occurs will move closer to the source as the fluid exterior to the plume becomes progressively more stratified. However, the flow of the plume near to the tank base must be allowed for: the fluid flowing away from the plume on the tank base effectively restricts the application of the numerical solution to all points except those sufficiently close to the base to be influenced by it. Finally, the numerical solution also predicted that as the radius of the plume becomes comparable to the container effective radius, and as the environment of the plume becomes more stratified, the rate of increase of the plume radius with increasing axial distance from the source increases faster than the linear relationship found in an infinite unstratified environment.

For containers of larger aspect ratio, the plume breakdown threshold above *will* be attained. This gives rise to a mixing region at the base of the plume, in which the downward plume fluid is mixed with the upward flowing environmental fluid. The unstable density gradient thus created drives mixing of the buoyant fluid at the base of the plume with the fluid further from the source. The convective region was found to be modelled well by a simple one-dimensional diffusion equation with an eddy diffusivity, although the experimental measurements exhibited quite large fluctuations about the predicted mean values due to the

underlying eddy nature of the mixing process. The main boundary condition of this flow is the concentration at the end nearest to the source. The reduced gravity at this point was estimated by using experimental measurements. Good agreement was found between the analytical solution and the experimental data when $\kappa_S = 1.52 \pm 0.03$, the value which was used in the numerical analysis of the whole system.

The plume and convective regions were then connected theoretically using a simple mixing-region hypothesis. Briefly, this hypothesis asserted that the buoyant fluid from the plume entering the mixing region would be immediately mixed over its length h_2. The subsequent value for the mixing region reduced gravity was then the boundary condition for the reduced gravity at the top of the convective region and also the reduced gravity of the fluid entering the plume environment to be re-entrained into the plume. These boundary conditions are then effectively set by the value of h_2. Good general agreement between the numerical solution and experimental measurements was found in all three regions when $h_2 \simeq 2$, i.e. the length of the mixing region is of the order of a tank diameter. The concentration values predicted by the numerical solution are in general slightly higher than those of the experiments, although this may be due to inaccuracies in the measurement of the experimental buoyancy flux. The numerical model demonstrated the experimental observation that the concentration increase in the plume region is no longer linear in time, the rate of increase decreasing. Hence it was concluded that the simple mixing region hypothesis used to link the plume and convective regions models the transfer of buoyancy between them reasonably well.

The practical implications of this work suggest that, if, say, there was a slow leak of natural gas at the bottom of a tall tower or lift shaft, the gas would *not* quickly rise to the top of the chamber as might be expected. In fact high gas concentrations (which are increasing in time) would be attained in the environment of the plume near to the source, with comparable concentrations achieved at the top of the tower only after a relatively long period of time. If the leak was at the bottom of a mine shaft, then the effects of ventilation are likely to be significant. Mine shafts are normally used for venting the mines, with fresh air flowing down one shaft and up another. If the gas leak was at the bottom of the shaft with up-flowing air, then the ventilation would act to disperse the gas. However if the leak was in the shaft with the down-flowing air, then, if the speed of the air was significantly less than that of the leak, then the ventilation system could act to suck high gas concentrations into the mine system.

Notation

Below is a list of the symbols used in this chapter, provided for reference purposes.

a	Aspect ratio
$B_{(0)}$	(Initial) specific buoyancy flux of the plume
b	Plume radius
g'_1	Reduced gravity of the plume fluid, relative to the environment fluid
$g'_{2,3,a,p}$	Reduced gravity of the mixing region/convective region/environment/plume fluid, relative to the reference density
$\mathcal{G}$	Total buoyancy in the convective region
H	Height of the tank
$h_{1,2,3}$	Height of the plume/mixing region/convective regions
$I(x,z)$	Intensity function
M	Local specific momentum flux of the plume
Q	Local specific volume flux of the plume
R	Effective radius of the tank
Ra	Rayleigh number
t	Time
U	Mean (vertical) velocity of the fluid in the environment of the plume
w	Mean (vertical) velocity of the plume fluid
z	Vertical coordinate
z'	Vertical coordinate in the convective region
α_p	Entrainment constant for a plume
$\gamma(t)$	Reduced gravity at the top of the convective region
ϵ_i	Coefficient in expansion of κ_S
κ	Thermal conductivity
κ_S	eddy diffusivity
λ	Buoyancy flux from the mixing to convective regions
ν	Kinematic viscosity
$\rho_{a,c,m,p}$	Density of the fluid in the environment/convective region/mixing region/plume
ρ_0	Reference density

Chapter Six

Buoyant Convection from a Source in a Tall, Angled Chamber

In this chapter the work of chapter 5 on buoyant sources in tall, vertical chambers is extended: the chamber is now placed at an angle to the vertical. Only chambers with aspect ratio greater than six are considered so that the plume breakdown threshold described in the previous chapter is reached.

In tall, angled chambers, the convective region observed in vertical chambers is replaced by a two-layer counterflow, with mixing between the layers. Dense fluid is mixed more quickly with the fluid far from the source than was observed in the vertical case.

A simple model of the motion of the counterflow is presented and the numerical solution is compared with experimental measurements. The counterflow is then mathematically linked with the plume region, in a manner analogous to that used in the previous chapter, to obtain an overall model of the flow. The theoretical predictions for the whole flow are compared with experimental data.

---

1. Introduction

In the previous chapter the flow resulting from a point source of buoyancy in a tall, vertical chamber was examined. It was found that at a distance of about six 'effective' chamber radii from the source the plume flow breaks down giving rise to a mixed region. Some of the fluid from this region then mixes with the fluid further from the source by a turbulent convection process. This convective region had no observable ordered structure.

In many practical cases the chamber will not be vertical and will be placed at an angle, $\theta > 0°$, to the vertical (for example, consider the flow of smoke or natural gas in an escalator shaft). Thus it is important to investigate the effect of placing the chamber at an angle on the flow observed in vertical chambers. In preliminary experiments it was observed that, even for small angles, the convective region was replaced by a two layer counterflow with dense fluid flowing down the lower side of the tank and ambient fluid flowing up the opposite side (see figure 1) with mixing between the two layers. Thus the flow is very different to the vertical case, the difference being due to the presence of a component of gravity perpendicular to the sides of the tank. However, in the plume and mixing regions, the flow appeared to be similar to that observed in the vertical case.

The flow of a buoyant layer or gravity current down a slope has received some attention. Gravity currents on slopes may occur naturally in, for example, thunderstorm outflows, and in industrial or domestic situations, such as the gas escape mentioned above. Britter & Linden (1980) list a number of authors who have reported experimental data for these flows. Britter & Linden (1980) cover the whole range of slopes $0° \leqslant \theta \leqslant 90°$ confirming the finding of Ellison & Turner (1959) that, for all but very small slopes, the velocity of the front is independent of position down the slope. They also found that the mixing at the front increased dramatically with the slope but that the front velocity was virtually independent of the slope for $0° < \theta \leqslant 85°$.

The form of this chapter will be similar to that of chapter 5. The experiments and general experimental observations will be described in section 2. In section 3 the model of the counterflow will be derived comparing the theoretical predictions with experimental measurements in this region. In section 4 the plume region will be coupled with the counterflow (analogous to section 4.2 of chapter 5) thus obtaining the overall model. The numerical solution to the whole model will be compared with experimental concentration and velocity measurements.

2. Experiments

As in chapter 5 some experimental observations and measurements will now be presented before analysing the problem theoretically. These measurements will show how the concentration behaviour varies in different regions of the flow and how it contrasts with that of the flow described in chapter 5.

2.1 Experimental technique and apparatus

The experiments were conducted using a perspex tank of length 1.2 m, with a square cross-section of side 8 cm. The lower end of the tank was closed. Dyed salt solution was pumped in slowly from the upper end of the tank with the nozzle pointing along the axis. The flow rate was chosen to be sufficiently slow so that the 'jet-length' (see chapter 2) was small compared with the width of the tank - the effects of initial source momentum may then be neglected. The buoyancy flux of the source could be varied by altering the salt concentration of the reservoir fluid or the flow rate of the source. The tank was clamped to background illumination, which consisted of two fluorescent lights placed behind a diffusing screen. The whole apparatus could be positioned at an angle to the vertical. Slopes in the range $1° \leqslant \theta \leqslant 60°$ were used in the experiments.

The experiments were recorded on video tape for subsequent image processing. The procedure was calibrated by recording pictures of the tank filled with fluid of known uniform concentration. The linear variation of pixel intensity with dye concentration, that has been reported previously (see chapter 4, figure 9*b*), was observed for all but the highest concentrations. The non-linearity for high dye concentrations was taken into account when calculating the reduced gravities from the intensities.

The investigation described here will be restricted to a consideration of very tall chambers (aspect ratio greater than six) so that the plume breakdown threshold, described in chapter 5, is reached. All of the experimental results presented here were made using an aspect ratio $a = H/R = 24$, where a is defined in terms of the length of the tank, H, and the 'effective radius', R - the radius of a circle with equal cross-sectional area to that of the tank. This was the largest aspect ratio obtainable practically, used because it should produce the largest possible variation in concentration.

2.2 Experimental observations

The observed flow is drawn schematically in figure 1. It has already been stated that the convective region of chapter 5 is now replaced by a two layered counterflow system. This is because there is now a component of gravity acting in the direction perpendicular to the walls of the tank, resulting in a pressure difference at points diametrically opposite in the mixed region. This results in a buoyant outflow from the mixed region, analogous to the gravity current flow produced by the release of buoyant fluid from a lock exchange (see

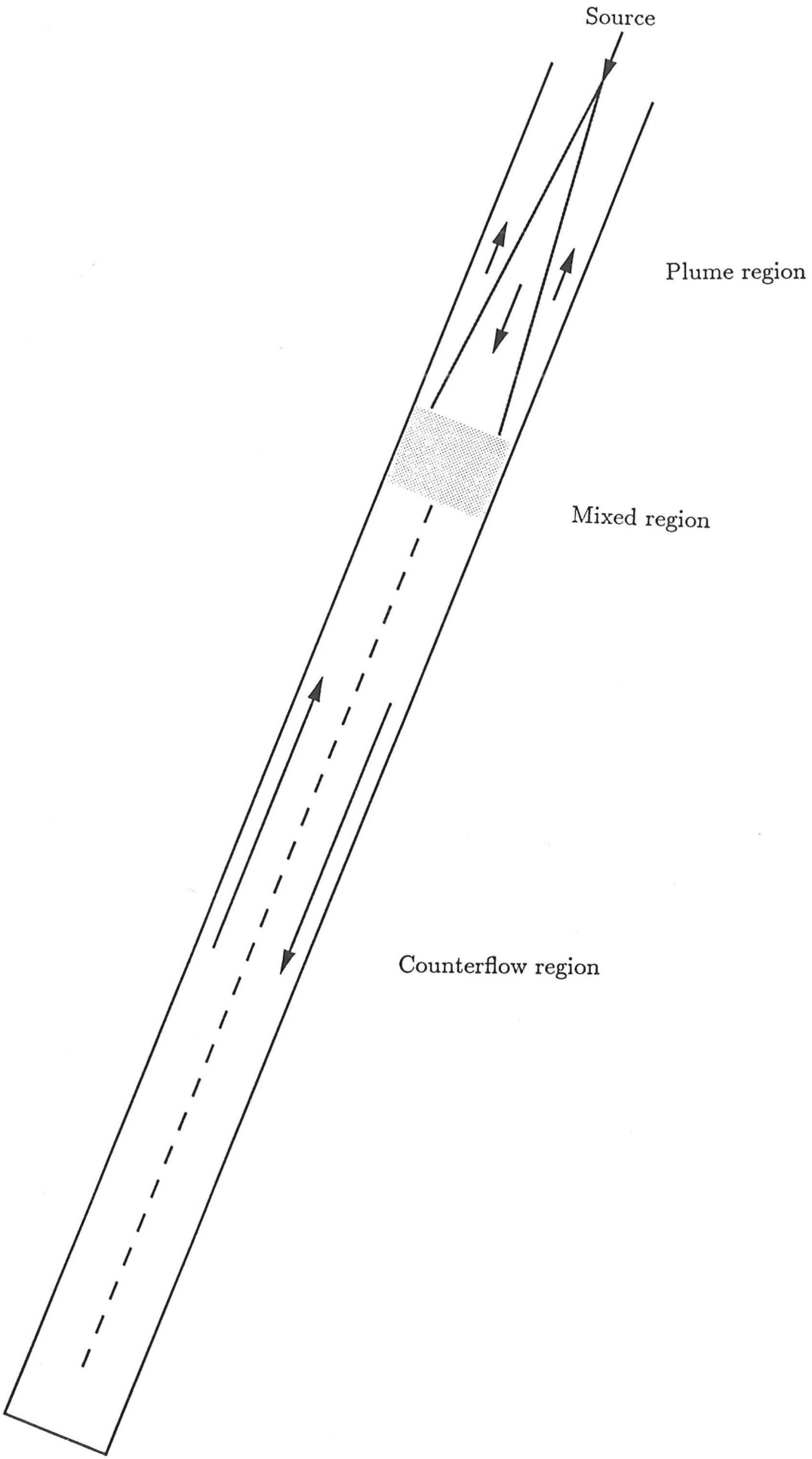

FIGURE 1. A schematic diagram of the flow resulting from a source of buoyancy in a tall angled chamber.

Simpson 1987). The buoyant layer occupies about half the depth of the tank and flows down the lower boundary.† The tank is closed at the lower end and consequently the fluid above the lower layer flows in the opposite direction, so that there is no net axial flow. The shear between the two layers causes mixing between them, although this is inhibited to some extent by the stable stratification.

In initial investigative experiments, the counterflow system appeared to develop for angles even as small as 2°. However, it is expected that there is a transition between the disorganised vertical case and the organised angled case, as θ varies between 0° and $\sim 2°$. For angles within this range it was observed that the counterflow still developed, but broke down at some point along the tank. The position of this point moves further from the source with increasing angle until the case of $\theta \simeq 2°$, when the counterflow extends to the base of the tank. Thus the following description of the flow and theoretical model is restricted to the case when $\theta \geqslant 2°$.

Concentration measurements from a single experiment (in which $\theta = 15°$), taken after equally spaced time intervals of one minute, are given in figure 2. In this figure measurements were made of the mean concentrations (averaged through the tank and over the whole width of the layer) on either side of the tank axis to see if there is a significant, measurable difference between them, due to placing the tank at an angle (compare this figure with figure 6 of chapter 5). The concentrations measured on the lower side of the tank are connected by a dashed line and those made on the upper side of the tank are connected by a solid line. It may been seen that there is a change between the concentration behaviour in the plume region $0 \leqslant z/R \lesssim 5.5$ and the counterflow region $7 \lesssim z/R \leqslant a$ analogous to that observed in the vertical case (see chapter 5, figure 6), where z is the axial coordinate. In the counterflow region is it also clear that the mean concentrations measured in the lower half of the counterflow are greater than those of the upper half, as is expected. However there is no such pattern in the plume region, indicating that the slope of the tank has had comparatively little effect there. These observations are consistent with conclusions reached on viewing of the experiments - the flow in the plume and mixing regions is very similar to that observed in vertical tanks, but the region beyond the mixing region is completely different.

One problem with performing digital analysis over the whole tank is that a picture of the whole tank must be recorded on tape, which consequently has a rather small image. This

† As in chapter 5, the description here will be given assuming that the source fluid is negatively buoyant, which is the case in the experiments.

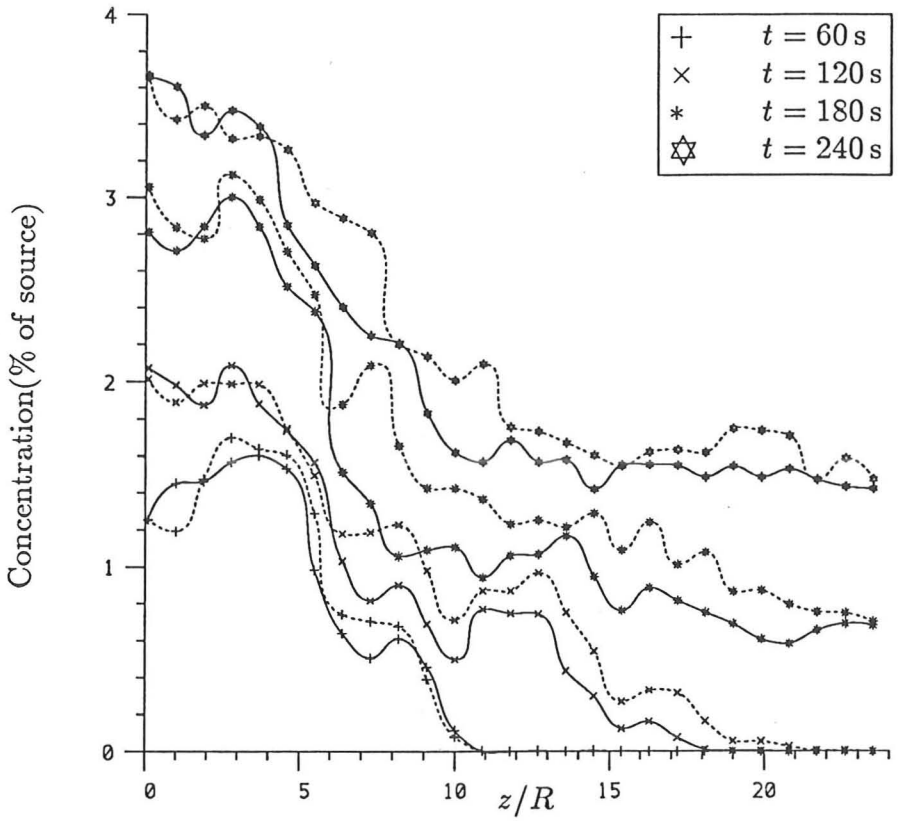

FIGURE 2. Mean concentration measurements made on either side of the tank axis, taken from an experiment in which $a = 24$, $\theta = 15°$.

- - - - Lower side —— Upper side.

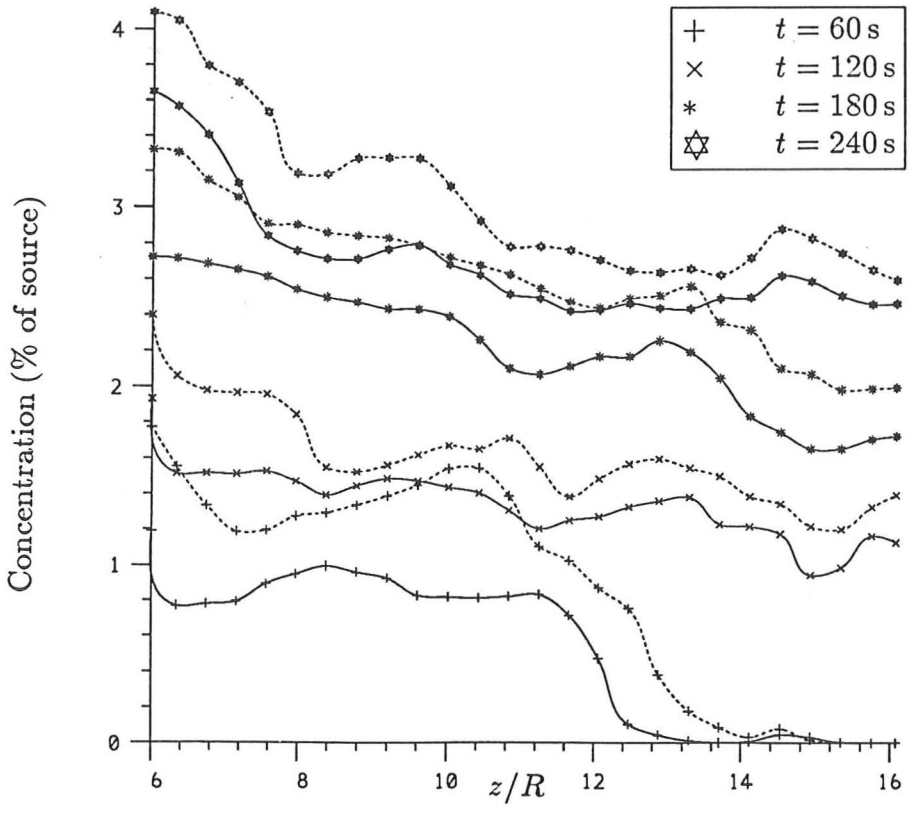

FIGURE 3. Mean concentration measurements made on either side of the axis, taken from an experiment in which $a = 24$, $\theta = 15°$ and $B_0 = 16.3\ \mathrm{cm^4 s^{-3}}$ - measurements made in the range $6 \leqslant z/R \leqslant 16.1$.

- - - - Lower side —— Upper side.

means that the number of pixels spanning the width of the tank is small thus increasing the errors in the measurements. In order to take more accurate measurements of the counterflow region, the video camera was zoomed in on a specific part of the flow. The image of the tank is consequently wider which enables more accurate measurements to be made. Measurements from such a run are shown in figure 3, in which attention has been focussed on the top half of the counterflow in the region $6 \leqslant z/R \leqslant 16$. This figure shows the difference in mean concentration between the upper (solid line) and lower (dotted line) layers very clearly.

It will become apparent in the following discussion that another flow variable of interest is the velocity of the layers in the counterflow. The velocity was measured by injecting green dye into the lower layer. The flow was recorded on video tape and the velocity could be calculated by measuring the time taken for the dye patch to travel between lines on the tank spaced at intervals of $2R$. The video image may be controlled very accurately, with the time measurements given to an accuracy of ± 0.04 s, i.e. to the accuracy of the time space between video frames. Thus, in theory, quite accurate measurements may be made. In practice, of course, the velocity distribution of each layer is not uniform and a range of velocity values may be measured. Also, the dye patch remains most well defined in the region of the flow that is near to the upper and lower walls - where the mixing is least. This is also where the velocity of the flow is greatest. Thus the mean values are expected to be, on average, less than the measured values. Measurements from a series of three experiments, all with the same source buoyancy flux, are given in figure 4 (the symbols simply denote measurements from the different experiments). The time value plotted is the mid-point of the time interval used to calculate the velocity. The velocities were measured at points within the range $6 \leqslant z/R \leqslant 20$ and there was no noticeable trend in the velocities measured as the dye patch travelled from the top to the bottom of this region. This supports the observations of Ellison & Turner (1959) and Britter & Linden (1980), that there is little variation in the velocity of the current with position along the slope. Also, except in the initial stages of the flow, there seems to be little variation in the velocity range measured in time.

3. A model of the counterflow region

It is now clear that to model the whole flow it will be necessary to substitute a model of the counterflow region for the convective region part of the combined model of chapter 5. In this section, the equations for the counterflow will be derived and the assumptions made

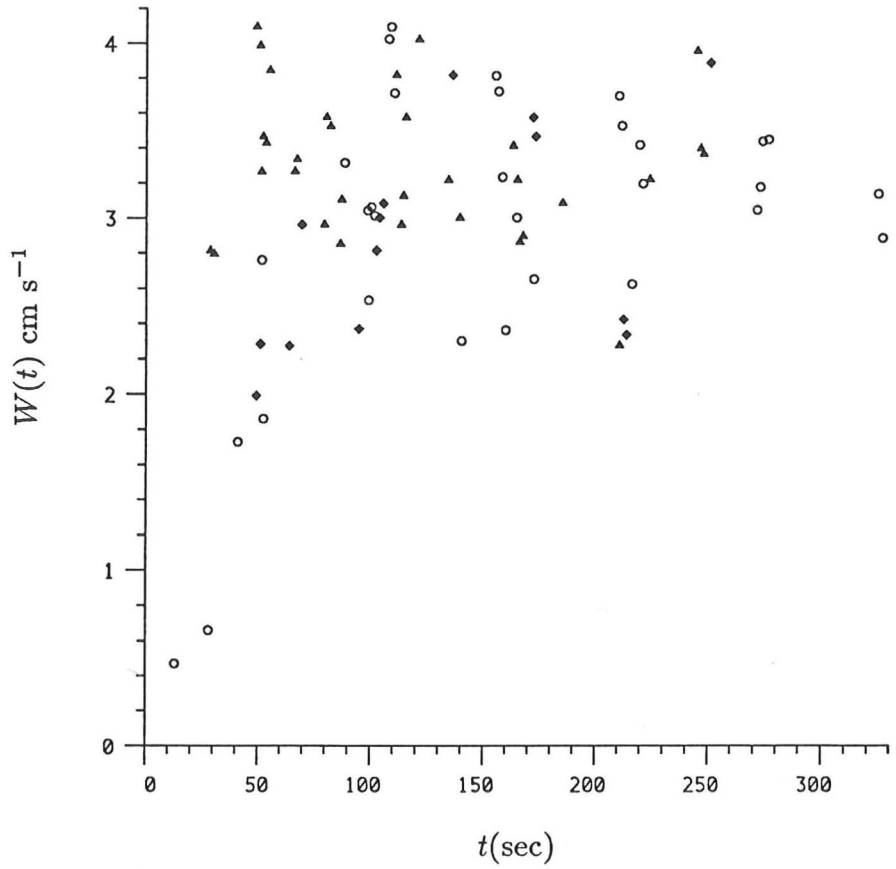

FIGURE 4. Velocity measurements made in the lower layer of the counterflow in three experiments in which $a = 24$, $\theta = 15°$ and $B_0 = 16.3$ cm^{4}s $^{-3}$.

will be discussed. The predictions of the model will then be compared with experimental measurements.

3.1 The basic features of the counterflow

The essential features of the counterflow system will now be recalled, as these form the assumptions on which the model is based.

3.1.1 The flow variables

A diagram of the counterflow is shown in figure 5. The lower layer has mean (averaged over a plane perpendicular to the axis through the layer) reduced gravity $g'_l(z',t)$ and the upper layer has mean reduced gravity $g'_u(z',t)$, where t is time - z' is used as the axial coordinate in the counterflow region, with $z' = 0$ at the top of the counterflow region. The mean axial velocity of the lower layer is $W(z',t)$. The counterflow region has length h_3 and the width of the tank is $2d$ (where d may be different from R). It is also assumed that the flow is approximately two-dimensional and that the component of velocity and density gradients in the y direction (through the page) are negligible.

It has already been stated that preliminary experiments supported the findings of Ellison & Turner (1959) and Britter & Linden (1980) that the velocity of a gravity current does not appear to change as it flows down a slope. The same property has been observed here and will be assumed in the analysis, i.e. it is assumed that W is a function of t only.

A second observation mentioned earlier was that both layers in the counterflow occupy approximately half the depth of the tank, i.e. they have thickness d. This is an analogous result to that of the counterflow in chapter 4. However in this case there is considerable mixing between the layers and thus there is no interface on which to apply the Bernoulli theorem to derive this result analytically. However, an immediate consequence of this assumption may be obtained by applying conservation of volume on planes perpendicular to the axis. Since there is no net flow (because the end of the tank is closed) this implies that the mean axial velocity of the upper layer must be $-W(t)$. The connection between the flow of chapter 4 and the present flow will be discussed further in the concluding section.

It was mentioned in section 1 that Britter & Linden (1980) also found that there was little variation of the front velocity with the slope, for a given source buoyancy flux. They wrote

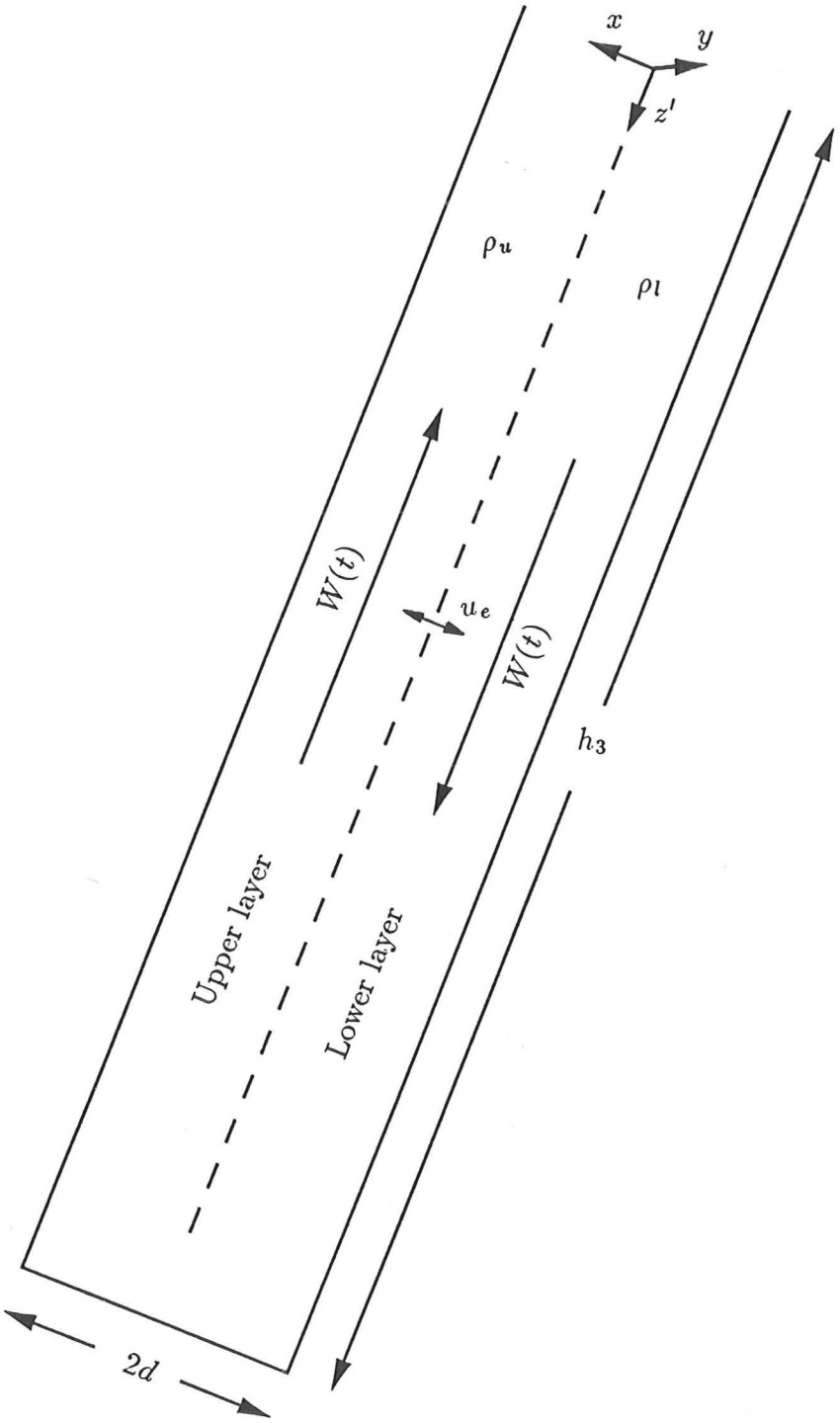

FIGURE 5. A schematic diagram of the counterflow region showing the flow variables.

this result in the form

$$U_f = (1.5 \pm 0.2)(g_0' Q)^{\frac{1}{3}} \quad \text{for} \quad 0° < \theta \leqslant 85°, \tag{3.1}$$

where U_f was their front velocity, and g_0' and Q were the reduced gravity and the volume flux of their line source respectively. In the present case the value of an equivalent g_0' may be given by the difference in density between the two layers at the top of the counterflow region, i.e. $g_0' \equiv g_l'(0,t) - g_u'(0,t)$ and the volume flux (of an equivalent line source) is given by Wd. This would imply that (in the present notation with front velocity W_f)

$$W_f = (1.5 \pm 0.2)([g_l'(0,t) - g_u'(0,t)]dW)^{\frac{1}{3}}. \tag{3.2}$$

Britter & Linden (1980) also found that for slopes with $\theta \lesssim 60°$ the front velocity was approximately 60% of the velocity of the following flow. Thus writing $W_f \simeq 0.6W$, equation (3.2) becomes

$$W(t) \simeq (4.0 \pm 0.8)\sqrt{[g_l'(0,t) - g_u'(0,t)]d}. \tag{3.3}$$

Of course, the flow discussed by Britter & Linden (1980) is different to the present flow in that there was no ambient flow present. In the present flow the 'ambient' fluid has equal and opposite velocity to that of the layer flow and may not be neglected. Thus it may be assumed that in equation (3.3), the velocity given is the *difference* between the layers. Taking this effect into account modifies equation (3.3) to

$$W(t) \simeq (2.0 \pm 0.4)\sqrt{[g_l'(0,t) - g_u'(0,t)]d}. \tag{3.4}$$

This is the form of the dependence of $W(t)$ on the density difference at $z' = 0$ that will be used in the model. Initially, however, it will be assumed that $W(t) = k_1\sqrt{g_l'(0,t) - g_u'(0,t)}$ and the constant k_1 will be determined by making a comparison between the theoretical predictions and experimental measurements, although from the above discussion it might be expected that $k_1 \sim O(2)$. Note again that there is no dependence on the angle of elevation but the use of (3.4) must be restricted to the case when $0° < \theta \leqslant 85°$ since (3.1) only applies in this range.

3.1.2 The mixing between the layers

It is now established that the counterflow is to be approximated by two layers of different density, each occupying half the depth of the tank, moving in equal and opposite directions

with the same mean axial speed. There is, however, a slight contradiction here: if W is constant in z', then this implies that there is a non-zero volume flux in the lower layer at the tank base. Of course, in practice, the layer velocity decreases to zero in the vicinity of the tank base (this deceleration appears to occur within about $4R$ from the base). This deceleration, though, is an aspect of the flow that is relatively unimportant here: it suffices to say that in the present model there is no *net* volume or buoyancy flux at the tank base. The deceleration of the layers near to the base is thus ignored.

The shear between the two layers causes instabilities in the interface and turbulence, resulting in mixing between the two layers. Mixing at a shear layer interface has been the subject of considerable discussion. Generally, experiments have consisted in examining the flow of a buoyant layer on a horizontal level or slope, measuring the rate of increase of the thickness of the layer in order to calculate the rate of entrainment (for a review see Turner 1986). In the current case the objective is to obtain a relation representing the dependence of the mixing effects on the velocity shear and density stratification.

In an infinite fluid the entrainment into a moving layer is generally calculated by the use of the entrainment assumption (see chapter 3)

$$u_e = E\Delta w. \tag{3.5}$$

This relates the entrainment velocity across the interface, u_e, to the axial velocity shear Δw by the use an entrainment function E, which will depend on the shear and the stratification.

Kato & Phillips (1969) measured values of the entrainment coefficient, E, in an experiment in which a constant stress was applied to the the top of a tank of initially still fluid, with a uniform density gradient. E was calculated by measuring the development of the turbulent layer. They found that the entrainment coefficient varied with the reciprocal of a flow Richardson number, i.e.

$$E = (2.5 \pm 0.75)Ri_*^{-1} = (2.5 \pm 0.75)\frac{\rho_0 u_*^2}{g\delta\rho D}, \tag{3.6}$$

in their notation, where u_* was the friction velocity and D was the layer depth. Ellison & Turner (1959) measured the entrainment into a buoyant layer flowing down a slope. They found that the entrainment could be related to the mean flow Richardson number. Their results may be approximated by (see Turner 1986)

$$E = \frac{0.08 - 0.1Ri}{1 + 5Ri} \quad \text{where} \quad Ri = \frac{g'd\sin\theta}{(\Delta w)^2}. \tag{3.7}$$

The physical situation for which (3.7) was found seems more similar to the current case than that of Kato & Phillips. Also, it is difficult to relate the value of the Richardson number measured by Kato & Phillips to the mean flow variables in the current problem, and their measurements do not extend to $Ri_* = 0$. Thus the form found by Ellison & Turner will be used in the present model.

Of course, their situation is still rather different to the current flow. They studied the entrainment into a single, thin, buoyant layer, whereas here the flow consists of two opposing layers of equal thickness. In a fluid of large depth with a single dense layer, entrainment results in an increase in the layer thickness. This is clearly not possible in the present case as each layer must maintain a thickness of half the width of the tank. Thus it will be assumed that the entrainment velocity u_e is simply the speed of fluid flowing from the lower to the upper layer and vice-versa, at each point on the 'interface' of the counterflow. In fluid of large depth this would result in the layer increasing in thickness as mentioned above, but here it simply represents the degree of mixing between the layers. However, it is not clear that the form of (3.7) should apply immediately to the present case. It is likely that the mixing between the layers will be somewhat higher than that observed with a single layer (due to the presence of the upper boundary). Therefore, in the model it will be assumed that there exists a mixing velocity u_e at the interface, related to W by equation (3.5), with

$$E = k_2 \frac{0.08 - 0.1Ri}{1 + 5Ri}, \tag{3.8}$$

for some constant $k_2 \gtrsim 1$, which may depend on the cross-sectional shape of the tank. The Richardson number will be evaluated at each point with the reduced gravity in equation (3.7) being given by the mean density difference between the layers at that point. Thus, using the fact that in the current case $\Delta w = 2W$, the Richardson number is given by

$$Ri(z',t) = \frac{[g'_l(z',t) - g'_u(z',t)]d\sin\theta}{4W(t)^2}. \tag{3.9}$$

The effect of the slope is therefore solely incorporated in the Richardson number and hence in the rate of mixing.

3.2 The equations of motion

The assumptions on which the model is based have now been described. The equations for the mean motion of the counterflow layers will now be presented. In the derivation here and

subsequently it will be assumed that the length and time scales have been non-dimensionalised by the source buoyancy flux, B_0, and effective tank radius, R. Thus, if the star denotes a dimensionless scale, then

$$[L]^* = R^{-1}[L], \qquad [T]^* = B_0^{\frac{1}{3}} R^{-\frac{4}{3}}[T],$$

where $[L]$ and $[T]$ are the scales of length and time respectively. The stars will be assumed to have been dropped from the variables.

For an incompressible fluid the rate of change of density following the flow is zero, i.e.

$$\frac{\partial \rho}{\partial t} + \mathbf{u}.\nabla\rho = 0, \tag{3.10}$$

where $\rho(\mathbf{x})$ is the density and $\mathbf{u}(\mathbf{x})$ is the mean velocity flow field. This equation may be integrated through each layer over a plane perpendicular to the axis.

Integrating the lower layer gives

$$\int_{-d}^{0} \frac{\partial \rho}{\partial t}\, dx + \int_{-d}^{0} \left(u\frac{\partial \rho}{\partial x} + v\frac{\partial \rho}{\partial y} + W\frac{\partial \rho}{\partial z'} \right) dx = 0, \tag{3.11}$$

where x is the coordinate in the plane of the motion, perpendicular to the axial (z') coordinate (see figure 5); the mean velocity flow field in the lower layer has components (u, v, W) in the (x, y, z') directions. Recall that $W(t)$ is a function of t only and that mean density distributions are considered, i.e. they are independent of x and y.

The flow is approximately two-dimensional ($v \simeq 0$) and so dependencies on y and gradients in this direction may be neglected. Thus the third term is approximately zero. Integrating the first, second and last terms gives

$$d\frac{\partial \rho_l}{\partial t} + (u\rho)|_{-d}^{0} - \int_{-d}^{0} \rho\frac{\partial u}{\partial x}\, dx + dW(t)\frac{\partial \rho_l}{\partial z'} = 0. \tag{3.12}$$

Clearly there can be no flow through or out of the lower boundary and so $u(-d, z', t) = 0$. Also, from the equation of incompressibility

$$\frac{\partial u}{\partial x} + \frac{\partial W}{\partial z'} = 0, \tag{3.13}$$

and so equation (3.12) may be written

$$d\frac{\partial \rho_l}{\partial t} + (u\rho)|^{0} + \int_{-d}^{0} \rho\frac{\partial W}{\partial z'}\, dx + dW(t)\frac{\partial \rho_l}{\partial z'} = 0. \tag{3.14}$$

However W is a function of t only and so the third term is zero.

The second term represents the mixing between the layers at the interface. In section 3.1.2 it was decided that the mixing would be given by an entrainment velocity at the interface $u_e = E\Delta W = 2EW$. Note, however, that there must be an equal volume flux of fluid flowing from the lower layer into the upper layer as there is from the upper layer into the lower. The second term is therefore $u_e(\rho_l - \rho_u)$. Thus equation (3.14) is then

$$\frac{\partial \rho_l}{\partial t} + \frac{2}{d}E(Ri)W(t)(\rho_l - \rho_u) + W(t)\frac{\partial \rho_l}{\partial z'} = 0, \tag{3.15}$$

where E and Ri have been defined in equations (3.8) and (3.9), respectively. By simple substitution this equation may be rewritten in terms of the layer reduced gravities

$$g'_{l,u} = \left(\frac{\rho_{l,u} - \rho_0}{\rho_0}\right) g, \tag{3.16}$$

where ρ_0 is a reference density, equal to that of the initial ambient fluid density. Thus equation (3.15) becomes finally

$$\frac{\partial g'_l}{\partial t} + \frac{2}{d}E(Ri)W(t)(g'_l - g'_u) + W(t)\frac{\partial g'_l}{\partial z'} = 0. \tag{3.17}$$

The upper layer may be integrated similarly giving

$$\frac{\partial g'_u}{\partial t} + \frac{2}{d}E(Ri)W(t)(g'_u - g'_l) - W(t)\frac{\partial g'_u}{\partial z'} = 0. \tag{3.18}$$

Equations (3.17) and (3.18) form the equations of motion of the counterflow, recalling that

$$E(Ri) = k_2\frac{0.08 - 0.1Ri}{1 + 5Ri} \quad \text{where} \quad Ri(z', t) = \frac{(g'_l - g'_u)d\sin\theta}{4W^2} \quad \text{and} \tag{3.19}$$

$$W(t) = k_1\sqrt{[g'_l(0,t) - g'_u(0,t)]d}. \tag{3.20}$$

The end of the tank is closed and thus the following boundary condition applies at $z' = h_3$

$$\rho_l(h_3, t) = \rho_u(h_3, t) \quad \text{or} \quad g'_l(h_3, t) = g'_u(h_3, t), \tag{3.21}$$

which states that fluid reaching the base of the container in the lower layer immediately begins to flow back up the tank in the upper layer. (Recall that the deceleration of the layers near to the base is ignored.)

The value of $g'_l(0, t)$ is the final boundary condition required to close the system. In practice this will be set by the behaviour of the plume and mixing regions (as was the reduced gravity

at the top of the convective region in the vertical chamber flow). In the following comparisons between the predictions of the above model and experimental data, the behaviour of $g_l'(0,t)$ will be estimated from the experimental results.

In summary, the model consists of equations (3.17)-(3.21) together with a further boundary condition setting $g_l'(0,t)$. The constants k_1 and k_2 must be set by comparison with experimental data.

3.3 The numerical solution

The equations for the model were integrated numerically using a finite-difference method. The results were compared with the data shown in figure 3 and data from six other experiments in the case when $\theta = 15°$ and $a = 24$. The behaviour of $g_l'(0,t)$ was approximated by

$$g_l'(0,t) \sim t^{0.63}, \tag{3.22}$$

obtained by making a power law fit to the experimental data (the same as that used in the comparison) at $z' = 0$ (or $z \simeq 6$).

3.3.1 Dependence of the solution on k_1 and k_2

The behaviour of the solution on the constants k_1 and k_2 is not at all obvious. For example, increasing the constant k_1 will increase the velocity of the layers, but this in turn increases the mixing. An increase in the mixing implies that the concentrations in the upper layer will rise, which means that the velocity will subsequently decrease (from (3.20)). It is clear that the balance between the effects of k_1 and k_2 needs investigation. Some initial solutions were calculated to study the effect of these constants on $g_{u,l}'(z',t)$ and $W(t)$.

The behaviour of $g_u'(0,t_4)$ with k_1 (where $t = t_4$ was chosen to be the final time-point shown in figure 3), is shown in figure 6*a* for a variety of values of k_2. It is clear from this figure that the dependence of $g_u'(0,t_4)$ on k_2 is very weak for $k_2 < 1.5$ compared with the dependence on k_1 (recall that it is expected that $k_1 \sim O(2)$). For a given value of k_2 an increase in k_1 acts to increase $g_u'(0,t_4)$ as explained above. Similarly figure 6*b* shows that increasing the value of k_1 increases the value of the reduced gravity in the lower layer at $z' = h_3/2$ whilst figure 6*c* shows that the difference between the layer reduced gravities at this point is reduced. The results of figures 6 a, c are indicative of an overall increase in the mixing with an increase in k_1. Figures 6 a, b, c also show that increasing the entrainment (by

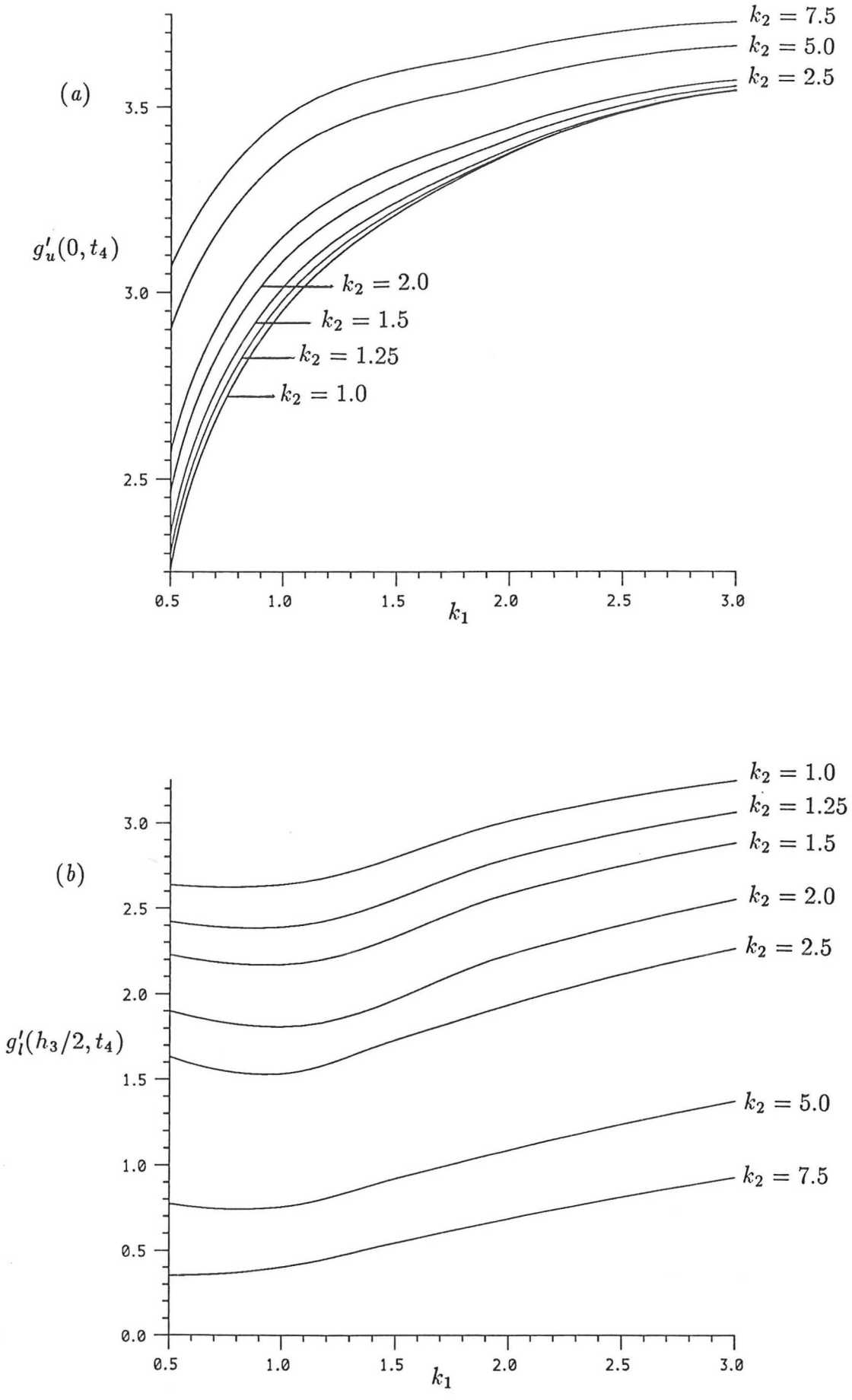

FIGURE 6. (a) The variation in $g'_u(0, t_4)$ with k_1 for several values of k_2; (b) the variation in $g'_l(h_3/2, t_4)$ with k_1 for several values of k_2; (c) the variation in $[g'_u(h_3/2, t_4) - g'_l(h_3/2, t_4)]$ with k_1 for several values of k_2.

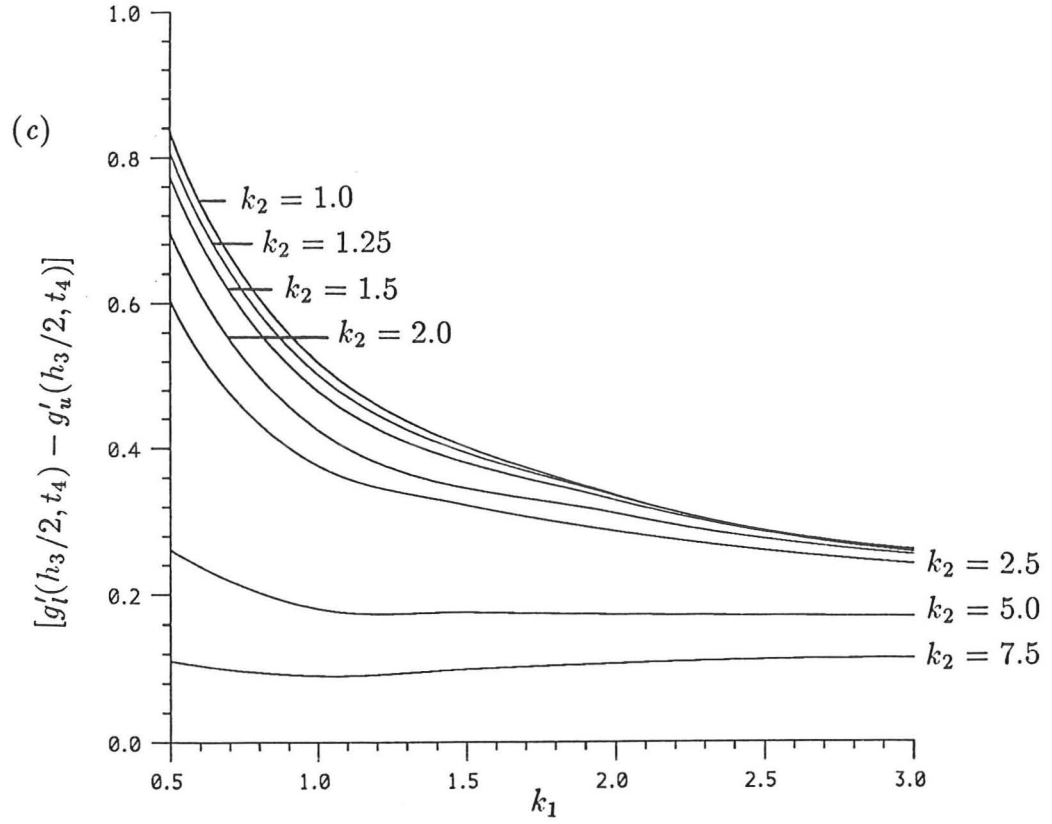

FIGURE 6. (c) The variation in $[g'u(h_3/2,t_4) - g'_l(h_3/2,t_4)]$ with k_1 for several values of k_2.

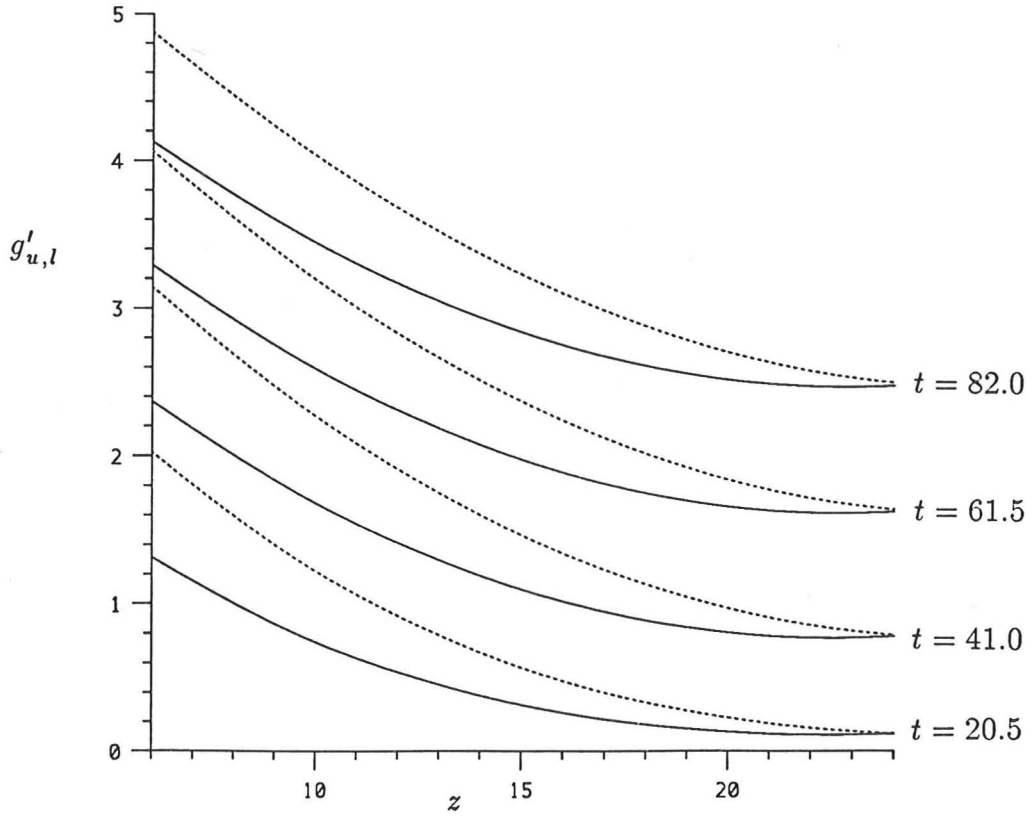

FIGURE 7. The numerical solution to the counterflow equations in the case when $h_3 = 18$, $\theta = 15°$, $k_1 = 2.43$ and $k_2 = 1.68$ - profiles are plotted after equally spaced t intervals, $\Delta t = 20.5$.

- - - - Lower layer —— Upper layer.

increasing k_2) results in an increase in the reduced gravity near to $z' = 0$ but a decrease (and a decrease in the difference between the layers) further along the tank. Overall it is clear that the solution is considerably more sensitive to the value of k_1 than to k_2.

The values obtained in this study were compared with measured concentrations, of which figure 3 shows a set from a typical experiment. By matching the values of $g'_u(0, t_4)$, $g'_l(h_3, t_4)$, $g'_l(h_3/2, t_4)$ and $g'_l(h_3/2, t_4) - g'_u(h_3/2, t_4)$ it was found that good agreement could be achieved when

$$\begin{aligned} k_1 &= 2.43 \pm 0.08 \\ k_2 &= 1.68 \pm 0.17. \end{aligned} \tag{3.23}$$

The values $k_1 = 2.43$ and $k_2 = 1.68$ were used in the final numerical solution. Note that these values have been chosen by comparison with experimental measurements at one particular value of t. It remains to be seen whether or not these values give a good agreement with experimental data for different values of t.

The values of k_1 and k_2 seem to be reasonable. The earlier estimate for k_1 from the measurements of Britter & Linden (1980) gave $k_1 \simeq 2$, which is comparable to the above value $k_1 = 2.43$. It was also anticipated that k_2 might be greater than one, i.e. there is a greater level of mixing taking place than was observed by Ellison & Turner (1959) due to the presence of the upper boundary. The value $k_2 = 1.68$ implies a maximum value for E of 0.1344, which is consistent with the measurements of Kato & Phillips (1969).

3.3.2 Comparison between the counterflow solution and experimental data

The solution obtained using the above values for k_1 and k_2, with $\theta = 15°$ is shown in figure 7, in which it has been assumed that $h_3 = 18$ (for comparison with experiments in which $H = 24$). The dotted line is the solution for the lower layer and the solid line is the solution for the upper layer. The numerical solution exhibits the expected features of the counterflow, namely that the reduced gravity of the lower layer is always higher than that of the upper layer, except at the end of the tank where they are required to be equal.

A comparison between this solution and the experimental measurements of figure 3 is given in figure 8. Figure 8*a* shows the solution for the lower layer (solid line) compared with experimental measurements (the points have been joined by a dotted line) and figure 8*b* shows the solution for the upper layer. The numerical solution follows the general pattern of the experimental data well although it should be emphasised that these are data points from a single experiment only. Consequently there is a considerable degree of fluctuation of the

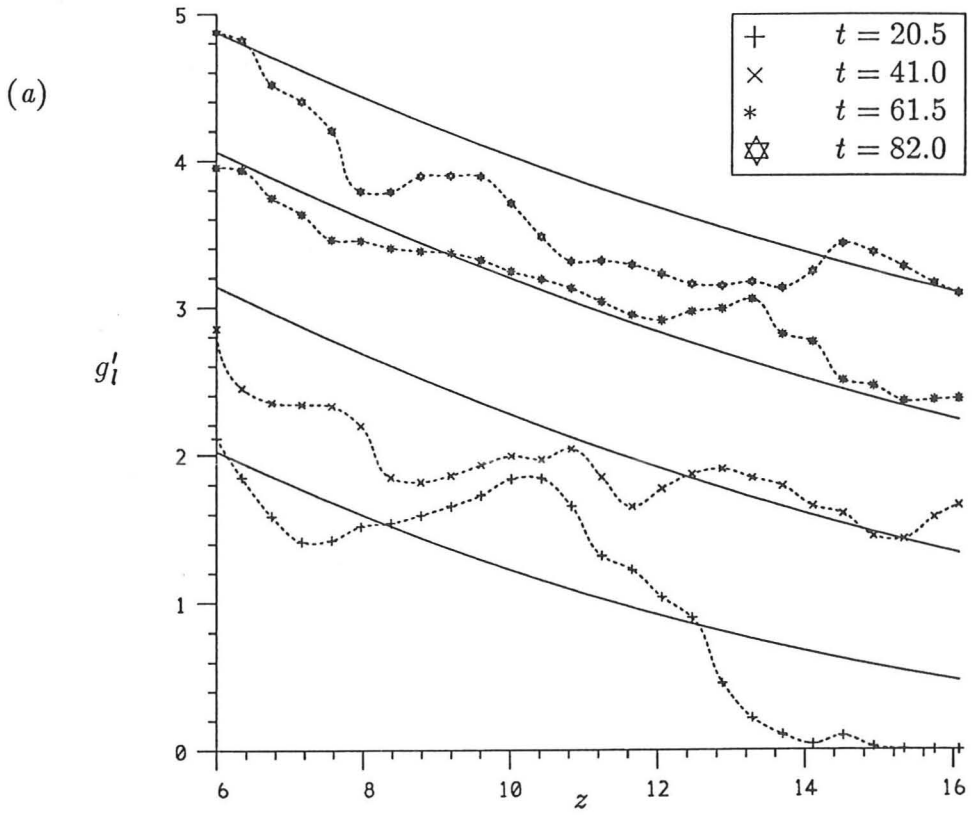

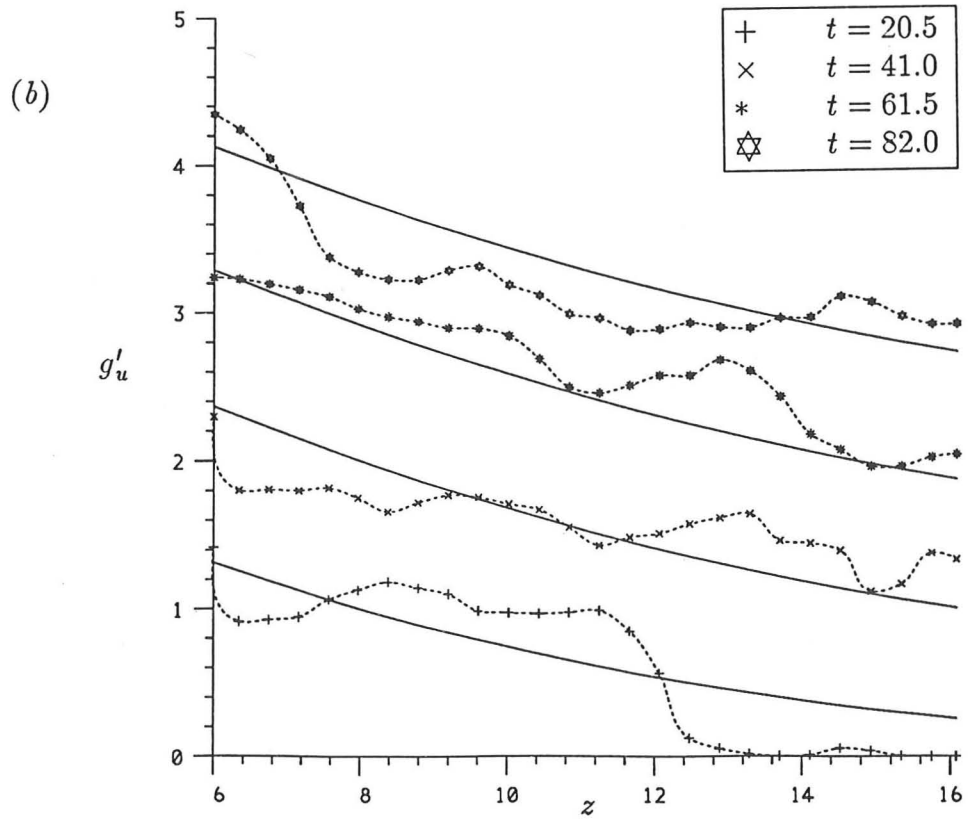

FIGURE 8. A comparison between the numerical solution (see figure 7) to the counterflow equations after equally spaced t intervals, $\Delta t = 20.5$, with experimental data from an experiment in which $a = 24$, $\theta = 15°$; (a) the lower layer; (b) the upper layer.

experimental profile about the numerical solution, associated with the fluctuating nature of the large-eddy mixing processes.

The boundary condition specifying $g_l(0,t)$ was, in this solution, given by an artificial function estimated from the experimental measurements. In practice, this will be set by the behaviour of the mixing region concentration. In the next section the model for the whole flow will be presented, comparing the numerical results with measurements from several experiments.

4. The model for the whole flow

The model for the counterflow region has been presented and shows good agreement with experimental data. It remains to derive the behaviour of the mixing region and to link the plume, mixing and counterflow regions to form a combined model (analogous to that of chapter 5).

4.1 The mixing region

In chapter 5 it was explained that in tanks with aspect ratio greater than about six, the plume flow breaks down giving rise to a mixed region at the base of the plume. In the vertical chamber case, dense fluid from this region mixed with fluid further down the tank by turbulent convection. Here, there is a pressure difference between the top and bottom points of the mixed region, due to the angle of the tank, which results in the counterflow described above.

It will be assumed that dense fluid flows from the mixed region into the lower layer of the counterflow and that fluid flows into the mixed region from the upper layer. There is also a supply of buoyancy from the plume and an equal flow into the environment of the plume. At each point in time, the fluid entering the mixed region is assumed to be instantaneously mixed, i.e. the mixed region is of uniform density (although this assumption may be increasingly less good for increasing values of θ). In the following derivation of an equation describing the concentration behaviour of the mixed region, it will be assumed that the mixed region is of constant length h_2, uniform density $\rho_m(t)$ and reduced gravity $g_2'(t)$, defined analogously to the layer reduced gravities (see equation (3.16)). The plume region has length $h_1 = H - h_2 - h_3$ and the notation used will be the same as that used in chapter 5 (i.e. mean axial velocity $w(z,t)$, radius $b(z,t)$, environment density $\rho_a(z,t)$, plume density $\rho_p(z,t)$,

reduced gravity $g_1'(z,t) = (\rho_p - \rho_a)/\rho_0$ and environment velocity $U(z,t)$, with $z' = z - h_1 - h_2$ - see chapter 5, figure 7).

In a small time interval δt, the flow of buoyancy from the mixed region to the lower layer of the counterflow is given by $\pi g_2'(t)W(t)\delta t/2$ and the flow of buoyancy from the upper layer into the mixed region is given by $\pi g_u'(0,t)W(t)\delta t/2$.

The supply of buoyancy from the plume is given by $\pi b^2(h_1,t)w(h_1,t)(\rho_p - \rho_0)/\rho_0 g\delta t$ and the flow of buoyancy into the environment of the plume is given by $\pi b^2(h_1,t)w(h_1,t)g_2'(t)\delta t$, in which it has been assumed that the density of the fluid flowing into the environment of the plume is equal to that of the mixed region (i.e. $\rho_a(h_1,t) = \rho_m(t)$).

Thus the change in the total buoyancy of the mixed region is given by the equation

$$h_2[g_2'(t+\delta t) - g_2'(t)] = \left(\frac{1}{2}[g_u'(0,t) - g_2'(t)]W(t) + \left(\frac{\rho_p - \rho_m}{\rho_0}\right) g\, b^2(h_1,t)w(h_1,t)\right)\delta t. \quad (4.1)$$

Hence in the limit $\delta t \to 0$ this gives

$$\frac{dg_2'}{dt} = \frac{1}{h_2}\left(\frac{1}{2}[g_u'(0,t) - g_2'(t)]W(t) + b^2(h_1,t)w(h_1,t)g_1'(h_1,t)\right). \quad (4.2)$$

This is the conservation equation for the mixing region that will now be used in the combined model of the whole flow.

4.2 The combined model

The models for the behaviour of the counterflow (section 3.3), mixing region (section 4.1) and plume region (chapter 5, sections 3.1 and 3.2) will now be combined to form an overall model of the flow resulting from a plume in a tall angled chamber.

In summary, the flow is divided into three regions, namely the plume, mixing and counterflow regions, of heights h_1, h_2 and $h_3 = H - h_1 - h_2$, respectively. The first region contains the source of the motion, a plume whose motion satisfies the equations given in chapter 5, section 3, although it should be noted that these equations were derived in the vertical case and may not be appropriate for large values of θ. The second region is a mixing region which connects the plume and counterflow regions and has been described in section 4.1 above. The third region is a two-layered stratified counterflow which exists for $\theta \gtrsim 2°$, described in section 3 above. The length and time scales have been non-dimensionalised using the effective radius, R and the source initial buoyancy flux, B_0. The equations of motion for the whole

flow may be summarised in non-dimensionalised form as follows

$$\left.\begin{aligned}
\frac{d}{dz}(b^2 w) &= 2\alpha_p b w, \\
\frac{d}{dz}(b^2 w^2 + (1-b^2)U^2) &= b^2 g_1', \\
\frac{d}{dz}(b^2 w g_1') &= -\frac{g b^2 w}{\rho_0}\frac{\partial \rho_a}{\partial z}, \\
(b^2-1)U &= b^2 w, \\
\frac{\partial \rho_a}{\partial t} &= -U\frac{\partial \rho_a}{\partial z}, \\
\left(\frac{\rho_a(h_1,t)-\rho_0}{\rho_0}\right) g &= g_2'(t), \\
\text{with} \qquad b(0,t) = U(0,t) &= 0 \quad \text{and} \quad b^2 w g_1'(0,t) = 1
\end{aligned}\right\} \; 0 \leqslant z \leqslant h_1, \tag{4.3}$$

$$\left.\frac{dg_2'}{dt} = \frac{1}{h_2}\left(b^2(h_1,t)w(h_1,t)g_1'(h_1,t) + \frac{1}{2}W(t)[g_u(0,t) - g_2'(t)]\right)\right\} \quad h_1 \leqslant z \leqslant h_1+h_2, \tag{4.4}$$

$$\left.\begin{aligned}
\frac{\partial g_l'}{\partial t} + \frac{2}{d}E(Ri)W(t)(g_l' - g_u') + W(t)\frac{\partial g_l'}{\partial z'} &= 0, \\
\frac{\partial g_u'}{\partial t} + \frac{2}{d}E(Ri)W(t)(g_u' - g_l') - W(t)\frac{\partial g_u'}{\partial z'} &= 0, \\
W(t) = k_1\sqrt{[g_l'(0,t) - g_u'(0,t)]d}, & \\
E(Ri) = k_2\frac{0.08 - 0.1Ri}{1+5Ri} \quad \text{where} \quad Ri &= \frac{(g_l' - g_u')d\sin\theta}{4W^2}, \\
g_l'(0,t) &= g_2'(t), \\
g_l'(h_3,t) &= g_u'(h_3,t).
\end{aligned}\right\} \; 0 \leqslant z' \leqslant h_3, \; z' = z - h_1 - h_2 \tag{4.5}$$

The initial conditions are

$$\rho_a(z,0) = \rho_0, \quad g_2'(0) = g_{l,u}'(0) = 0. \tag{4.6}$$

For a given tank aspect ratio the solution will be set by the values of H, h_1, h_2, k_1 and k_2 (although the latter two have been determined already). Note that now, the $g_l'(0,t)$ boundary condition is set by the mixing region reduced gravity, whereas in section 3 this was estimated from experimental measurements.

4.3 The numerical solution and comparison with experiments

The system of equations (4.3)-(4.6) was solved using a finite-difference iterative method. The constants k_1 and k_2 were set according to the values previously estimated and thus the solution depends only on the heights H, h_1 and h_2. Following the results of chapter 5, h_1 was chosen to be $h_1 = 5.5$, and H is set by the comparative experiment - in this case $H = 24$. The dependence of the numerical solution on h_2 was found to be weak, with the value of $g_2'(t_4)$ varying by about 4% over the range $0.5 < h_2 < 2$. The most accurate fit to the experimental data shown in figure **3** was obtained when $h_2 = 1.23$. Thus, given the degree of experimental error, it was concluded that a value of $h_2 = 1.23 \pm 0.15$ is appropriate. This value is also in agreement with initial experimental observations, in which it was clear that the mixing region in angled tanks is shorter than that in vertical tanks (in which a value of $h_2 \simeq 2$ was used). Physically, this also seems reasonable, as the two-layer flow may develop more quickly (in space) than the convective flow observed in the vertical case.

The overall solution with the above values and $\theta = 15°$, after equally spaced t intervals, Δt, is shown in figure 9. In this figure the solid line in the range $0 < z < h_1$ is the average reduced gravity along a line through and perpendicular to the axis of the tank, in the y direction. The dotted line in the plume region is the environment reduced gravity, which joins continuously to the reduced gravity of the mixed region (see the sixth of equations (4.3)). In the counterflow region, the dotted line is the lower layer reduced gravity (equal to that of the mixed region at $z' = 0$) and the solid line is the upper layer reduced gravity. The numerical solution is compared with experimental data from four experiments, with $\theta = 15°$, in figures $10a - d$. These figures are divided, separating the data for the upper and lower layers and showing comparisons after alternate t intervals (i.e. figure $10a$ shows the lower layer solution for $t = \Delta t,\ 3\Delta t$, figure $10b$ for $t = 2\Delta t,\ 4\Delta t$ *etc.*). In the experiments the source reduced gravity was kept constant - the buoyancy flux was varied by altering the volume flux of the source. Experimental errors in the measurement of the source buoyancy flux mean that the theoretical profiles are accurate to $\pm 4\%$.

The agreement is, in general, good although the spread of the experimental data about the numerical solutions is quite large. Perhaps the weakest agreement is seen in the plume region, $z \lesssim 5.5$, where the numerical solution slightly underestimates the experimental measurements. This effect was also noticed in the vertical tank case and was attributed to the non-uniformity of the environment velocity profile, resulting in a more rapid flow of dense

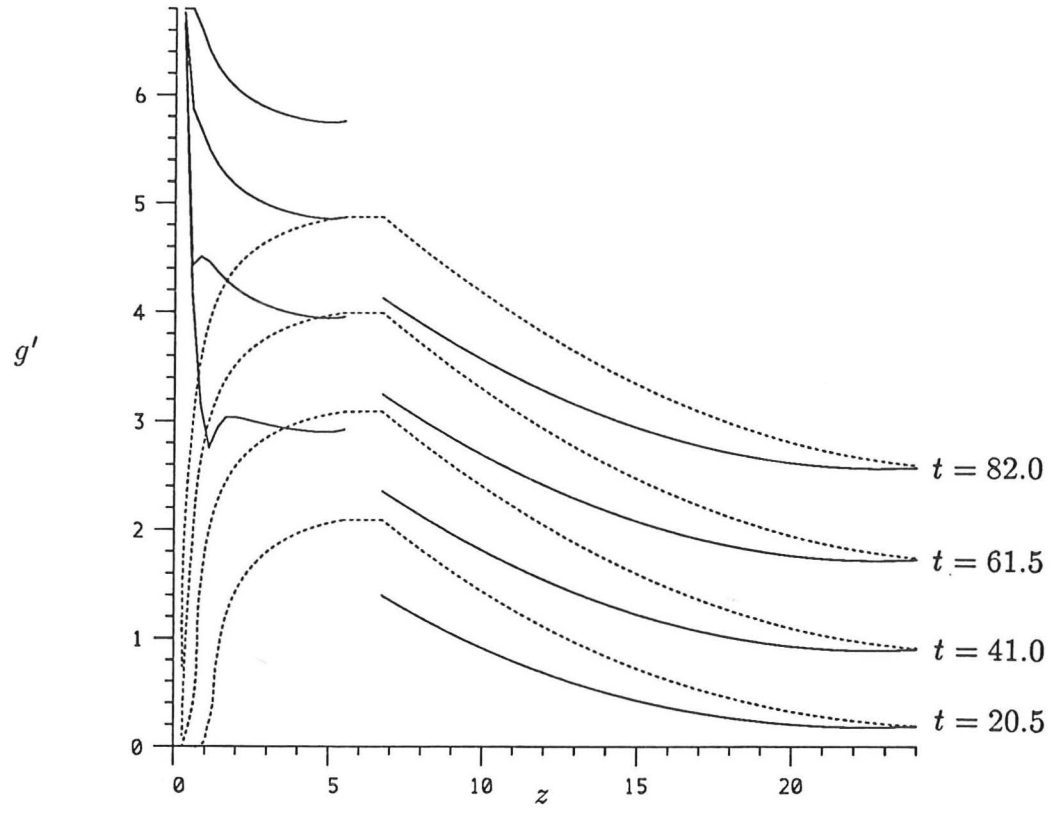

FIGURE 9. The numerical solution to the equations for the combined model in the case when $a = 24$, $\theta = 15°$, $h_1 = 5.5$, $h_2 = 1.23$, $k_1 = 2.43$ and $k_2 = 1.68$ - profiles are plotted after equally spaced t intervals, $\Delta t = 20.5$.

- - - - Environment of plume, mixed region and lower layer.
—— 'Centre-slice' concentration ($0 \leqslant z \leqslant h_1$), upper layer ($z \geqslant h_1 + h_2$).

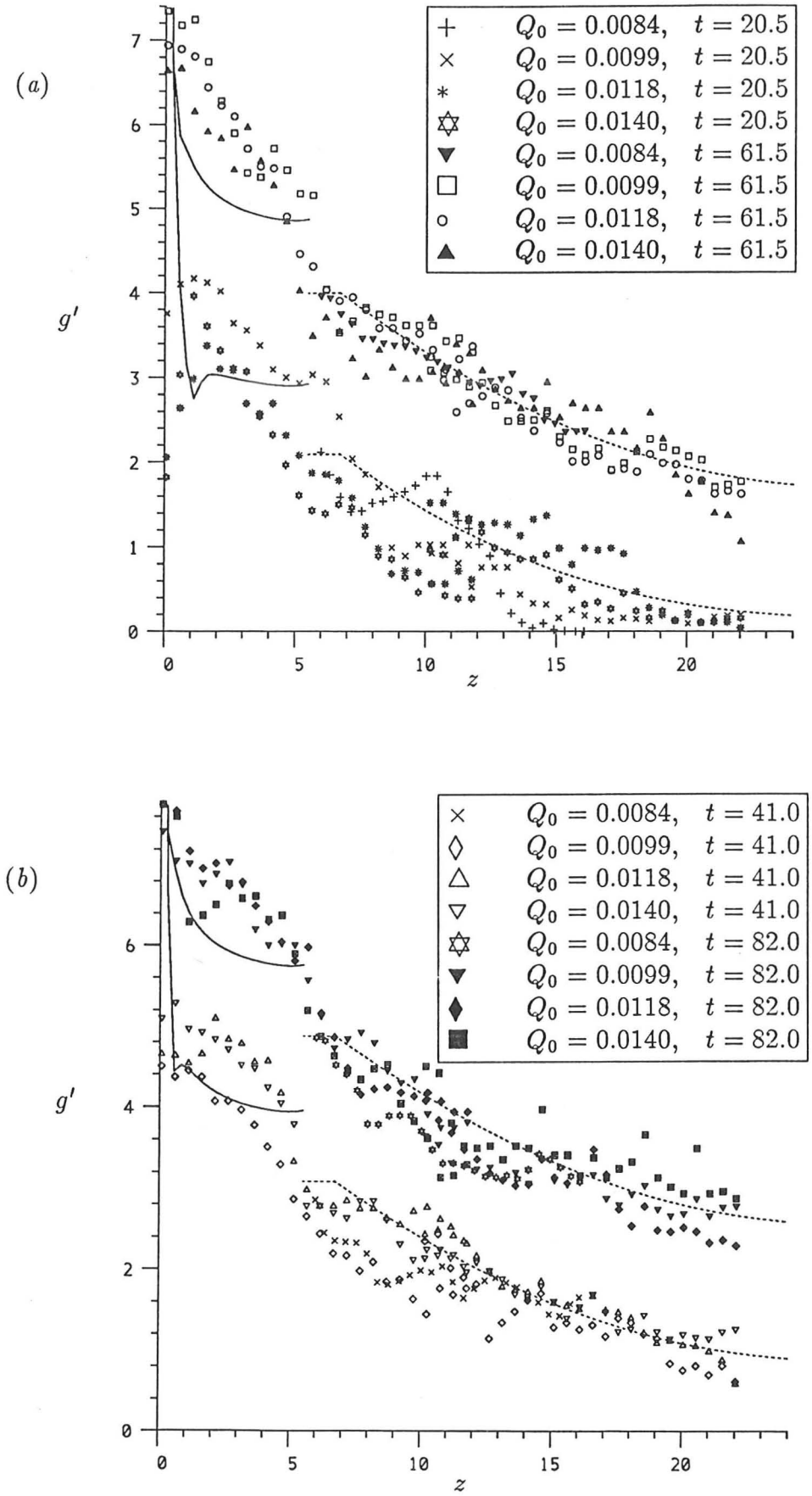

FIGURE 10. A comparison between the numerical solution (of figure 9) to the combined model and measurements from experiments in which $a = 24$ and $\theta = 15°$; (a) lower layer at $t = \Delta t$, $3\Delta t$; (b) lower layer at $t = 2\Delta t$, $4\Delta t$; (c) upper layer at $t = \Delta t$, $3\Delta t$; (d) upper layer at $t = 2\Delta t$, $4\Delta t$; where $\Delta t = 20.5$.

- - - - Mixed region and lower layer.

—— 'Centre-slice' concentration ($0 \leqslant z \leqslant h_1$), upper layer ($z \geqslant h_1 + h_2$).

(c)

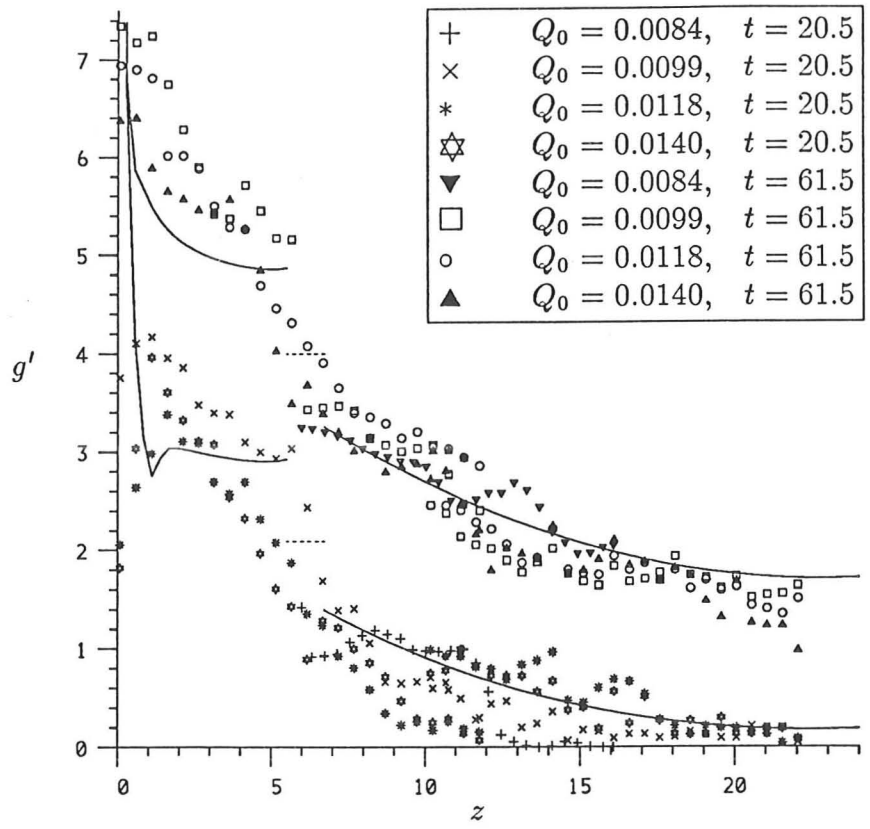

(d)

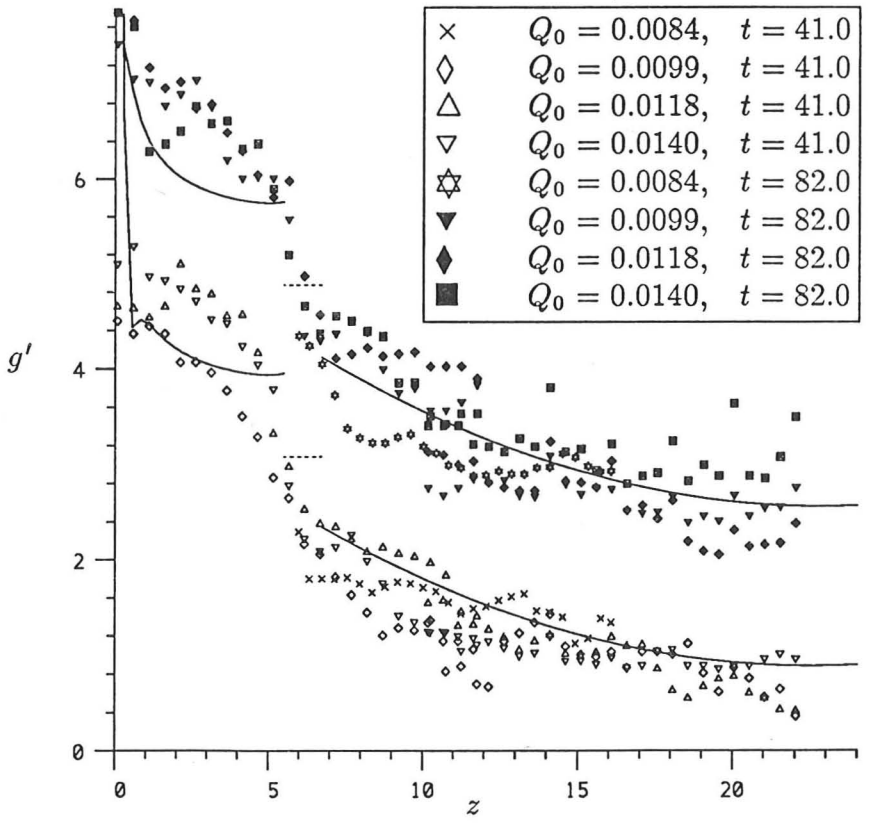

FIGURE 10. ct'd. A comparison between the numerical solution (of figure 9) to the combined model and measurements from experiments in which $a = 24$ and $\theta = 15°$; (c) upper layer at $t = \Delta t$, $3\Delta t$; (d) upper layer at $t = 2\Delta t$, $4\Delta t$; where $\Delta t = 20.5$.

- - - - Mixed region and lower layer.

—— 'Centre-slice' concentration ($0 \leqslant z \leqslant h_1$), upper layer ($z \geqslant h_1 + h_2$).

fluid into the plume environment than the model will predict (since it assumes uniform profiles). The agreement in the mixing region and counterflow is good for each profile. This means that the values chosen for the constants k_1 and k_2 work well in the whole model, even though they were chosen by comparison with the counterflow only and for one particular value of t (equal to $t_4 = 4\Delta t$ in the present comparison). The mixing region concentration approximately increases with $t^{0.61}$ which is in excellent agreement with the experimental estimation used in section 3.3.

Experiments were also carried out in order to measure the behaviour of the layer velocity, $W(t)$. The data (see figure 4) are plotted in figure 11, together with the theoretical behaviour of the layer velocity. Again there is considerable scatter of the experimental measurements, but the theoretical curve appears to agree well with the general behaviour. The theoretical solution demonstrates the general experimental observation that there is little variation in the layer velocity with time, except in the initial stages.

4.4 Application of the model

One of the motivations of this investigation was the knowledge that in many practical cases the orientation of a tall chamber will not be vertical but inclined. For practical reasons, most of the experiments were carried out with the tank placed at a small angle to the vertical although in many real situations the angle would be greater (around 60° for an escalator shaft, for example). For completeness, the model should be tested at larger values of θ than have been presented here so far. Four experiments were carried out to do this. Figures 12 and 13 show a comparison between experimental measurements and the theoretical predictions, in the cases $\theta = 38°$ and $\theta = 60°$, respectively. In the experiments, the region $4 \leqslant z \leqslant 20$ was recorded on video tape and so the measurements are restricted to this interval. It may be seen from the figures that the model still accurately predicts the experimentally measured values in the $\theta = 38°$ case, but the agreement is less good for $\theta = 60°$ (although the agreement is still reasonable). This may be because at large values of θ the confined plume equations may become inappropriate, as there may be significant interaction between the plume and the tank lower boundary. The value $\theta = 60°$ must therefore be regarded as the largest angle for which the model can be reliably applied.

In the experiments the end of the tube is closed. However, in many physical situations this may not be the case and the tunnel may have a space of large volume at the end (for

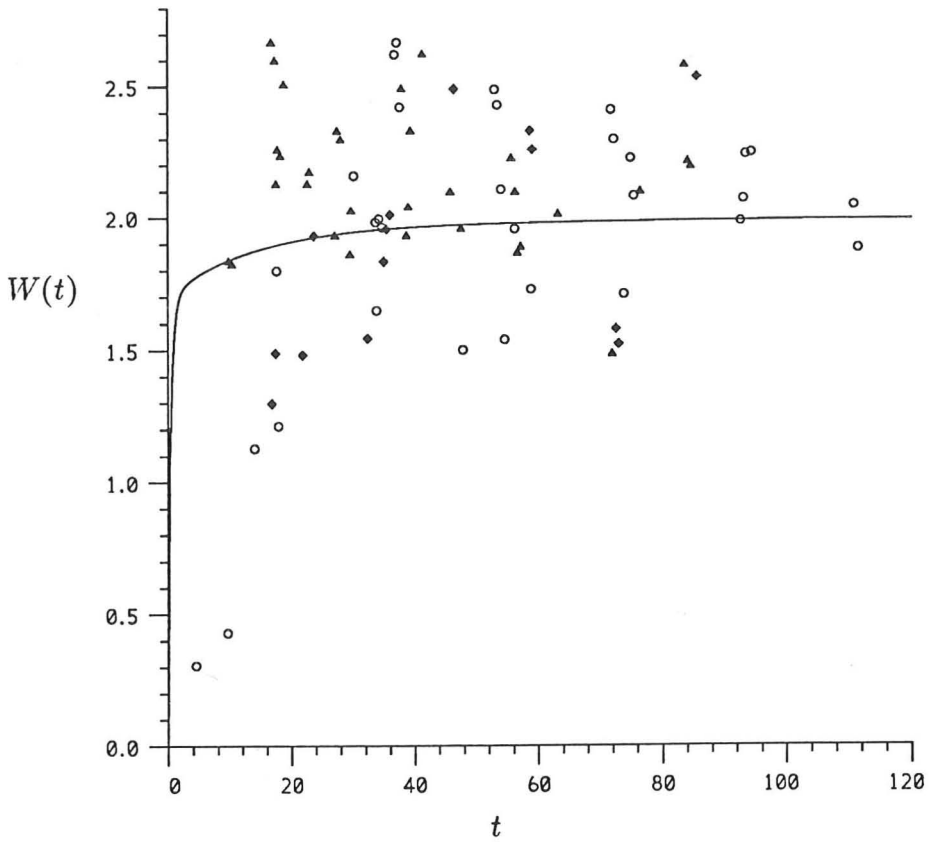

FIGURE 11. A comparison between the velocity measurements shown in figure 4 with the theoretical prediction in the case $a = 24$, $\theta = 15°$.

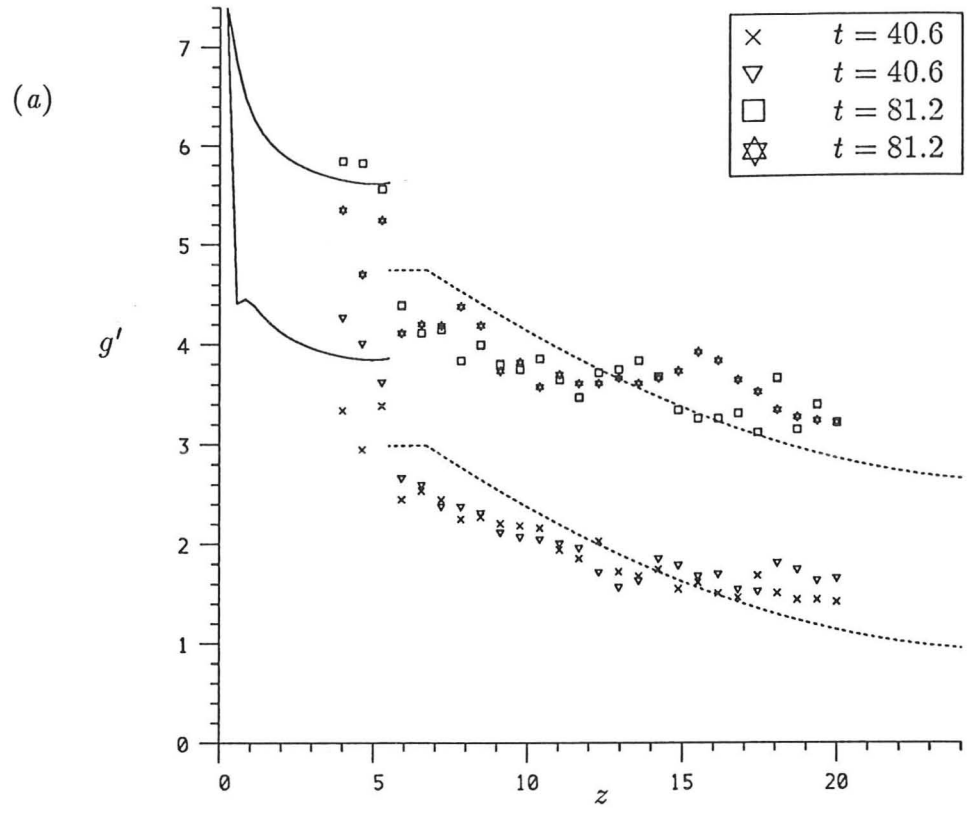

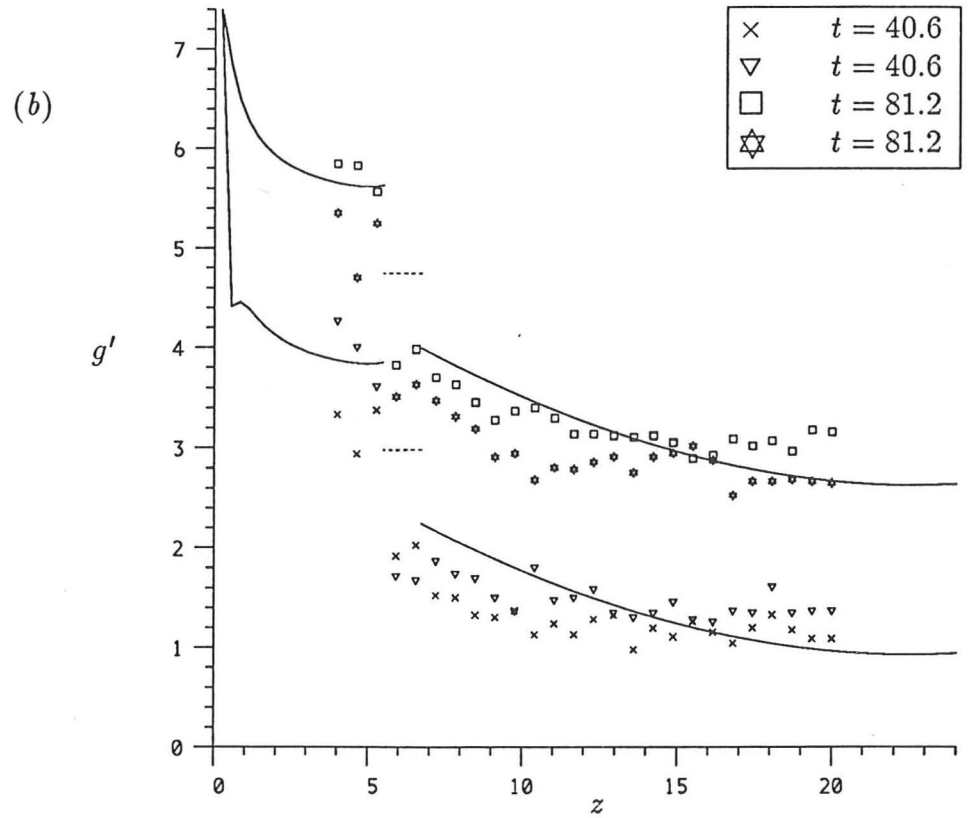

FIGURE 12. A comparison between the numerical solution to the combined model and measurements from experiments in which $a = 24$ and $\theta = 38°$; (a) lower layer at $t = \Delta t, 2\Delta t$; (b) upper layer at $t = \Delta t, 2\Delta t$; where $\Delta t = 40.6$.

- - - - Mixed region and lower layer.

—— 'Centre-slice' concentration ($0 \leqslant z \leqslant h_1$), upper layer ($z \geqslant h_1 + h_2$).

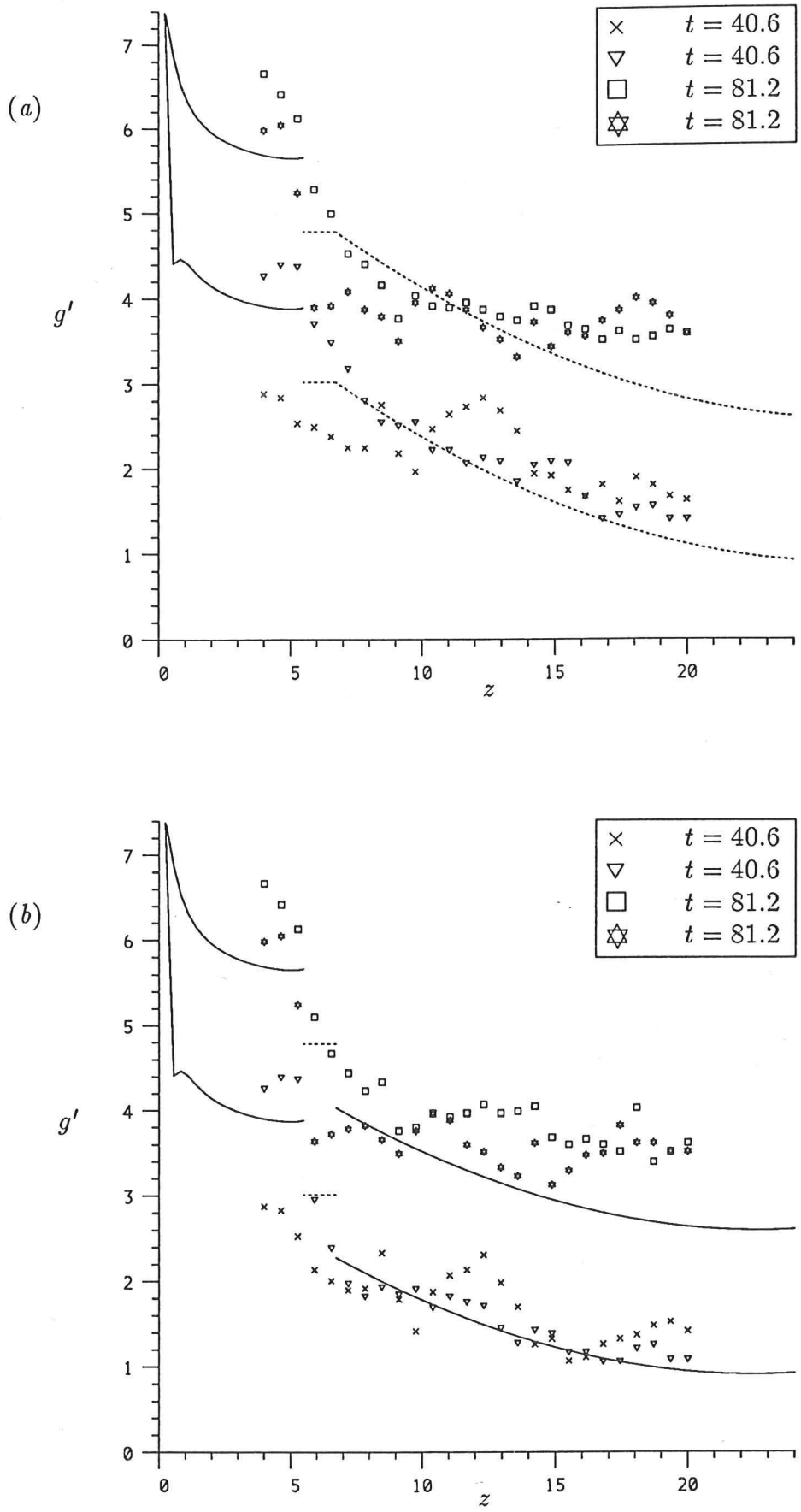

FIGURE 13. A comparison between the numerical solution to the combined model and measurements from experiments in which $a = 24$ and $\theta = 60°$; (a) lower layer at $t = \Delta t, 2\Delta t$; (b) upper layer at $t = \Delta t, 2\Delta t$; where $\Delta t = 40.6$.

- - - - Mixed region and lower layer.

—— 'Centre-slice' concentration ($0 \leqslant z \leqslant h_1$), upper layer ($z \geqslant h_1 + h_2$).

example, a hall above an underground escalator). The model could be easily adapted to such situations. One approach could be to assume that the large space is effectively another mixed region at the end of the tank. Buoyant fluid then flows in from the lower layer and is rapidly mixed throughout the large volume, whilst fluid from this region flows into the upper layer, back up the tunnel. Alternatively it could be assumed that the fluid entering the large space from the end of the tunnel forms a plume, which fills the large volume in the 'filling-box' manner.

Also, in many cases there may be a ventilation flow within the tunnel. In the case of the Underground, for example, ventilation is largely achieved by the piston effect of trains entering the station. This ventilation flow may be large and could significantly affect the flow. However, there may be circumstances in which the ventilation flow is negligible, or at least much smaller than the velocity of the buoyant layer. In this case the flow described here could be set up and the model applied. Ventilation of a large volume at the end of the tunnel could be achieved by incorporating an exchange flow through a vent in it, with a volume flux which could be estimated from the work of Linden, Lane-Serff & Smeed (1990, see also chapter 4).

5. Discussion and Conclusions

In this chapter the work of the previous chapter has been extended to cover the flow resulting from a source of buoyant fluid in a tall chamber placed at an angle $\theta > 0°$ to the vertical. Whilst θ is not too large, the plume and mixing region flows are similar to that observed in vertical chambers, but when $\theta \gtrsim 2°$ the convective region is now replaced by a two-layered stratified counterflow.

A model for the counterflow was developed, making the following assumptions: i) the speed of the layers depends only on the density difference at the top of the counterflow system (which varies in time); ii) each layer occupies half the total width of the tank; and iii) the mixing between the layers is dependent on the local bulk Richardson number of the flow according to the form found by Ellison & Turner (1959). These assumptions were based on experimental observations and the results of previous researchers. The first of these assumptions is based on the results of Britter & Linden (1980), namely that there is little dependence of the layer velocity on the angle for $0° < \theta \leqslant 85°$.

The theoretical predictions of the model were compared with experimental data in order to

determine appropriate values of the two constants k_1 and k_2. Consideration of the results of Britter & Linden (1980) suggested that k_1 was expected to be approximately $k_1 \simeq 2$. Perfect agreement with the results of Ellison & Turner (1959) would require $k_2 = 1$; however, it was suggested that greater mixing may take place in the present case than they measured due to the presence of the upper boundary, i.e. it was expected that $k_1 \gtrsim 1$. The best agreement was found when $k_1 = 2.43 \pm 0.08$ and $k_2 = 1.68 \pm 0.17$, both of which are consistent with the estimated values above. This value of k_2 implies a larger value of entrainment than was measured by Ellison & Turner (1959), as expected, but is nevertheless consistent with values measured by other experimenters. The numerical solution for the counterflow obtained using these values was found to agree well with experimental data.

The model of the counterflow was then incorporated into an overall model of the whole flow. The plume flow was modelled using the confined plume equations discussed in chapter 5, section 3. A mixing region of uniform density was used to couple the plume and counterflow regions, analogous to that used in chapter 5. The reduced gravity of the mixing region was used to define the reduced gravity of the fluid flowing into the environment of the plume and the reduced gravity of the fluid flowing into the lower layer of the counterflow. Good agreement with experimental data was found when the length of the mixing region was $h_2 = 1.23 \pm 0.15$, although there is considerable scatter in the data points. The theoretical behaviour of the layer velocity also agreed well with the experimental measurements. It was expected that the model would become increasingly less accurate as θ increases, because the equations for the plume and mixing regions were developed for the vertical case. However, reasonable agreement between the theoretical prediction and experimental measurements was still observed for $\theta = 60°$. Thus the application of the model is restricted to the range $2° \lesssim \theta \leqslant 60°$.

It was also described how the model could be easily applied to cases in which the end of the tunnel is not closed, instead leading to a large volume.

In summary, the effect of placing the tank at an angle to the vertical is to replace the convective region observed in vertical tanks with the counterflow, that has been the focus of attention in this chapter. The dependence on the actual value of the angle is solely incorporated in the Richardson number and thus on the mixing between the layers. In the experiments, the velocity of the buoyant layer was quite large - thus source fluid is more rapidly mixed with environmental fluid far from the source than in the vertical tank case. This is similar to the result observed in chapter 4 - the volume flow induced within the tank

is much greater than that of the source causing it. There is clearly a transition between the flows observed in chapter 5 to that of chapter 6 to that of chapter 4, as θ varies from 0° to 90°. With a vertical tank the plume breakdown gives rise to the dense mixed region which flows further down the tank in a completely disorganised manner ($Ri = 0$); when the tank is inclined, the flow becomes increasingly more organised as the angle increases ($Ri \propto \sin\theta$). In chapter 4, although the source had a large momentum flux, a region of dense fluid was still present, flowing further from the source in a counterflow. In this case there was negligible mixing between the layers and may be regarded as the extreme of the above transition ($Ri \simeq 1$).

Notation

Below is a list of the symbols used in this chapter, provided for reference purposes.

a	Aspect ratio
$B_{(0)}$	(Initial) specific buoyancy flux of the plume
b	Plume radius
d	Thickness of each layer in the counterflow
g	Acceleration due to gravity
$g'_{0,p,a,2,u,l}$	Reduced gravity of the source/plume/ambient/mixing/counterflow region fluid, relative to the reference density
g'_1	Reduced gravity of the plume fluid relative to the ambient density
H	Height of the tank
$h_{1,2,3}$	Height of the plume/mixing region/counterflow regions
$k_{1,2}$	Constants in the counterflow model
R	Effective radius of the tank
Ri	Richardson number
t	Time (non-dimensionalised using B_0)
u	Mean velocity in the x direction in the counterflow region
U	Mean (axial) velocity of the fluid in the environment of the plume
u_e	Entrainment velocity
v	Mean velocity in the y direction
w	Mean (axial) velocity of the plume fluid
W	Mean (axial) velocity of the lower layer
x	Cartesian coordinate perpendicular to axis and the interface between the buoyant layers
y	Cartesian coordinate
z	Axial coordinate
z'	Axial coordinate in the counterflow region
α_p	Entrainment constant for a plume
$\rho_{a,u,l,m,p,0}$	Density of the fluid in the plume environment, the upper and lower layers of the counterflow, the mixing region, the plume region and a reference density
θ	Angle of inclination of the tank to the vertical

Chapter Seven

General Conclusions

The general results of the work described in this thesis are summarised briefly, outlining industrial and other applications. The overall position of the understanding of flows resulting from the flow of a buoyant jet in a confined space is then presented in a simple tabular form, which also indicates areas for further research.

---

1. A brief summary of the general results

In this thesis, some of the flows that may result from the release of a buoyant fluid in a volume of limited extent have been examined. Many such flows may be described by using the 'filling-box' model (Baines & Turner 1969). In chapter 1 the 'filling-box' model was described, together with a discussion of its limitations and a review of some of the further work that has been based on it. From the latter it was apparent that the 'filling-box' model has been successfully applied to a large variety of flows. However, it was also clear that in a large number of practical flows (particularly industrial flows) some of the assumptions made in the model may not be appropriate, thus limiting its application. It was explained that there are three main limitations of the model, namely: i) that the source should be a pure plume; ii) that the source should be sufficiently far from the side boundaries so that there is no interaction between the side boundaries and the plume; iii) the aspect ratio (height/width) of the container is less than unity.

In general, there has been little work done on flows which do not satisfy the above restrictions. In this thesis, some flows which do not satisfy all of the above restrictions (i.e. the 'filling-box' model may not be applied) have been examined.

Throughout this thesis, the source of the buoyant fluid has been modelled as a turbulent jet, plume or buoyant jet. In chapter 2, the established knowledge of turbulent jets and plumes was summarised briefly. The main experimental investigations were listed and simple dimensional arguments were used to theoretically predict the axial variation of the mean flow variables.

Two established methods of predicting the transverse distribution of the axial velocity of a pure jet were then summarised. Neither of these solutions agrees well with the experimental measurements over the whole cross-section of the jet. An investigation of the possible causes of the disagreement between the theoretical predictions and the experimental measurements was then carried out, concentrating on the simplifications made in the two established solutions. It was found that including the neglected smaller terms in the analysis made little difference to the overall solution. However, on including the variation of the turbulent intermittency in the analysis, the theoretical prediction for the axial velocity distribution showed an improvement of up to 76% at the edge of the jet. During the analysis it was noted that the eddy viscosity turbulence model did not predict the turbulent product term ($\overline{v'^2} - \overline{u'^2}$) well. Further work is required to investigate whether a more sophisticated turbulence model might predict this term more accurately and possibly improve the theoretical predictions further still.

An important aspect of the flow of a confined buoyant release is the path followed by the source fluid. Knowledge of the trajectory will show whether the jet will impinge on the side boundaries of the container. If it does not, then the 'filling-box' model may be applied (depending on the nature of the source). However, if the jet impinges on a side wall, in most cases, the 'filling-box' model will be inappropriate. Knowledge of the mean concentration within the buoyant jet at points along its path may also be useful in applications to industrial waste removal. In chapter 3 a simple model of the flow of a buoyant jet was presented, derived by integrating the inviscid equations of motion over a cross-section through the jet flow. The resulting equations were investigated when applied to the flow of an initially horizontal release. Such integral models have been presented before but in this study the effect of the assumption determining the entrainment into the jet was investigated. The analysis may be readily applied to flows resulting from initially off-horizontal releases, and to releases in stratified environments.

In an initial investigation of the conservation equations it was found that, at all points along the trajectory, the reduced gravity is proportional to the horizontal mean velocity component. It was also shown that the buoyant jet follows an initially cubic trajectory

and that the centerline may only reach a maximum horizontal distance. The numerical solution showed that this maximum distance is approximately equal to ten jet-lengths from the source and that the jet-plume transition took place between about 2.2 and 7.6 jet-lengths from the source (horizontal displacement). The theoretically predicted trajectory agreed well with experimental measurements. Two assumptions about the nature of the entrainment were considered with surprisingly similar numerical solutions. Using both hypotheses, the numerical solution showed that the entrainment into the buoyant jet is greatest during the jet-plume transition part of the flow, possibly due to the high curvature of the jet trajectory there. It was not possible to choose between the two hypotheses using the experimental measurements and it would require further experiments of extreme accuracy to do so. This implies that both hypotheses are equally valid and that the actual form of the entrainment assumption seems to make little difference, as long as it is physically realistic. The results do, however, support the original assertion that it is not sufficient to assume that the entrainment constant is single-valued over the whole flow of a buoyant jet.

In chapter 4 the flow resulting from a vertical source of high momentum confined to a long, ventilated, tunnel was investigated. In this case the 'filling-box' requirement that the aspect ratio must be less than one was satisfied, however the source had high momentum as well as buoyancy. In fact it was observed that the impingement of the high velocity jet on the horizontal boundary gave rise to a well mixed region containing a circulation cell on either side of the source. Thus the 'filling-box' model could not be applied. It was concluded that the general effect of high source momentum on the resultant flow within the confining volume is to mix the source fluid rapidly with that of the environment to an extent dependent on the container geometry. In this case the mixed region was observed to extend to about 2.5 times the height of the tunnel on either side of the source. Thus for tanks with aspect ratio (height/width) greater than 1/5, it is expected that (assuming that the source is reasonably central and vertically directed) the tank will be well mixed (although this result may not apply for very tall tanks and for sources in which the jet-length is less than about three times the shortest distance between the nozzle and the opposite boundary). In the case considered in chapter 4, however, the aspect ratio was approximately 1/20 and the buoyancy forces become increasingly dominant (over momentum forces) with increasing distance from the source. At a distance of about 2.5 times the depth of the tank either side of the source, the mixing flow driven by the source momentum gives way to a two-layer stratified counterflow system.

The values of the mean flow variables in the steady state were deduced by analysing the flow over the 'head' of the buoyant layer. It was found that the depth of the buoyant layer is approximately half the depth of the tunnel, which agreed with experimental observations. By considering conservation of buoyancy and volume, it was found that the volume flux of the buoyant layers within the tunnel is several times larger than that of the source (about thirty times larger in the experiments) and that the reduced gravity of the buoyant layer is smaller than that of the source by an equal factor. The time dependent increase in the mean reduced gravity of the primary cell was also calculated. The theoretical prediction agreed well with the experimental measurements under the assumption that the fluid flowing into the buoyant layer from the mixed region has a concentration slightly lower than the mean concentration of the mixed region. This time dependent solution for the mixed region concentration could be used to derive a time dependent solution for the other flow variables. However, in most practical cases the steady state will be reached quickly and so the steady state solution will be of greater importance. The effect of ventilation within the tunnel was then studied. A method for calculating the flow out of and over a vent far from the source was deduced, which may be used to calculate the minimum number of vents required to vent all of the buoyant layer. When a vent is located near to the source, the flow becomes more complicated as environmental fluid may be 'sucked' in through this vent. The above solutions for the bulk flow variables and the primary cell reduced gravity may all be modified to include this effect, although further research is required to determine the precise relationship between the volume flux of the fluid sucked in through this vent on the position of the vent, the strength of the source and the tunnel geometry.

This work has obvious applications to the flow of a release of buoyant gas within a ventilated tunnel or duct, using the theoretical model to calculate the values of the flow variables. In this case the effect of the ventilation may be of great importance, for if the gas is hazardous, then it is desirable that it should be removed from the tunnel as effectively as possible. In practice, of course, it is not possible to predict the position of a release originating from a small crack or hole in a pipe caused by corrosion. In such cases the tunnel should ideally have vents of sufficiently large area, so that all of the buoyant gas layer resulting from a leak may be vented with one vent only. The vents should be placed sufficiently far apart so that the chance of a leak occurring near to a vent is small, although if this was the case, any air 'sucked' in through this vent would act to reduce the overall concentrations reached.

Another of the restrictions on the 'filling-box' model, namely that the aspect ratio must be

less than one, was investigated in chapter 5. In this chapter the flow resulting from a release of buoyancy from a point source at one end of a tall chamber (aspect ratio greater than one) was studied. Experimental observations revealed that the main difference between the resultant flow in moderate aspect ratio containers and the 'filling-box' flow was to produce non-uniformities, on horizontal levels, of the velocity and density distributions of the fluid in the environment of the plume. This is because in containers with aspect ratio less than one, the area occupied by the plume (on a horizontal plane) is negligible compared with that of the environmental fluid and thus the effect of the plume flow on the environmental fluid flow is small. Consequently the profiles of velocity and density are approximately uniform on horizontal levels in the environment of the plume. However, in taller containers, the plume area may become comparable to that of the environmental fluid and thus there is a proportionately greater effect of the plume flow on the environmental fluid, resulting in non-uniformities in the velocity and density profiles.

The 'filling-box' model equations were modified to include the momentum flux of the environmental fluid (which may now be large far from the source), although mean values on horizontal planes were still considered in the analysis. It was found that the predictions of these equations agreed well with the observed concentrations, particularly at the tank base (for a negatively buoyant source), in spite of neglecting any additional effects due to the non-uniformity of the environment velocity and density.

However, in tanks of very large aspect ratio $a \gtrsim 5.8$, the environment momentum flux may become equal to that of the plume. In practice this was observed to result in a breakdown in the plume flow, giving rise to a region of dense fluid (for a negatively buoyant source) at the base of the plume. This region is unstably stratified and the dense fluid mixes with the fluid further from the source by turbulent convection. The numerical solution to the modified confined plume equations in an unstratified environment revealed that this plume breakdown is expected to occur at approximately 5.8 effective radii downstream of the source. Thus two flow regimes exist depending on the aspect ratio of the tank. If the aspect ratio is sufficiently small such that this plume breakdown does not occur ($a < 5.8$), then the flow is like the 'filling-box' flow with horizontal non-uniformities (described above); but if the aspect ratio is larger, then this plume breakdown threshold is reached giving rise to the convective region mentioned above.

In the model of the latter case, the mean flow in the convective region was modelled using a one dimensional diffusion equation with a constant eddy diffusivity and the flows

of the plume and convective regions were coupled by the use of a mixing region of uniform density. The numerical solution agreed well with the experimental results when the length of the mixing region was approximately equal to the effective diameter of the container, which is consistent with experimental observations. One of the main features of the overall flow is that the buoyant fluid is mixed throughout the convective region more slowly than the concentration increases in the plume region. Thus in the case of a natural gas leak at the bottom of a tall tower, for example, the gas concentration will increase rapidly near to the source (in the plume region), but will increase more slowly near to the top of the tower (see chapter 5).

The study of flows in containers with large aspect ratios was continued in chapter 6. In this chapter the chamber was placed at an angle to the vertical with a buoyant source at one end. The plume and mixing regions appeared to exist as in the vertical chamber case above but now fluid flows from the mixed region as a gravity current occupying approximately half the depth of the tank. This is because there is now a component of gravity acting perpendicular to the axis of the tank. The end of the tank is closed and so an equal and opposite flow exists in the other half of the tank, with mixing between the layers (see chapter 6, figure 1).

A simple model of the two layered region was presented which assumed that the acceleration of the buoyant layers along the slope was negligible and that each layer occupied half the depth. The mixing between the two layers was assumed to be dependent on the local Richardson number of the flow. The two-layer flow was coupled to the plume flow by using a mixed region of uniform density (as in the model for flows in vertical chambers). The numerical solution for the reduced gravities and layer velocity agreed well with the experimental measurements. Comparison between this case and the vertical case of chapter 5 revealed that the two-layer flow mixes the buoyant fluid from the plume with that further from the source more rapidly than was observed with the convective flow obtained with a vertical chamber. Thus gas from a slow leak at the base of an angled (unventilated) tunnel would be expected to reach points further along the tunnel more quickly than would be found in a vertical tower.

Of course, in many practical cases, the end of the tunnel would not be closed (consider, for example, a slow gas leak at the bottom of an escalator shaft in an Underground station) and would lead to a large space (for example, the entrance hall). It was explained that in such cases the model could be adapted by using another mixed region, representing the large space, at the base of the tunnel (for dense sources). A flow of buoyancy out of the large mixed region could be incorporated to simulate ventilation of the large region.

2. A summary of confined jet flows: areas for further research

It was stated in chapter 1 that the flow resulting from a release of buoyant fluid in a confined space will depend on several factors, including: the source characteristics and orientation, the geometry of the container, interaction between the source fluid and the container boundaries, and ventilation of the container. The flows resulting from buoyant sources with small volume fluxes are summarised in table 1. The source momentum is defined as 'high' if the jet-length (see chapter 2) is greater than the distance between the source and the nearest boundary ($\delta > 1$) and 'low' if the opposite is true. Vertical and horizontal source orientations are included - with vertical sources the momentum may be either in the direction that the buoyancy force acts ($\uparrow$) or against the buoyancy ($\downarrow$). The flows also depend on the aspect ratio (height/width), a, of the container and its angle to the vertical.

The table reveals several areas requiring further research. The effect of high source momentum has been investigated in low to moderate aspect ratio containers but the effect of high source momentum on the flows described in chapters 5 and 6 is unclear. If the source is directed along the axis of the tank, then it is probable that the jet flow will still breakdown at some point downstream from the source. However, the increased momentum of the source may cause a greater mixing of the fluid there, resulting in an increase in the length of the mixing region. The effect of placing the source at some other orientation (high or low source momentum flux) has not been investigated. If the source has little or no initial momentum flux (as was assumed in chapters 5 and 6) then the jet length will be small and so the flow will quickly become plume-like. In this case the orientation of the source is unlikely to have a significant effect. However, if the source has high momentum (i.e. $\delta > 1$) then the jet may impinge on the walls of the container. This could result in a greater level of mixing in the source region and circulation cells may be driven. The effect of placing the source along the axis of the tunnel in chapter 4 has also not been studied (for both high and low source momentum fluxes). In this case the flow will be very different to that studied, as the circulation cells will not be present.

Table 1 is restricted to sources with small volume fluxes - that is, cases in which the time that would be taken for the source fluid to fill the tank is large. There is currently little knowledge of the flows that may result from a source with a large volume flux (although in chapter 4 it was noted that for sufficiently large volume fluxes, the flow altered to a situation in which the source fluid formed a 'plug', which simply pushed all of the environmental fluid

Container Geometry	Source Momentum	Source Orientation	Flow Expected
Moderate	Low	V↑	'Filling-box' flow; Baines & Turner (1969)
Aspect Ratio	$\delta < 1$	V↓	'Fountain' flow; Baines, Turner & Campbell (1990)
		H	Possibly 'filling-box' depending on L_j; see chapter 3
$a \sim O(1)$	High	V↑	Mixing of interior depending
	$\delta > 1$	V↓	on orientation, δ and a.
		H	(see Linden, Marshall & Cleaver 1991)
High	Low	V↑	See chapter 5
Aspect Ratio	$\delta < 1$	V↓	Probably 'fountain' flow
		H	Possibly as chapter 5, depending on L_j
$a \gg 1$	High	V↑	Not yet studied
	$\delta > 1$	V↓	Not yet studied
		H	Not yet studied
Low	Low	V↑	'Filling-box' flow; Baines & Turner (1969)
Aspect Ratio	$\delta < 1$	V↓	'Fountain' flow; Baines, Turner & Campbell (1990)
		H	Not yet studied
$a \ll 1$	High	V↑	See chapter 4
	$\delta > 1$	V↓	See chapter 4
		H	Not yet studied
Tall, Angled	Low	$\perp$	Possibly as chapter 6, depending on L_j
Containers	$\delta < 1$	$\parallel$	See chapter 6
	High	$\perp$	See chapter 4
	$\delta > 1$	$\parallel$	Not yet studied

a is the aspect ratio (height/width) of the container; $\delta = L_j/P$ is the ratio between the jet-length (L_j) and the distance between the source and the nearest boundary (P); 'V' denotes a vertical release, ↑: buoyancy forces acting in the same direction as the momentum flux, ↓: buoyancy forces oppose momentum; 'H' denotes a horizontal release; in angled containers '$\perp$' and '$\parallel$' denote releases perpendicular and parallel to the axis respectively.

TABLE 1. The flows resulting from confined buoyant sources with small volume fluxes.

from the tunnel). It is likely that in such cases the large volume flux of the source will dominate the flow, with the container being rapidly filled with source fluid. Also, such flows can be relatively difficult to achieve in the laboratory. Obtaining volume fluxes sufficiently large, so that the time taken for the source fluid to fill the tank would be small, may require that a very small scale model is used, which consequently makes experimental measurements awkward and less reliable.

The effect of an overall ventilation flow also needs further attention. Clearly the effect of ventilation will depend on the relative orders of magnitude between the ventilation flow and the buoyant fluid flow. In many practical situations the velocities induced by ventilation systems may be quite small and thus may have little effect on the flow resulting from the buoyant release.

One final area of interest requiring investigation is the flow of a buoyant release in two or more connected regions. In many industrial and domestic cases, confining volumes will not be completely sealed and will be connected to other spaces by a doorway, corridor or ventilation system. It would therefore be useful to investigate the spread of a release in one space into another. For a purely buoyant source, the flow in each region would probably be similar to the 'filling-box' flow. However, if the source had a large jet-length, then fluid from the adjacent tank could be 'sucked' into the region containing the source, in a manner similar to that observed in the flow of chapter 4 (section 2.2.3).

From the 'filling-box' model, the previous work based on it and the work contained in this thesis, it is clear that the range of possible confining containers and source types give rise to a large variety of possible flows that may result from the release of a buoyant fluid in a confined space. Whilst there are a few general areas of interest which still require further investigation, there is now a good understanding of the dependence of the flow on the source type, container geometry and ventilation. This understanding allows a reliable prediction of the flow in a given situation to be made. In the case of a hazardous release, such predictions may be used to incorporate design features which will reduce the concentrations reached, thus improving public safety.

Notation

Below is a list of the symbols used in this chapter, provided for reference purposes.

a	The aspect ratio (height/width) of the container
L_j	Length scale of a buoyant jet or 'jet-length'
P	The shortest distance between the nozzle and a boundary of the container
δ	Ratio of L_j to P
u'	Turbulent velocity component (see chapter 2)
v'	Turbulent velocity component (see chapter 2)

References

ABRAMOVITCH, G.N. 1963 *The theory of turbulent jets.* MIT Press

BAINES, W.D. 1975 Entrainment by a plume or jet at a density interface. *J. Fluid Mech.* **68**, 309-320.

BAINES, W.D. & TURNER, J.S. 1969 Turbulent buoyant convection from a source in a confined region. *J. Fluid Mech.* **37**, 51-80.

BAINES, W.D., TURNER, J.S. & CAMPBELL, I.H. 1990 Turbulent fountains in an open chamber. *J. Fluid Mech.* **212**, 557-592.

BENJAMIN, T.B. 1968 Gravity Currents and related phenomena. *J. Fluid Mech.* **31**, 209-248.

BRADBURY, L.J.S. 1965 The structure of a self-preserving turbulent plane jet. *J. Fluid Mech.* **23**, 31-64.

BRADSHAW, P. 1977 Effect of external disturbances on the spreading rate of a plane turbulent jet. *J. Fluid Mech.* **80**, 795-797.

BRITTER, R.E. & LINDEN, P.F. 1980 The motion of the front of a gravity current travelling down an incline. *J. Fluid Mech.* **99**, 531-453.

CHAN, D.T.L. & KENNEDY, J.F. 1975 Submerged buoyant jets in quiescent fluids. *J. Hydraul. Div. ASCE* **101**, 733-747.

ELLISON, T.H. & TURNER, J.S. 1959 Turbulent entrainment in stratified flows. *J. Fluid Mech.* **6**, 423-448.

FAN, L.-N. 1967 Turbulent buoyant jets into stratified or flowing ambient fluids. *Tech. Report no. KH-R-18* W. M. Keck Lab. Hydraul. & Water Res., Calif. Inst. Tech., Pasadena, Calif..

FISCHER, H.B., LIST, E.J., KOH, R.C.Y, IMBERGER, J. & BROOKS, N.H. 1979 *Mixing in inland and coastal waters.* Academic Press Inc..

FORTHMANN, E. 1936 Turbulent jet expansion. *NACA, TM-***789**. (Details of this paper may be obtained from Rajaratnam 1976).

GERMELES, A.E. 1975 Forced plumes and mixing of liquids in tanks. *J. Fluid Mech.* **71**, 601-623.

GEORGE W.K., ALPERT, R.L. & TAMANINI, F. 1977 Turbulence measurements in an axisymmetric buoyant plume. *Int. J. Heat Mass Transfer* **20**, 1145-1154.

GOERTLER, B. 1942 Berechnung von Aufgaben der freien Turbulenz auf Grund eines neuen Naherungsanstazes. *ZAMM* **22**, 244-254.

GUTMARK, E. & WYGNANSKI, I. 1976 The planar turbulent jet. *J. Fluid Mech.* **73**, 465-495.

HESKESTAD, G. 1965 Hot wire measurements in a plane turbulent jet. *Trans. ASME J. Appl. Mech.* **32**, 721-734.

HUPPERT, H.E., SPARKS, R.S.J., WHITEHEAD, J.A. & HALLWORTH, M.A. 1986 Replenishment of magma chambers by light inputs. J. Geophys. Res. **91**, 6113-6122.

JIRKA, G.H. & HARLEMAN, D.R.F. 1979 Stability and mixing of a vertical plane buoyant jet in confined depth. *J. Fluid Mech.* **94**, 275-304.

KATO, H. & PHILLIPS, O.M. 1969 On the penetration of a turbulent layer into stratified fluid. *J. Fluid Mech.* **37**, 643-655.

KILLWORTH, P.D. & TURNER, J.S. 1982 Plumes with time-varying buoyancy in a confined region. *Geophys. Astrophys. Fluid Dynamics* **20**, 265-291.

KOTSOVINOS, N.E. 1976 A note on the spreading rate and virtual origin of a plane turbulent jet. *J. Fluid Mech.* **77**, 305-311.

KOTSOVINOS, N.E. & LIST, E.J. 1977 Plane turbulent buoyant jets. Part 1. Integral properties. *J. Fluid Mech.* **81**, 25-44.

KOTSOVINOS, N.E. 1977 Plane turbulent buoyant jets. Part 2. Turbulence structure. *J. Fluid Mech.* **81**, 45-62.

KOTSOVINOS, N.E. 1985 Temperature measurements in a turbulent round plume. *Int. J. Heat Mass Transfer* **28**, 771-777.

KOTSOVINOS, N.E. & ANGELIDIS, P.B. 1991 The momentum flux in turbulent submerged jets. *J. Fluid Mech.* **229**, 453-470.

KUMAGAI, M. 1984 Turbulent buoyant convection from a source in a confined two-layered region. *J. Fluid Mech.* **147**, 105-131.

LANE-SERFF, G.F. 1989 *Heat flow and air movement in buildings.* PhD. thesis, University of Cambridge.

LANE-SERFF, G.F., LINDEN, P.F. & HILLEL, M. 1990 Angled buoyant plumes. *Submitted to J. Haz. Materials*

LEE, H.-W. 1980 Stability and mixing of a round buoyant discharge in shallow water. *2nd Int. Symp. on Stratified Flows, Trondheim, Norway* 881-897.

LEE, S.-L. & EMMONS, H. W. 1961 A study of natural convection above a line fire. *J. Fluid Mech.* **11**, 353-368.

LIANG, S.F., VIDAL, A. & ACRIVOS, A. 1969 Buoyancy-driven convection in cylindrical geometries. *J. Fluid Mech.* **36**, 239-256.

LINDEN, P.F., LANE-SERFF, G.F. & SMEED, D.A. 1990 Emptying filling boxes: the fluid mechanics of natural ventilation. *J. Fluid Mech.* **212**, 309-335.

LINDEN, P.F., MARSHALL, M.R. & CLEAVER, R.P. 1991 *In preparation.*

LIST, E. J. 1982 Turbulent jets and plumes. *Ann. Rev. Fluid Mech.* **14**, 189-212.

MCDOUGALL, T.J. 1983 Double-diffusive plumes in unconfined and confined environments. *J. Fluid Mech.* **133**, 321-343.

MANINS, P.C. 1979 Turbulent buoyant convection from a source in a confined region. *J. Fluid Mech.* **91**, 765-781.

MARSHALL, M.R. & CLEAVER, R.P. 1991 *In preparation.*

MILLER, D.R. & COMINGS, E.W. 1957 Static pressure distribution in the free turbulent jet. *J. Fluid Mech.* **3**, 1-16.

MIH, W.C. & HOOPES J.A. 1972 Mean and turbulent velocities for plane jet. *J. Hydraul. Div. ASCE* **98**, 1275-1294.

MONCRIEFF, M.W. & SO, D.W.K. 1989 A hydrodynamical theory of conservative bounded density currents. *J. Fluid Mech.* **198**, 177-197.

MORTON, B.R. 1959 Forced Plumes. *J. Fluid Mech.* **5**, 151-163.

MORTON, B.R., TAYLOR, G. & TURNER J.S. 1956 Turbulent gravitational convection from maintained and instantaneous sources. *Proc. Roy. Soc.* **234**, 1-23.

NEUMANN, G. 1990 Three-dimensional numerical simulation of buoyancy-driven convection in vertical cylinders heated from below. *J. Fluid mech.* **214**, 559-578.

OLSEN, J.M. & ROSENBERGER, F. 1979 Convective instabilities in a closed vertical cylinder heated from below. Part 1. Monocomponent gases. *J. Fluid mech.* **92**, 609-629.

PAPANICOLAOU, P.N. & LIST, E. J. 1988 Investigations of round vertical turbulent buoyant jets. *J. Fluid Mech.* **195**, 341-391.

PRIESTLEY, C.H.B. & BALL, F.K. 1955 Continuous convection from an isolated source of heat. *Q. J. Royal Met. Soc.* **81**, 144-157.

RAJARATNAM, N. 1976 *Turbulent jets.* Elsevier Scientific Publ. Co..

RAMAPRIAN, B.R. & CHANDRASEKHARA, M.S. 1983 Study of vertical plane turbulent jets and plumes. *IIHR Rep. 257*, Iowa Inst. of Hydraulic Research.

RICOU, F.P. & SPALDING, D.B. 1961 Measurements of entrainment by axisymmetrical turbulent jets. *J. Fluid Mech.* **11**, 21-32.

ROUSE, H., YIH, C.S. & HUMPHREYS, H.W. 1952 Gravitational convection from a boundary source. *Tellus* **4**, 201-210.

SAMI, S., CARMODY, T. & ROUSE, H. 1967 Jet diffusion in the region of flow establishment. *J. Fluid Mech.* **27**, 231-252.

SCHATZMANN, M. 1976 Auftriebsstrahlen in natürlichen Strömungen entwicklung eines mathematischen modells. *Rep. SFB 80/T/86.* University of Karlsruhe.

SCHATZMANN, M. 1979 An integral model of plume rise. *Atmos. Envir.* **13**, 721-731.

SIMPSON, J.E. 1987 *Gravity currents: in the environment and the laboratory.* Ellis Horwood Ltd..

TOLLMIEN, W. 1926 Berechnung turbulenter Ausbreitungsvorgänge. *ZAMM* **6**, 468-478.

TOWNSEND, A.A. 1956 *The structure of turbulent shear flow.* Cambridge University Press

TURNER, J.S. 1973 *Buoyancy effects in fluids.* Cambridge University Press.

TURNER, J.S. 1986 Turbulent entrainment: the development of the entrainment assumption, and its application to geophysical flows. *J. Fluid Mech.* **173**, 431-471.

WILKINSON, D.L. & WOOD, I.R. 1971 A rapidly varied flow phenomenon in a two-layer flow. *J. Fluid Mech.* **47**, 241-256.

WORSTER, M.G. & HUPPERT, H.E. 1983 Time-dependent profiles in a filling box. *J. Fluid Mech.* **132**, 457-466.

WYGNANSKI, I.J. & FIEDLER, H.E. 1969 Some measurements in the self-preserving jet. *J. Fluid mech.* **38**, 577-612.

YIH, C.-S. & WU, F. 1981 Round buoyant laminar and turbulent plumes. *Phys. Fluids* **24**, 794-801

ZIJNEN, B.G. 1958 Measurement of the velocity distribution in a plane turbulent jet of air. *Appl. Sci. Res. Sect. A* **7**, 256-276.